Novel Ultra-Violet/Blue Optoelectronic Materials and Devices Based on Copper Halides (CuHa)

By

Aidan James Cowley

B.Sc in Computer Applications, M.Eng in Electronic Systems

Thesis Submitted for the degree of Doctor of Philosophy

Research Supervisor

Prof. Patrick J. McNally

Dublin City University School of Electronic Engineering

2011

Declaration

I hereby certify that this material, which I now submit for assessment on the programme of study leading to the award of PhD is entirely my own work, that I have exercised reasonable care to ensure that the work is original, and does not to the best of my knowledge breach any law of copyright, and has not been taken from the work of others save and to the extent that such work has been cited and acknowledged within the text of my work.

Signed: _____

ID No.: _____

Date: _____

Acknowledgments

I am lucky in having benefited from the support, teaching and guidance of some truly excellent people during the time taken for this PhD. It is a pleasure, therefore, to accord those involved (directly and otherwise) a grateful and heartfelt acknowledgment.

None of this work would have been possible were it not for the opportunity many years ago to become involved with the Copper Halide materials during my M.Eng degree. Little did I realize then that, in addition to destroying many perfectly fine printer cartridges with acid, I would be most fortuitous in having Prof. Patrick McNally as my supervisor. Having the opportunity to do a PhD years later under the same supervisor would allow me to fulfill this great personal ambition and has been an awesome and enlightening experience. Thank you kindly for all the great support, advice and supervision over the years (and for the simple opportunity to allow this erstwhile programmer the chance to do something *completely* different).

So much background work involving the procedures for dealing with, depositing and investigating CuCl material was previously established by the excellent work of NPL alumni. I am thusly indebted to Dr. Lisa O'Reilly and Dr. Francis Olabanji Lucas for laying so much of the groundwork for my own research and providing many valuable insights. I am also grateful to have worked alongside fellow Copper Halide enthusiasts and NPL/NCPST colleagues Rajani, Monjarul and Barry.

Many thanks to Dr. Andreas Danilewsky of Freiburg University, for the chance to visit his faculty in order to advance my knowledge of LPE as well as being kindly generous with his time in visiting

our own labs to assist with our own LPE system. I am also indebted to Dr. Stephen Daniels for his sage advice and assistance over the years.

My thanks to the NPL/NCPST technical staff, particularly Mr. Billy Roarty for his continuously educational engineering solutions, as well as Mr. Robert Clare, Mr. Conor Murphy and Ms. Jennifer Stopford for their technical support and friendship. Likewise, to my NPL/NCPST colleagues Ken, Nick, Dave, Evgueni, Niall and Ameera for making the lab a great place to work in to this day.

To my friends, who endured many, many rants about various esoteric aspects of my work. Particular thanks to my good friend Brian and Dr. Stuart Corr, for being excellent sounding boards for all sorts of ‘out-there’ ideas.

To my girlfriend, Kimberly, for always being there with love and support.

To my family; my brother John - you may still call me ‘legi’ but we’re two volumes of the same book. Lastly, but most importantly, I am eternally grateful to my mother and father, Phyl and Jim Cowley. Their unwavering support, encouragement and love has been the foundation for all my endeavors. To them, I dedicate this thesis.

Abstract

Considerable research is being carried out in the area of wide band gap semiconductor materials for light emission applications in the UV/Blue (300-400 nm) spectral range. This project explores the novel use of the Copper Halides (CuHa), specifically γ-CuCl and γ-CuBr, I–VII wide band gap mixed ionic–electronic semiconducting materials with light emitting properties suitable for novel UV/blue light applications.

This project details novel research carried out towards achieving single crystal growth of γ-CuCl from solution via Liquid Phase Epitaxy (LPE) based techniques. LPE growth runs are undertaken using an alkali halide flux compound (KCl) to depress the liquidus temperature of CuCl below its solid phase wurtzite-zincblende (β → γ) transition temperature for solution based epitaxy on lattice matched Si substrates (lattice constant of γ-CuCl (0.541 nm) is closely matched to that of Si (0.543 nm). Results show that the resulting KCl flux-driven deposition of CuCl onto the Si substrate has yielded superior photoluminescence (PL) and X-ray excited optical luminescence (XEOL) behaviour relative to comparatively observed spectra for GaN or polycrystalline CuCl. The resulting deposited material is a textured CuCl/K_2CuCl_3 polycrystalline intermix, with strong broad luminescence and novel luminescent characteristics not previously observed in CuCl. Difficulties inherent to LPE with CuCl/KCl melts, particularly with the CuCl/KCl eutectic system and the CuCl/Si surface reaction, are detailed.

The use of γ-CuBr for thin film based blue light emitting devices is investigated. Its structural and physical properties allow for vacuum deposition on a variety of substrates and herein we report on the deposition of γ-CuBr on Si, glass and indium tin oxide coated glass substrates via vacuum evaporation with controllable film thickness from 100 to 500 nm. Temperature dependent

photoluminescence characteristics of these γ-CuBr films on Si substrates reveal familiar Z_f and I_1 excitonic features. Work towards the development of a thin film electroluminescent device using a γ-CuBr active layer is outlined.

Recently, dramatic improvements in the luminescent intensity of CuBr generated by the chemical interaction between CuCl films and KBr substrates have been demonstrated. The potential improvements in excitonic PL that can be gained from novel approaches to film preparation involving KBr and existing CuBr deposition techniques is promising. We report on the one such novel approach, the vacuum deposition of KBr spots (~30 μm radius) onto similarly deposited γ-CuBr epitaxial layer on a Si substrate. Post-deposition annealing of the samples at 220 °C in conjunction with a small CuBr flux from a target source leads to the formation of intermixed CuBr/ KBr microdots. PL characterisation reveals enhanced UV-Blue excitonic emission centered on the Z_f free exciton peak at ~418 nm, far superior to Z_f emission from γ-CuBr films deposited previously. An overview of the deposition process involving shadow masks to lay down an ordered array of KBr spots onto a γ-CuBr vacuum evaporated layer is presented, and the samples are characterised using XRD, EDX and spatially resolved room temperature PL.

List of Abbreviations

AC	*Alternating Current*
ACTFELD	*Alternating Current Thin Film Electroluminescent Device*
AFM	*Atomic Force Microscope*
DC	*Direct Current*
EDX	*Energy Dispersive X-Ray Analysis*
ELD	*Electroluminescent Device*
ELOG	*Epitaxial Lateral Overgrowth*
FWHM	*Full Width at Half Maximum*
HVPE	*Hydride Vapor Phase Epitaxy*
HWHM	*Half Width at Half Maximum*
IR	*Infra Red*
LD	*Laser Diode*
LED	*Light Emitting Diode*
LPE	*Liquid Phase Epitaxy*
MBE	*Molecular Beam Epitaxy*
MOCVD	*Metal-Organic Chemical Vapor Deposition*
MOVPE	*Metal-Organic Vapor Phase Epitaxy*
NIC	*Nomarski Interference Contrast*
PL	*Photoluminescence*
PLD	*Pulsed Laser Deposition*
PVD	*Physical Vapor Deposition*
RA	*Roughness Average*
RMS	*Roughness Mean Square Average*
SEM	*Scanning Electron Microscope*
SIMS	*Secondary Ion Mass Spectroscopy*
TFELD	*Thin Film Electroluminescent Device*
UV-Vis	*Ultra-Violet - Visible Spectroscopy*

Chapter 1 - Introduction

1.1 Introduction

The use of semiconductor devices in society is undisputedly pervasive and their effects are profoundly far reaching. Society's technological progress is arguably driven by leveraging the scientific and engineering capacity of semiconductor materials, whether for further iteration of established technologies or for entirely new areas of application. Solid state lighting, the application of light emitting semiconductor devices for efficient light emission, is poised to have a considerable impact on energy usage due to the direct transfer of electrical energy into light via light emitting diodes (LEDs) [1]. Similarly, laser diodes (LDs) based on semiconductor materials such as InGaN and GaAlAs exemplify the iterative effect on established technologies; InGaN is most notably now used for Blu-ray™ DVD players and GaAlAs based lasers have been used from homeostasis of blood in medicine to the humble optical computer mouse [2, 3].

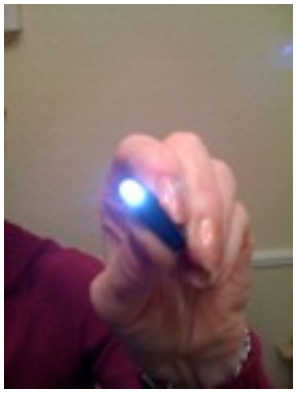

Figure 1.1 *- The revolutionary blue LED*

The market for LDs and LEDs has continued to grow and is widely expected to continue to do so as economies of scale and further processing improvements lead to greater affordability and as new utilizations for LEDs/LDs are envisioned. Figure 1.2 illustrates the rising adoption of these semiconductor devices as evidenced by their growing market valuations.

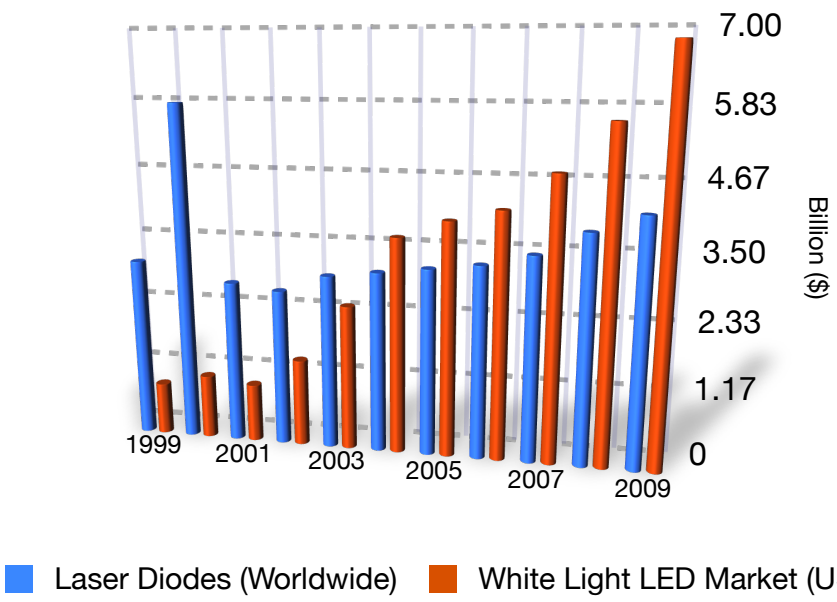

Figure 1.2 *- Worldwide LD and US solid state lighting market valuations in US Dollars ($).*

Source: Strategies Unlimited Market Research.

A number of recent advances in semiconductors, most notably the GaN 'revolution' heralded by Nichia Corporation's pioneering work with blue light emitting GaN devices [4], are behind the upsurge in value - with the realization of blue LEDs along with existing red and green LEDs, solid state lighting is close to becoming a pervasive reality [5]. The ascendancy of GaN shows the impact of a novel material brought to full development. This thesis focuses on another such semiconductor material group, the Copper Halides (CuHa), and their application to the field of wide band gap optoelectronics for potential light emitting and lasing applications.

1.2 Wide Band-gap Materials

A semiconductor band-gap refers to the difference in energy from the top of the valence band to the bottom of the conduction band, as measured in electron volts (eV). The exact threshold for the

determination of what constitutes a wide band-gap material is not well defined, being dependent on the application envisioned for the material (optical or power based devices), however it can usually be ascribed to materials with band-gap energies in excess of 1.7 eV.

Optoelectronic devices operating beyond the 3 eV range have drawn considerable interest from researchers owing to the wealth of enabling devices that are envisioned. Such devices have considerable technical properties allowing for applications in environmental contaminant decomposition [6], UV lasers and sensors [7], novel optical storage media and violet-blue-green LEDs. UV/blue LEDs and LDs are of particular interest and a wide range of materials has been identified as having desirable properties for such devices. Table 1.1 contains some properties of a selection of major wide band-gap materials (with Si and GaAs as reference).

Material	**E_g (eV)**	**Exciton Binding Energy (meV)**	**Lattice Constant (Å)**	**Unit Cell**
GaN	3.4	23	4.53	Wurtzite
ZnO	3.44	63.1	3.249	Wurtzite
γ-CuCl	3.399	190	5.41	Zincblende
γ-CuBr	3.072	108	5.677	Zincblende
Si	1.12	-	5.431	Diamond
GaAs	1.43	-	5.653	Zincblende

***Table 1.1** - Selection of characteristics for various semiconductor materials [8]*

The leading materials group for such applications are the III-Nitrides, where the aforementioned GaN and its alloys, with Al and In, are now in commercial production [9]. High brightness UV, blue and green LEDs as well as blue LDs are now becoming increasingly commonplace. Their large direct band-gap, high electron velocities and thermal stability make them ideal for high-frequency

control devices, as well as for white LEDs. GaN and its alloys, however, could not be fabricated as single wafers until recently, where a modified autoclave system and a proprietary ammonia-thermal growth method developed by Ammono [10], have yielded commercially available wafers with diameters of approximately 50mm. Initially with GaN though, deposition was carried out via metal organic chemical vapour deposition (MOCVD) of p-type and n-type (GaAlIn)N resulting in the formation of epitaxial layers on sapphire substrates [11].

One of the major obstacles to the successful fabrication of these III-N devices has been the large dislocation densities present within the crystals produced via this method. In the case of GaN, it has been found that MOCVD epilayers have dislocation densities as high as 10^8 - 10^{10} cm^{-2}, and take the form of threading dislocations [12]. These dislocations are primarily the result of the lattice mismatch between the GaN epilayers and the substrate utilized (primarily 6H-SiC and Al_2O_3).

ZnO, with a room temperature band-gap of 3.37 eV and an exciton binding energy of ~60 meV, is an attractive candidate material for efficient room temperature ultra-violet LEDs. However, the difficulty of growing reproducible, low-resistivity p-type ZnO has limited the development in this arena [13]. P-type ZnO growth is usually characterized by film instability and poor hole mobility and concentrations [14, 15]. Epitaxial growth for ZnO photonic applications has focused mainly on pulsed laser deposition (PLD), molecular beam epitaxy (MBE) and MOCVD type processes [15].

The situation is similar for the other Zn based materials; however in spite of these difficulties II-VI compound semiconductors (ZnO, ZnS, ZnSe, etc) continue to progress with proven applications in flat panel displays, AC driven thin film electroluminescent devices (TFELDs) [16] as well as lasing applications [17].

1.3 Issues with Existing Materials

With both the III-Nitrides and II-VI materials there still exist a number of device limiting and production problems. For GaN, the lack of large high quality, cheap single crystal wafers is an issue. This has retarded efforts towards a homoepitaxial approach and instead forced the practical necessity of heteroepitaxial growth. Current GaN devices are fabricated on foreign expensive substrates of different material type (predominantly Al_2O_3 for LEDs). The inherent lattice mismatch between GaN and the substrate leads to dislocation generation; mismatch between the wurtzite phase GaN and the underlying hexagonal Al_2O_3 substrate can be as high as 13.9% [10]. The predominant defects, threading dislocations rising vertically from the substrate, seem to have little effect on the electroluminescent properties of GaN, but result in large leakage currents when under reverse bias [**ref5p2**]. A number of novel epitaxial techniques have been applied to GaN, such as epitaxial lateral overgrowth (ELOG), with the aim of reducing these defect densities. Growth runs carried out via ELOG have helped reduce defect density to values nearing 10^6 cm^{-2} [18]. It is the use of this technique that has allowed the fabrication of GaN devices with lifetimes of >10,000 hours. High intensity blue and green LEDs and low power laser diodes are now commercially available based on this fabrication process [4].

Substrate materials with a closer lattice match to GaN, such as γ-$LiAlO_2$ [19] and β-$LiGaO_2$ [20] were also investigated, with the hope that the reduced mismatch (approximately 2%) would mitigate the high defect densities. However it was found that unintentional contamination as well as rough growth substantially reduced the quality of the GaN epilayer. Regardless, the ideal of a single crystal GaN that can be cleaved into wafers remains. The high pressure, high temperature prerequisite for ingot-type growth of GaN is a cost limiter relative to Si and GaAs – both readily grown from their stoichometric melts. Hydride Vapour Phase Epitaxy (HVPE) of free standing GaN

substrates and high-pressure liquid phase epitaxy (LPE) have shown some promise towards this goal [10, 21].

II-VI materials, such as ZnO, are also heavily researched with a similar aim. They have advantages relative to GaN due in part to availability in bulk, single-crystal form and their larger exciton binding energies (e.g. ~60 meV for ZnO compared to ~25 meV for GaN). The issue of reliable doping is still relevant, however. N-type conduction is relatively easy to obtain, in part due to the intrinsic n-type nature of undoped ZnO. Hole conduction remains difficult and is currently a limiting factor for ZnO – alternate methods such as heteroepitaxy of n-type ZnO on p-type substrates to form p-n heterostructures have led to the development of high-intensity UV emission from n-ZnO/p-AlGaN [22].

1.4 Short Wavelength Optoelectronics on Silicon

Silicon is undeniably the most dominant material used within the semiconductor industry due to its electronic properties, low price compared to other substrate materials, as well as established processes for Si and large wafer sizes which are readily available. Unsurprisingly, research has been undertaken into combining III-N as well as II-VI material with Si.

Investigations have shown that GaN-based materials on Si are of a lesser quality than such materials grown on sapphire and on SiC, mainly due to the large lattice and thermal mismatches between GaN and Si. In spite of this, however, the development of UV emitting GaN LEDs on Silicon <111> via molecular beam epitaxy (MBE) has been achieved [23]. However, the quality of the fabricated device was poor owing to the highly defective microstructure as a result of the large mismatch between the epilayer and substrate of 17%.

Research has also been carried out with regard to deposition of ZnO on Si substrates. This has been achieved via the reactive e-beam evaporation technique [11], although the issue of a highly mismatched substrate remains. A low pressure MOCVD technique was used to deposit ZnO onto Si <111>, albeit with the use of a 6H-SiC buffer layer. This SiC layer was used to better alleviate the mismatch between the ZnO and the Si. Layers produced by this method had improved crystal quality and improved UV emission [24].

The weakness in these approaches to LED and LD fabrication remains: growth on highly lattice mismatched substrates (for example, growth of GaN on SiC or sapphire) invariably results in dislocations and sub-optimum crystallinity, in turn affecting device performance.

1.5 Liquid Phase Epitaxy (LPE)

LPE is the precipitation of a material from a liquid phase solution onto a underlying substrate such that the crystallinity of the substrate layer is replicated onto the grown epilayer. From early work in 1836 by Frankenheim [25], LPE did not fully develop until Nelson *et al.* [26] in 1963 when it was used to grow high quality GaAs laser diodes and Ge tunnelling diodes. The growth from near thermal equilibrium between substrate and liquid phase melt results in high structural perfection and epilayers possessing lower dislocation densities than the substrate upon which they were grown [27]. Subsequent to Nelson's seminal work, considerable work was carried out on the application of LPE to III-V materials. Single crystal layers of compound semiconductors such as InP, InGaAsP, GaAs, GaAlAs and GaP have been achieved and many applied commercially [28, 29, 30, 31]. LPE can yield single crystal layers of specified composition and thickness for well established material solutions - in part due to the controllable nature of the growth parameters, namely substrate type, solution composition, temperature, cooling rate and growth time of the melt on the substrate.

Although developed most thoroughly for III-V growth, LPE has been used for other novel systems including group IV and II-VI materials, such as single crystal Silicon for photovoltaic applications [32, 33], HgCdTe for IR photodiode arrays [34] as well as for the growth of magnetic garnets [35] for optoelectronic and magnetic bubble devices. A number of configurations exist for LPE. The work reported herein was performed primarily using a horizontal sliding boat type system. The experimental setup used can be seen in Figure 1.3. Further details regarding epitaxy, the LPE process and apparatus itself shall be discussed within chapter 3.

Figure 1.3 *- Conventional horizontal sliding boat type Liquid Phase Epitaxy system*

1.6 Liquid Phase Epitaxy for Wide Band-gap Semiconductors

For II-VI compounds such as ZnO (as well as ZnSe, ZnTe and ZnS), LPE has been used to grow these materials albeit with limited success [36]. Low resistivity p-type epilayers of ZnSe have been grown with carrier concentrations of ~ 10^{18} cm^{-3} comparable to similarly produced samples via MOCVD and MBE [37]. Direct homoepitaxial growth via LPE of ZnO from a LiCl-$ZnCl_2$-K_2CO_3 flux has been achieved, with a high degree of structural perfection in the resulting epilayers [38].The remaining difficulty with ZnO is the issue of stable p-type doping. The fact that the melt

will invariably contain some degree of included impurities that can effect doping does not help this issue and also effects the reproducibility of ZnO LPE. A large number of solutes have been investigated for II-VI based LPE growth (namely Bi, Sn, Te and Se [39, 40]). Their high melting points, ionicity and the necessity for detailed solubility and phase diagram information have made LPE of II-VI materials technically difficult.

GaN has experienced some success with LPE growth on sapphire, $LiGaO_2$ and $LiAlO_2$ substrates [41], although a hybrid homoepitaxial approach using a HVPE seed layer of GaN on sapphire upon which the subsequent LPE GaN growth was carried out proved most successful by neatly avoiding the substrate mismatch issue. The challenging problems with regards to growth from high-temperature solutions and the particular issue of suitable solvents remain (owing to the issue of the poor solubility of Nitrogen in Gallium) and progress with GaN grown via MBE and MOCVD still eclipses the slow progress from LPE. The considerable problem of the misfit between GaN on sapphire and GaN on SiC substrates remains unresolved (with misfits of 8.4% and 2.5% respectively) [42].

With respect to the III-Nitrides and II-VI materials, there exists a driving force for the development of cheap, controllable and efficient light emitting materials which can be readily deposited on well-known substrate materials (e.g. Si). It is clear that there exists an opportunity for a material that would be lattice matched to Si substrates which also possesses the qualities of wide bandgap materials. As can be seen from figure 1.4, the Copper Halides (CuCl and CuBr) tentatively meet these criteria.

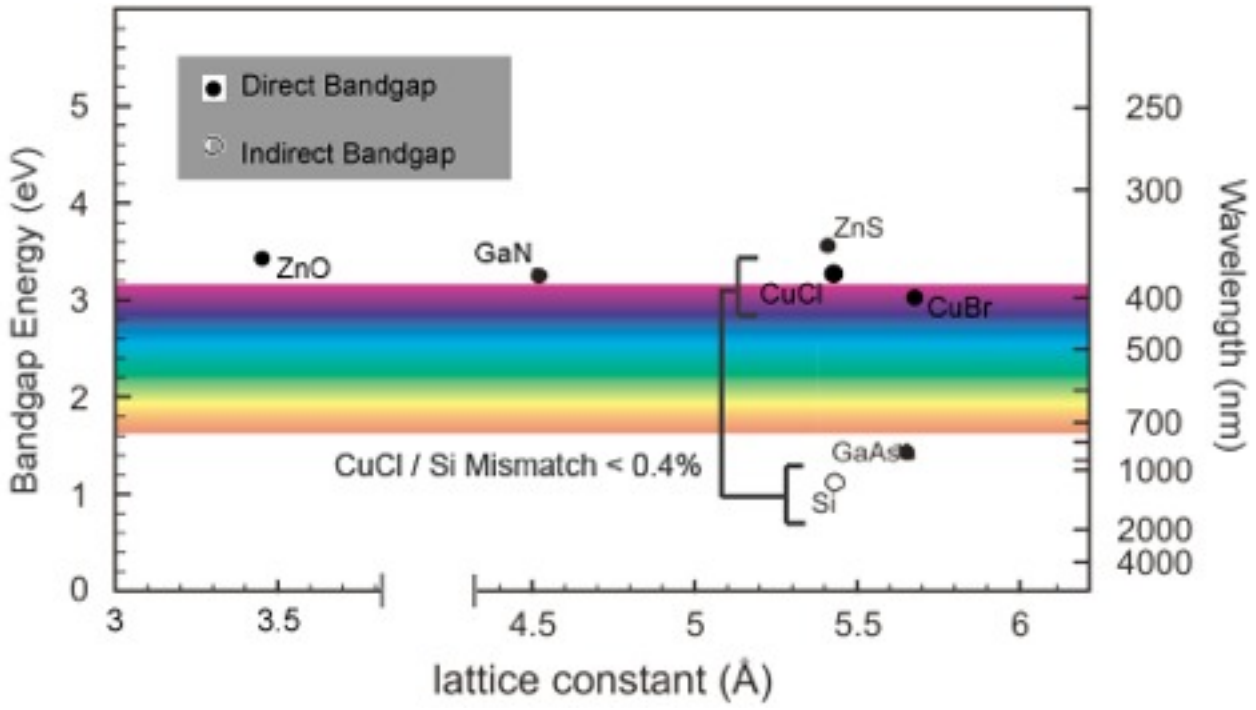

Figure 1.4 *- Band-gap energy of different semiconductor compounds as a function of lattice constant [8]*

1.7 Copper Halides

The Copper Halides have received considerable attention in the 1960s and 1970s, primarily for their excitonic properties but also due to their potential applications to optoelectronics. Owing to their interesting band structure and excitonic features, theoretical studies on CuCl and CuBr were performed [43, 44]. CuCl and CuBr nanocrystals embedded in NaCl were also studied for a better understanding of diffusion and nucleation of CuHa within the NaCl eutectic system [45, 46] , leading to spectroscopic studies of the CuHa/NaCl exciton peaks for quantum confinement effects.

For optoelectronics, CuCl in particular was examined. With transparency ranging from infrared to ultraviolet (0.4μm - 20μm [47]), large refractive index and possessing a large Pockels effect, CuCl based electro-optic modulators were envisioned. This drove the need for the growth of CuCl single

crystals. Various growth techniques were applied: growth by the traveling heater method [48], Czochralski growth [49], vertical Bridgeman and top seeded solution [50] growth as well as gel growth [51]. In some cases, the necessity for transitioning through the solid phase transition temperature for CuCl (zincblende γ-CuCl transitions to wurtzite β-CuCl at temperatures above 407 °C, below the CuCl melting point at 422 °C) required the use of a fluxing material in order to depress the melting point below the zincblende to wurtzite phase change temperature. Failure to avoid the solid state phase transition with a flux material results in highly strained crystals, with a high degree of random birefringence, which is of no practical use for optical modulators.

Both CuCl and CuBr have received attention for their potential application as gas sensors. CuCl has been used to create a CO sensor - deposition of CuCl mixed with tetraethylorthosilicate and terpinol onto gold interdigitated electrodes yielded an electrical resistance based sensor [52]. CuBr has also been used for sensors, wherein it displays an exploitable molecular recognition of NH_3. CuBr films for this purpose have been prepared via magnetron sputtering as well electrochemical oxidization of copper in the presence of Bromine gas [53].

More recently, CuCl has been investigated as a potential material for UV/Blue light emission, particularly in part due to its close lattice match with Si. Deposition on Si via magnetron sputtering [54] as well as vacuum evaporation [55] have resulted in polycrystalline γ-CuCl on Si with notably strong UV excitonic emission. CuCl on Si and GaAs has also been demonstrated via MBE [56] wherein single crystal CuCl was grown. These films were stoichometric and stable at room temperature. O'Reilly *et al.* [57] have developed a structured electroluminescent device (ELD) based on γ-CuCl and reported light emission at 380 nm and 387 nm. One issue surrounding CuHa materials is their susceptibility to degradation in ambient atmosphere, with CuCl and CuBr both degrading and forming oxyhalide complexes, though CuBr is notably more stable in ambient

atmosphere for longer periods, as will be reported in this thesis. For CuCl, work on encapsulation to prevent decomposition has been successfully carried out with the use of polysilsesquioxane (PSSQ) or cyclo-olefin copolymer (COC) capping layers [58].

Both CuCl and CuBr, with their wide band-gaps, large exciton binding energies and the possibility of thin film growth using a variety of techniques have numerous potential applications. Their emission in the near-UV and blue wavelengths is desirable, as this introduction outlines. CuCl, with its relatively close lattice match with Si (< 0.4% mismatch) and ready ability to form flux melts with a number of compounds opens the way for growth experiments using LPE. CuBr, with its improved stability relative to CuCl and its luminescent properties is also enticing and its development as a candidate for electroluminescence studies would be entirely novel.

1.7.1 CuBr Devices

Predominant attention has been given to γ-CuCl as a candidate material for Si based UV devices. As presented in figure 1.4, γ-CuCl has a desirable combination of a large band-gap and exciton binding energy as well as a compatibility with Si substrates via a near lattice match. However, the structural stability of γ-CuCl when exposed to ambient atmosphere for extended periods has been shown to be poor, becoming unstable and resulting in the formation of oxyhalides and a degeneration of the luminescent properties [59].

From a reactivity perspective, moving from the more reactive CuCl to the more stable CuBr group material could prove fruitful. Apart from the aforementioned use of CuBr as a gas sensor materials candidate, only fundamental spectroscopic and theoretical studies of the excitonic transitions of CuBr have been carried out. The improved stability of a CuBr thin film over existing CuCl deposited films is desirable - the potential application in optoelectronics owing to its high efficiency

light emitting mechanism is perhaps somewhat lessened owing to the reduced band gap energy (3.07 eV) and exciton binding energy (108 meV).

To the author's knowledge, no fundamental work has been carried out in attempting to make a device structure using a γ-CuBr active layer.

1.7.2 Solid State Chemical Interaction of CuHa and KHa Materials

Recently, it has been shown that the interaction of alkali-halide flux materials with the Copper Halides can lead to dramatic improvements in the excitonic PL emission of these films. It has been shown that CuBr films generated by a simple CuCl-film/KBr substrate reaction exhibit 10^4 times brighter excitonic PL than conventional CuBr films [60]. Similarly, work by Lucas, Cowley, *et al.* [61], in which the behavior of co-evaporated CuCl/KCl films was investigated, shows that the addition of ~5% molar flux of KCl can lead to substantial improvements in excitonic luminescence relative to normal γ-CuCl thin films. This improvement is achieved by exploiting the vacancy rich nature of CuHa relative to the vacancy free KHa crystals, and will be discussed in further detail in this thesis.

1.8 Thesis Objective

The fundamental objective of this work has been the investigation of CuHa material for novel applications in optoelectronic devices such as LEDs and LDs. Within this mandate, the feasibility of growth of single crystal γ-CuCl epilayers on Si substrates using LPE processes was examined utlizing the horizontal sliding boat method (and later, a modified tipping boat method). The use of an appropriate flux material was investigated in order to form a CuCl melt so as to avoid the wurtzite-zincblende phase change by sufficiently depressing the phase change temperature. An LPE system was built and commissioned specifically for this work with CuHa material. Analysis of

grown layers was carried out via X-Ray diffraction (XRD), EDX, photoluminescence (PL) and x-ray enhanced optical luminescence (XEOL).

Fundamental work on electroluminescence of γ-CuBr on transparent substrates, hitherto unreported, was also undertaken. Growth via vacuum evaporation physical vapour deposition (PVD) on Si, Glass and Indium Tin Oxide (ITO) coated substrates was examined via XRD and AFM. The luminescent properties of γ-CuBr were examined via PL, UV-Vis and electroluminescence (EL). Comparative work using ultra-violet visible spectroscopy (UV-Vis) absorption measurements with deposited γ-CuCl samples was carried out in order to quantify stability of CuBr thin films relative to CuCl films over a period of time. Finally, a prototype device structure for an AC thin film electroluminescent device (ACTFELD) is proposed with a γ-CuBr active region and examined using electroluminescence (EL).

The potential improvement in excitonic PL that can be gained from novel approaches to film preparation involving alkali halides and existing CuBr deposition techniques is promising, as outlined in Kondo's review [62]. This thesis details an approach taken to form highly luminescent micron sized arrays of intermixed CuBr/KBr 'microdots' using vacuum evaporation and specifically machined vacuum evaporation shadow masks. Using this novel approach, vacuum deposition of an array of KBr spots (~30 μm radius) onto similarly deposited γ-CuBr epitaxial layer on a Si substrate is carried out. Post-deposition annealing of the samples at 220 °C in conjunction with a small CuBr flux from a target source leads to the formation of the intermixed CuBr/KBr microdot with substantially improved excitonic luminescence relative to previously observed PVD deposited γ-CuBr thin films.

It is hoped that from this work, a greater understanding of the applicable growth methods and luminescent properties of CuHa material has been derived. The development of a process for LPE of CuCl on Si has been reported and tested, with conclusions and recommendations reached. The move from γ-CuCl thin film process to the more stable γ-CuBr process has been outlined and its potential demonstrated with work towards the development of an ELD. Additionally, the continuing investigation of the interaction of alkali halide compounds with CuHa materials is furthered with the formation of CuBr/KBr microdot arrays.

1.9 Layout of Thesis

Chapter 1 outlines the background and rationale for the project, discussing the importance of wide bandgap materials for optoelectronics, the existing research behind the most significant III-N and II-VII materials (GaN and ZnO) as well their shortcomings. LPE is highlighted as a means for growth of highly crystalline epilayers and a review of the existing wide bandgap materials growth processes involving LPE is presented. Finally, the Copper Halides are identified as a potential candidate materials system for blue/UV (λ ~380 - 410 nm) optoelectronic devices, their history is reviewed as is that of CuBr thin film devices. The objective of the project is identified as well as the characterization techniques to be employed.

Chapter 2 outlines the fundamental theory for semiconducting materials, optical processes for light emission as well as outlining the various characterization techniques and equipment used during the project.

Chapter 3 details epitaxial growth methods used for this work, including detailed information on LPE and its application to CuHa growth as well as the PVD process used for thin film deposition.

Chapter 4 reports on the Copper Halide materials, outlining fundamental structural, electrical and optical properties as well as reported single crystal growth using flux methods for these materials.

Chapter 5 details the results for LPE growth of CuCl on Si including the experimental methodology, characterization and conclusions.

Similarly, Chapter 6 describes the work carried out on the PVD of γ-CuBr thin films, their characterization, stability and details the progress towards the development of a prototype ACTFELD γ-CuBr based device.

Chapter 7 is given over to the work carried out in the formation of mixed CuBr/KBr microdots and details the fabrication process for the formation of these novel structures.

Finally, chapter 8 concludes this thesis by providing an overall summary of the work and outlines recommendations for future work based on the findings of this thesis.

1.10 References

[1] S. Pimputkar, J. S. Speck, S. P. DenBaars, Nature Photonics, Volume 3, 2009, pages 180-182.

[2] H. Deppe, H. Horch, Lasers in Medical Science, Volume 22, 2007, pages 217-221.

[3] T. Karu, Journal of Photochemistry and Photobiology B: Biology, Volume 49, Issue 1, March 1999, pages 1-17.

[4] S. Nakamura, 'The blue laser diode : GaN based light emitters and lasers', Springer, 1997.

[5] C. Humphreys, MRS Bulletin, Volume 33, 2008, page 459.

[6] Y. Taniyasu, M. Kasu & T. Makimoto, Nature, Volume 441, 2006, Pages 325-328.

[7] E. Monroy, F. Calle, J.L. Pau, E. Muñoz, F. Omnès, B. Beaumont and P. Gibart, Journal of Crystal Growth, Volume 230, 2001, pages 537-543.

[8] O. Madelung, 'Semiconductors: Data Handbook', Springer, 2004.

[9] H. Morkoc, S. Strite, G.B. Gao, M.E. Lin, B. Sverdlov, M. Burns, Journal Applied Physics, Volume 76, pages 1363-1398.

[10] IEE Spectrum Web Magazine: http://spectrum.ieee.org/semiconductors/materials/the-worlds-best-gallium-nitride

[11] P. J. McNally, T. Tuomi, D. Lowney, K. Jacobs, A. N. Danilewsky, R. Rantamaki, M. O'Hare, L. Considine, Physica Status Solidi (a), Volume 185, page 373.

[12] J. S. Speck & S. J. Rosner, Physica B: Condensed Matter, Volumes 273-274, 1999, pages 24-32.

[13] L. Schmidt-Mende & J. L. MacManus-Driscoll, Materials Today, Volume 10, Issue 5, 2007, Pages 40-48.

[14] S. Pearton, D. Norton, K. Ip, Y. Heo, Progress in Materials Science, Volume 50, 2005, pages 293–340.

[15] R. Triboulet, J. Perriere, Progress in Crystal Growth and Characterization of Materials, Volume 47, 2003, pages 65-138.

[16] L. Yi, Y. Hou, H. Zhao, D. He, Z. Xu, Y. Wang, X. Xu, Displays, Volume 21, 2001, page 147.

[17] M. Haase, J. Qui, K. DePurdt and H. Cheng, Applied Physics Letters, Volume 59, 1991, pages 1272-1275.

[18] X. Li, S. G. Bishop, J. J. Coleman, Applied Physics Letters, Volume 73, 1998, page 1179.

[19] E. Hellman, Z. Liliental-Weber, MRS Internet J.Nitride Semicond.Res. Volume 2, 1997, page 30.

[20] P. Kung, A. Saxler, X. Zhang, D. Walker, R. Lavado, Applied Physics Letters, Volume 69, 1996, page 2116.

[21] M. Bockowski, Crystal Research Technology, Volume 42, 2007, page 1162.

[22] Y. I. Alivov, E. V. Kalinina, A. E Cherenkov, D. C. Look, B. M. Ataev, A. K. Omaev, M. V. Chukichev, D. M. Bagnall, Applied Physics Letters, Volume 83, 2003, pages 4719-4722.

[23] S. Guha & N.A. Bojarczuk, Applied Physics Letters, Volume 72, 1998, Pages 415.

[24] J, Zhu, B. Lin, X. Sun, R. Yao, C. Shi &Z.Fu, Thin Solid Films, Volume 478, 2005, Pages 218-222.

[25] X. Qi, J. L. MacManus-Driscoll, Current Opinion in Solid State & Materials Science, Volume 5, 2001, pages. 291-300.

[26] H. Nelson, RCA Review, Volume 24, 1963, Page 603.

[27] R. H. Saul, J. Electrochem. Soc., Volume 118, 1971, pages 793-796.

[28] H. H. Weider, A. R. Clawson, G. E. McWilliams, Applied Physics Letters, Volume 31, 1977, page 468.

[29] R. F. Leheny, R. E. Nahory, M.A. Pollock, Electronic Letters, Volume 15, 1979, page 713.

[30]T. Sukegawa, T. Hiraguchi, A. Tanaka, Applied Physics Letters, Volume 32, 1978, page 376.

[31] C. E. Hurwitz, J. J. Hsieh, Applied Physics Letters, Volume 32, 1978, page 487.

[32] K. Weber, A. Blakers, M. Stocks, A. Thompson, World Conference on Photovoltaic Energy Conversion 2003, 2003.

[33] K. Weber, A. Blakers, Journal of Crystal Growth, Volume 154, 1995, page 54.

[34] G. Bostrup, K. Hess, J. Ellsworth, D. Cooper, Journal of Electronic Materials, Volume 30, 2001, pages 560-565.

[35] R.C. Linares, R.B. McGraw and J.B. Schroeder, Journal Applied Physics, Volume 36, 1965, page 2884.

[36] J.F Wang and M. Isshiki, 'Liquid Phase Epitaxy of Electronic, Optical and Optoelectronic Materials', Wiley, Editors: P. Capper and M. Mauk, page 289-302.

[37] F. Sakurai, M. Motozawa, Journal of Crystal Growth, Volume 172, 1997, page 75.

[38] G. Pei, C. Xia, F. Wu, J.g Zhang, Y. Wu & J. Xu, Materials Letters, Volume 61, 2007, pages 2299-2302.

[39] H. Nakamura, M. Aoki, Japanese Journal of Applied Physics, Volume 2, 1981, Page 11.

[40] K. Kosai, B. Fitzpatrick, H. Grimmeiss, Applied Physics Letters, Volume 35, 1979, pages 194-196.

[41] C. Klemenz, H.J. Scheel, Journal of Crystal Growth, Volume 211, 2002, Pages 62-67.

[42] P. Capper, 'Liquid Phase Epitaxy of Electronic, Optical and Optoelectronic Materials' Wiley, 2007.

[43] M. Nakayama, A. Soumura, K. Hamasaki, H. Takeuchi, H. Nishimura, Physical Review B, Volume 55, 1997, pages 10099-10104.

[44] M. Nakayama, H. Ichida, H. Nishimura, Journal of Physics.: Condensed Matter, Volume 11, 1999, pages 7653–766.

[45] M. Haselhoff, H. Weber, Materials Research Bulletin, Volume 30, 1995, pages 607-612.

[46] M. Haselhoff, K. Reimann, H. Weber, Journal of Crystal Growth, Volume 196, 1999, pages 135-140.

[47] J. Rivera, L. A. Murray, P. A. Hoss, Journal of Crystal Growth, Volume 1, 1967, pages 171-176.

[48] B. Perner,Journal of Crystal Growth, Volume 6, 1969, Pages 86-90.

[49] W. R. Wilcox, R. A. Corley, Material Research Bulletins, Volume 2, 1967, pages 571-579.

[50] T. Inoue, M. Kuriyama & H. Komatsu, Journal of Crystal Growth, Volume 112, 1991, pages 531-538.

[51] J. J. O'Connor, M. A. DiPietro, A. F. Armington, B. Rubin, Nature, Volume 212, 1966, page 68.

[52] P Dutta, R Rao, S Swartz, C Holt, Sensors and Actuators B, Volume 84, 2002, pages 189–193.

[53] M. Bendahan, P. Lauque, J. L. Seguin, K. Aguir, P. Knauth, Sensors and Actuators B, Volume 95, 2003, pages 170–176.

[54] G. Natarajan, S. Daniels, D. C Cameron, L. O'Reilly, A. Mitra, P. J. McNally, O. F. Lucas, A. L Bradley, Journal of Applied Physics, Volume 100, 2006, page 33520.

[55] L. O'Reilly, G Natarajan, P. J. McNally, D. Cameron, O. F. Lucas, M. Martinez-Rosas, L. Bradley, A. Reader, S. Daniels, Journal of Materials Science: Materials in Electronics, Volume 16, 2005, pages 415–419.

[56] N. Nishida, K. Saiki &A. Koma, Surface Science., Volume 324, 1995, page 149.

[57] L. O'Reilly, O. F. Lucas, P. J. McNally, A. Reader, 'Room-temperature ultraviolet luminescence from γ-CuCl grown on near lattice-matched silicon', Journal of Applied Physics, Volume 98, 2005, page 113512.

[58] F. O. Lucas, L. O'Reilly, G. Natarajan, P. J. McNally, S.Daniels, D.M. Taylor, S. William, D.C. Cameron, A.L. Bradley, A. Miltra, Journal of Crystal Growth, Volume 287, 2006, Pages 112-117.

[59] L. O'Reilly, 'Growth and characterisation of wide-bandgap γ-CuCl on near lattice-matched Si', PhD thesis, 2006, Dublin City University.

[60] S. Kondo, Y. Hata, & T. Saito, Materials Letters, Volume 62, 2008, pages 33-36.

[61] O. F. Lucas, A. Cowley, P. J. McNally, Physica Status Solidi (c), 2009.

[62] S. Kondo & T. Saito, Journal of Luminescence, 2009.

Chapter 2 - Theory & Characterization Techniques

2.1 Introduction

This work makes use of a number of characterization techniques in order to investigate the structure and properties of the CuHa semiconductor group. An outline of these semiconductor materials and some of their specific properties is presented, and the background theory and characterization techniques used and encountered throughout the project are described in this chapter.

2.1.1 Semiconductors

Isolated atoms that are brought together in a crystal structure give rise to overlapping periodic potentials as their electron wave functions overlap due to shorter inter-atomic spacing. Since Pauli's exclusion principle states that no two electrons can possess the same quantum state, this leads to the broadening of the discrete electron states into 'bands', separated by a forbidden region. Thus in semiconductors we have the valence band (the highest filled band) and the conduction band (the next highest band above the valence). The distance between these bands through the forbidden band is called the band-gap, E_g, of the material. Crystalline solids are classified as metals, insulators and semiconductors based on the band-gap energy and the position of the Fermi energy, relative to their valence and conduction bands. Materials where the Fermi energy is inside the conduction or valence band (or these respective bands overlap) are classified as metals. If the Fermi energy is between the conduction and valence bands, the material is a semiconductor or possibly an insulator, depending on the magnitude of the band gap energy. Illustrative band structures for the three cases are shown in figure 2.1.

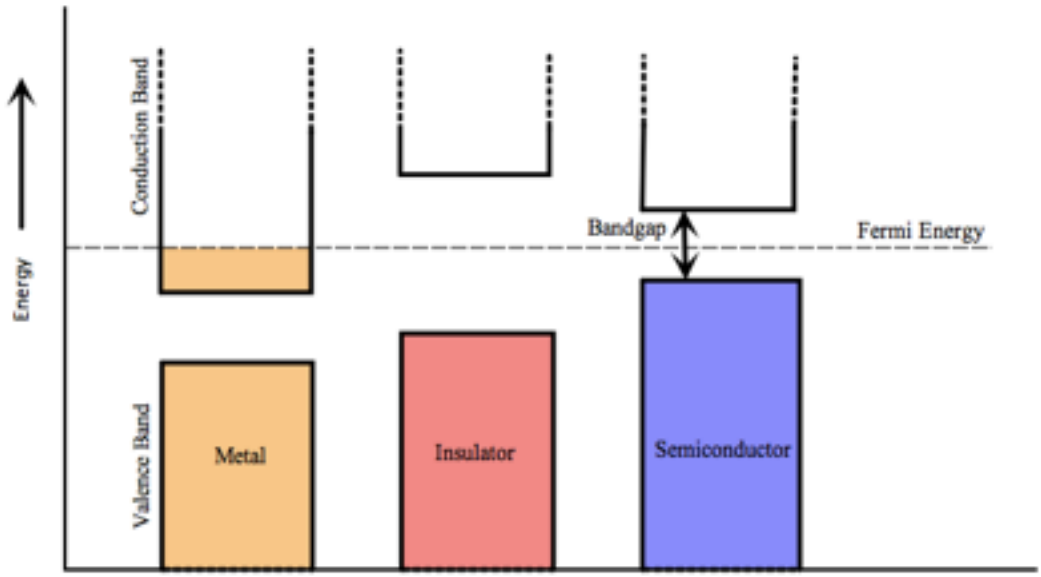

Figure 2.1 *- Representative energy band structures for metal, insulators and semiconductor materials.*

2.1.2 Energy-Band Theory of Solids

As mentioned, the energy band structure for materials arises due to the behaviour of electrons in periodic potentials. A theoretical description involves the treatment of the Schrödinger equation in conjunction with Bloch's theorem. The Schrödinger equation for a free particle needs to be expanded to provide for the potential *U(r)* and can be expressed as

$$H\psi_{nk}(\vec{r}) = \left[-\frac{\hbar^2}{2m_e}\nabla^2 + U(\vec{r}) \right] \psi_{nk}(\vec{r}) = E_n(k)\psi_{nk}(\vec{r}) \qquad (2.1)$$

The elimination of the time parameter, *t*, gives the time independent Schrödinger equation as shown above. The potential, *U(r)*, can be said to have the same periodicity as the underlying Bravais lattice:

$$\vec{R} = n_1 a_1 + n_2 a_2 + n_3 a_3 \qquad (2.2)$$

where n_i are integers and a_i are vectors describing the edges of the base unit cell. This gives a periodic potential function:

$$U(\vec{r}) = U(\vec{r} + \vec{R}) \tag{2.3}$$

for all R of the appropriate Bravais lattice vector. Using a nearly free electron approximation, whereby the interaction between electrons is dismissed, allows for solutions to the Schrödinger equation using Bloch's theorem [1], which states that a wave function can be written as a plane wave multiplied by a function with the periodicity of the lattice.

$$\psi_{nk}(\vec{r}) = e^{ikr} u_{nk}(\vec{r}) \tag{2.4}$$

where $u_{nk}(r)$ can be written in terms of the previously defined periodic potential function, i.e.

$$u_{nk}(\vec{r}) = u_{nk}(\vec{r} + \vec{R}) \tag{2.5}$$

The energies at various indices, n, vary with wave vector k and form an energy band for that index. A change in k will lead to a continuous variation of the eigenvalues E_n since for a different k there exist many solutions to the Schrödinger equation with different eigenvalues E_n and as a continuous function $E_n(k)$, they form bands with a band index n. Since this function is periodic, each band will have an upper and a lower range of energies. In order to visualize the energies for $E_n(k)$, the lines of high symmetry, illustrated for a face centered cubic system in figure 2.2, are considered through the Brillouin zone and are graphed as a schematic representation known as a band diagram.

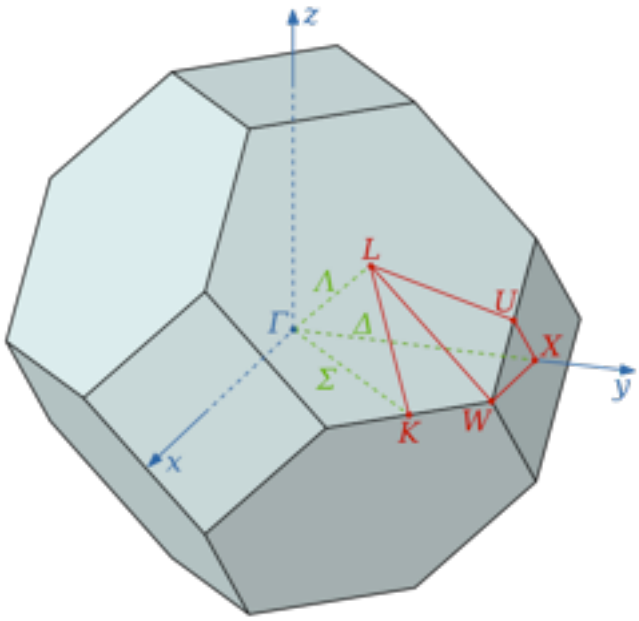

Figure 2.2 *- Brillouin zone for face centered cubic (FCC) lattice illustrating the points of high symmetry*

From the band diagram, should a minimum in the conduction band and a maximum in the valence band occur at the same position within *k*-space, direct electron transition to the conduction band can take place without momentum change, as shown in figure 2.3. Materials where this direct transition at $k = 0$ (i.e, Γ symmetry point) is allowed are known as direct band gap semiconductors, and direct optical excitation with photons at $E_g = hv$ can occur. From figure 2.3, indirect transitions from the valence to conduction band require the creation of a phonon quasiparticle in order to satisfy energy-momentum conservation.

Energy band diagrams for both CuBr and CuCl can be found in Chapter 4, wherein it can be clearly seen that they exhibit a direct band gap at $k = 0$, and are thus considered direct band gap materials.

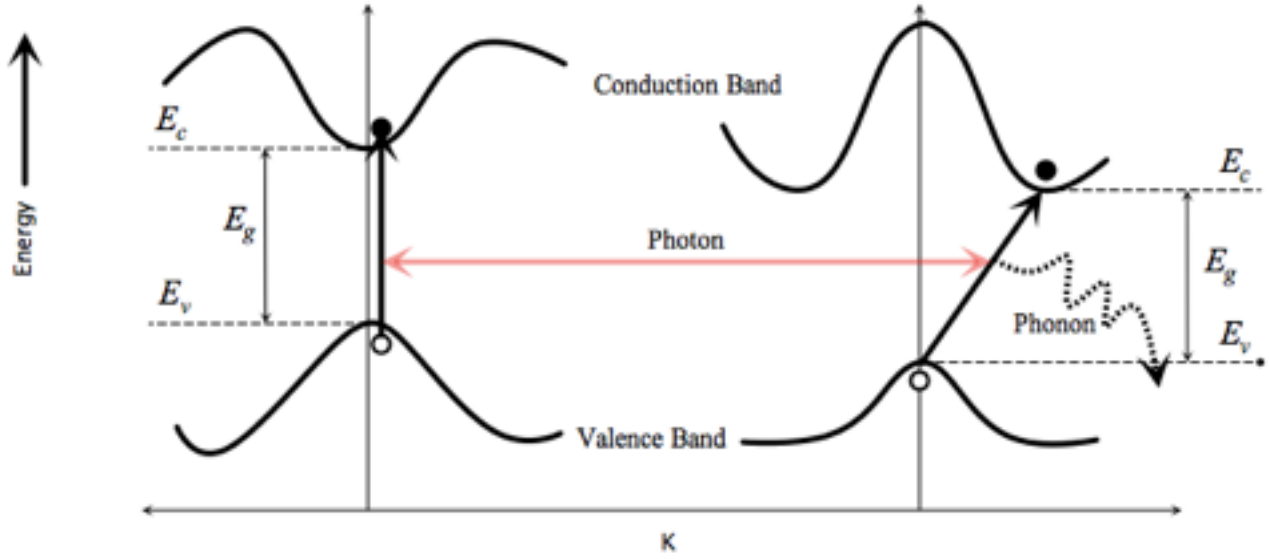

Figure 2.3 *- Illustrative band structure for direct and indirect gap semiconductors.*

2.2 Photoluminescence in Semiconductors

Photoluminescence is the process whereby a material absorbs electromagnetic radiation (i.e. photons) and then radiates photons back out (i.e. emission). In a semiconductor, this process of absorption creates excess carriers beyond what the material would usually possess at thermal equilibrium. These excess carriers are ultimately resolved by a recombination process. As illustrated in figure 2.3, understanding the nature of the recombination process requires that the material be classified by its band gap, i.e. whether the material is a direct band-gap material or an indirect band-gap material. Figure 2.4 illustrates schematically the basic recombination transitions that excess carriers in a semiconductor undertake.

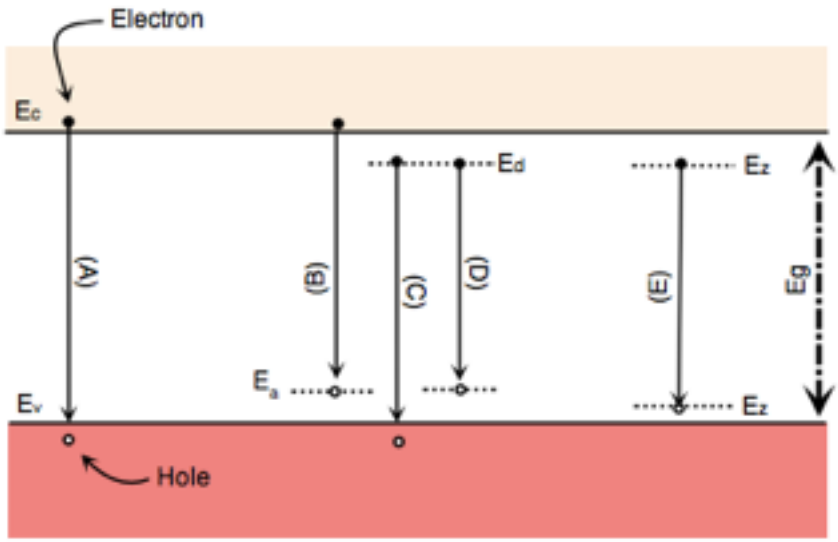

Figure 2.4 *- Basic recombination transitions found in semiconductors - E_c, E_v, E_g, E_d, E_a, E_z are the conduction band, valence band, energy band gap, donor traps, acceptor traps and excitonic recombination, respectively. Reproduced from [2].*

From Figure 2.4, the transitions can be detailed as follows. The transition (A) is the inter-band transition between the conduction and valence bands, corresponding closely to the energy band-gap of the material. Transitions (B), (C) and (D) originate from chemical impurities or defects within the crystal. By way of example, transition (B) originates from the conduction band to an acceptor just above the valence band. Similarly, transition (C) originates from a donor near the conduction band while transition (D) represents a donor-acceptor transition. Transition (E), excitonic recombination, requires a treatment of the subject of excitons, which is discussed below.

2.2.1 Excitons

In a direct band-gap semiconductor, when light with a photon energy in excess of the band-gap illuminates a sample, electrons are excited to the conduction band. The vacated electrons leave holes in the valence band, which via Coulombic attraction, can form an exciton. For CuHa material,

these excitons can be described as Wannier-Mott type pairings [3, 4], in which the electron and hole are only weakly bound due to the large screening potential of the valence band electrons and are thus separated by a number of interatomic spacings, *d*. As a bound electron-hole pair, an exciton is analogous to that of a Hydrogen atom, and has a correlated movement and an effective mass approximation equal to that of the two particles moving with the effective masses of the valence and conduction band. Thus the excitons can be investigated from this assumption, starting with an unbound electron with wavevector k_e in the conduction band, expressed as [5]

$$E_e(k_e) = E_g + \frac{\hbar k_e^2}{2m_e} \tag{2.6}$$

where E_g is the band-gap, and m_e is the electron's effective mass. Similarly, an unbound hole with wavevector k_h in the valence band can be expressed as

$$E_h(k_h) = \frac{\hbar k_h^2}{2m_h} \tag{2.7}$$

where m_h is the effective mass of the hole. Bloch functions can be used to represent the electron and hole, $\psi_{ke}(r_e)$ and $\psi_{kh}(r_h)$, respectively. The wavefunction for the exciton can then be expressed as the combination of the electron and hole wavefunctions.

Owing to the hydrogenic nature of the exciton, the Rydberg constant for an exciton can be expressed as [5]

$$R = \frac{\mu e^4}{2\hbar^2 (4\pi\varepsilon_0)^2 \varepsilon_0^2} = \left(\frac{\mu}{m\varepsilon_0^2} \right) \times 13.6eV \tag{2.8}$$

where μ is the reduced mass of the system, given by

$$\frac{1}{\mu} = \frac{1}{m_e} + \frac{1}{m_h} \tag{2.9}$$

and ε_o is the permittivity. Since this will always equate to a positive number, the effect of the Coulomb attraction places the exciton energy states below the conduction band.

As explained for excitons, the recombination of the electron-hole pair results in the emission of a photon with energy lower than that of the band-gap energy. The energy difference corresponds to the binding energy of the exciton and is called the free exciton energy, E_f. The difference between the free exciton energy and the band-gap energy is the binding energy of the electron-hole pair, E_x:

$$E_f = E_g - E_x \tag{2.10}$$

where E_g is the band-gap energy and E_x the energy of the exciton. Trapping of excitons near impurities and defect states within the crystal will also lower the binding energy of the exciton. For most semiconductor materials, excitonic recombination is only observable at low temperatures, where *k*T is less than the binding energy of the exciton (k being the Boltzmann constant). However, the CuHa are notable for having large exciton binding energies (~190 meV and ~108 meV for CuCl and CuBr, respectively, see table 1.1) and are thus directly observable at room temperature (i.e., kT ~26 meV). Excitonic states for the Copper Halides used in this work are discussed in further detail in Chapter 4.

2.2.2 PL Experimental Setup

Room temperature PL measurements were carried out using a 325 nm UV He–Cd excitation laser. The PL was measured by a liquid Nitrogen cooled CCD detector in conjunction with a 40 x UV objective lens on a JY Horiba LabRam 800 Raman-PL spectroscopy system. For temperature

dependent measurements, a standard closed circuit liquid Helium cryostat was used. Excitation was provided by a 244 nm laser, supplied by the frequency doubling of the 488 nm line from an Argon ion laser using a BBO (β-BaB_2O_4) crystal.

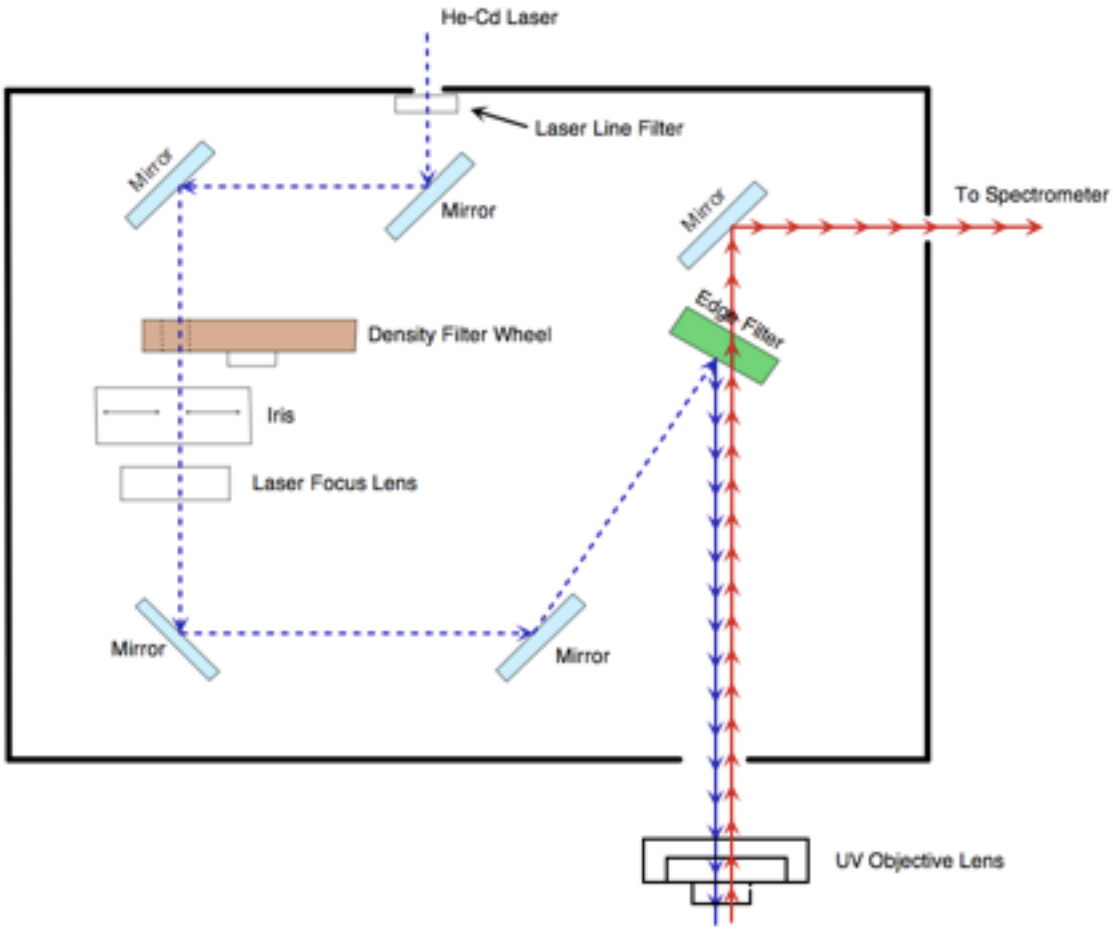

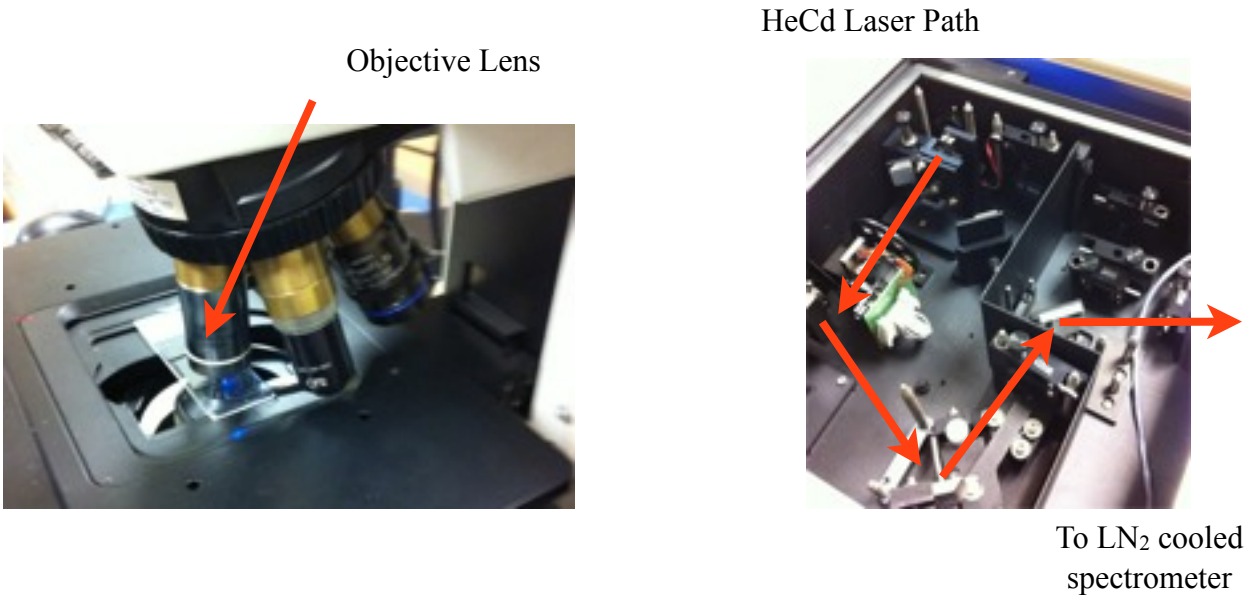

Figure 2.5 *- Experimental setup for room temperature PL measurements using He-Cd laser.*

2.3 Electroluminescence (EL)

Electroluminescence is an optical emission process in which an electrical potential is converted by a luminescent material into photons. Similar to photoluminescence, it is the result of radiative recombination of electrons and holes within the semiconductor, however the process is achieved via electrical potential rather than optical excitation with a laser as is the case with PL. A typical ACTFEL device structure is illustrated in figure 2.6 below.

With the application of a sufficiently large voltage to such a device, electrons are injected from the electrode into the active layer region. These 'hot' electrons are accelerated under the influence of the electric field and can, after sufficient energy has been supplied, interact with the luminescent centre of the material within the active layer to excite an electron of the active layer material from valence to conduction band. This process is known as impact excitation [7].

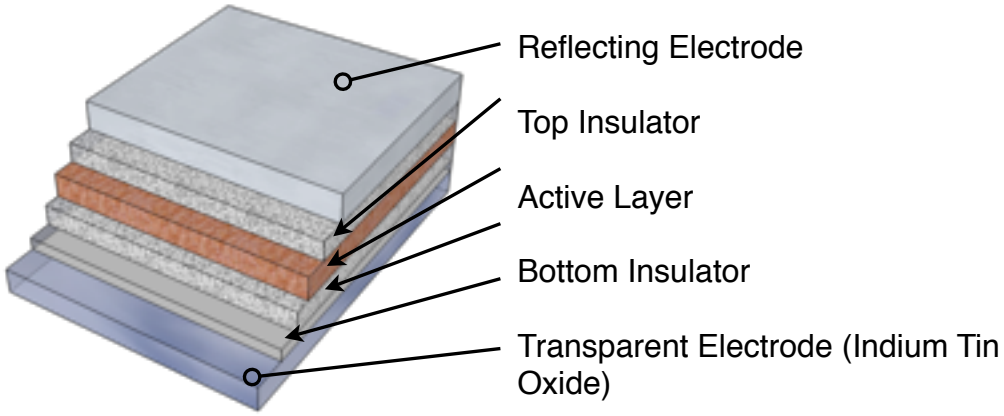

Figure 2.6 *- Standard MISIM (metal-insulator-semiconductor-insulator-metal) device structure, reproduced from [6]*

Subsequently, the luminescent centre will relax back to the ground state via a de-excitation process. This can either be a radiative, light emitting event (i.e. photon produced) or a non-radiative process. Figure 2.4 previously showed the radiative transitions that can occur from this process that can result in light emission. Non-radiative relaxation will result in the production of a phonon - the structural quality of the active layer is an important factor in these events as crystal defects, grain boundaries, interstitials and vacancies can all act as non-radiative recombination centers which can adversely effect the quality of emission from the ELD. Figure 2.7 below shows a schematic of the sequence of processes leading to a radiative emission event.

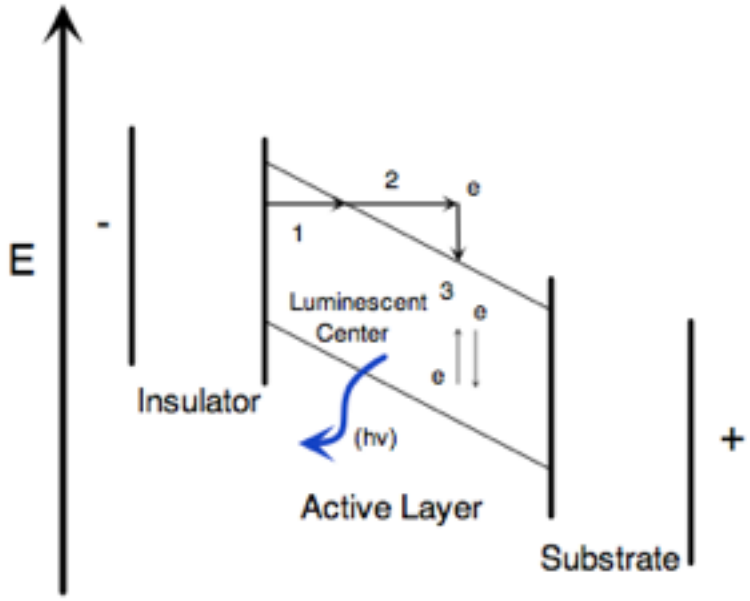

Figure 2.6 *-Schematic of the four fundamental process in a ELD which can result in light emission, (1) Injection of charge carrier into the active layer, (2) acceleration of charge carriers, (3) impact excitation of luminescence centers by the 'hot' electrons and finally the radiative relaxation back to the ground state. Reproduced from [6]*

2.3 UV-Vis Spectroscopy (UV-Vis)

In a UV-Vis system, an incident photon of known energy excites an electron within the material from a lower to a higher energy state as the atoms within a material will undergo electronic excitation via absorption of this light energy. By measurement of the changes in the resulting absorption from the excitation it is possible to examine the transitions undertaken by the electron [8]. The spectrometer measures the intensity of light from the sample (referred to as I), and compares it to the intensity of the incident light before hitting the sample (I_o). The relationship between I and I_o is defined as a ratio, which is called the transmittance.

The measured absorbance of a material, A, is related to the transmittance thus:

$$A = \log\left(\frac{I_o}{I}\right) \tag{2.11}$$

In this work, the UV-Vis technique is used to examine the absorption charateristics of CuHa materials from an excitonic and band-to-band point of view. Absorption spectra were taken using a Perkin Elmer Lambda 40 UV-Vis spectrometer, as seen in figure 2.7 below.

(a)

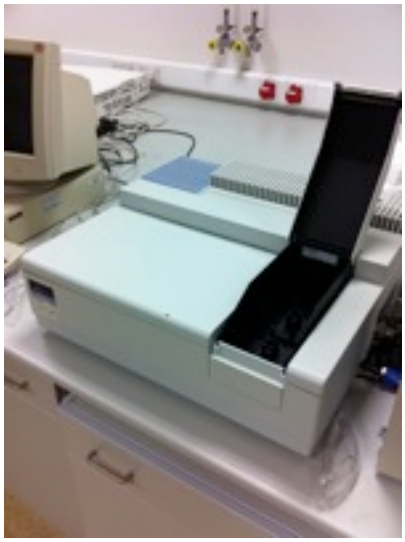

(b)

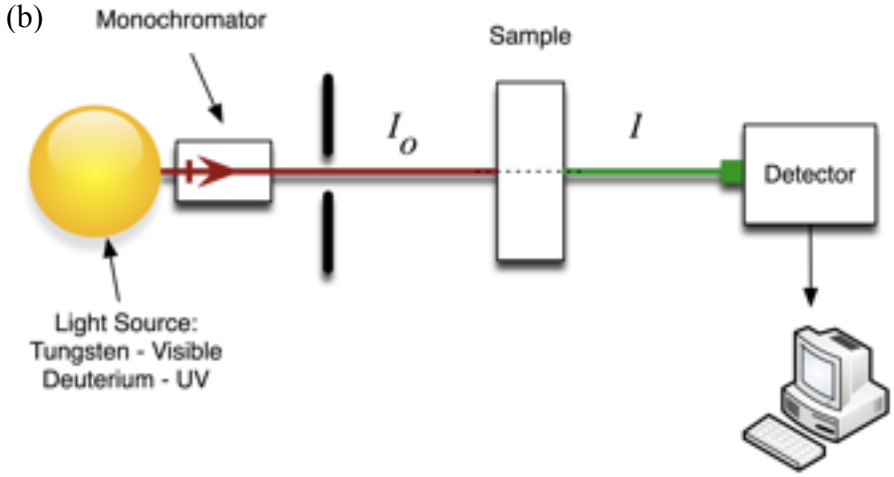

Figure 2.7 *- (a) Perkin-Elmer Lambda 40 UV-VIS spectrometer and (b) schematic of UV-Vis spectrophotometer*

A Deuterium lamp is used to generate the UV component of the light while a Tungsten lamp is used for the visible spectrum. The UV-Vis spectral range is approximately 190 nm to 900 nm and the system has a given spectral resolution of 1 nm.

Absorption based spectroscopy can also be used to estimate the band-gap of a material [9], and can be used to determine the compositional makeup of wide band-gap semiconductor alloys such as AlGaN, as illustrated in figure 2.8. However, in the case of materials with excitonic processes close to the band-gap edge, such an estimation of the band-gap is not possible due to interference of said processes with band-gap mediated absorption processes (although the observed absorption edge is an approximate indicator of the location of the band-gap). This is the case for the CuCl and CuBr material.

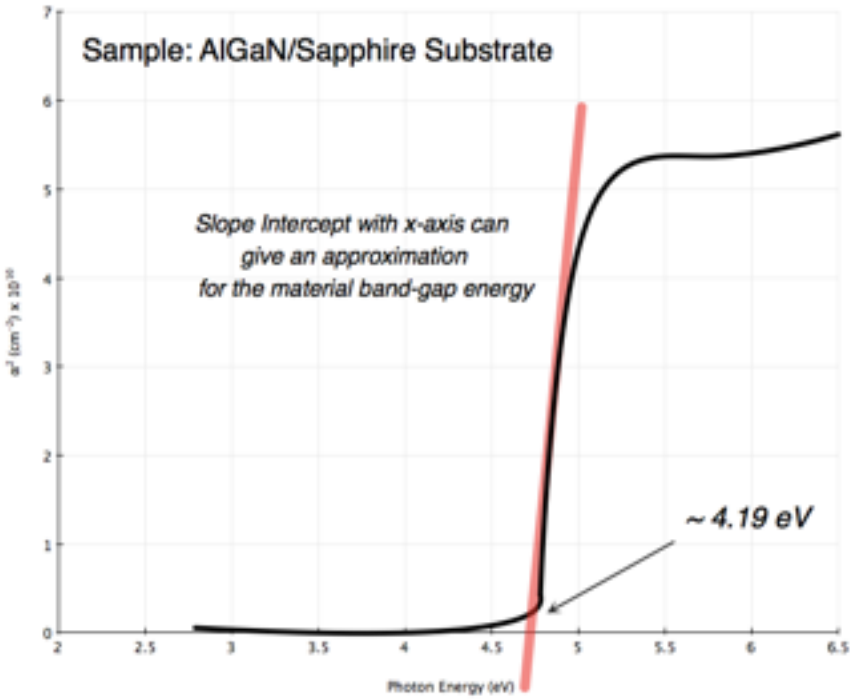

Figure 2.8 *- Illustration of means of determining band-gap energy of material from UV-Vis absorbance measurement.*

2.4 X-Ray Diffraction (XRD)

X-rays are part of the electromagnetic spectrum with photons of suitably short wavelengths for use in diffraction studies of crystallographic materials. XRD is a non-destructive and versatile technique for revealing information on the crystallographic structure of a material as well as the chemical make-up and physical properties thereof. The technique stems from the interplay of fundamental aspects of the crystal lattice and constructive interference from a diffracted crystal as elucidated by Bragg's Law [10]. A crystal is fundamentally a regular, three dimensional ordering of atoms in space forming a series of planes. These planes are parallel to one another but separated by a distance, *d*. This parameter is known as the inter-planar distance and varies depending on the nature of the material, since each crystalline material potentially has a differing atomic structure.

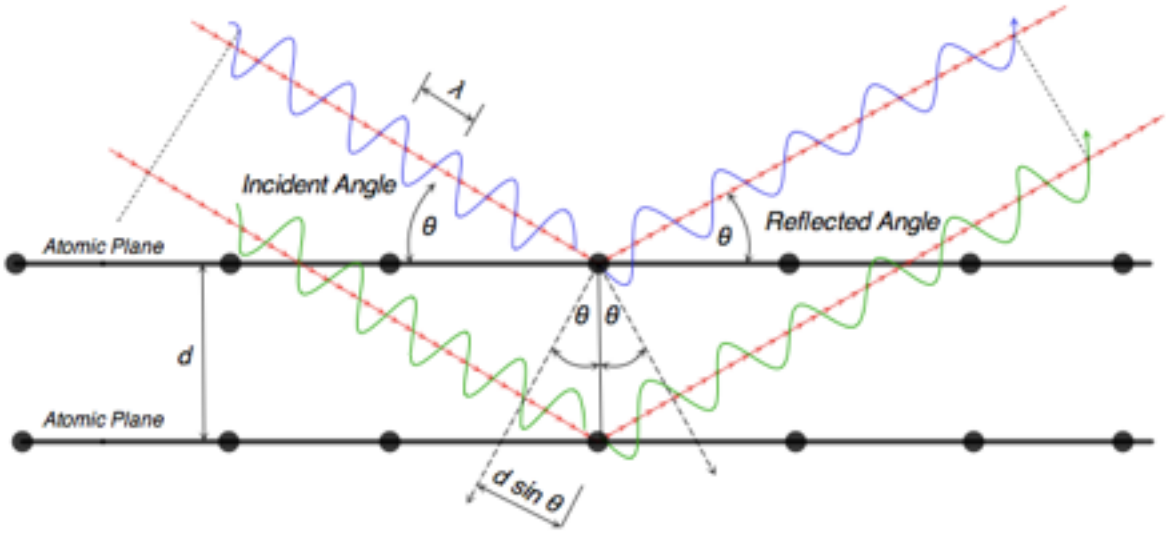

Figure 2.9 *- Illustration of Bragg diffraction from a series of lattice planes*

When a monochromatic x-ray with beam wavelength λ is directed onto a crystal structure at a specific angle, θ, diffraction can occur should it satisfy Bragg' Law:

$$2d\sin\theta = n\lambda \tag{2.12}$$

Such diffraction resulting from the interaction of x-rays and a three-dimensional lattice structure is known as Bragg diffraction, but is often colloquially called a reflection and is illustrated in figure 2.9. By varying the Bragg angle θ, solutions exist for different inter-planar spacings in crystal and polycrystalline materials. By calculating and plotting the angular positions and diffraction peak intensities produced from the monochromatic x-ray beam, a characteristic pattern is produced for a sample that yields information regarding the composition and crystallographic orientation of a sample.

An XRD diffractometer system allows for precise control of the incident beam and the resultant diffracted beam. The diffractometer motors are used to bring the diffraction planes (i.e. described by <hkl> indices), which are orientated in a characteristic way within the sample, into the diffraction condition of Bragg's Law - i.e to align the resulting normal of the <hkl> planes parallel to the diffraction plane. Diffraction measurements for this work will be taken with the use of a Bruker AXS D8 Advance x-ray diffractometer [11]. The X-Ray generator is a Cu target that is excited by electrons accelerated by a 40kV voltage. The Cu K_α wavelength of the x-ray generator is given as λ = 0.154 nm. The D8 system makes use of what is known as the parallel beam geometry - this arrangement of the x-ray source, sample and detector allows for the sample to be rotated at a specified angular speed such that the angle of the incident x-ray varies as the detector is rotated at twice the relative angular speed of the sample. This geometry can be seen in figure 2.10 below.

Using this geometry, as the incident x-ray beam is moved around the sample (via the indicated focusing circle), the detector is correspondingly maintained at twice the incident x-ray angle (i.e., 2θ). The detector can measure the relative strength of the reflection occurring across a range of 2θ values and plot it against the incident angle via the supplied D8 software.

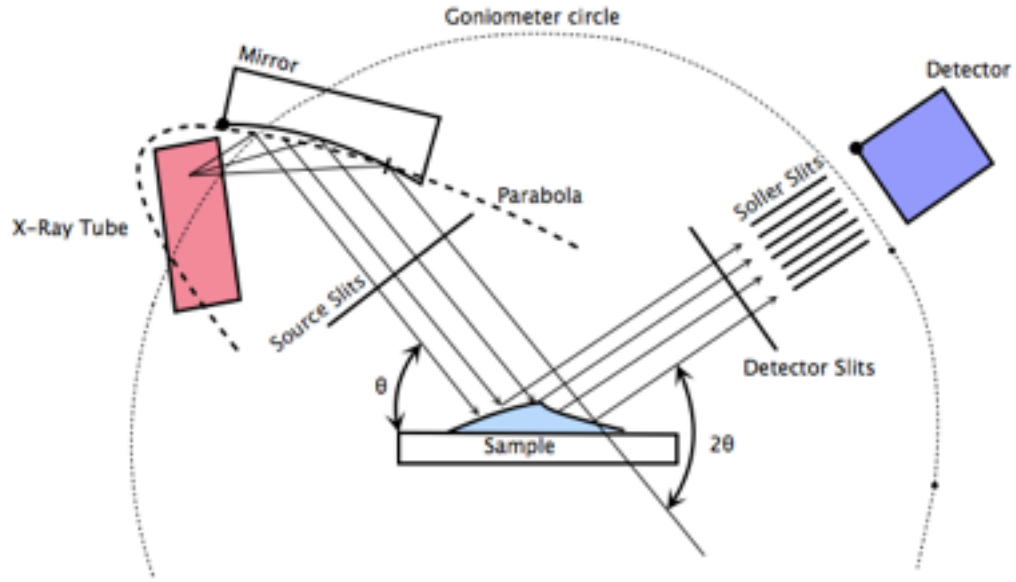

Figure 2.10 *- The parallel beam geometry used with the D8 Advance XRD system*

2.4.1 Glancing Incidence X-Ray Diffraction (GIXRD)

For thin surface adjacent films, such as those deposited via PVD as will be discussed in Chapter 6, the XRD measurement of specific properties such as crystallite orientation in polycrystalline samples is possible by using small angles of incidence for the x-rays relative to the sample surface. By 'glancing' the x-rays in this manner across the sample, the sampling volume of the x-rays is reduced to a small volume at the surface since the penetration depth is much reduced. This in turn leads to higher resulting diffracted intensities from the surface region than with a conventional XRD scan.

2.4.2 Crystallite Size Calculation using Scherrer Formula

The Scherrer formula is a commonly used statistical approach to estimate the size of crystallites found in polycrystalline thin film samples. It is given by the expression [12]:

$$d = \frac{K\lambda}{w\cos\theta} \tag{2.13}$$

where d is the nano-particle size, θ is the angle of the Bragg reflection, w is the broadening width of a 2θ range, K is a constant and λ is the wavelength of the incident radiation. The parameter, w, represents the corrected FWHM, that is:

$$w = w_{measured} - w_{instrument} \tag{2.14}$$

where $w_{instrument}$ is estimated from the width of a single Si Bragg peak. For this work, K was set as 0.9. Using this approach, the average crystallite size for the thin film samples used during this work was estimated.

2.5 Atomic Force Microscopy (AFM)

AFM allows for the imaging of nanometre scale surface features, and is a valuable tool for morphological studies of thin films. An AFM system consists of a cantilever and attached tip that can be rastered across a sample surface in order to generate an image of the scanned area. The tip is brought into close proximity of the surface of the sample where forces between the sample and the tip result in a deflection of the cantilever as described by Hooke's Law [13]. Forces that can affect the cantilever and thus are measurable by the AFM include van der Waals forces, capillary forces, chemical and electrostatic forces as well as mechanical pressure. For the AFM used in this study, the deflection on the cantilever caused by the force feedback is measured by a laser that is focused onto the cantilever top, which is fed into a control system (e.g. computer software). For this work, a Pacific Nanotechnology AFM 9000 was used, operating in contact mode.

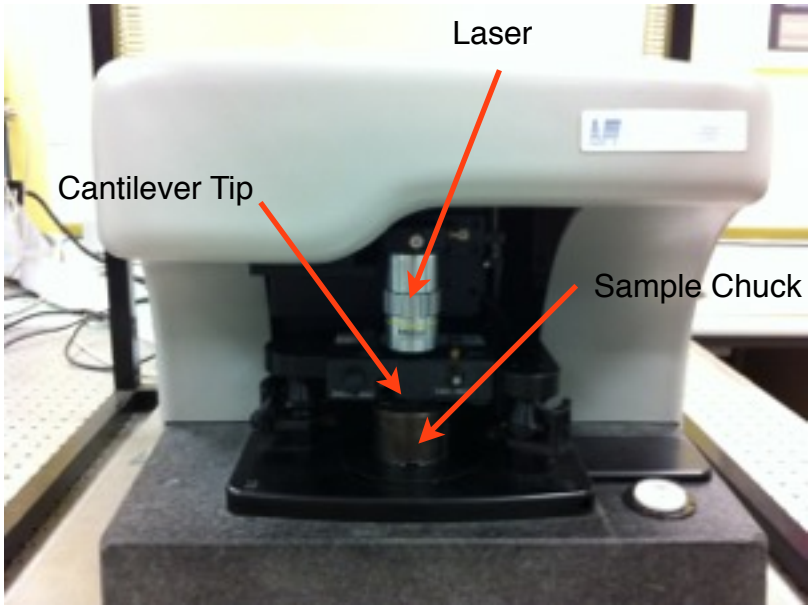

Figure 2.11 *- Annotated image of the Pacific Nanotechnology 9000 AFM system*

2.6 Scanning Electron Microscope (SEM)

Scanning electron microscopy is a widely used tool for surface analysis and characterization. It makes use of a high energy, well controlled beam of electrons,which is raster scanned across the sample surface. The interaction of the beam of electrons with the surface produces a number of signals, namely backscattered electrons, secondary electrons, characteristic x-rays (which is used for energy dispersive x-ray analysis, detailed further on), as well as electron induced luminescence (cathodoluminescence). The SEM tool is designed to detect these signals and using the imaging software, can generate an image of the surface of the sample, detailing the topology down to nanometer scale resolution. Due to the collimated nature of the beam, SEM images have a high degree of depth of field, giving an intuitive, three dimensional image of the sample

Figure 2.12 shows a schematic of a typical SEM column. Electrons originate from the electron gun (generated from a tungsten hairpin filament) and are then collimated using the electromagnetic condenser lens and the objective lens before reaching the sample. A secondary electron (SE)

detector as well as a back-scattered electron detector (BSE) are used to collect the sample information. Samples are maintained under 10^{-5} mbar vacuum conditions in the specimen chamber. For this work, a Carl Zeiss EVO SEM was used.

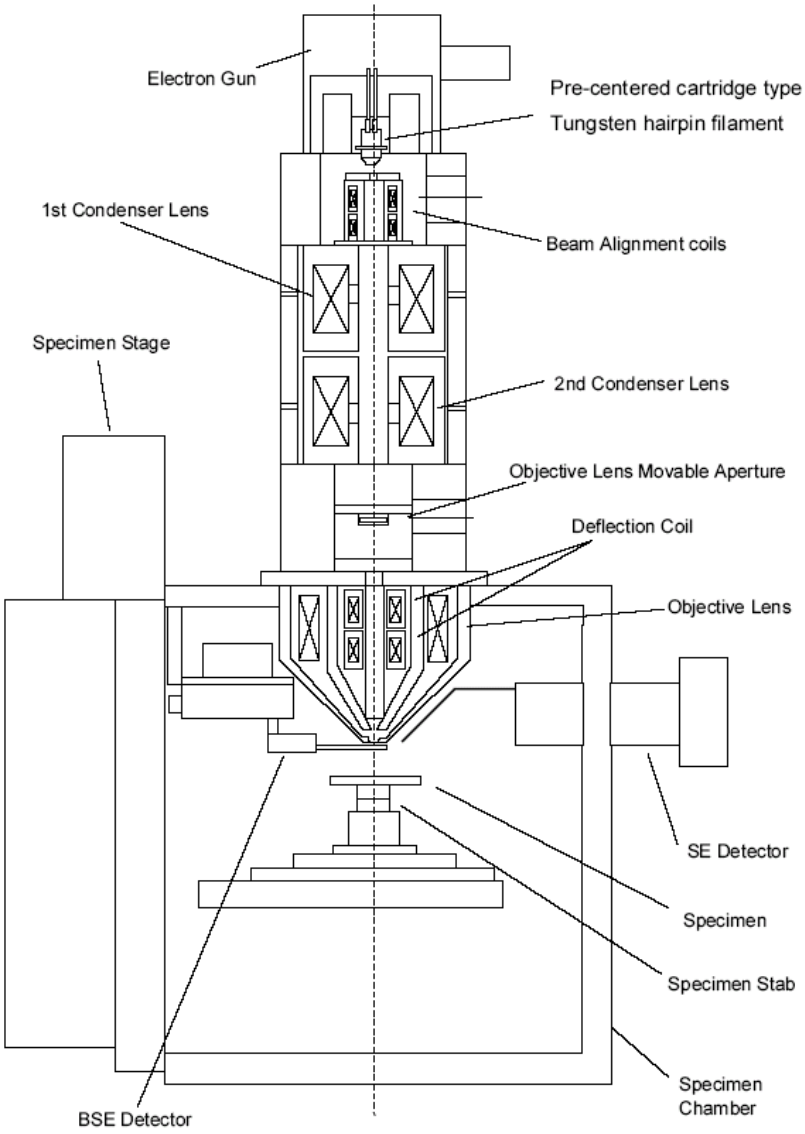

Figure 2.12 *- SEM column schematic for a typical SEM system*

2.6.1 Energy Dispersive X-Ray Spectroscopy (EDX)

Energy Dispersive X-Ray Spectroscopy is an analytical technique used to determine the chemical composition of a sample under investigation. As each element has a unique atomic structure of orbital electrons and nucleus, it provides each element with a unique fingerprint. EDX relies on

characterizing a sample from the analysis of X-rays emitted by directing the beam from the SEM column at the sample and causing the ejection of an electron from the sample atoms shell. The now-excited atom will relax to a ground state, and the re-configuration of the electron shell structure will result in the emission of an x-ray photon, returning the sample atom to its lowest energy state. In the SEM instrument, generated X-rays can be detected with an energy dispersive spectrometer which will measure the number and energy of the emitted X-rays. The energy of these X-rays can be related back to specific elements as stated by Moseley's law [14], allowing for the elemental classification of the sample.

2.7 X-Ray Enhanced Optical Luminescence (XEOL)

Synchrotron radiation has led to the development of many novel material characterization techniques. Synchrotron facilities utilize a particle source, booster and storage ring to generate and hold the accelerated electrons [15]. High energy electrons are created and accelerated to near relativistic speeds using a linear accelerator. Accelerated particles are then directed to and stored in an ultra-high vacuum ring without any further acceleration, known as a storage ring. In this storage ring, the electrons are subjected to magnetic fields created by powerful bending magnets and as the electrons pass along the storage ring and are accelerated by the bending magnets, they emit synchrotron radiation, which with appropriate design is much more intense than conventionally generated x-rays. The synchrotron radiation is projected from the storage ring tangentially and captured by beamline stations, where the experimental apparatus is set up (see figure 2.13).

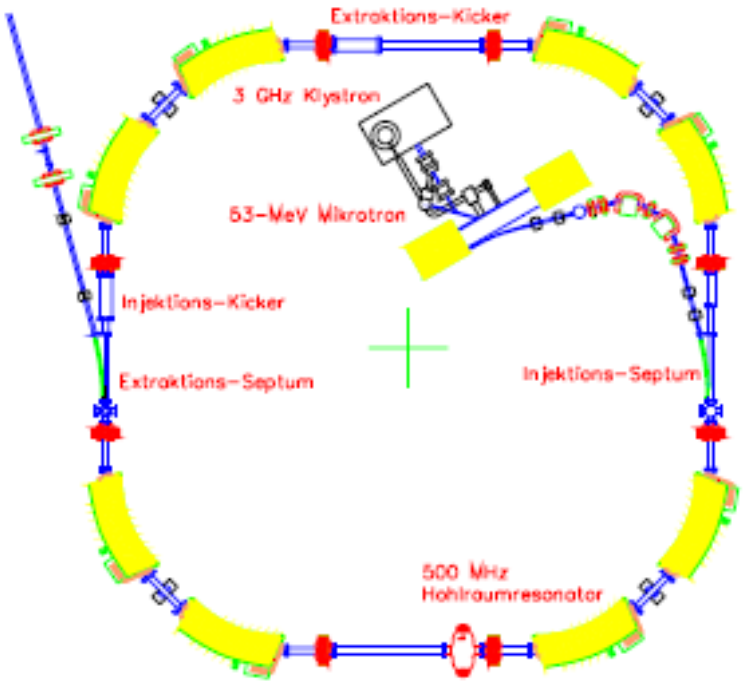

Figure 2.13 *- Schematic of synchrotron storage ring at ANKA, Karlsruhe [17].*

One synchrotron-based optical characterization technique is known as XEOL [16]. The sample under investigation is subjected to high flux synchrotron radiation at a beamline station. The absorption of the incident x-ray photons produces a large amount of electrons within the sample, which in turn causes further excitation and ionization. This energy leads to the creation of holes in the valence band as well as excess electrons in the conduction band, and the resulting recombination of electron-hole pairs results in photoemission. The experimental setup for XEOL is illustrated in figure 2.14 below.

XEOL measurements were undertaken at the ANKA Synchrotron, Karlsruhe, Germany [17] using the TopoTomo beamline. The storage ring nominally operates at an energy of 2.5 GeV at 200mA and following an injection, has a lifetime of approximately 20 hours.

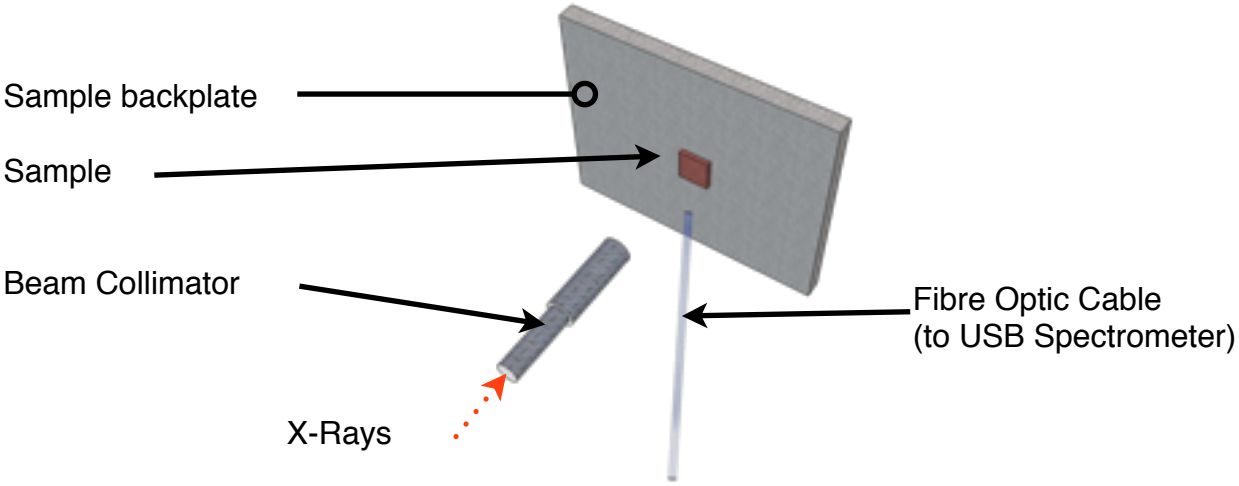

Figure 2.14 *- Experimental setup for XEOL measurements*

Similarly, at HASYLAB-DESY, Hamburg, Germany [18], XEOL experiments were undertaken at the F-1 beamline at the Doris III storage ring. This ring operates at a positron energy of 4.450 GeV with beamline currents of 80-150 mA. Post injection lifetime is approximately 10-80 hours. XEOL spectra were acquired using an Ocean Optics USB 2000 Spectrometer, with a detector spectral acquisition range from 200 nm to 1100 nm.

2.8 Secondary Ion Mass Spectrometry (SIMS)

SIMS allows for compositional analysis of a thin film surface by sputtering the surface with a focused ion-beam and collecting and analyzing the generated secondary ions via a mass spectrometer. Measurements are undertaken under high vacuum (greater than 10^{-6} mbar) in order to ensure that the secondary ions do not collide with background chamber gases en route to the mass spectrometer as well as avoiding issues with adsorption of chamber gases into the sample during the measurement. By successive scanning of the same location on a sample, layers of the region under test are successively etched away giving access to deeper levels and allowing for the compositional characterisation of these levels. This gives a compositional profile of the thin film and is known as depth profiling. Figure 2.15 below illustrates the technique.

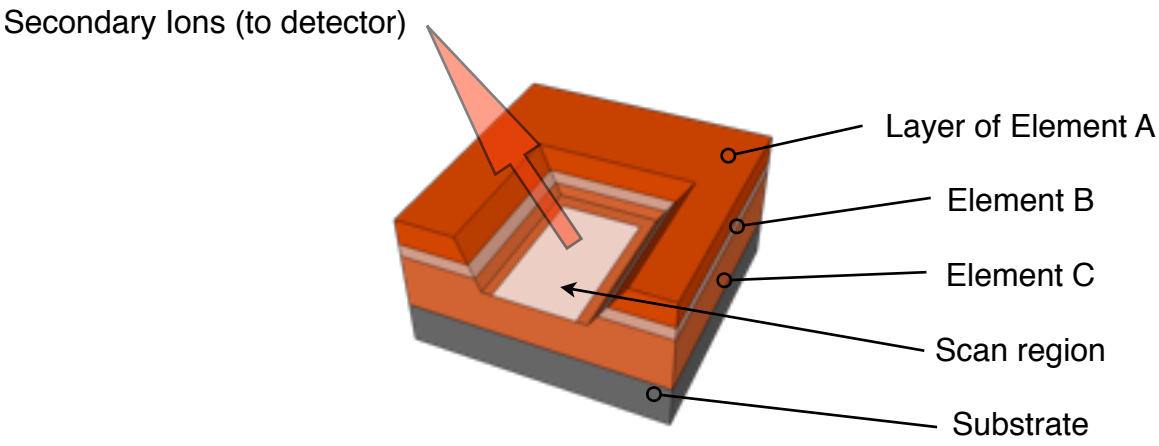

Figure 2.15 *- Depth profiling of a compositionally varied thin film sample. As the SIMS measurement proceeds, successive layers are exposed for characterisation, generating an elemental profile vs depth.*

SIMS measurements of as deposited γ-CuBr thin film samples were undertaken with the collaboration of Dr. Richard Morris at the Department of Physics, University of Warrick. The SIMS system used is known as a uleSIMS (ultra low energy SIMS) - the specific apparatus used was an Atomika 4500 Ultra-Shallow SIMS which allows for depth measurements and profiling at nano-scale resolution (~0.9 nm) [19].

2.9 References

[1] R. Martin, 'Electronic Structure: Basic theory and practical methods' Cambridge University Press, 2004.

[2] S. M. Sze, Ng. Kwok Kwok, 'Physics of semiconductor devices', Wiley, 2007.

[3] A.A. Cofolla, S.E. Schnatterly and C. Tarrio, Physical Review Letters, Volume 55, 1985, page 2818.

[4] E. I. Rashba & M. D. Sruge, 'Excitons', North-Holland Publishing Company, 1982.

[5] M. Ueta, 'Excitonic Processes in Solids', Wiley, 1986.

[6] P.D. Rack & P.H. Holloway, Mater. Science Eng., Volume 21, 1998, page 171.

[7] J. W. Allen, Journal of Luminescence, Volume 23, 1981, pages 127-139.

[8] H. H. Perkampus, 'UV-VIS spectroscopy and its applications', Wiley, 1992.

[9]R. Rusdi, A. A. Rahman, N. S. Mohamed, N. Kamarudin, N. Kamarulzaman, Powder Technology, Volume 210, 2011, Pages 18-22,

[10] B. Tanner, 'High Resolution X-Ray Difractometry & Topography', Taylor & Francis, 1998.

[11] Bruker AXS - D8 System X-Ray Diffractometer, manufacturer website: http://www.bruker-axs.de

[12] K. Bowen & B. Tanner, 'X–Ray Metrology in Semiconductor Manufacturing', CRC Press, 2006.

[13] T. J. Senden, Current Opinion in Colloid & Interface Science, Volume 6, Issue 2, May 2001, Pages 95-101,

[14] J. Goldstein, 'Scanning electron microscopy and x-ray microanalysis', Springer, 2003.

[15] G. O'Neill, Physical Review, 1956, page 1418.

[16] T. Sham, R. Sammynaiken, Y. Zhu, and P. Zhang, Thin Solid Films, 2000, pages 318-321.

[17] ANKA Synchrotron Website: http://ankaweb.fzk.de

[18] HASYLAB Synchrotron Website: http://hasylab.desy.de

[19] R. Morris, M. Dowsett, & S. Dalal, Surface and Interface Analysis, 2007, pages 898-901.

Chapter 3 - Epitaxial Methods

3.1 Introduction

As outlined in Chapter 1, epitaxy of semiconducting materials is of considerable importance in modern electronics, whether for crystal epilayers for LEDs or the increasingly important growth of self organized nano-structures [1]. A subset of epitaxial techniques used in this project towards the development of novel methodologies for CuHa growth, and their underlying principles, are outlined herein.

3.2 Epitaxy

Epitaxy, the ordered deposition of a crystalline material on to a single crystal substrate, has been observed since the 19th century. The name, derived from the Greek words ‘epi’ and ‘taxis’ (which translates to ‘to be arranged upon’) is also indicative of its 19th century pedigree. Though studied for its insights into crystallography, it has not been until the advent of the semiconductor industry that epitaxy has become an essential process for industrial application. For materials such as GaN, GaAs, InP to name but a few, epitaxial methods are the only cost effective means to achieve high quality crystal growth of these materials [2-5]. This work involved a number of forms of epitaxy, most notably LPE and PVD type processes, and a review of the fundamentals and driving forces of epitaxy and their specific methods as applied is presented.

As with all forms of crystal growth, epitaxy is fundamentally a controlled phase transition from a precursor state (solid, liquid or gas phase) into a solid, crystalline state. The growth of an epilayer represents a relationship between the underlying single crystal material (i.e. the substrate) and the

nascent crystalline phase that is being grown from its precursor state. Figure 3.1 shows a time lapse diagram of a typical epilayer growth.

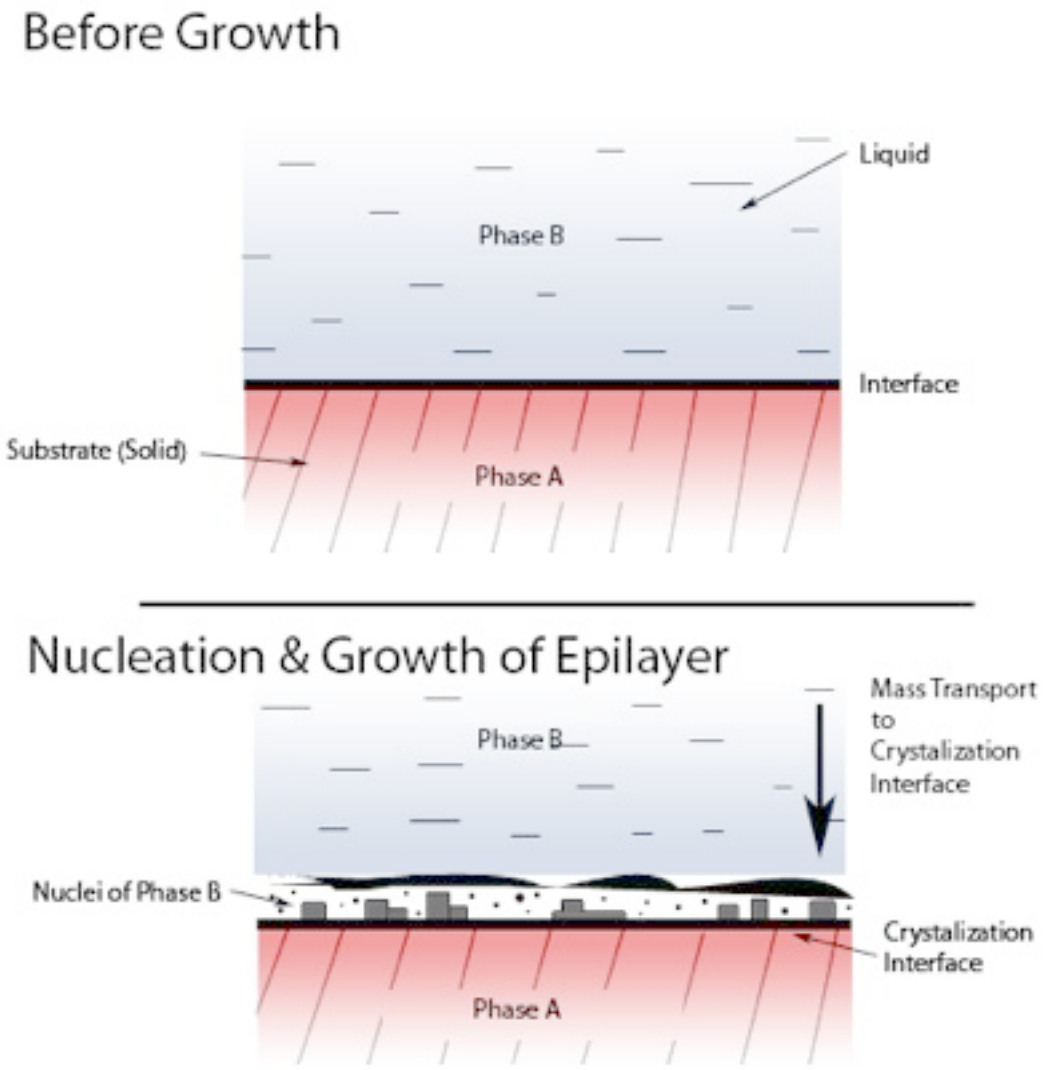

Figure 3.1 *- Illustration of nucleation and growth from a liquid phase of an epitaxial layer. Reproduced from [7].*

From a systemic point of view, epitaxy can be reduced to a number of driving processes. Since crystalline layers are typically 'grown', the 'fuel' used to drive this growth is a consideration. The phase transition between the solid, liquid or gas precursor phase into the growing epilayer is a rate limited reaction. Though the reaction type varies across the different epitaxial methods, it can be summarized as relating to the mass transport of the constituent material species from the precursor

phase towards the growth front of the crystal. This growth front is known as the crystallization interface. In order to maintain the growth of the epilayer, the 'fuel' supply must be maintained via a local supersaturation of the growth constituents at the interface.

The relationship between the substrate and the grown layer is also important - most notably, the alignment of the crystal lattice structure between the epilayer and substrate. In homoepitaxial situations, where the substrate and the epilayer are the same material, this is not an issue, due to the shared crystal structure. For heteroepitaxial growth, the misalignment of the substrate's crystal structure with that of the epilayers is known as misfit, and can be expressed as a percentage thus:

$$100\left(\frac{a_f - a_s}{a_s}\right) \tag{3.1}$$

where a_s is the lattice constant of the substrate material and a_f is the lattice constant of the epilayer material. Epitaxially grown layers usually contain many crystalline defects such as dislocations, point defects, etc., and the density of such defects is usually dependent on the misfit and the resultant growth mode. If the misfit is small, defects primarily arise due to the loss of coherency between the substrate and epilayer during growth, whereas with large misfit the defects arise from the lack of an exact lattice registry between the nucleating islands [6].

The actual growth of the epilayer is driven by nucleation of the constituent material onto the underlying substrate at the interface. Nuclei, embryonic atomic/molecular clusters of the material, coalesce and begin to form islands. Providing the growth conditions are maintained, these islands will enlarge and eventually agglomerate to form a continuous layer, driven by a specific growth mode.

Classically, it is understood that five modes of epitaxial growth exist; Volmer-Weber (VM), Frank-Van der Merwe (FM), Stranski-Krastanov (SK), Columnar growth (CG), and Step Flow (SF). The VM, FM, SK and Columnar growth modes are illustrated in Figure 3.2. In VM growth, the nuclei are more attracted to each other than to the surface, and nucleate around each other to form islands - as more of the nuclei coalesce on existing islands, they begin to dominate the overall film structure [7, 8]. For FM growth, a stable monolayer forms on the surface prior to any further layer growth and results in a smooth film [9]. In the SK growth mode, a layer by layer film will grow until stress builds up in the film and the mode switches to a 3-dimensional island growth as in FM growth mode. The free surfaces on these islands can deform to locally relieve accumulated layer strain. Step flow (SF) growth mode is also similar to the layer by layer FM mode, however the layers in this mode form as a series of planar steps which can lead to a terrace like epilayer [7, 10]. The last growth mode is the columnar growth mode, which is similar to VM and SK combined - merging islands coalesce and form an underlying structure that can propagate upwards throughout the epilayer.

Which mode is expressed during the epilayer formation depends upon the lattice misfit between the epilayer and substrate, the flux/supersaturation of the growth material, temperature of the constituent species during growth and the interaction between adhesive/cohesive energies of the epilayer and substrate.

As mentioned previously, growth proceeds from the crystallization interface. The stability of the interface is thus an important step in realizing epilayer growth. Chemical reactions between the growth material and the substrate can be deleterious to successful epitaxy - this is particularly the case for LPE.

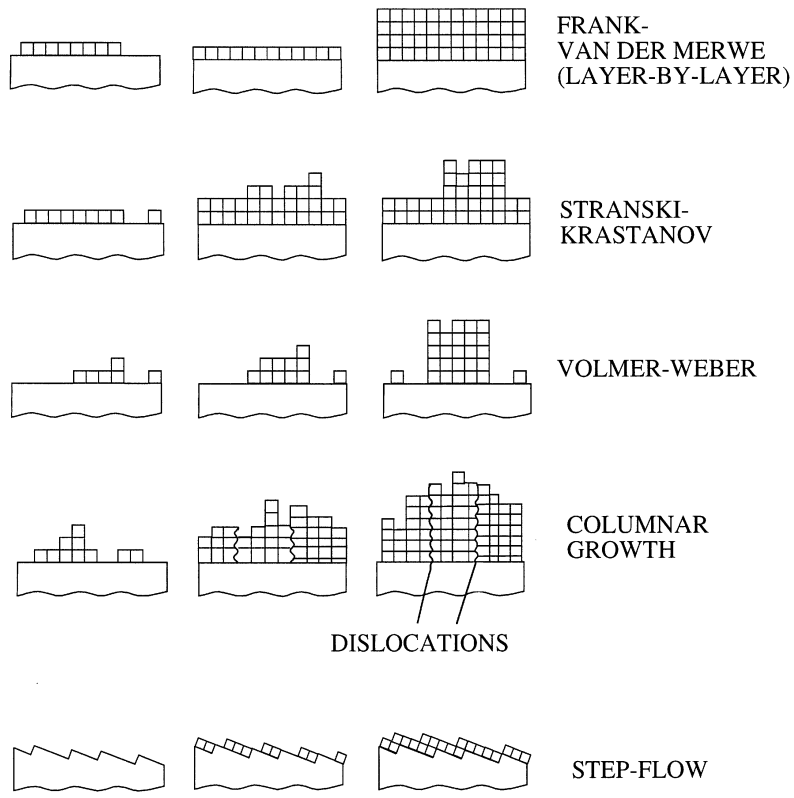

Figure 3.2 *- Illustration of the various growth modes: Frank van der Merwe, Stranski-Krastanov, Volmer-Weber and Columnar type growth. Reproduced from [10].*

3.3 Liquid Phase Epitaxy

LPE has been widely used for the past five decades to successfully grow epitaxial layers, most notably of III-V compound semiconductors for optoelectronic devices [11-15]. The most notable advantage of LPE over other growth techniques is the high crystalline quality of the epilayers produced. The near-equilibrium based growth conditions result in low densities of point defects and the segregation of impurities into the liquid phase results in low background impurities in a properly conducted growth run [16]. Its basis on phase equilibria allows a much wider range of materials to be used for growth, thus allowing for investigations into novel materials such as those investigated in this project.

The LPE growth process can be broken up into three steps:

- Formation of nuclei at the substrate.
- Surface attachment of the nuclei and the initiation of a growth mode (e.g. FM) leading to the formation of macroscopic features. This forms the crystallization interface.
- Transport of solute to the crystallization interface to continue growth by diffusion of solute species in the melt.

Fundamental to the LPE process is the understanding of the phase diagram - a graph indicating the conditions for which thermodynamically distinct phases can exist in equilibrium. This graph is based on Gibb's phase rule, which states that the degrees of freedom in a system is given by

$$F = C - p + 2 \tag{3.2}$$

where C is the number of components and p the number of phases in thermodynamic equilibrium. LPE growth conditions are carried out at approximately 1 atm and thus pressure can be ignored, giving $F = C - p + 1$. For binary (e.g, Ga-As), ternary (e.g, In-Ga-As) and quaternary (e.g, Ga-Al-As-Sb), the degrees of freedom for the phases would be 1, 2 and 3 respectively. The phase rule informs the phase diagram, with ternary and quaternary phase diagrams having more complexity compared to binary systems like CuCl-KCl and Ga-As. The phase diagram for the KCl-CuCl system is presented in figure 3.3 below.

From this diagram, consider a composition of $KCl_{(20)}CuCl_{(80)}$. This melt composition is subjected to an isothermal heating regime in order to enter the liquid phase. Once the equilibration of the solution is complete, the temperature of the furnace is slowly lowered and the melt will move from the liquid phase into the liquid and CuCl (solid) stage, shaded green.

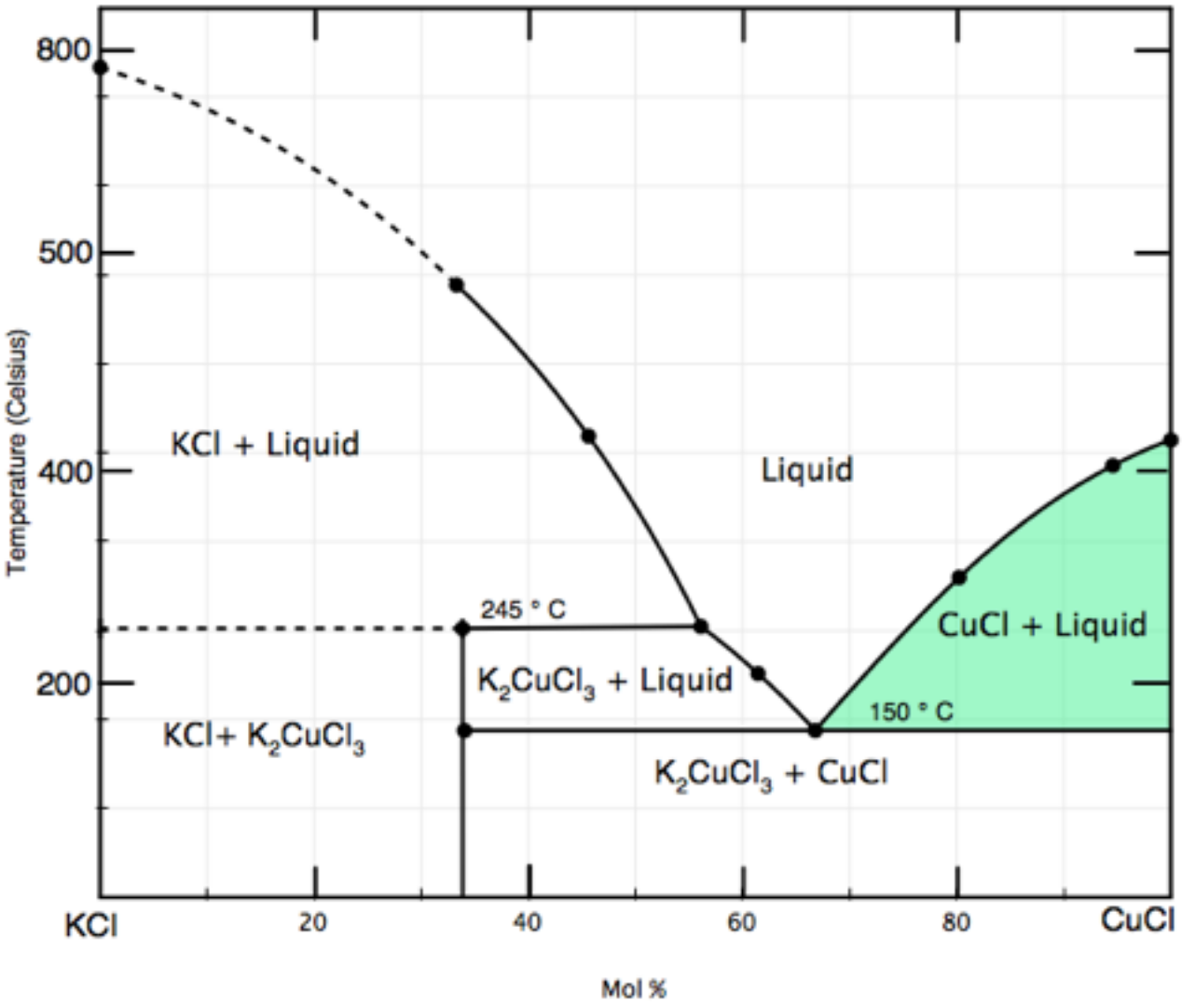

Figure 3.3 *- Binary phase diagram of the KCl-CuCl system. Highlighted region shows the parameter space for precipitation of CuCl out of the liquid as a solid. Reproduced from [17].*

When the solution is cooled through the liquidus curve the solid phase CuCl will begin to precipitate out of the liquid phase. Should a substrate be present during the precipitation of the material from its liquid phase, then the epitaxial deposition can occur of this compound onto the substrate. This is the essence of LPE, though grossly simplified for illustrative purposes.

While theoretically simple, it is not such an easy process to master and there exists a large matrix of parameters that must be precisely controlled and accounted for relative to each LPE system and its

constituent parts and melt choices. Isothermal conditions for the melt during the growth phase, wetting between the melt and the graphite boat and maintenance of a contaminant free system are but a sampling of these parameters - a considerable body of LPE literature is given over to the determination of experimental parameters that affect growth [18, 19, 20].

Exposing the melt to the substrate is also an important experimental parameter - a large number of methods have been developed for contacting the melt to the substrate when growth is to be started. Methods include tipping [21], sliding boat [22], rotary slider [11], dipping [23], and piston slide boat [24]. The most commonly used LPE technique for III-V growth is the horizontal sliding boat system. Specific problems with the horizontal slide-boat LPE technique include poor wipe-off and the issue of abrasive scratching. Droplets from the melt can sometimes remain on any epitaxial layer grown from that melt after the slider has been moved to remove excess melt. LPE can often produce poor quality surfaces, frequently rough and blemished. The surface can be rough because the excess melt droplets can dissolve the underlying layer/substrate, resulting in dissolution pits. The surface scratching is a result of the sliding-boat movement over the grown epilayer, although this is only an issue if the growth was carried out for too long a period of time (i.e., resulting in the overgrowth of the epilayer beyond the recess and putting the epilayer in the path of the wipe-off mechanism).

LPE is advantageous with regards to dopants. The nature of the solution growth means that essentially any element introduced into the melt can be incorporated in the epilayer to some degree. This opens up a huge range of choices for potential doping research. The multi-bin structure of the conventional sliding-boat system also allows for the use of multiple solutions and thus the fabrication of multi-layer samples. Alternatively, the multiple bins can be used to hold solutions chosen to prepare the substrate such as a precursor Gallium melt for etching purposes [25]. Relative

to other crystal growth techniques, the machinery for LPE growth can be procured and maintained relatively cheaply compared to the more expensive molecular beam epitaxy (MBE) or metal organic chemical vapor deposition (MOCVD) systems.

3.3.1 LPE Process & Equipment

A number of experimental geometries exist to expose the melt to the substrate for LPE growth - the two used for this project are the tipping system and the conventional sliding boat system. In all cases for this project, the pieces were machined from high quality graphite (POCO grade [26]) which has exceptional thermal properties - necessary for the isothermal conditions needed for LPE. One disadvantage of using graphite, however, is its porous nature. When exposed to air, the graphite will absorb atmospheric gases, which can affect the purity and behaviour of a melt in a graphite boat [27]. Care when handling boats is therefore important - storage of boats in non-contaminating environment (e.g. vacuum) was an impractical solution for this work. Instead, boats that had been recovered from previous LPE growths would be cleaned, dried and then stored in clean-room quality cloth and placed into sterile boxes. Best possible care was given while handling the boats outside of the LPE system and stringent pre-growth baking was undertaken for each boat prior to loading of the melt. Details of the bake-out procedure is given in the experimental details of chapter 5.

3.3.2 Tipping System

Tipping systems were the first used for LPE as shown by [21]. When the time for the melt to be exposed to the substrate is reached, the assembly containing the melt is rotated or tipped, such that gravity moves the melt into contact with the substrate and growth can commence. This setup is simple, and removes any damage that can be caused by abrasion of graphite pieces with the epilayer. It is limited to a single melt, however.

The tipping system usually involves either a rotation of a boat or the tipping of the whole LPE assembly, as per Hsieh [28]. Since direct tipping of the furnace and LPE system was unfeasible for this project, a solution was engineered that used the existing sliding boat mechanics to move a wedge under a suspended boat. Moving the wedge out would lower the back side of the boat and allow the melt to run onto the substrate, while pushing the wedge back in would tip the melt off the substrate at the end of the growth run. The melt bin was designed to be sufficiently large to accommodate the 5g melt size commonly used. The substrate recess dimensions were 18mm x 16mm. The engineered boat system can be seen in figure 3.4 below.

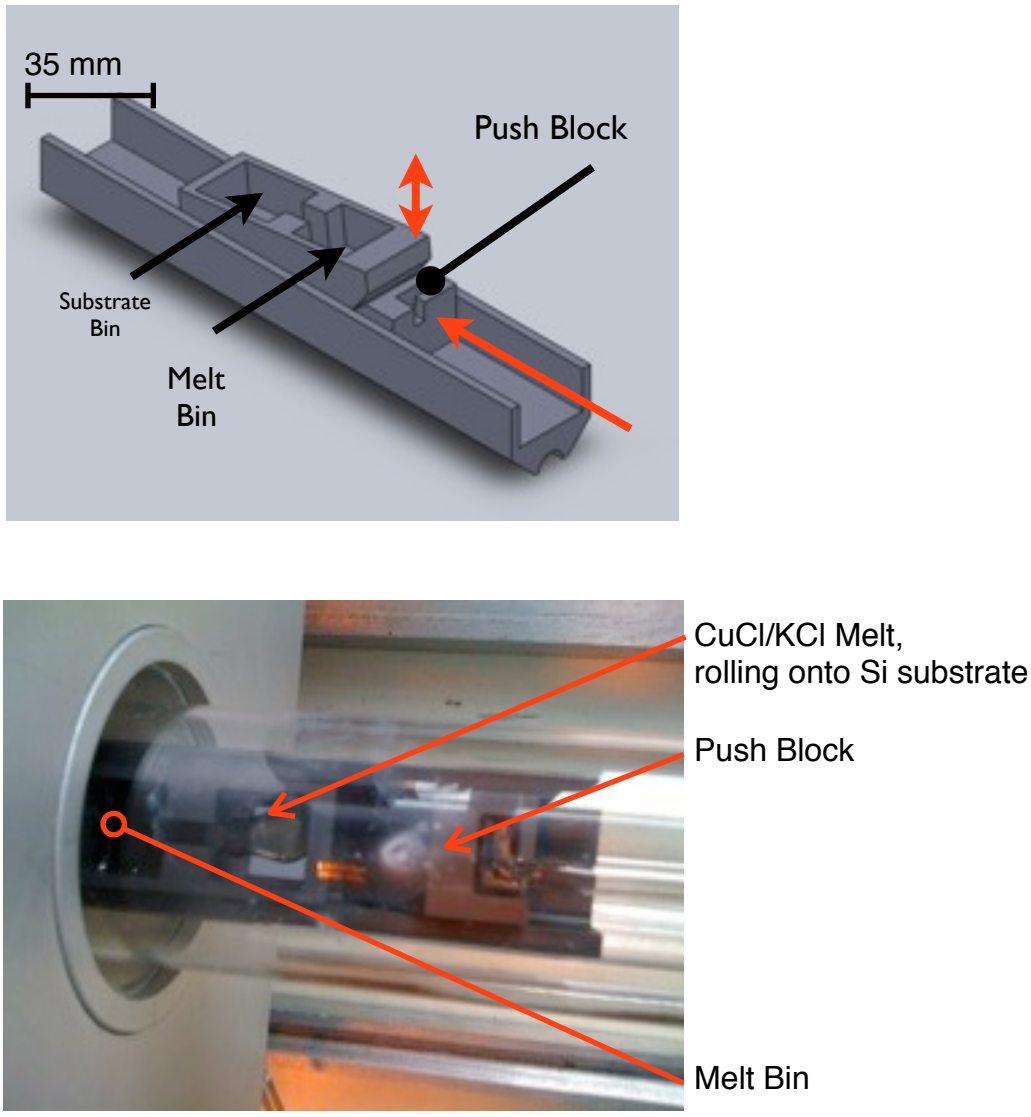

Figure 3.4 *- Custom tipping boat design, illustrating the push block moved by the quartz glass rod attached to the pushing block.*

3.3.3 Sliding Boat

The sliding boat system is more complex but allows for multiple growth solutions and thus, multi-layer structures. Even for single melt regimes, however, the multi bin sliding boat has advantages over a tipping system, namely being that the empty bins can be useful in removing excess melt during wipe off. The melt bins can have a graphite lid placed to reduce contamination from the gas flow.

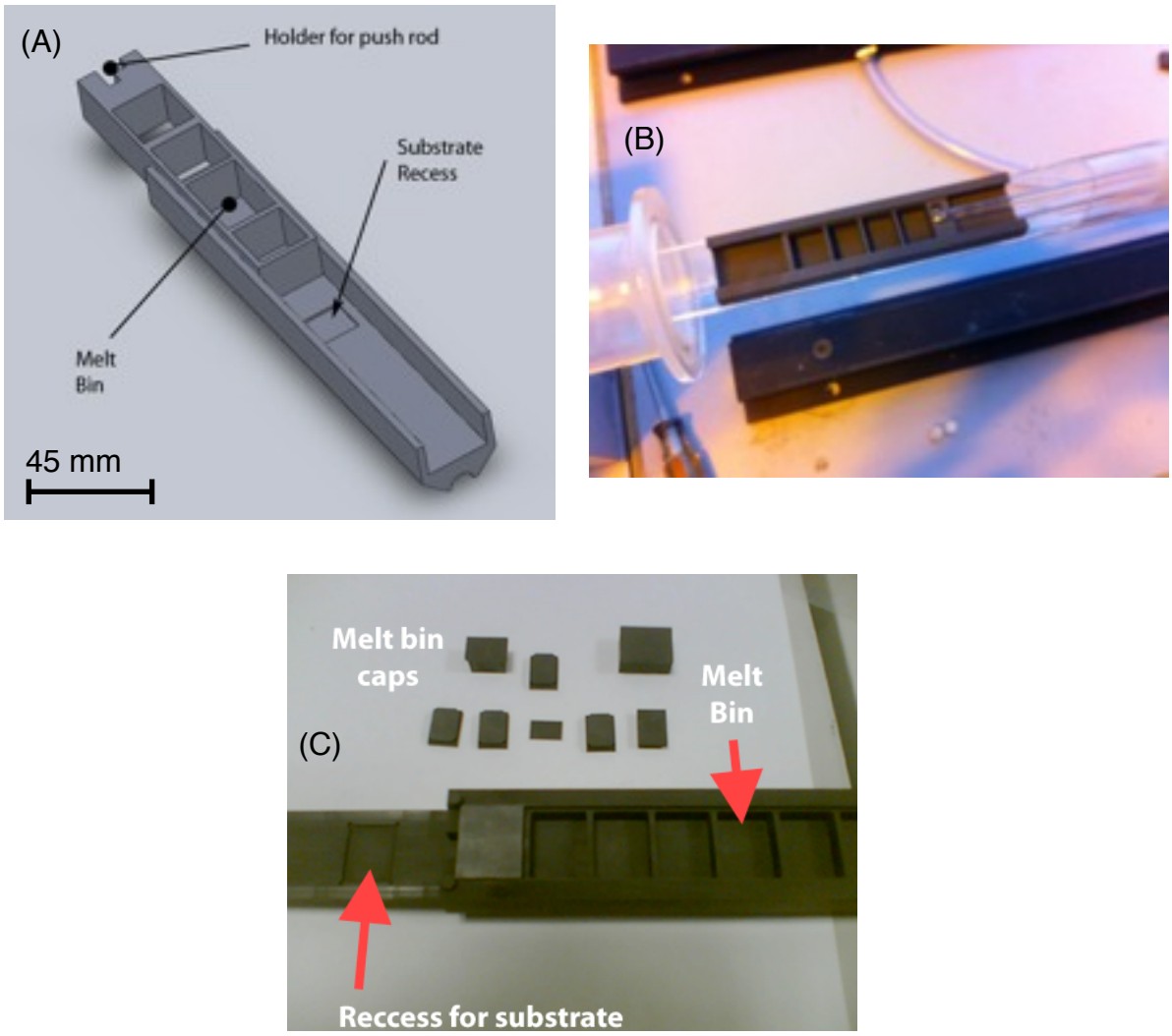

Figure 3.5 *- Sliding Boat system; (a) Parametric CAD outline of sliding boat arrangement, (b) boat held in quartz glass boat holder (push rod can be seen to the right) (c) Actual machined graphite boat (POCO graphite) with melt bin caps displayed.*

A number of different sized sliding boats were available for this work, usually with varying melt bin sizes and substrate dimension requirements. The most commonly used boats had a melt bin capacity sufficient for the 5g melt used and had substrate dimensions of approximately 18mm x 14mm. Smaller graphite pieces were used to raise the substrate up so that the clearance between the substrate and the sliding boat would be ~20 μm, sufficiently large to accommodate for any growth but also to ensure that mechanical jamming of the boats does not occur.

3.4 LPE Growth Techniques & Theory

Generating the required supersaturation in a liquid is the basis for LPE growth and a number of growth conditions can be utilized in order to achieve this. The three most commonly used conditions are ramp cooled growth, step cooled growth and super cooled growth, and they are illustrated in figure 3.6.

For ramp cooling, once the melt is in contact with the substrate, the temperature of the melt is lowered at a rate R (°C min^{-1}) from the liquidus temperature. This was the original growth condition used for LPE by Nelson [21]. It was found experimentally that the surface morphology and thickness uniformity were inferior compared to those epilayers grown by the step cooled growth [28, 29]. Step cooled growth involves lowering the temperature by an amount, ΔT_s, below the liquidus and then exposing the substrate while maintaing this temperature. The supercooling step enhances the nucleation by increasing the supersaturation and the constant temperature profile over growth can help with impurity incorporation during growth. The final approach is supercooled growth, which mixes ramp cooling and step cooling, and gains the benefit of the enhanced nucleation as well as faster layer growth.

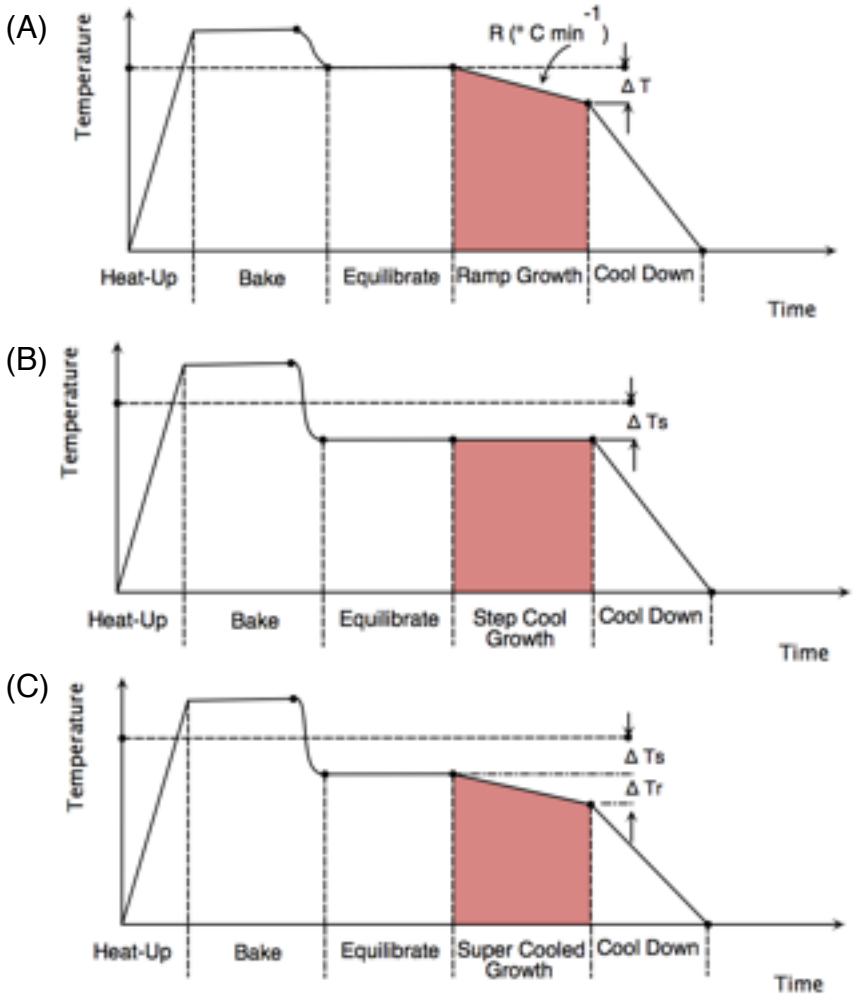

Figure 3.6 *- Temperature profiles for LPE growth, illustrating; (a) Ramp cooling, (b) Step cooling and (c) Supercooling. Reproduced from [29].*

For all these growth modes, diffusion limited growth theory has been used to describe the LPE growth as well as to determine the growth rates and layer thicknesses. The basis is that the rate limiting step for growth is the diffusion of solute species to the crystallization interface.

The one-dimensional diffusion equation can be stated as [29]:

$$\frac{\Delta C}{\Delta t} = D\frac{\Delta^2 C}{\Delta x^2} + v\frac{\Delta C}{\Delta x} \tag{3.3}$$

which is essentially Fick's second law of diffusion combined with a growth velocity element, *v*. *C* is the solute concentration as a function of time *t, D* is the diffusion coefficient for solute *C* in the

liquid solution and x is the position from the crystallization interface in a direction normal to the solid-liquid phase boundary. This expression can be visualized in figure 3.7.

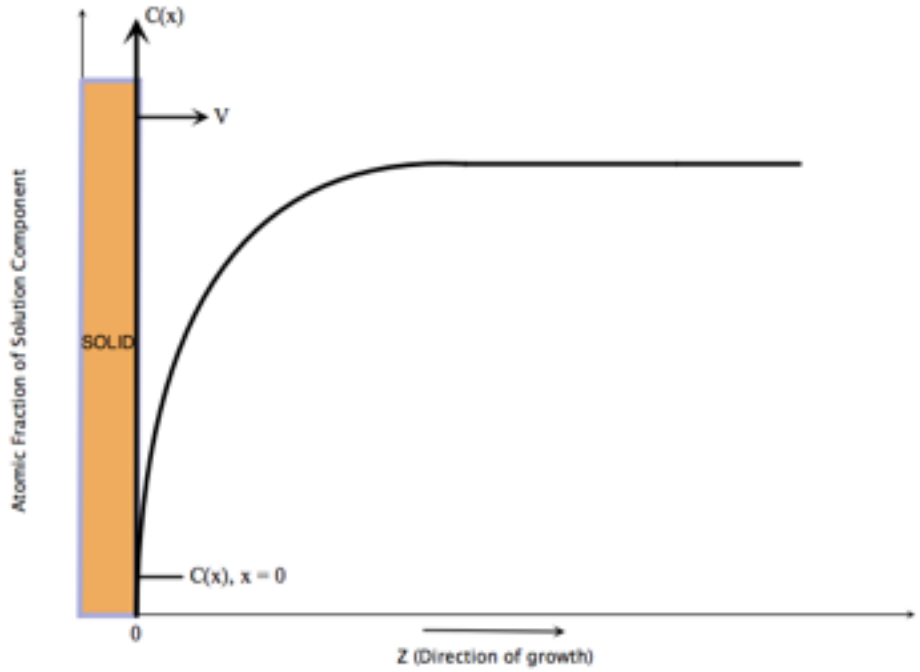

Figure 3.7 *- Solute concentration profile at crystallization interface during growth, with z-axis denoting the growth direction, reproduced from [29]*

A number of assumptions and boundary conditions have been made to explain the state of the LPE system in terms of diffusion limited growth. Growth is carried out under isothermal conditions, the solution is considered infinite (i.e., the solution surface is not reached), the growth velocity at the crystallization interface is negligibly slow and the solution depth is small enough to disregard convection within the solute [28, 29]. This gives the solution for the diffusion equation to be

$$\frac{\Delta C(x,t)}{\Delta t} = D\frac{\Delta^2(x,t)}{\Delta x^2} \tag{3.4}$$

for position x at time, t. The thickness of a grown layer can be determined for a specified time, as shown here:

$$d(t) = \frac{1}{C}\int_0^t D\left(\frac{\Delta C}{\Delta x}\right)dt \tag{3.5}$$

Additional boundary conditions are applied for the different growth conditions. For ramp growth, the temperature is reduced linearly with a known rate. Further assumptions are made regarding the liquidus composition behaving as a linear function and there being a uniform concentration of the solute, which gives the ramp cooled thickness to be

$$d(t) = \frac{4}{3}\left(\frac{D}{\pi}\right)^{1/2}\left(\frac{\alpha}{Cm}\right)t^{3/2} \tag{3.6}$$

where α is the cooling rate and m the slope of the liquidus curve nearing the crystallization interface. Similar thickness calculations have been derived for the step cooling growth and the supercooled growth [30, 31].

3.4.1 Wetting

Consideration of the wetting relationship between the melt, substrate and graphite crucible is also an important growth. Wetting is the relationship between a liquid and a solid brought into contact. The degree to which wetting (see figure 3.8) occurs is dependent on the surface energies of the two components and the measure of this interaction is known as the contact angle (or wetting angle).

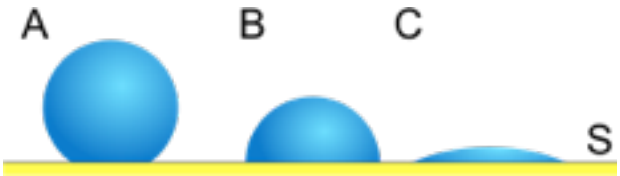

Figure 3.8 *- Examples of wetting behavior. A poorly wets the surface, S, while B and C have progressively improved wetting behaviour, respectively [32].*

Thomas Young proposed that the interaction between the forces of cohesion and adhesion would determine whether or not wetting would occur. He derived the following equation [33]:

$$Y_{SL} + Y_{LG}\cos\theta = Y_{SG} \tag{3.7}$$

Here, Y_{SL} , Y_{LG}, and Y_{SG} are the interfacial tensions between the liquid and the solid, the liquid and the ambient gas and the solid and the gas respectively. θ is the contact angle the drop makes with the flat surface.

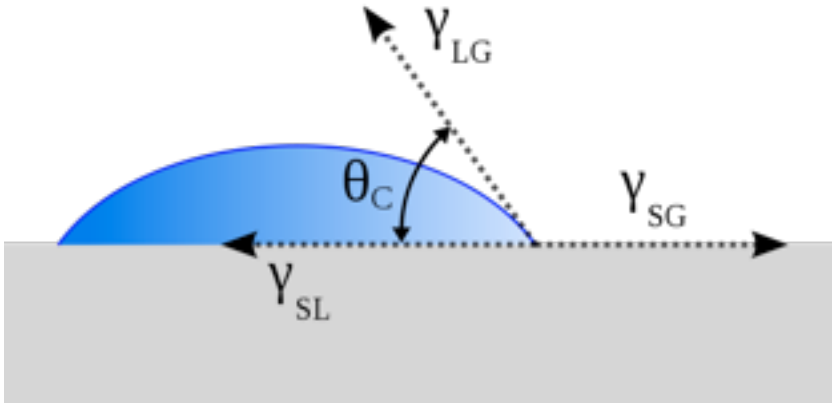

Figure 3.9 *- The various components making up a contact angle. Sample illustrated represents a liquid droplet on a solid surface [32].*

The relationship between the melt and the graphite is important as it is a factor in the passing of contaminants from the porous graphite into the melt and thus the epilayers grown. Interaction between the graphite walls of a melt bin, the melt and the substrate can also affect the mechanical stress present in any grown epilayer and thus dislocation densities [27]. Also, a small contact angle between the graphite and the melt material increases the chance of the melt creeping under the slider-boat compartment walls, which leads to issues with carry over in multi-bin solution runs and general wipe off and post-growth crucible cleaning problems.

A small contact angle between the substrate and the melt is also important as a low wetting angle is necessary for uniform growth [34]. The melt will behave as a liquid on the substrate and will be subject to the same forces of adhesion and cohesion due to varying surface energies as outlined by Young. These surface and interfacial energies have a large impact on growth. They are also used for determining the nucleation rate of the melt onto the substrate.

3.5 LPE Apparatus Development

Construction of our LPE system for this project began in October 2006. The inventory of initial parts provided by Dr. Andreas Danilewsky of Freiburg University, Germany, included the 3 zone tube furnaces, a number of quartz glass furnace tubes and sundry graphite pieces and sliding boats. The initial objective was to operate and control the tube furnaces, however much of the existent control system for the tube furnaces was antiquated and without the original micro-controller unit, and was not directly operational without beginning significant software development of an interface software layer to communicate with the legacy Analog Devices uMacBASIC control boards. It was decided to bypass the existing components and directly control the furnace. The original control blocks were therefore removed and a direct control system using the furnace thermocouples (K-type) and the thyristor control block was envisioned and developed. Control of the furnace would be driven by a proportional-integral-derivative (PID) device, which would use the existing thermocouples and feed back to the thyristor unit. A Eurotherm PID controller was obtained and integrated into the system - since the furnace had not been operated in some time, a number of ramp heating experiments were carried out to allow the furnace to equilibrate and help tune the PID unit. Eventually, the three zones were calibrated to ensure a flat temperature profile across the middle zone of the furnace, where the graphite slide boat/tipping system would be positioned.

A vacuum system also had to be added to the LPE system - a standard rotary vane backing pump with oil trap provides the roughing while a turbo-molecular pump provides the backing. The system supports a high-vacuum capability (10^{-5} mbar) as well as high purity Argon and Hydrogen (99.99995%) gas flow. Figure 3.10 below shows the LPE system assembled as of December 2007.

Figure 3.10 *- DCU's LPE system assembled as of December 2007*

DCU's custom built LPE apparatus utilizes the sliding boat & tipping approach, as outlined previously. A quartz push rod, driven by a computer controlled stepper motor, is used to drive the sliding boat melt bins over a second graphite piece containing the substrate material at a predetermined time during the cooling process. This push rod also controls the tipping system when that setup is being used.

The graphite pieces are supported within a quartz glass tube, which sits into the cylindrical bore, 3-zone tube furnace. The furnace can be rolled back on tracks to allow visual observation of the melt *in situ* during an applied temperature regime. Figure 3.11 shows the layout of the LPE system components.

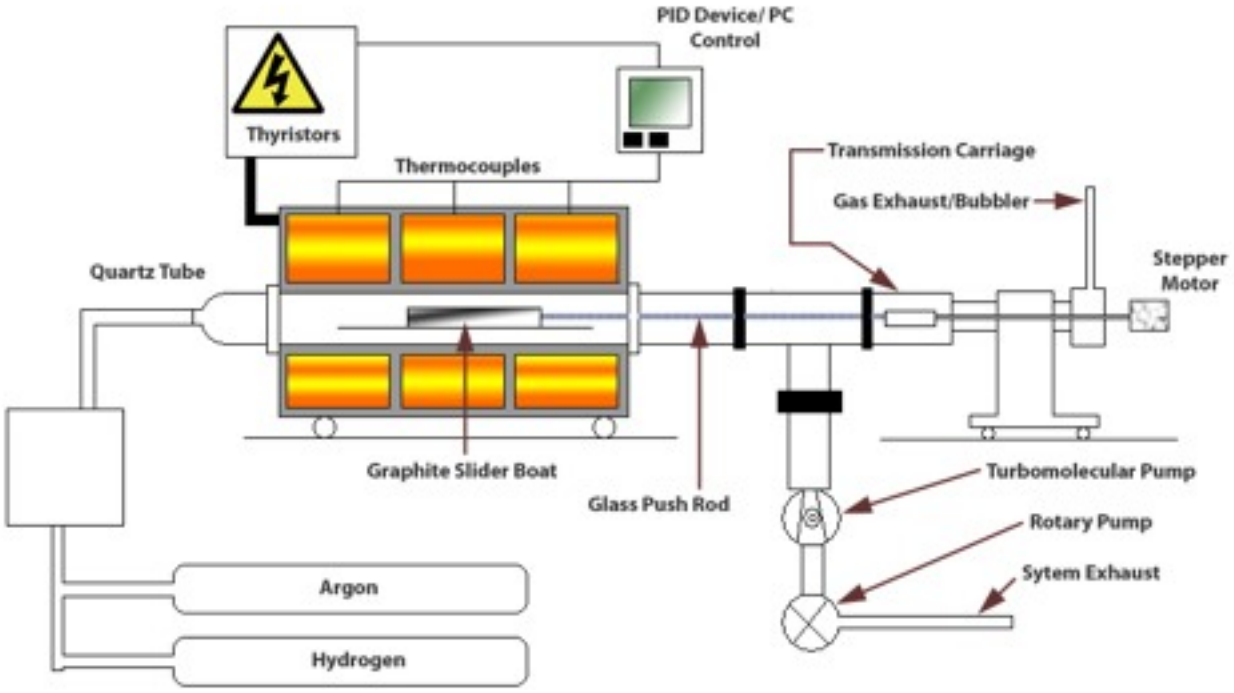

Figure 3.11 *- Annotated schematic illustration of the LPE setup*

3.6 Physical Vapour Deposition (PVD)

Physical Vapour Deposition is used for many types of epitaxial deposition, namely vacuum evaporation (or deposition), ion plating and sputter deposition [35]. This work makes use of the vacuum evaporation process for CuHa deposition, which is a relatively simple material to work with for PVD.

Material that is to be deposited is placed into a thermal boat (of which a number of geometries exist: dimple boat, wire, quartz crucible to name but a few), and is subjected to thermal vaporization while under vacuum. Predominantly, this is done via resistive heating of the boat, which also

controls the evaporation rate of the material. Thus the growth rate can be readily controlled via the current supplied to the boat. When carried out under vacuum, the ejected evaporated material can reach the substrate with very few collisions from other gas molecules present, and can then nucleate and grow on the substrate to form the thin film.

Application of adsorption kinetics allows for the rate of adsorption of a molecule onto a surface to be described. This rate is defined by the flux of arriving molecules to the substrate and the proportion of those molecules which undergo adsorption to the surface. Simply stated,

$$R = S \times \Gamma \tag{3.8}$$

where the rate, R is the product of the incident flux, Γ, and the probability of attachment to the surface, known as the sticking probability, S [35]. The flux is given by the Hertz-Knudsen equation,

$$\Gamma = \frac{p}{(2\pi mkT)^{1/2}} \tag{3.9}$$

where k is Boltzman's constant, P is the gas pressure, T the absolute temperature and m the mass of the vaporized species. The sticking probability is related to substrate and, as a probability, lies between zero and one. It is dependent upon the cleanliness of the substrate as well as existing coverage of adsorbed species. The mass of vaporized species per unit area, however, is dependent on the geometry of arriving vaporized material, as can be seen in figure 3.11.

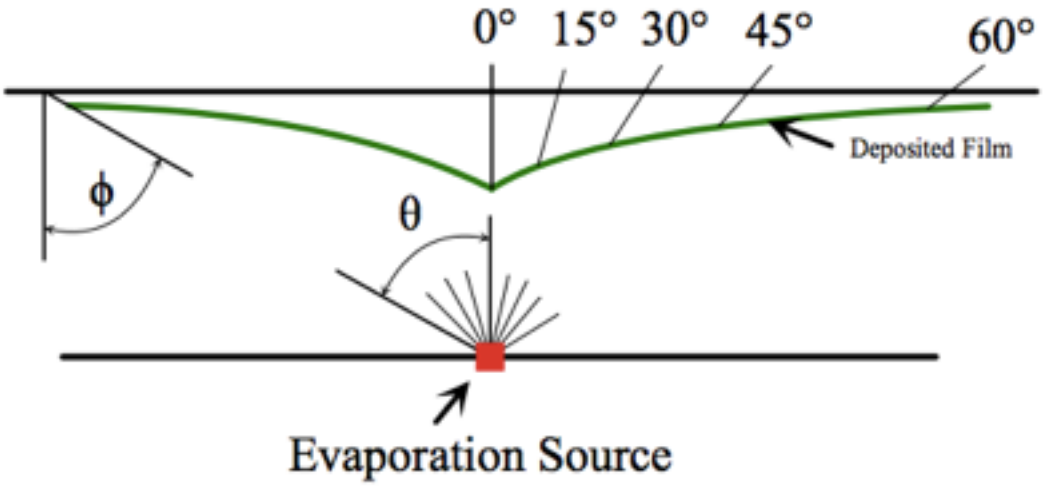

Figure 3.11 *- Distribution of evaporated material from an evaporation point on a flat surface above the source, reproduced from [35].*

This can be expressed in terms of a cosine deposition distribution, given as

$$\frac{dm}{dA} = (E / \pi r^2)\cos\phi\cos\theta \tag{3.10}$$

where E is the total evaporated mass, r the distance from substrate to source, ϕ is the angle of the normal to the substrate and θ the angle of the source to substrate. Clearly, from fig 3.11, uniformity can be a problem, but this can be alleviated by judicious placement of the substrate such that

$$\cos\phi = \cos\theta \tag{3.11}$$

and the source-substrate distance is

$$d = 2R\cos\theta \tag{3.12}$$

Thus deposition can be kept uniform for any point on the circumference of circle *R*. Successful deposition is dependent upon the cleanliness of the substrate as well as the cleanliness of the evaporator system itself. Secondary evaporation of unwanted contaminants can be an issue, depending on their vapour pressure and evaporation temperature relative to the evaporated material. Likewise, use of a clean, non-reactive boat is important. For single compound evaporations such as the CuHa, vaporization is very straightforward. However, for some of this work evaporation of a $CuHa_{(1-x)}KHa_{(x)}$ mixture is undertaken. As per Raoult's Law, this results in a concentration gradient in the substrate as each evaporant is selectively vaporized. This co-evaporation of $CuHa_{(1-x)}KHa_{(x)}$ will be discussed further in chapter 4.

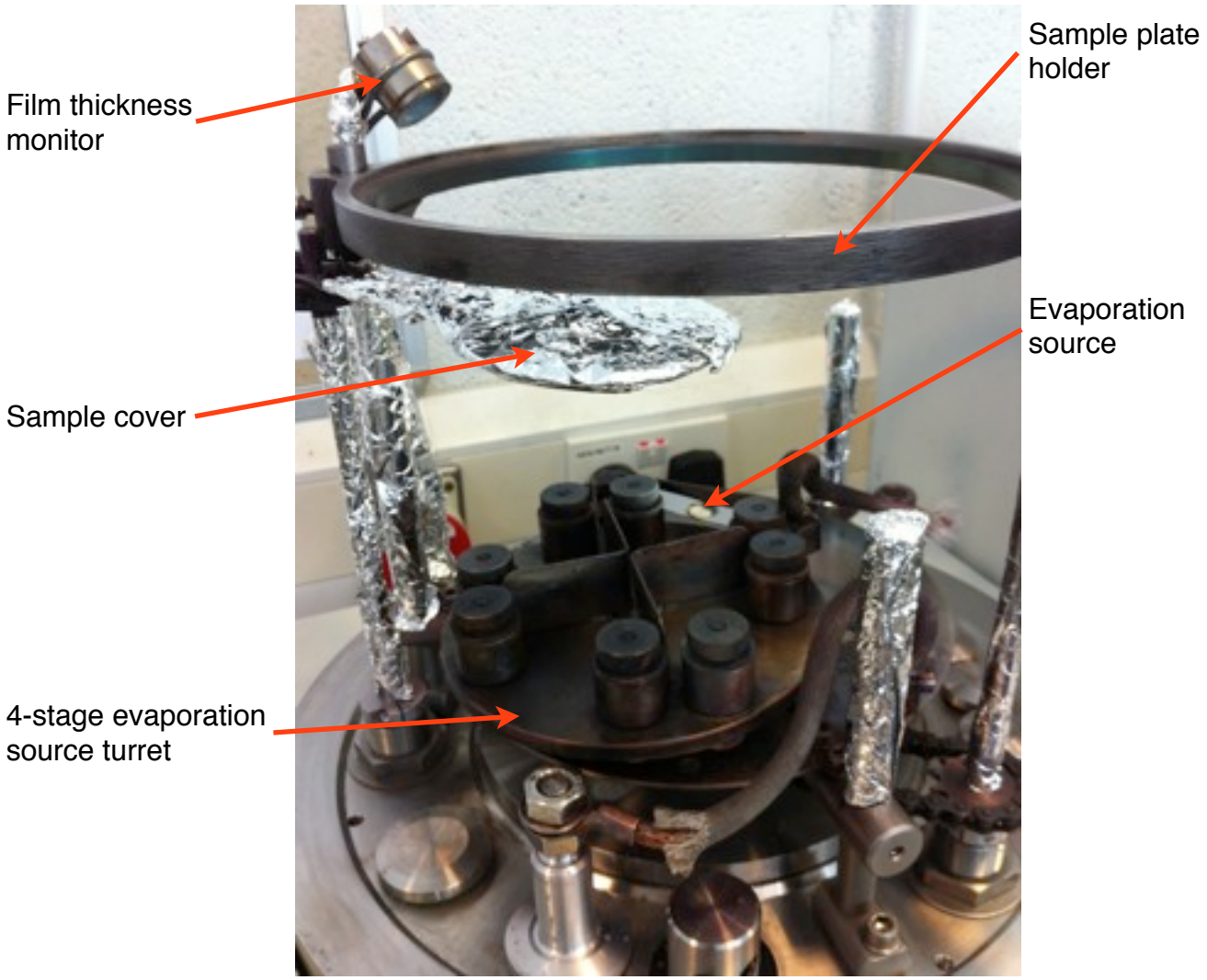

Figure 3.12 *- Edwards E306 Vacuum Evaporator.*

For this work, an Edwards Auto E306 thermal resistance evaporator was used [36] and can be seen in figure 3.12. All evaporations were carried out under vacuum conditions (~5 x 10^{-6} mbar) and the system is serviced by a roughing rotary pump and a backing diffusion pump pairing. The E306 has a FTM6 water cooled thickness monitor which can be used to determine the thickness of deposited films. This monitor needs to be calibrated to different materials prior to deposition, as each material affects the thickness monitor quartz crystal differently. A number of material specific parameters need to be calculated in order to correctly calibrate the thickness monitor for different materials. Once known, the film thickness, T_c, is given by the equation,

$$T_c = \frac{FD_qN_q(P_q - P_6)}{D_e} \tag{3.13}$$

where D_q is the density of quartz, N_q is the frequency constant of quartz, P_q is the loaded crystal period, P_6 is the period of the 6 MHz crystal used by the monitor, D_e is the density of the deposition material and F is the tooling factor. Both D_e and F are calculated thus:

$$D_e = D_a \frac{T_i}{T_m} \tag{3.14}$$

$$F = \frac{T_m}{T_i} \tag{3.15}$$

where T_m is the average thickness and T_i the thickness measured by the FTM6 system. Resistively heated tungsten dimple boats were used as holders. A value of 3.16 was previously calculated as the tooling factor for CuCl [37] and a similar calculation for CuBr yields a tooling factor of 2.8. A schematic of the evaporator system and dimple boat can be seen in figure 3.12.

3.7 References

[1] C. Rao, F. Deepak, G. Gundiah, A. Govindaraj, Progress in Solid State Chemistry, Volume 31 2003, pages 5–147.

[2] S. Nakamura, Thin Solid Films,Volumes 343-344, 1999, pages 345-349.

[3] H. Morkoc & L. Eastman, Journal of The Electrochemical Society, Volume 123, 1976, pages 906-912.

[4] K. T. Ip, L. F. Eastman, V. L. Wrick, Electron. Lett., Volume 13, 1977, page 682.

[5] C. Klemenz, H. J. Scheel, Journal of Crystal Growth, Volume 211, 2000, Pages 62-67.

[6] W. Matthews, A. E. Blakeslee, Journal of Crystal Growth, Volume 29, 1975, Pages 273-280.

[7] M. A. Herman, W. Richter, H. Sitter, 'Epitaxy: Physical Principles and Technical Implementation', Springer-Verlag, 2004.

[8] H. Luth. 'Solid Surfaces, Interfaces and Thin Films', Springer, 2001.

[9] J. M. Howe. 'Interfaces in Materials: Atomic Structure, Thermodynamics and Kinetics of Solid-Vapor, Solid-Liquid, and Solid-Solid Interfaces'. Wiley, 1997.

[10] H. Scheel, Journal of Crystal Growth, Volume 211, 2000, pages 1-12.

[11] D. Alexiev, D. A. Prokopovich, S. Thomson, L. Mo, A. B. Rosenfeld & M. Reinhard, 'A Review of Liquid Phase Epitaxial Grown Gallium Arsenide', 2007.

[12] X. Y. Gong, Crystal Research and Technology Volume 35, 2000, pages 549-555.

[13] S. Dhar, Bulletin of Materials Science, Volume 28, 2005, pages 349-353.

[14] G. A. Antypas, Journal of The Electrochemical Society, Volume 170, 1973, pages 1574-1577.

[15] Z. Xu, Applied Physics A: Materials Science & Processing, Volume 66, 1998, pages 565-567.

[16] J. Vilms, J.P. Garrett, Solid-State Electronics, Volume 15, 1972, Pages 443-452.

[17] D.E. Etter & C.J. Wiedeheft, Solar Energy Materials 2, 1980, pages 423-431.

[18] H. Morkoc, L. F. Eastman, Journal of Crystal Growth, Volume 36, 1976, pages 109-114.

[19] S. Yamazaki, K. Nakajima, T. Takanohashi, Y. Kishi, K. Akita, Journal of Crystal Growth, Volume 61, 1983, pages 289-294,

[20] O. Prochazkova, J. Zavadil, K. Zdansky, Materials Science and Engineering: B, Volume 80, 2001, Pages 14-17.

[21] H. Nelson, RCA Review, Volume 24, 1963, page 603.

[22] J.J. Hsieh, Journal of Crystal Growth, Volume 27, 1974, pages 49-61.

[23] J.M. Robertson, W. Tolksdorf, H.D. Jonker, Journal of Crystal Growth, Volume 27, 1974, pages 241-248.

[24] Z. Zytkiewicz, D. Dobosz, M. Pawlowska, Semiconductor Science and Technology, 1999.

[25] B. E. Sunmer, Journal Applied Physics, Volume 49, 1978, pages 4291-4293.

[26] POCO Graphite Company website: http://www.poco.com/

[27] A, Croll, R. Lantzsch, S. Kitanov, N. Salk, F.R. Szofran, A. Tegetmeier, Crystal Research Technologies, Volume 38, 2003, pages 669-675.

[28] T.S. Moss, 'Handbook on Semiconductors', Elsevier, 1980.

[29] M.G. Astles, 'Liquid-phase epitaxial growth of III-V compound semiconductor materials and their device applications', Taylor & Francis, 1990.

[30] E. Kuphal, Applied Physics A Solids and Surfaces, Volume 52, 1991, pages 380-409.

[31] Kazuo Nakajima, Journal of Crystal Growth, Volume 98, 1989, pages 329-340.

[32] Images used under Wikipedia Commons free use license. http://en.wikipedia.org/ wiki/Image:Surface_tension.svg) and (http://en.wikipedia.org/wiki/ Image:Contact_angle.svg)

[33] Young, 'An Essay on the Cohesion of Fluid' Phil. Trans. R. Soc. Lond., 1805.

[34] R. Yakimova & M. Syvajarvi, 'Liquid Phase Epitaxy of Silicon Carbide, Liquid Phase Epitaxy of Electronic, Optical and Optoelectronic Materials', Editors: P. Capper and M. Mauk, page 216,

[35] D. M. Mattox, 'Handbook of physical vapor deposition (PVD) processing', William Andrew, 2007.

[36] Edwards Auto 306 Evaporator manufacturer homepage: http://www.edwardsvacuum.com

[37] L. O'Reilly, 'Growth and characterisation of wide-bandgap γ-CuCl on near lattice-matched Si', PhD thesis, 2006, Dublin City University.

Chapter 4 - Copper Halides

4.1 Introduction

The Copper Halides (CuHa) are I-VII materials, and consist of CuCl, CuBr, CuI and their alloys. As outlined in Chapter 1, the CuHa materials have been the focus of much research during the 1960s and 1970s for prototype applications arising from their optical non-linearity [1] as well as micro-crystal type growth [2]. CuHa materials have also driven more fundamental studies arising from their unique properties: exciton polariton dispersion in CuCl [3], and various studies on the electrical characteristics of CuHa at their high pressure phases [4, 5] among many others. The focus of this project is on a subset of the CuHa group, CuCl and CuBr, and their relevant structural, optical and electrical properties are presented herewith.

4.2 Structural Properties

Both CuCl and CuBr exhibit many similarities in structure and chemistry. Both of these halides are ionic compounds and crystallize naturally at room temperature in the zincblende structure, as illustrated in figure 4.1.

From figure 4.1, each group VII atom (Cl^-, Br^-) is surrounded by a regular tetrahedron constructed from four atoms of Cu^+, forming its next neighbours at a distance of $(a\sqrt{3}/4)$, where a is the lattice parameter. The next nearest Cu^+ neighbours are at a distance of $(a\sqrt{2}/2)$ and number twelve in all.

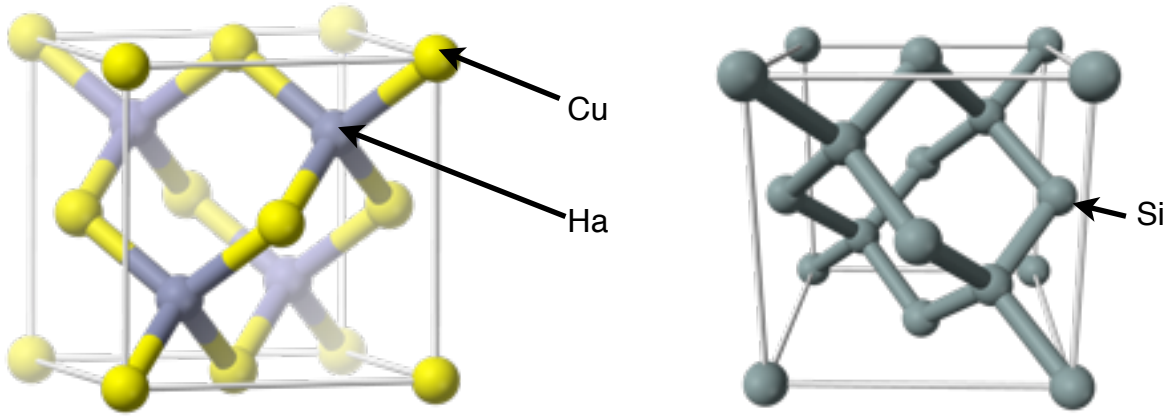

Figure 4.1 *- (a) Representative unit cell of cubic zincblende γ-CuCl and γ-CuBr, (b) Face centered cubic (FCC) crystal structure of Si.*

The notable feature of this configuration is the lack of an inversion or symmetry centre. The structure is also consistent with Cu(I) (or Cu^{+}) forming tetrahedral complexes, crystallizing into a zincblende configuration. The asymmetrical nature of CuCl/CuBr cells leads to the existence of the aforementioned Pockels electro-optic effect, whereby a proportional change in birefringence of incident light can be achieved by varying the electric field in an optical material, and was the catalyst for much of the early work on CuCl single crystal growth [6, 7, 8].

The Philips scale ionicity, f_i, is a measure of the ionic bonding and anti-bonding states separated by an energy gap. For CuCl and CuBr the ionicities are given as $f_i = 0.746$ and $f_i = 0.735$, respectively [9] - the decreasing series of the ionicity also correlates with the ionicity of the bonds in the CuHa family, i.e. CuCl → CuBr → CuI. This high ionicity is close to the critical value ($f_i = 0.785$) which is the boundary between zincblende and wurtzite type structures. From an epitaxial growth perspective on Si substrates, these ionicities represent an extreme of heteroepitaxial growth by having an extremely ionic epilayer on a highly covalent substrate. These properties are summarized in table 4.1.

Molecular Formula	CuCl	CuBr	Si
Molar Mass	98.999 g/mol	143.45 g/mol	28.05 g/mol
Density	4.145 g/cm^3	4.71 g/cm^3	2.329 g/cm^3
Melting Point	426 ˚C (703 K)	492 ˚C (765 K)	1414 ˚C (1687 K)
Boiling Point	1490 ˚C (1760 K)	1345 ˚C (1618 K)	2355 ˚C (2628 K)
Refractive Index (n_D)	1.930	2.09	-
Lattice Parameters	a = 5.41 (Zincblende)	a = 5.6773 (Zincblende)	5.430
Thermal Expansion Coefficient (Volumetric)	5.55 x 10^{-5} K^{-1} (@ T = 295 K)	4.83 x 10^{-5} K^{-1} (@T = 295 K)	2.92 x 10-6 K^{-1} (@T = 293 K)
Phillips Ionicity (f_i)	0.746	0.735	0

Table 4.1 *- Notable structural properties of the CuHa materials, CuCl and CuBr. Comparative Si properties also included [10]*

4.2.1 X-Ray Diffraction Characteristics

Using XRD, fundamental structural characteristics of CuCl and CuBr can be discerned from their Bragg reflections as detailed in Chapter 2. Deposition of CuCl and CuBr on various substrates and their resulting XRD measurement have been carried out, as experimentally detailed in Chapter 2. Comparison with known powder diffraction measurements provides an informative basis for further structural studies of these materials. These powder diffraction measurements are supplied within a software database supplied by the International Centre for Diffraction Data (ICDD) [11] and can be accessed using the "Diffrac$^+$ PDFMaint" program supplied by the manufacturer of the D8 XRD system, detailed in Chapter 2. The powder diffraction entries for both CuCl and CuBr are listed in table 4.2. Additionally, full powder diffraction entries for CuCl and CuBr can be found in Appendix A.

γ-CuBr	Index <h k l>	Intensity (%)	2-theta (deg)
	111	100	27.123
	220	60	45.021
	311	35	53.345

γ-CuCl	<h k l>	Intensity (%)	2-theta
	111	100	28.522
	220	55	47.437
	311	30	56.290

Table 4.2 *- Powder diffraction measurements for γ-CuBr and γ-CuCl [11]*

For a comparison with these known diffraction values, samples of γ-CuBr and γ-CuCl thin films on glass substrates were prepared using vacuum evaporation using commercially available powders from Sigma-Aldrich with 99.999% purity. For both experiments, a thin film of ~500 nm was deposited on de-greased and cleaned glass substrates. A standard evaporation rate of ~ 0.3 nm/sec was used. Deposition was carried out under vacuum conditions (10^{-6} mbar) at room temperature using a standard tungsten boat, resistively heated using a current between ~2-2.5 A. Sample thickness was measured using the correctly tooled thickness monitor. Greater detail of the cleaning and evaporation procedure can be found in Chapter 6. The diffraction measurement for both CuBr and CuCl on glass is presented in figure 4.2.

From these measurements, it can be seen that both CuBr and CuCl exhibit well defined Bragg peaks and share a strong preferential growth along the <111> crystallographic orientation, with secondary and tertiary reflections along the <220> and <311> orientations, respectively.

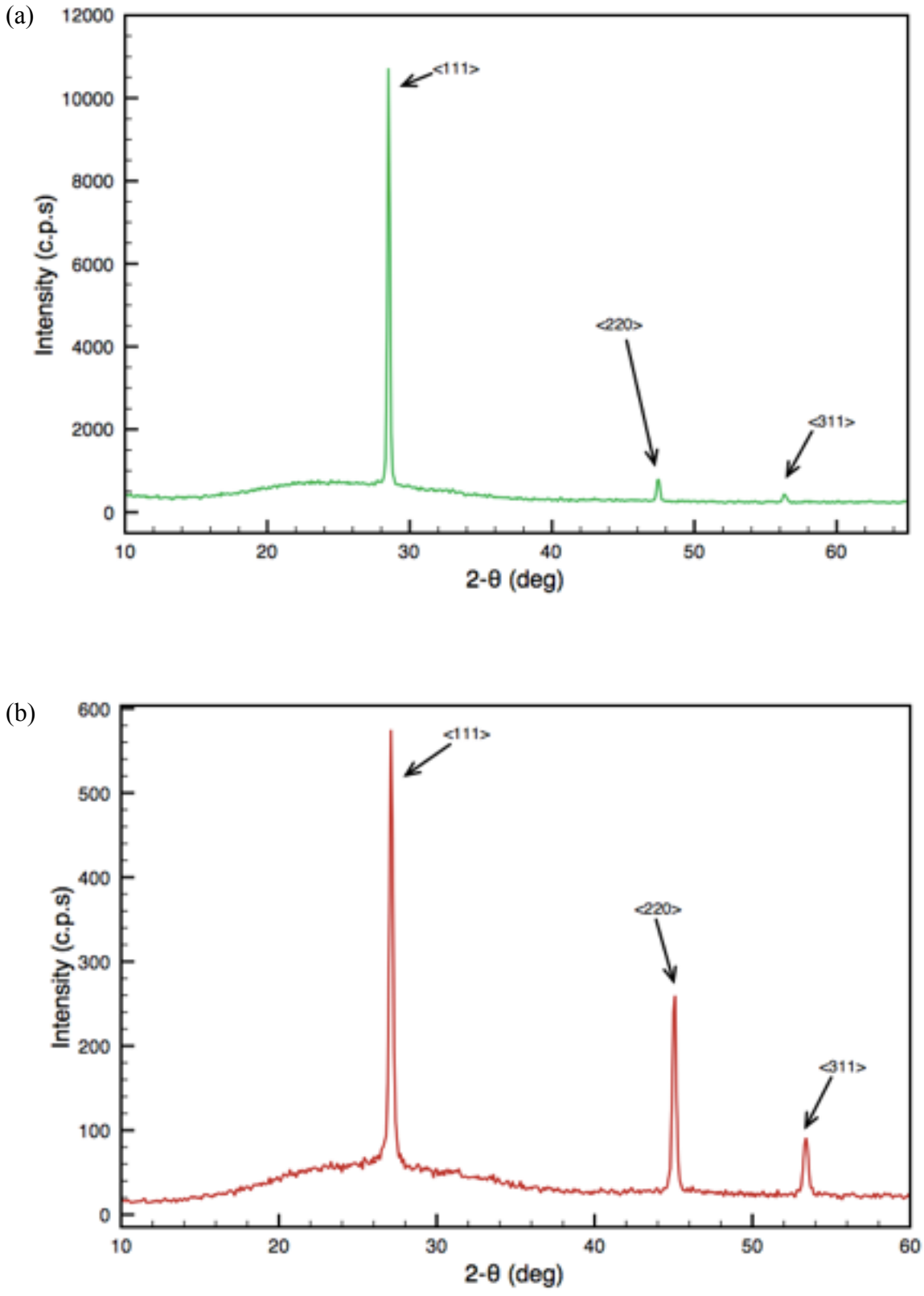

Figure 4.2 *- XRD θ -2θ scans for as deposited (a) γ-CuCl and (b) γ-CuBr on glass substrates, showing characteristic Bragg reflections*

The very weak and broad peak in the ~15° to ~35° range for both samples is attributable to the amorphous nature of the underlying glass substrate. Intensities for all three reflections are in good agreement for the reported values within the ICDD powder diffraction files. The <111> preferential growth is also in line with studies of vacuum deposited CuBr and CuCl on Al_2O_3 substrates [12].

4.2.2 Phase Changes for CuHa

At room temperature and normal pressure, CuHa crystallize naturally in the zincblende structure. When subjected to an increase in temperature, new phases are observed. For both CuCl and CuBr, at 657 K and 680 K respectively, they undergo a solid phase transition from their zincblende γ-phase to their wurtzite β-phase. There exist no further phase changes for CuCl under normal conditions, as the transition to its liquid state occurs with additional heating (i.e. above 696 K). Unique to CuBr and CuI however is a third high temperature super-ionic α-phase, reported as a disordered cubic phase [13]. Studies on high pressure phases of the CuHa up to 100 kbar have revealed additional phases, including the normally absent cubic α-phase for CuCl as well as tetragonal and rhombohedral structures [14]. However these phases cannot be stabilized at normal atmospheric conditions and have little direct applicability. A listing of phases relating to CuBr and CuCl is presented in table 4.3.

Cu(X)	γ-phase (zincblende)	β-phase (wurtzite)	α-phase (cubic)
-Cl	0-680 K	680-696 K	-
-Br	0-657 K	657-741 K	741-759 K

Table 4.3 *- Various phases for CuCl and CuBr under atmospheric conditions and their transformation temperatures.*

4.2.3 Stability

Due to the reactivity and photosensitive nature of CuHa materials, the issue of stability is of considerable import. CuHa reactivity with moisture suggests a hygroscopic behaviour; however this is not exactly the case [14]: ambient atmosphere (and the inherent moisture present therein) and lighting will degrade CuHa material and precipitate the formation of hydrated Cu^{++} oxyhalides. This gives the degradation a classical 'green' cupric compound colour and is itself a useful indicator for sample quality.

This reactivity for CuHa necessitates a means of preservation for epitaxially grown films. One method that has been shown as suitable for such preservation is via capping - by utilizing an encapsulation approach, films can be protected from decomposition in ambient atmosphere. Work by previous DCU colleagues has demonstrated the efficacy of capping layers for CuCl thin films [15]. Conventional encapsulation for CuCl using glass and subsequent curing cannot be utilized for γ-CuCl on Si substrates, owing to the solid-state reaction between CuCl and Si at temperatures in excess of 250 ˚C [16], thus alternate capping materials were investigated. Such capping layers had to be dielectric, non-reactive with CuCl, have a low curing or deposition temperature and be transparent to CuCl light emission. Cyclo olefin polymer (COC) and polysilsequioxane (PSSQ) polymers were identified as candidates, as well as PECVD deposited SiO_2. Of these three, COC and PSSQ layers successfully encapsulated CuCl epilayers for periods in excess of 28 days. PSSQ was demonstrated to slow the oxidation of CuCl, but did not stop oxidation.

4.3 Band Structure & Electronic Properties

The origin for the energy bands in materials is presented in a general fashion in Chapter 2. As for all materials, the electronic properties of the Copper halides are determined by the energy positions of the various electron orbitals. The valence band for Copper halides is dependent on both the noble

metal component (Cu) and the halide component (Cl, Br), in this case the filled d^{10} shell of the Cu^{+} ($[Ar].3d^{10}.4s^{1}$) and the rare gas configuration s^2p^6 halide ions ($[Ne].3s^2.3p^5$). As discussed previously, the Copper halides crystalize as zincblende structured semiconductors at room temperature. The usual bond in a zincblende structure is derived from an sp^3-sp^3 electronic configuration, but with the Copper halides the valence bands are derived from an sp^3-sd^3 configuration [17]. The metal Cu d orbitals and the Halide p orbitals are hybdrized ($s^2p^6d^{10}$ configuration), which is in contrast to the isoelectronic III-V materials (themselves typically s^2p^6 configuration). This hybridization changes the physical properties of the CuHa compared with other semiconductor materials and has made the CuHa a platform for studying hybridized p-d bonds [18]. The band structures for CuBr and CuCl are shown in figure 4.3, with the direct band-gap for both illustrated.

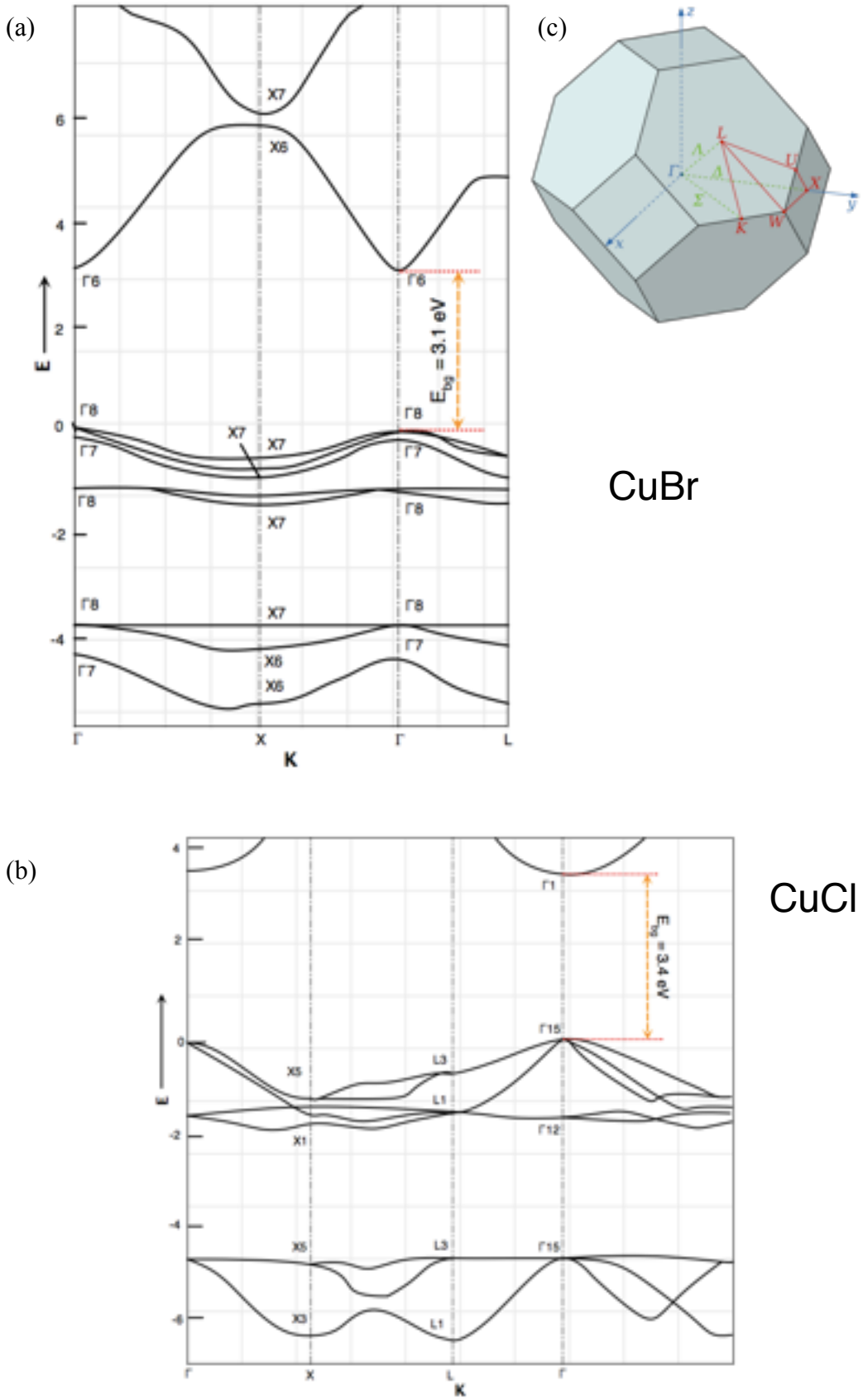

Figure 4.3 *- Energy band diagrams for (a) CuBr and (b) CuCl with k = 0(direct) band-gap marked. For reference, model of first Brillouin zone of FCC lattice with symmetry labels is shown in (c) [19].*

In the case of CuCl, there is a notable deviation from the regular zincblende spin orbit splitting that is observed for CuHa and AgHa materials. This anomalous spin orbit interaction results in the *p* and *d* orbital states at T_{15} splitting into separate levels at Γ_7 and Γ_8 (as shown schematically below in figure 4.4). The Γ_7 states are higher in energy than the Γ_8 states since *d* states contribute to the spin-orbit splitting with opposite sign as compared to *p* orbitals.

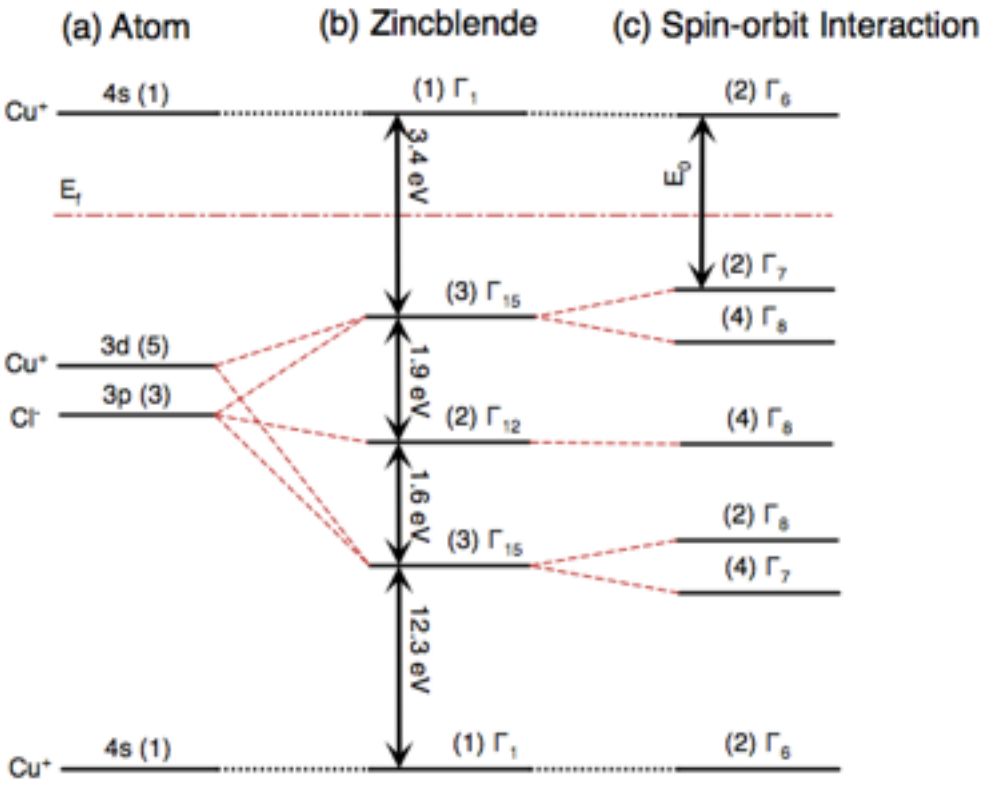

Figure 4.4 *- Representation of the conduction and valence states in CuCl due to s, p and d electrons at the symmetry point Γ in the cubic crystal field of the zincblende structure. Bracketed numbers indicate the degeneracy of the associated state. Reproduced from [20].*

All CuHa are mixed ionic and electronic conductors at low temperature. Below room temperature, the electronic conductivity is prevalent while at room temperature and higher the ionic conduction begins to dominate, becoming superionic conductors (1 Ω^{-1} cm^{-1}) at phase change temperatures [21]. This is understood to result from the insufficient thermal energy to promote ionic movement below a certain temperature, leaving the electronic mechanism as the dominant conduction path.

Fundamental studies of the electronic conductivity of CuHa were performed by Wagner and Wagner [22], in which the electron and hole conductivity for CuHa was calculated. These measurements were carried out using an DC polarization electrochemical technique whereby a cell consisting of Cu/CuX/Graphite (where X is Cl or Br) was created. Measurements were carried out under inert (Argon) gas flow and within a temperature range of 250 to 450 ˚C. Under an applied voltage, Cu^{+} ions are drawn from the graphite electrode towards the Cu electrode, while electrons move in the opposite direction. As the graphite does not contain Cu (i.e., a blocking electrode), a Cu^{+} deficit is created at this electrode. The current is then carried exclusively by excess electrons or electron/hole pairs. Measurement of the CuHa electronic conductivity thus requires the use of specific experimental approaches utilizing such blocking electrodes in order to sequester the ionic component from any measurement.

For evaporated CuCl thin films, work by Lucas [23] in which ~500 nm thick CuCl samples were used, gave an electronic conductivity of approximately 2.3 x 10^{-7} S/cm for films using irreversible electrodes (Au) and a conductivity of approximately 6.5 x 10^{-7} S/cm was calculated for reversible Cu electrodes at room temperature. This work also verified the distinct mixed electronic-ionic character of CuCl, where below ~270 K the electronic conduction mechanism was dominant, while the Cu+ ionic mechanism dominates at higher temperatures. CuCl thin films have also shown

improved conductivity by treatment with a low pressure plasma system using an Oxygen plasma to effectively dope the samples with Oxygen. Substantial improvements in the conductivity were observed from this method owing to the post-treatment inclusion of oxygen within the anionic sites of CuCl, creating an acceptor state for conduction.

Improvements in the conductivity of CuHa material have been reported via means of a number of dopants and techniques. The large number of eutectic forming materials found in the Alkali Halides (as outlined presently for CuCl in table 4.4) has led to investigations on their conductivity effects. Reported improvements in CuBr ionic conductivity from the use of the eutectic-forming Cs element with CuBr have been shown [24]. Additionally, work involving CuCl and co-evaporated KCl have shown that the electrical conductance is dependant on the amount of evaporated KCl - the conductance of CuCl/KCl thin films was observed to increase with respect to the KCl percentage used during deposition [25].

4.4 Optical Properties

Optical excitation results in the creation of electrons in the conduction band and holes in the valence band of a semiconductor. There exists a Coulombic attraction between the holes and electrons, which results in the formation of an electron-hole pair analogous to that of a hydrogen atom. This quasiparticle is known as an exciton and was theoretically discussed previously in Chapter 2.

Radiative emission from an exciton recombination has a much higher transition probability than emission from an electron-hole transition, in part due to the highly correlated movement of the electron and hole pair in their exciton form. Thus, materials with excitonic properties are important for efficient optical emission. Thermal energy at room temperature can be enough to break the bond

between the electron-hole pairs due to the fact that room temperature thermal energy is ~37 meV and most excitonic binding energies are of the order of 10 meV or below. However, the excitons in CuHa materials have a large binding energy (190 meV for CuCl, 108 meV for CuBr) and this allows for a high density exciton state to exist up to room temperature.

In CuHa, the exciton is of the Wannier-Mott type [26] and owing to the direct band-gap nature of CuHa the exciton arises at k = 0 transition. For CuCl, two excitons are observed in the near-ultraviolet region at 10K - a singlet and doublet, Z_3 and $Z_{1,2}$ respectively [27, 28], corresponding to the coupling of the conduction band state $\Gamma 6$ to the valence band holes Γ_7 and Γ_8. Additionally, further excitonic structures are frequently observed for CuCl, notably the intrinsic impurity bound exciton, I_1, and the free biexcitonic molecule, M. I_1 has been documented as a neutral acceptor and this is ascribed to a Cu^+ or Cl^- vacancy within the films [29] and is observed at λ = 389.8 nm (E = 3.18 eV). The biexciton M, which is comprised of two free excitons and is analogous to a hydrogen atom, has been observed in emission spectra at λ = 391.2 nm (E = 3.16 eV).

In CuBr (and CuI) the doublet exciton $Z_{1,2}$ band is positioned on the low energy side of the singlet Z_3, however for CuCl this positioning is inverted, with the $Z_{1,2}$ on the high energy side of Z_3 due to the negative contribution of copper in the spin-orbit splitting as mentioned previously [20]. The inversion was also confirmed by Cardona utilizing mixed grading of $Cu(Br_xCl_{1-x})$ solid solutions and measuring the absorption intensities for $Z_{1,2}$ and Z_3 at 8 K [28]. As the compositional gradient varied from Cl to Br, the exciton intensities were observed to match and then invert - at $Cu(Br_{0.23}Cl_{0.77})$, the $Z_{1,2}$ and Z_3 peak intensities are near equal and the spin-orbit splitting becomes zero.

Investigations determining the energy values for $Z_{1,2}$ and Z_3 excitons have been carried out [27] using emission, absorption and reflection spectroscopy for both CuCl and CuBr. From absorption

studies of CuHa single crystals, Goto *et al.* [30] evaluated the exciton energies for CuHa materials. For CuCl, $Z_{1,2}$ and Z_3 absorption was determined to be λ = 378.5 nm (E = 3.27 eV) and λ = 387.0 nm (E = 3.2 eV), respectively, while for CuBr, $Z_{1,2}$ and Z_3 was found to be λ = 417.6 nm (E = 2.96 eV) and λ = 397.9 (E = 3.11 eV). Emission studies on CuBr reveals two peaks at λ = 418.4 nm (E = 2.963 eV) and λ = 420.2 nm (E = 2.95 eV), which are attributed to the Z_f exciton emission and the I_1 impurity bound exciton emission respectively. The λ = 418.4 nm line is found at the same energy as the Z_1 absorption, separated from the $Z_{1,2}$ doublet. This emission is usually forbidden, and was assigned as the Z_f emission; however it is commonly observed within evaporated γ-CuBr spectroscopic studies and originates from the emission of the lowest energy triplet exciton.

4.5 Growth of CuHa Materials

The nature of the wurtzite to zincblende phase change makes direct growth of CuHa material from the melt difficult, although efforts were undertaken in this regard. CuCl was the target for much of these attempts, where the $\gamma \rightarrow \beta$ phase change was close enough to the melting point. Growth using the Czochralski [31] and Stockbarger [32] methods was attempted, but the resulting crystals were small (5 x 5 x 2 mm^3), highly strained and of no value for their targeted optoelectronic applications.

The addition of a small amount of a second compound to another compound in order to depress the melting point of the compound is a well known technique with numerous applications. The strain induced from the phase change in CuCl melt growth could potentially be avoided by the use of a flux compound to depress the melting point sufficiently. Growth using the Czochralski, Bridgman, Stockbarger methods and the top-seeded solution method [33] all resulted in the growth of relatively strain free single crystal CuCl using this flux approach. For Czochralski and Bridgman growths, the continuous change of the melt composition leads to a point where the growth interface

becomes saturated by the flux material and growth ceases, thus limiting the maximum attainable size of the CuCl crystal. Improvements using the travelling heater method, whereby the flux is added to the molten zone only, can alleviate this issue [34]. More recently, larger crystals have been grown from top seeded solution growths, where CuCl polycrystals were located at the bottom of the growth crucible, below the CuCl-KCl mixture, in order to maintain a higher concentration of CuCl in the solution during the growth.

The use of flux compounds also leads to their inclusion in the grown crystals. For CuCl growths using KCl, impurities of Potassium were found to range as high as 0.3% to 1% by weight within the flux grown crystals [34], with impurity inclusion being dependent on growth rate. Schwab *et al.*[34] also noted the potential for dopant inclusion into single crystal growth by the simple addition of dopant compounds into the molten melt. Table 4.4 presents the predominant fluxes used experimentally for CuCl. Experimental flux growth data for CuBr is not available, although CuBr readily fluxes with the Bromide variations of these compounds, e.g. KBr, $BaBr_2$, etc. Schwab carried out CuBr single crystal growths using a travelling heater setup with both KBr and $BaBr_2$, producing transparent crystals of ~3 cm^3 with no twinning. It was also noted that KBr appeared to be the better flux, though criteria for that assessment were not given.

Among the fluxes utilized, predominant attention was given to KCl. Perner has stated that KCl was the best flux material in order to grow single crystal CuCl, noting that for their travelling heater experiment sufficient KCl to depress the melting point to 390 C° gave the best optical and electrical properties [14]. KCl concentration also affected CuCl transparency, whereby a decrease in KCl concentration increased the transparency of the resulting ingot [34].

Flux Material	Technique	Reference
RbCl	Bridgman	[34]
NH_4Cl	Bridgman	[14]
KCl	Bridgman , Czochralski, THM	[34]
$SrCl_2$	Bridgman , Czochralski	[33]
$BaCl_2$	Bridgman , THM	[33]
$PbCl_2$	Bridgman , Czochralski,	[14]

Table 4.4 *- Fluxing materials for CuCl*

4.6 References

[1] A. Goldmann, Physica Status Solidi(b),Volume 81, 1977, pages 9-47.

[2] Y. Masumoto, T. Kawamura, and K. Era, Applied Physics Letters, Volume 62, 1993, page 225.

[3] D. Frohlich, E. Mohler, P. Wiesner, Phys. Rev. Lett. 26, 1971, page 554.

[4] A. Blacha, N. E. Christensen, M. Cardona, Physical Review B, Volume 33, 1986, page 2413.

[5] H. C. Hsueh and J. R. Maclean, Physical Review B, Volume 51, 1995, page 12216.

[6] M. Soga, R. Imaizumi, Y. Kondo, T. Okabe, J. Electrochem. Soc. Volume 114, 1967, pages 388-390

[7] Y. Kaifu, Y. Kawate, S. Nakanishi, I. Niwa, K. Nakazawa, M. Koba, Journal of the Physical Society of Japan, Volume 22, 1967, page 517.

[8] W.R.Wilcox, R.A.Corley, Materials Research Bulletin, Volume 2, 1967, pages 571-579.

[9] J.C.Phillips, Rev. Mod. Phys., Volume 42, 1970, page 317.

[10] O. Madelung, 'Semiconductors: Data Handbook', Springer, 2004.

[11] International Centre for Diffraction Data website: http://www.icdd.com/

[12] N. Nishida, K. Saiki, A. Koma, Surface Science,Volume 324, 1995, page 149.

[13] alpha phase

[14] C. Schwab & A. Goltzené, Progress in Crystal Growth Characterisation, Volume 5, 1982, page 233-276.

[15] F. O. Lucas, L. O'Reilly, G. Natarajan, P. J. McNally, S.Daniels, D.M. Taylor, S. William, D.C. Cameron, A.L. Bradley, A. Miltra, Journal of Crystal Growth, Volume 287, 2006, pages 112-117.

[16] L. O'Reilly, G. Natarajan, P.J. McNally, D. Cameron, O.F. Lucas, M. Martinez-Rosas, L. Bradley, A. Reader, J. Mater. Sci.: Mater. Electron., Volume 16, 2005, page 415.

[17] R. Matzdorf, J. Skonieczny, J. Westhof, H. Engelhard, A. Goldmann, Journal of Physics: Condensed Matter, Volume 5, 1993, pages 3827-3827.

[18] A. Göbel, Physical Review B, Volume 57, 1998, pages 15183–15190.

[19] O. Madelung, 'Semiconductors: Data Handbook', Springer, 2004.

[20] A. Göbel, Physical Review B, Volume 57, 1998, pages 15183–15190.

[21] W. Sekkal, H. Aourag, M. Certier, Journal of Physics and Chemistry of Solids, Volume 59, 1998, page 1293.

[22] J. B. Wagner and C. Wagner, Journal of Chemical Physics. Volume 26, 1957, page 1597.

[23] F. O. Lucas, 'Evaluation of the microstructural, electronic and optoelectronic properties of γ-CuCl thin films and their fabrication on Si substrates', PhD Thesis, Dublin City University.

[24] J. Bazan, R. Pettigrosso, N. Garcia, Solid State Ionics, 1996.

[25] F. O. Lucas, P. McNally, and A. Cowley, Physica Status Solidi(c), 2009.

[26] A.A. Cofolla, S.E. Schnatterly, C. Tarrio, Physical Review Letters, Volume 55, 1985, page 2818.

[27] M. Nakayama, H. Ichida, H. Nishimura, Journal of Physics: Condensed Matter, Volume 11, 1999, page 7653.

[28] M. Ueta, 'Excitonic Processes in Solids', Wiley, 1986.

[29] M. Certier, C. Wecker, S. Nikitine, Journal of Physics and Chemistry of Solids, Volume 30, 1969, page 2135.

[30] T. Goto, T. Takahashi, M. Ueta, Journal of the Physical Society of Japan, Volume 24, 1968, page 314.

[31] W.R. Wilcox, R.A. Corley, Materials Research Bulletin, Volume 2, 1967, Pages 571-579.

[32] D. S.Robertson, O. .Jones, British.Journal of.Applied Physics, Volume 17, 1966, pages 1043-1046.

[33] B. Perner, J. Cryst. Growth, 6, pp.86-90 (1969)

[34] J. Rivera, L.A. Murray, P.A. Hoss, Journal of Crystal Growth, Volume 1, 1967, pages 171-176.

Chapter 5 - Liquid Phase Epitaxy of γ-CuCl on Silicon

5.1 Introduction

Towards the objective of this study, as outlined in Chapter 1, LPE has been used in order to investigate the growth single crystal γ-CuCl on Si substrates. This chapter outlines the methodology for LPE growth of CuCl, detailing the parameter space utilized and the reasoning for the choices made during experimentation. The results of these experiments are outlined, detailing the structural and optical properties of the resulting deposited bulk textured polycrystalline γ-CuCl material. Finally, difficulties encountered while working towards the objective of single crystal CuCl growth are discussed as well as a number of differing experimental approaches undertaken to overcome these problems.

5.2 Methodology

In order to investigate the growth of single crystal γ-CuCl on Si, a large number of growths using the LPE system were undertaken. Fundamental to determining the parameter space within which to

LPE Geometry	Conventional Slide Boat, Modified Tipping Boat
Substrate	Si <111>, Si <100>
Substrate Thickness	545 μm +-45μm
Liquidus Temperature Range	150 - 250 °C
Saturation Method	Ramp Cooled
Growth Temperature Range	210 - 260 °C
Growth Time	20 - 60 mins
Ambient Gas	Ar, N, H_2

Table 5.1 *- Nominal experimental range for growth of CuCl on Si via LPE*

operate is an understanding of the CuCl material as well as the flux selected for the project, KCl.

5.2.1 The CuCl/KCl Eutectic System

The use of a flux material to depress the melting point of CuCl was discussed in Chapter 4. The impetus for the γ → β phase change can be described by a model proposed by Rice *et al.* [1] whereby the phase transition takes place with rising temperature when a critical concentration of defects in the crystal is reached which the crystal can no longer accommodate. An appropriate flux can lower the transition temperature since it supplies the system with additional defects, depressing the phase change temperature. For the desired single crystal LPE growth, avoiding the γ → β phase necessitates the use of a flux. In addition, the LPE method requires the precipitation of the desired epilayer material from the liquid phase.

Fundamentally, all of these growth runs were informed by the CuCl/KCl phase diagram, from which the constituent molar weights of the melt components were derived. The phase diagram also provided the temperature where the substrate would be exposed to the melt via the sliding boat mechanism, and later, the modified tipping system. This temperature is given by the intersection of the molar composition of the melt with the liquidus curve.

Highlighted previously in figure 3.3 is the concurrent CuCl and liquid phase. It is clear that only melts with a CuCl molar percentage of ~66% or greater would precipitate out CuCl in the solid phase at a temperature of approximately 150 °C. Below this CuCl precipitation phase, solidification of the liquid occurs, and the melt enters the final sub-solidus K_2CuCl_3 and CuCl mixed phase. The highlighted area forms the area of investigation for the LPE experiments, as the temperature range

and molar percentage given is the known boundary for the precipitation of CuCl from the liquid CuCl/KCl melt.

Early experiments were also informed by the known CuCl/Si reaction at ~250 °C, which will be discussed in further detail later in this chapter. It was initially decided to avoid this reaction, since it had been previously reported to be deleterious to achieving epitaxial growth [2]. In addition, there exists some evidence that decomposition of CuCl can occur at elevated temperatures irrespective of the substrate [3] - metallic elemental Cu peaks were detected via XRD studies in CuCl-doped nanocrystal glass which were annealed at ~250 °C.

From the phase diagram above, mixtures comprised of $CuCl_{(66)}KCl_{(44)}$ to $CuCl_{(77)}KCl_{(33)}$ melts would initially seem to provide an optimal range for growth experiments and avoid the CuCl/Si reaction. In working towards experimental completeness for this work, however, many attempts were made at growth outside of the highlighted range, in order to gain a better understanding of the melt behaviour and LPE procedure as it relates to the CuCl-KCl system.

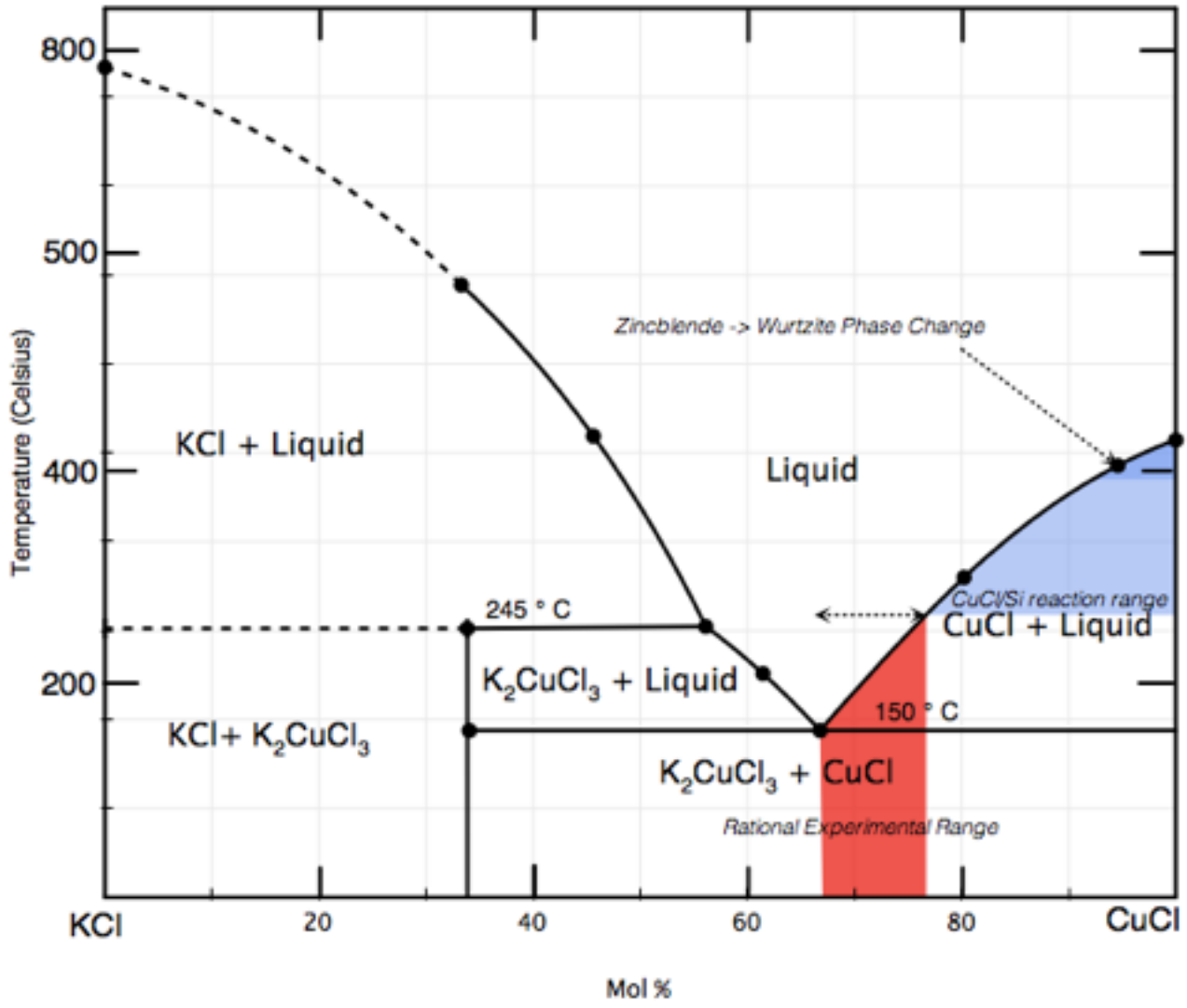

Figure 5.1 *- The CuCl/KCl phase diagram, red highlighted section shows the logical experimental range for attempted y-CuCl on Si growth. Blue highlighted section indicates the temperature range where the CuCl/Si reaction is known to occur.*

5.3 Experimental setup for LPE

The experimental setup for the LPE system, detailing its construction and commissioning, was detailed in Chapter 3. Prior to a LPE growth run, a number of preparatory steps were carried out. Additionally, prolonged usage of the system necessitates a cleaning protocol, which is detailed in this section.

5.3.1 Materials & LPE System Preparation

The quartz tube of the LPE system is frequently cleaned in order to minimize contaminants entering the system and after any period of time where the tube has been exposed to ambient atmosphere for prolonged periods. Aqua Regia (3:1 HCl/HNO_3) is used for this inorganic clean. A stopper is used to seal one end of the tube and the acid is poured in and left to sit for 4 hours. Subsequently, the tube is washed down with de-ionised (DI) water and the exterior of the tube cleaned. No organic solvents should be used in cleaning the tube so as to avoid contaminants with organics and the DI water was from a Millipore Q DI system [4].

The use of graphite for the sliding boat and tipping systems necessitates precursor cleaning and preparation steps for their proper use due to their porous nature. In order to remove the melt from a used boat, they were bathed in DI water and gently hosed with DI water to remove the immediately soluble components. A small amount of HCl was then added and the graphite subjected to ultrasonic cleaning. Once the melt has been removed or dissolved, the graphite was cleaned again in DI water. Recovered graphite pieces are kept wrapped within cleanroom grade lint-free cloth and stored in individual sealable containers between active use.

Prior to use of a graphite boat for LPE, it must be purged of contaminants using a high temperature bake-out regime. The boat is loaded into the LPE system and the furnace is ramped up to 900 °C for 6-7 hours under vacuum (10^{-6} mbar). A useful visual indicator is the fact that the graphite will turn bright orange during this regime. After this bake out, the boat is ready for use, however it should not be exposed to the atmosphere to avoid oxygen and water vapor contamination. Ideally, this bake out is carried out the day prior to the growth run, so that the boat can be stored under high vacuum

within the LPE system itself. When loading the tube, a steady flow of Argon is run in order to limit contamination of the ambient atmosphere upstream while the tube is open.

Whenever possible, the highest grade materials were used. Commercially available CuCl beads of 99.999% quality (Sigma-Aldrich) were used. These beads are stored under vacuum between uses. Similarly, commercially available 99.999% KCl (Sigma-Aldrich) was used for the flux. As a salt, KCl is hygroscopic and must be baked out separately before use. The KCl was heated at 200 °C for 8 hours in order to sufficiently dehydrate it prior to use in the melt.

5.3.2 Substrate Cleaning & Preparation

Substrate cleanliness and surface homogeneity is an important consideration for LPE growth. Ideally, a flat, uniform, hydrogen terminated Si surface is ideal for growth. Such a surface has had its native SiO_2 removed via etching resulting in a Silicon surface such that the Si atoms are covalently bonded to hydrogen.

Figure 5.2 *- PFTE Beakers used for holding cleaning liquids and etchants, arranged as an 'assembly line' leading from one step to the next.*

An 'assembly line' of cleaned Teflon beakers (see figure 5.2) is used to hold the cleaning liquids and the substrates so as to avoid contamination from contact with gloves, tweezers, etc. Post-etch,

the substrate is dried off using an inert Nitrogen gas flow and immediately placed in the graphite boat within the LPE system. The time from the dry off to placement within the LPE system is kept as short as possible. With experience, the substrate can be loaded from the final beaker to the LPE system in a few seconds. Initially, all substrates are organically cleaned using a strong detergent, Decon 90. Substrates were placed in a beaker with the detergent solution and ultrasonically cleaned for 10 minutes. The most commonly used routine for LPE is outlined below:

1. Rinse in Acetone
2. Ultrasonic in Acetone for 3 minutes
3. Rinse in DI water
4. Rinse with IPA (Isopropanol Alcohol)
5. Rinse in DI water.

Acetone is commonly used to remove organic impurities from substrates and can handle greasy and oily contaminants. It has a high evaporation rate which necessitates a subsequent cleaning step, in this case IPA, otherwise striations on the substrate can occur. As well as rinsing the acetone away, the IPA is also a means for removing additional particles from the substrate surface.

Following the organic cleaning routine, an inorganic preparation and etch procedure was carried out as follows:

1. HNO_3 (70%) + H_2SO_4 (96%) (1:3) for 3 minutes
2. Rinse in DI water
3. HF (10%) Dip for 1 minute
4. Rinse in DI water

5. H_2O_2 (30%) + H_2SO_4 (96%) (1:1) for 3 minutes
6. Rinse in DI water
7. HF (10%) Dip for 1 minute
8. Rinse in DI water (this stage can be ignored for situations where the HF etch is used to hydrogen-terminate the surface)
9. Dry sample with inert gas

The etching step is used to remove the native SiO_2 oxide present on Si wafers, but also weighs heavily in contributing to successful growth. Creating a clean, featureless epi-ready surface for LPE is a non-trivial endeavor, and it was only with specific expertise of the University of Freiburg that this was achieved. Even nominally 'epi-ready' wafers were prepared using the above protocol.

Step 1 is a selective isotropic etch of the SiO_2 native layer on the substrate which is commonly used in semiconductor fabrication. Step 5 is colloquially known as a 'piranha' etch, cleaning the substrate of any residual organic residues. It also serves to hydroxolate the surface and improves the hydrophilicity of the substrate. Of critical importance is the rinse step after each stage. Substrates are rinsed by first cleaning them with DI water from a wash bottle. They are then dipped into a beaker of DI water and stirred, before being removed and rinsed with the wash bottle again. This ensures that any residual solution from the previous step does not transfer into the next PTFE beaker. Improper cleaning from stage to stage can lead to residual solutions reacting with the next stage solution, most notably this can be observed in the reaction with the piranha solution where bubbles begin to form on the substrate and can cause the substrate to float free from its PTFE holder.

In order to qualitatively assess the cleaning procedure, a Si substrate was prepared using the outlined procedure and the surface morphology examined using Nomarski Interference Contrast (NIC) microscopy and CCD images of the surfaces were acquired. An un-cleaned Si substrate is shown in figure 5.3 below, in which dust particulates and a notable scratch on the substrate can be seen.

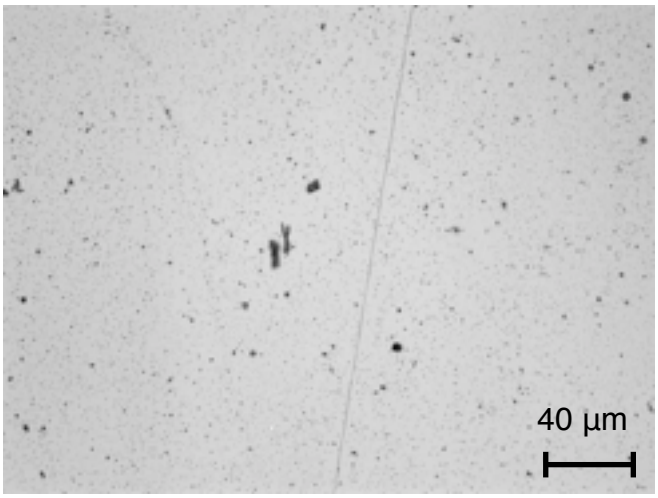

Figure 5.3 *- Nomarski Interference Contrast (NIC) microscope CCD image of un-treated Si surface prior to organic and inorganic cleaning. Foreign surface contaminates (and a notable scratch) dominate.*

Figure 5.4 shows another Si substrate that has undergone a similar etch procedure but without the piranha solution step and during which proper clean off using DI water was not carried out. Features such as striations from poor acetone removal, etch pits and hillocks dominate.

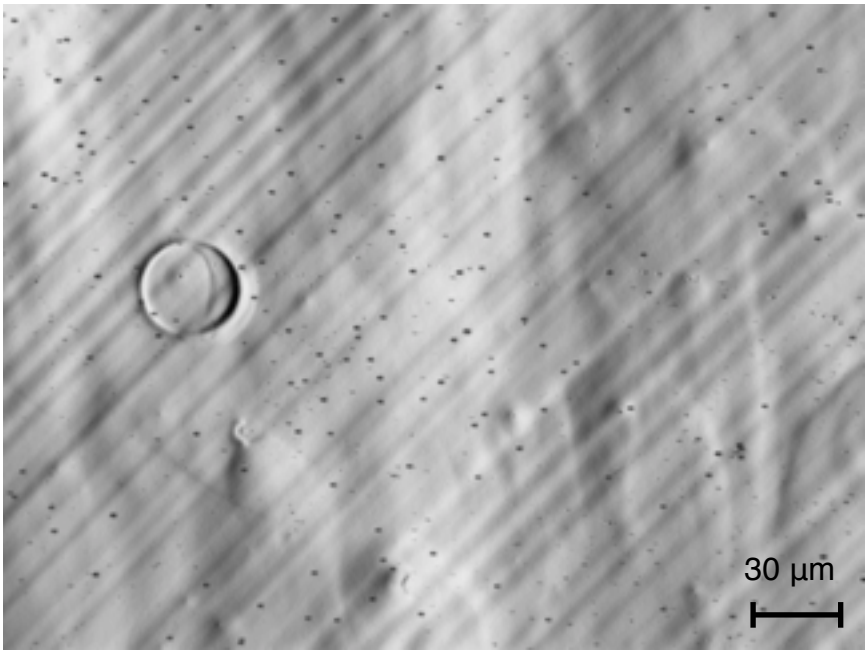

Figure 5.4 *- NIC microscope CCD image of imperfectly cleaned Si surface, hillocks, striations and etch pits can be clearly seen.*

In comparison, figure 5.5 (a) shows a Si substrate that is ready for LPE using the procedure outlined. The surface is homogenous and clean of any imperfections from particulates and etch artifacts such as pits and hillocks. Again to show the importance of proper rinsing, figure 5.4 (b) is an image of a Si substrate that did not have proper cleaning from step 4 to step 5, leaving residue from the previous steps. This caused the formation of distinct etch pits in the substrate. Judicious cleaning and rinsing, as outlined, results in a Si substrate that is ready for a growth run.

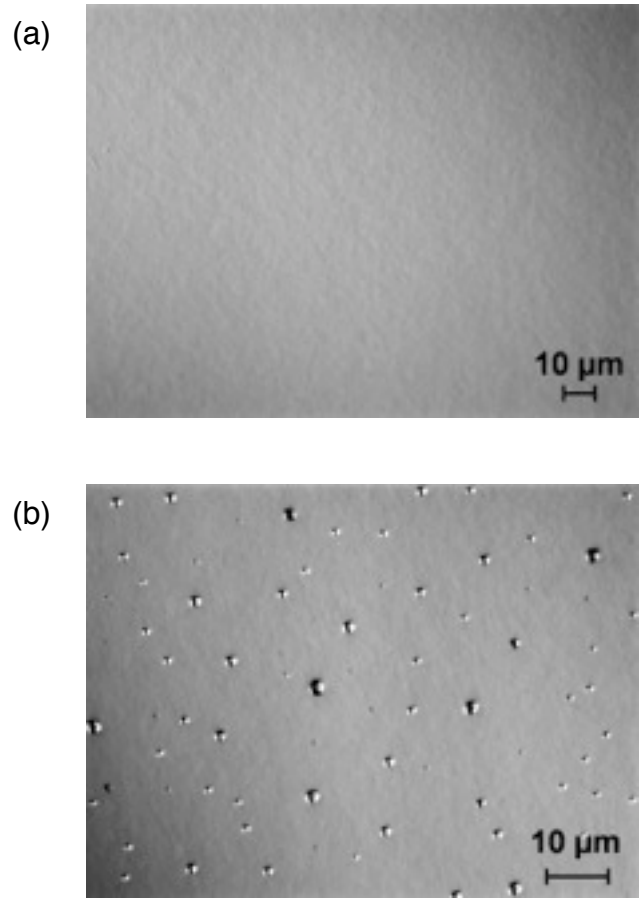

Figure 5.5 *- (a) LPE ready Si substrate, showing a clean homogenous surface, (b) etch pits on Si substrate formed by inadequate cleaning of etch chemicals from step to step.*

5.4 LPE growth using CuCl/KCl Eutectic Melts

A typical LPE experiment is detailed using the CuCl-KCl eutectic system. For the melt composition, a mixture of CuCl-KCl was prepared in 23:77 ratio, by molar weight. From the CuCl-KCl phase diagram, this percentage produces a liquidus temperature of approximately 250 °C. Once the melt constituents and substrate were prepared as detailed previously, the furnace was brought online and a predetermined heating program was executed.

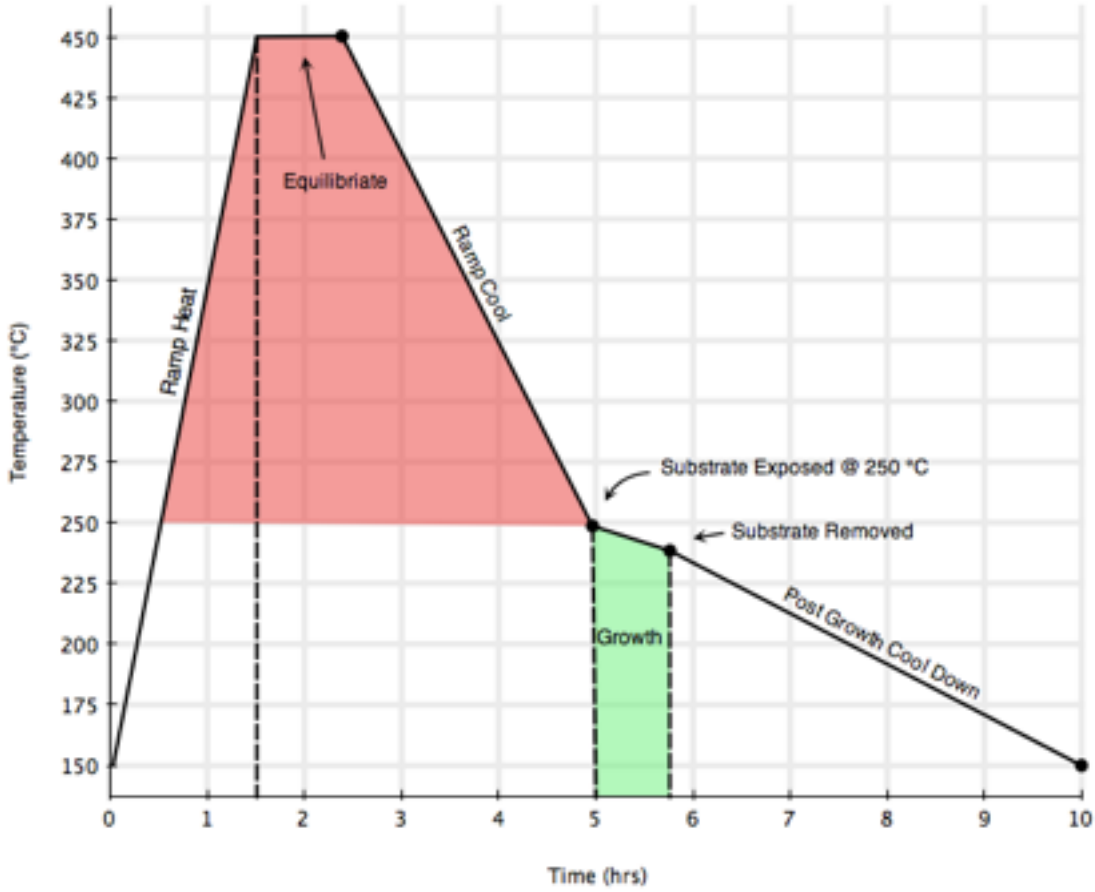

Figure 5.6 *- Annotated temperature program used by the LPE furnace.*

Figure 5.6 illustrates a typical heating regime used for a growth run using a $CuCl_{(77)}KCl_{(23)}$ mixture, which would give a liquidus point of ~250 °C. There are two distinct sections, highlighted in the above illustration, during the LPE growth. The first stage, highlighted in red, is the pre-heat and preparation of the supersaturated melt and is independent of the growth phase. It is used to prepare the melt for the growth. The second phase, highlighted in green, is the growth phase where the melt is exposed to the substrate in order to start epitaxial growth, and ends at the lower temperature value of the range when the melt is then rolled off the substrate via tipping or pushed off with the slide boat setup. After 45 minutes (~ 0.5 °C per minute), the melt would be moved off the substrate and the system left to cool down. During all stages, a steady flow of high purity Ar is maintained and measured using an oil bubbler leading from the exhaust of the LPE system.

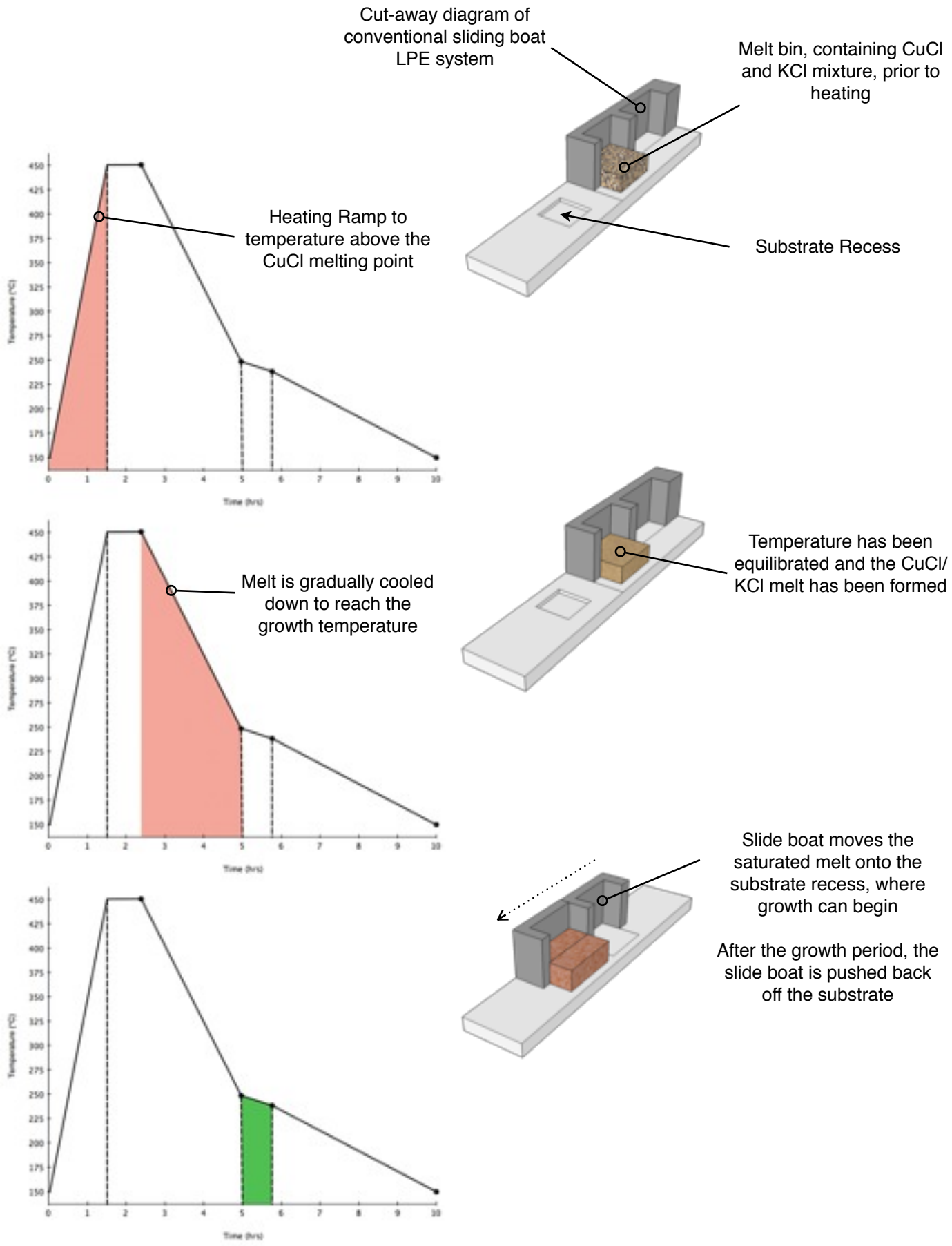

Figure 5.7 *- Illustration of LPE sliding boat positions during a growth experiment.*

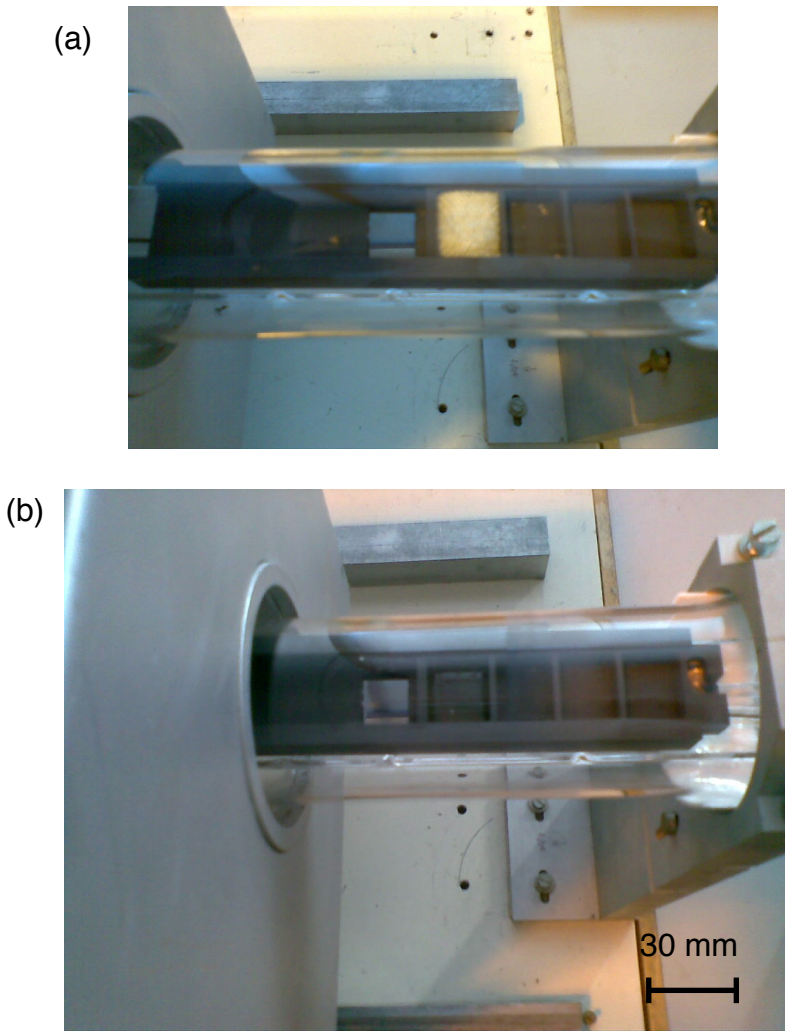

Figure 5.8 *- In-situ photograph of the melt with the furnace rolled back; (a) prior to heating, (b) at ~450 oC - the constituent KCl and CuCl can be observed to have completely dissolved and the melt is transparent.*

Figure 5.8 shows images taken of the LPE run at the beginning and then again at the equilibration stage. It is difficult to see directly from the image, but the melt becomes transparent albeit with a brownish tinge at 450 °C. It is observed that this coloration changes to a green tinge below ~400 °C. This coloration change is likely resulting from the wurtzite → zincblende phase change.

During early LPE experiments, as the temperature approached the liquidus value for the eutectic mixture, the off-white coloured CuCl/KCl powder would begin to melt, with the melt having a notable black colour. This is contrary to previous research carried out by D.E. Etter *et al.* [5] in which the mixture is described as turning clear. It was later determined that this is due to insufficient preparation of the KCl salt. The hygroscopic KCl would trap moisture and cause the probable formation of CuO within the melt. It should be noted though that while this CuO formation causes a substantial change in the coloration of the melt, during cooling the resulting grown layers (and the remaining melt in the sliding boat melt bin) would revert to a clear white colour. Etter noted that the addition of small amounts of elemental Cu would also return the melt to its transparent state. Further LPE experiments were undertaken with baked KCl and the melt behavior was subsequently consistently transparent.

5.5 Structural Properties of LPE Deposited Samples

Initial samples grown by the LPE methodology outlined have yielded intermixed CuCl/K_2CuCl_3 films on Si substrates, with thicknesses typically in the range of 5 – 13 μm. The crystalline quality of the films was examined using XRD in the parallel beam (θ - 2θ) configuration. Figure 5.8 below is indicative of the typical scan carried out and shows a large number of diffraction peaks. It is clear that the samples produced are not of the single crystal material desired, but rather of a textured polycrystalline nature composed of KCl and CuCl formed compounds.

Analysis of all LPE samples reveals commonly occurring compounds and their respective peaks, however run to run reproducibility of samples and thus reproducible θ-2θ scans was unachievable. Figure 5.9 is an indicative scan for the growth runs, as it details the host of peaks consistently observed. Indicated are the characteristic γ-CuCl <111>, <220> and <311> peaks, respectively found at 2θ ≈

28.51°, 47.43° and 56.25°, which are in excellent agreement with the previously reported values for CuCl (detailed in table 4.2 previously).

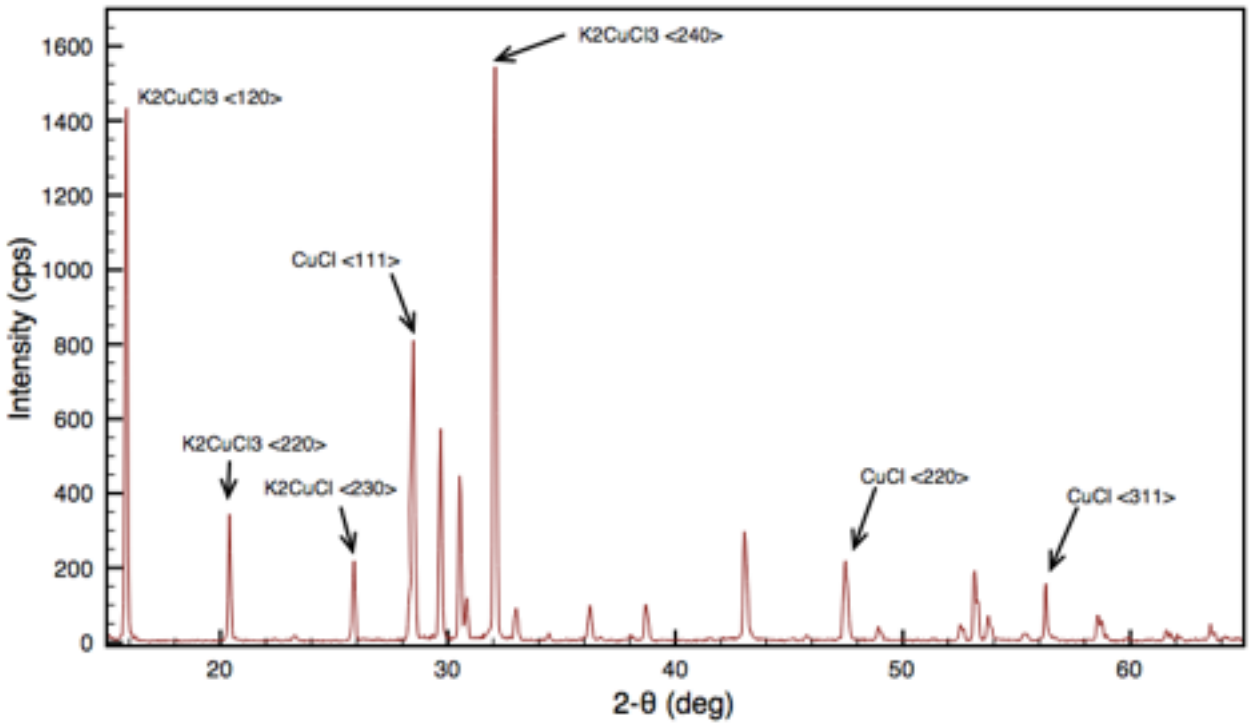

Figure 5.9 *- XRD θ-2θ scan of a typical LPE growth run using a $CuCl_{77}KCl_{23}$*

Additionally, a multitude of peaks can be attributed to the diffraction values given for the isomorphic orthorhombic compound K_2CuCl_3. The formation of this compound is a result of the solution growth inherent to LPE and its origins can be seen from the previously detailed CuCl/KCl phase diagram, as illustrated in figure 3.3. From the phase diagram, once a CuCl-KCl melt of CuCl molar composition greater then ~ 35% drops below the phase temperature line at ~180 °C, the remaining melt will solidify into K_2CuCl_3 and CuCl. Owing to the orthorhombic crystal structure of K_2CuCl_3, a substantially large number of reflections are observed (see appendix 1 for a full listing of K_2CuCl_3 and K_2CuBr_3 diffraction data). For θ-2θ scans from sample to sample, the intensity of the K_2CuCl_3 reflections is observed to change. This can be understood in terms of the essentially random spatial distribution of K_2CuCl_3 crystallites within the bulk deposition, although it is

interesting to note that the observed γ-CuCl reflections follow broadly expected intensity variations, i.e. the γ-CuCl <111> is always observed to be the most intense for CuCl, followed by the <220> and <311> reflection.

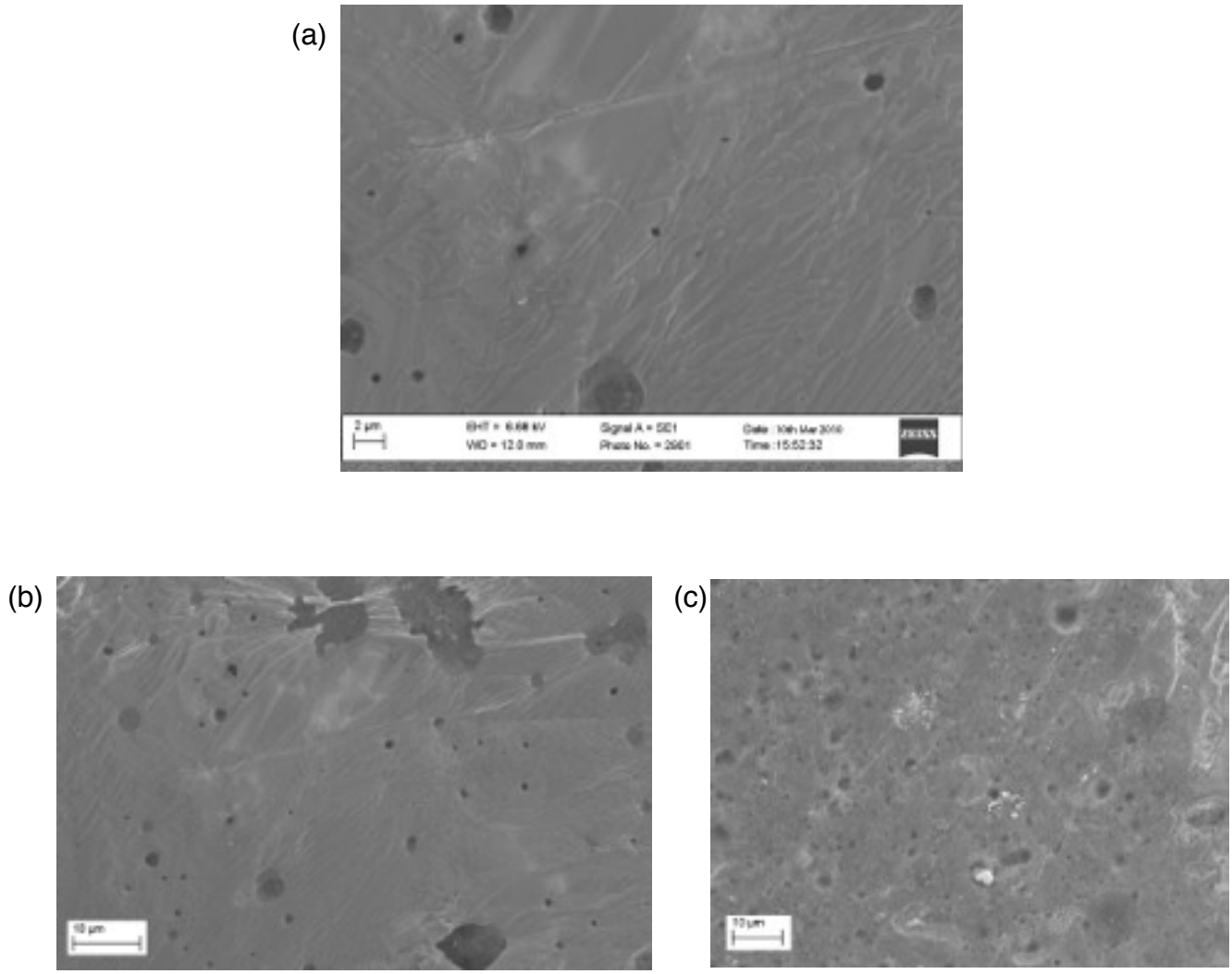

Figure 5.10 *- SEM images of the surface morphology of a LPE grown sample using (a) $CuCl_{(73)}KCl_{(27)}$ melt, (b) $CuCl_{(75)}KCl_{(25)}$ melt and (c) $CuCl_{(77)}KCl_{(23)}$ melt.*

Surface morphology from sample to sample also varies and is further complicated by the poor surface morphology inherent to LPE growth. A number of SEM images of various surface spots across a number of samples is presented in figure 5.10. Numerous pits can be seen randomly distributed across the surface of the examined samples. In some samples, the topography is defined

by rivulets of residual melt, although this was not always consistently observed from run to run on identical melt compositions (as can be observed from Fig 5.10 (c)). It is likely that the random fractional crystallization that occurs during the solution cool down of the melt on the substrate surface is responsible for the differing topographies. It should also be noted that while <111> Si was used as a substrate, some experiments were carried out with <100> orientated Si. There was no difference in how these growth runs were carried out, nor any recognizable variation between using <100> in lieu of <111> substrates.

5.5.1 CuCl-Si Interface Reactions

It is well documented that there exists a solid-state reaction between CuCl and Si at elevated temperatures [2, 6]. Within the group at DCU, prior work by O'Reilly [7], in which thin films of PVD deposited CuCl on Si were annealed at various temperatures in order to trigger this reaction, showed that the resultant product of these reactions can be detected by XRD. It was found that at ~250 °C, the CuCl/Si interface would become chemically unstable and the formation of copper silicides and chlorosilane complexes would occur. These reactions take the form of successive reductions of CuCl by Si, and is summarized in equations (1) and (2), given below:

$$n\mathrm{Si} + 4\mathrm{CuCl} \rightarrow (n - 1)\mathrm{Si} + 4\mathrm{Cu} + \mathrm{SiCl_4}\ (\mathrm{gas}) \qquad (5.1)$$

$$3\mathrm{Cu} + \mathrm{Si} \rightarrow \mathrm{Cu_3Si} \qquad (5.2)$$

The full reaction pathway for Cu3Si is described by Webber *et al.* [6] and given below in equations (3), (4) and (5):

$$7\mathrm{Si} + 12\mathrm{CuCl} \rightarrow 3\mathrm{SiCl_4} + 4\mathrm{Cu_3Si} \qquad (5.3)$$

$$9\mathrm{Cu_3Si} + 8\mathrm{CuCl} \rightarrow 7\mathrm{Cu5Si} + \mathrm{SiCl_4}\ (\mathrm{gas}) \qquad (5.4)$$

$$\mathrm{Cu_5Si} + 4\mathrm{CuCl} \rightarrow 9\mathrm{Cu} + \mathrm{SiCl_4}\ (\mathrm{gas}) \qquad (5.5)$$

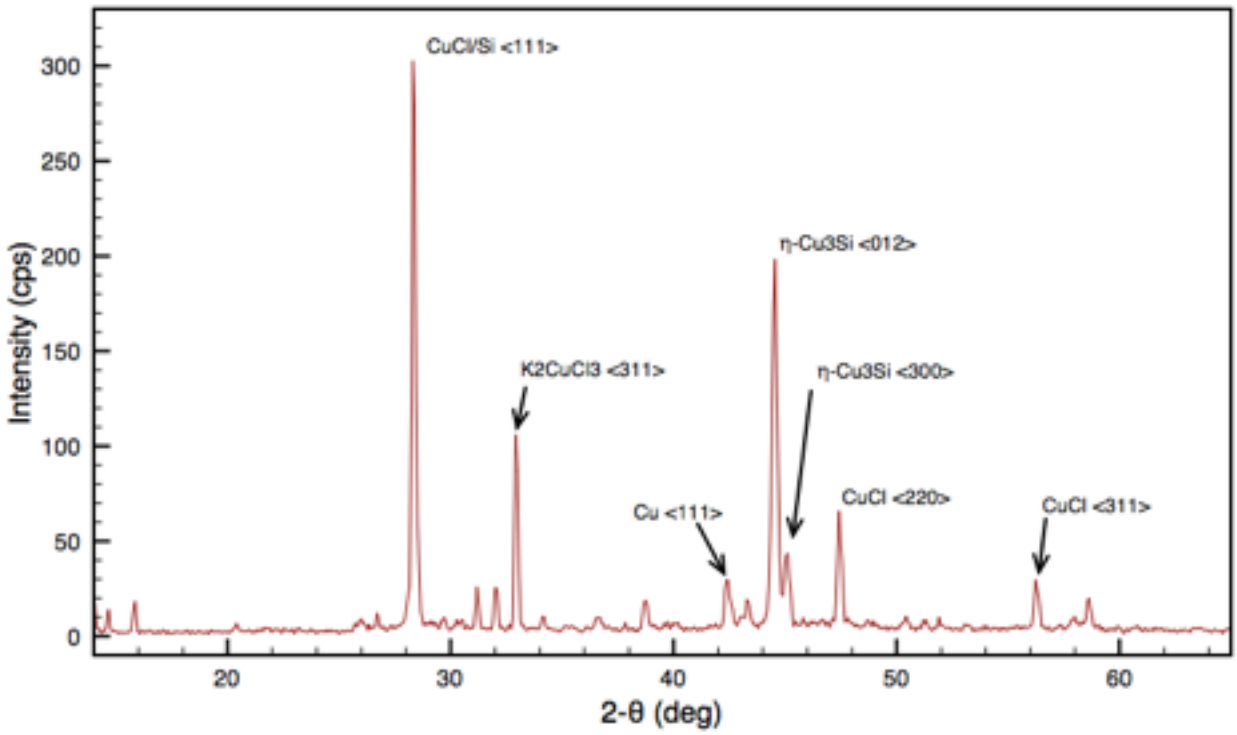

Figure 5.11 *- XRD θ-2θ scan of a typical LPE growth run using a $CuCl_{77}KCl_{23}$ mixture in which the melt was exposed to the substrate at 280 °C.*

Figure 5.11 shows an XRD θ-2θ scan of a LPE growth run experiment, with a melt comprising of $CuCl_{77}KCl_{23}$ in which the melt was exposed to the substrate at 280 °C. This would be above the ideal temperature at which this melt composition should be exposed to the Si substrate, but the experiment was intentionally carried out this way in order to investigate the effect of the CuCl-KCl melt on the substrate. In the scan, many features indicative of the CuCl-KCl melt are present, namely the characteristic CuCl <111>, <220> and <311> peaks. Many of the smaller peaks attributable to the orthorhombic K_2CuCl_3 are also present. The most notable new feature is the presence of new peaks at $2\theta \approx 44.35°$ and 44.5° which can be explained by comparing the diffraction pattern for the Cu_3Si copper silicide compound from equation 2. In addition, the peak at $2\theta \approx 43°$ can be attributed to the <111> Cu peak position. From the reaction pathway in (4) $SiCl_4$ is

also expected, however since the $SiCl_4$ generated in the reaction pathway is gaseous, its presence is non-existent in the scan. The formation of Cu and the Cu_3Si compound is in good agreement with the previous work on the CuCl/Si reaction.

Using our tipping boat LPE geometry, an experiment was devised in order to investigate the Si surface after exposure to the CuCl/KCl melt but without attempting growth. A melt mixture of $CuCl_{75}KCl_{25}$ was prepared and heated following the standard heating regime outlined in section 5.4, but the substrate was exposed to the melt at ~300 °C. The temperature was held at this point for 30 minutes before the melt was rolled off. The surface was then examined using SEM, EDX and XRD. Figure 5.12 below shows an SEM image of the damaged surface.

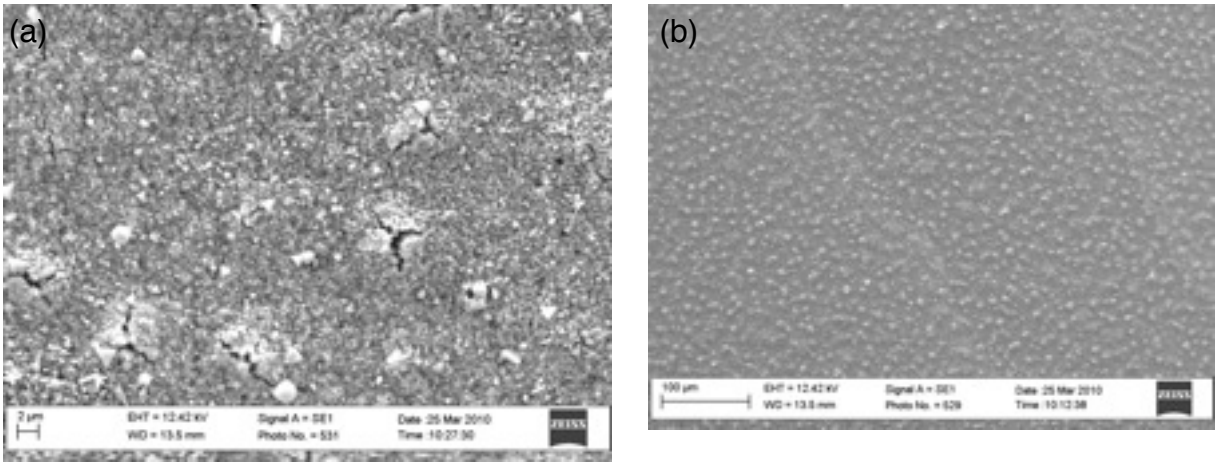

Figure 5.12 *- (a) SEM image of CuCl reacted Si substrate, post melt roll off, (b) zoomed out SEM image of same area*

From the image, the homogeneously flat Si substrate surface has been substantially transformed by contact with the melt. This has resulted in the formation of a coarse surface morphology with notable cracked protrusions and a number of small triangular crystallites (probably residual CuCl) can be seen distributed randomly across the surface. It is clear that the CuCl/Si reaction arising from

the presence of the melt has damaged the Si-melt interface substantially. EDX confirmed the presence of constituent compounds (Cu, Cl, K, Si), which agrees well with the surface comprising of Cu_3Si and probable trace CuCl and K_2CuCl_3 compounds.

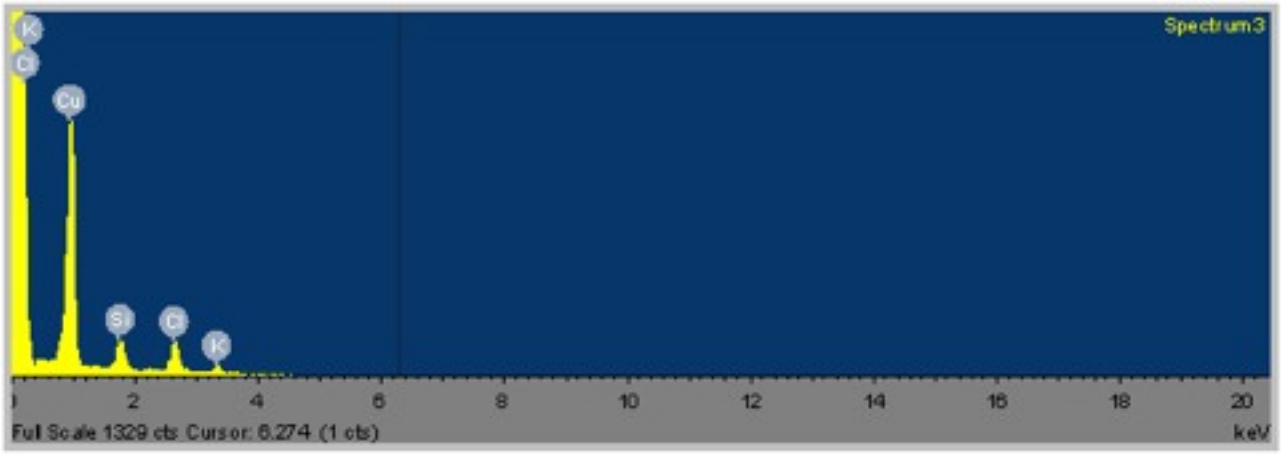

Figure 5.13 *- Acquired EDX spectra for damaged Si substrate*

Figure 5.14 shows the XRD scan for the sample. From the scan, it is clear that the Cu_3Si reaction dominates, with only trace CuCl quantities being detected. Elemental copper is again observed and the smaller peaks can be readily attributed to K_2CuCl_3. The doublet peak attached to CuCl at 2θ ~29.1° is unknown and does not correspond to any of the expected compounds present or arising from the melt and the CuCl/Si reaction. The cause of this small peak is currently unknown.

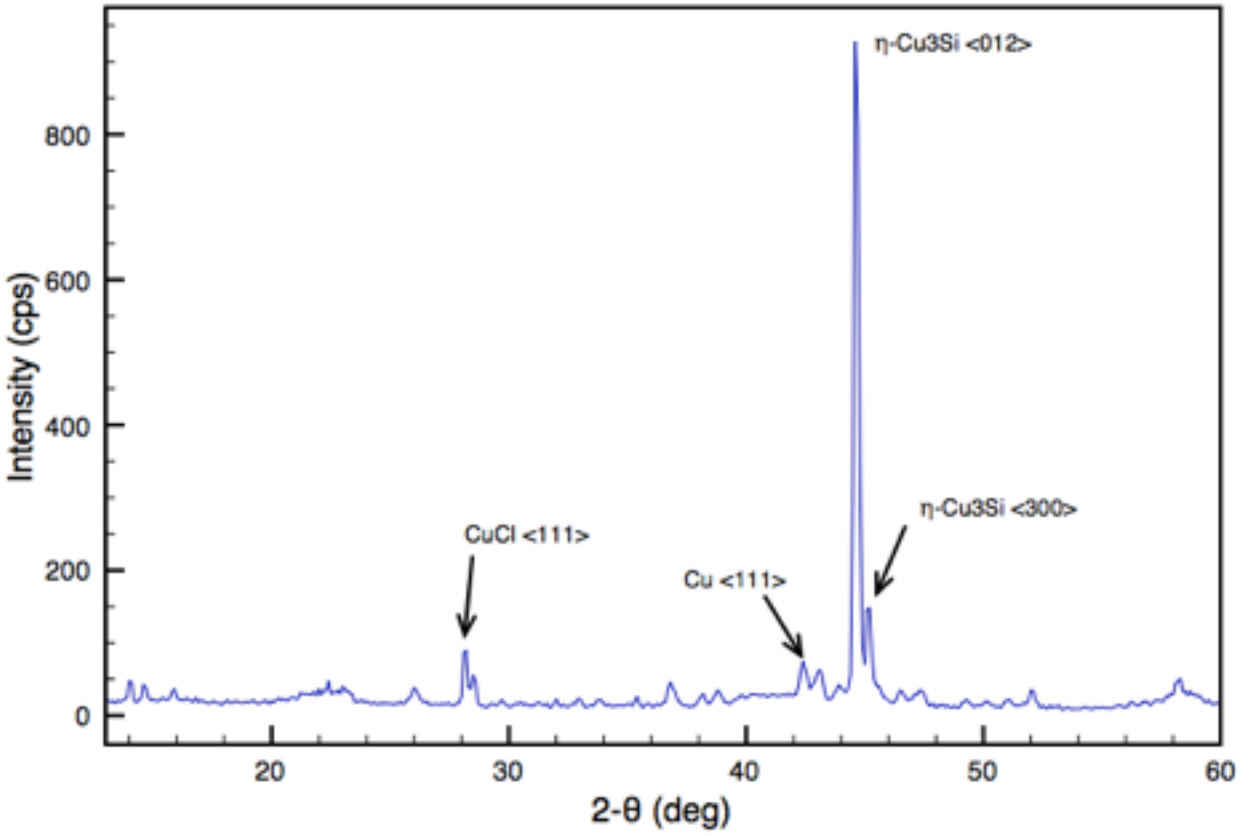

Figure 5.14 *- XRD θ-2θ scan of damaged Si substrate, the notable Cu_3Si peak dominates, arising from the CuCl/Si solid state reaction*

5.5.2 Hybrid Layer Liquid Phase Epitaxy

The deleterious CuCl/Si surface reaction at elevated temperatures presents an opportunity to utilize an approach known as hybrid layer LPE. This technique was developed initially for LPE growth of InP/GaAs on Si substrates [8, 9], in which the lattice mismatch is relatively high (~ 4%) leading to high defect levels in resultant epilayers and three dimensional growth. Classically, this approach uses an intermediate GaAs 'buffer' layer to help offset the lattice mismatch between the desired GaAs/AlGaAs epilayer and substrate, as well as protecting the bare substrate from any dissolution from the native melt.

For CuCl on Si substrates, the lattice mismatch is negligible for this technique, but the side effect of buffering the substrate from dissolution (or, specifically for this case, CuCl/Si reactions) is beneficial. CVD and MBE processes are used to deposit such hybrid layers, before the actual LPE growth stage, however the PVD process may also be used experimentally. The rationale is that the buffer layer would be entirely polycrystalline, as XRD confirmed from previous vacuum evaporations, but may provide an adequate 'bridge' between the substrate and CuCl/Si melt to allow for improved wetting on account of identical ionicities, buffer the CuCl//Si reaction and potentially improve the growth of γ-CuCl on Si using LPE.

In order to test this approach, a set of experiments was envisioned using PVD deposited γ-CuCl and KCl on Si. These substrates were prepared as though for an LPE growth run and then CuCl and KCl thin films were thermally evaporated, respectively. For both these experiments, melt compositions of $CuCl_{(80)}KCl_{(20)}$, $CuCl_{(77)}KCl_{(23)}$ and $CuCl_{(73)}KCl_{(27)}$ were used. There was no appreciable improvement in the samples deposited by these experiments.

It is clear from the heating regime used for the LPE growth (illustrated in Fig 5.5) that the CuCl hybrid layer would not persist until the growth phase, since the thin film would evaporate off the substrate as well as react during heating; however the reaction may 'prepare' the substrate and thus may prove somewhat beneficial during the growth at ~250 °C. For this approach, however, there was no discernible improvement in the resulting growth and the retrieved samples comprised of the textured polycrystalline material previously produced.

For the KCl hybrid layer, a similar growth run was executed, but growth was carried out at a higher temperature. Unfortunately, this strategy also did not work since the as-deposited KCl, when exposed to the melt during the growth run, would be dissolved and added to the melt and slightly

increase the KCl melt concentration. The higher growth temperature was selected in order to minimize the time between the dwell and growth to reduce any desorption of the KCl layer. Also of consideration would be the lattice mismatch for these hybrid layers; the CuCl layer would essentially be akin to homoeptiaxy, however the KCl layer, even had it succeeded, would have a mismatch of ~13% and most likely be non-conducive to LPE growth.

Notwithstanding these difficulties, the textured polycrystalline CuCl film that we did succeed in growing displayed remarkable optical properties, which will be outlined in the following section.

5.6 Optical Characterization

The aforementioned LPE grown textured CuCl samples were optically characterized using both room temperature and low temperature PL as well as XEOL using the experimental setups described in chapter 2. Due to the non-uniformity of the surface of the sample and the highly textured K_2CuCl_3/CuCl nature of the film, sample to sample reproducibility was difficult to maintain for PL studies. Instead, a qualitative approach is presented. Within the samples that have been studied there exists a large variation of melt compositions, however a number of characteristic features are present within the PL spectra obtained across all samples.

Figure 5.15 shows the room temperature PL spectrum for a $CuCl_{77}KCl_{23}$ melt sample on a <111> Si substrate, prepared using the nominal growth process outlined previously. The spectrum features broad emission originating from the bulk textured material. From previous work on PVD deposited CuCl thin films [7], at room temperature one expects to observe PL emission from the Z_3 exciton centered at $\lambda \sim 387$ nm. From this figure, it is clear that there are a number of other emission mechanisms also occurring.

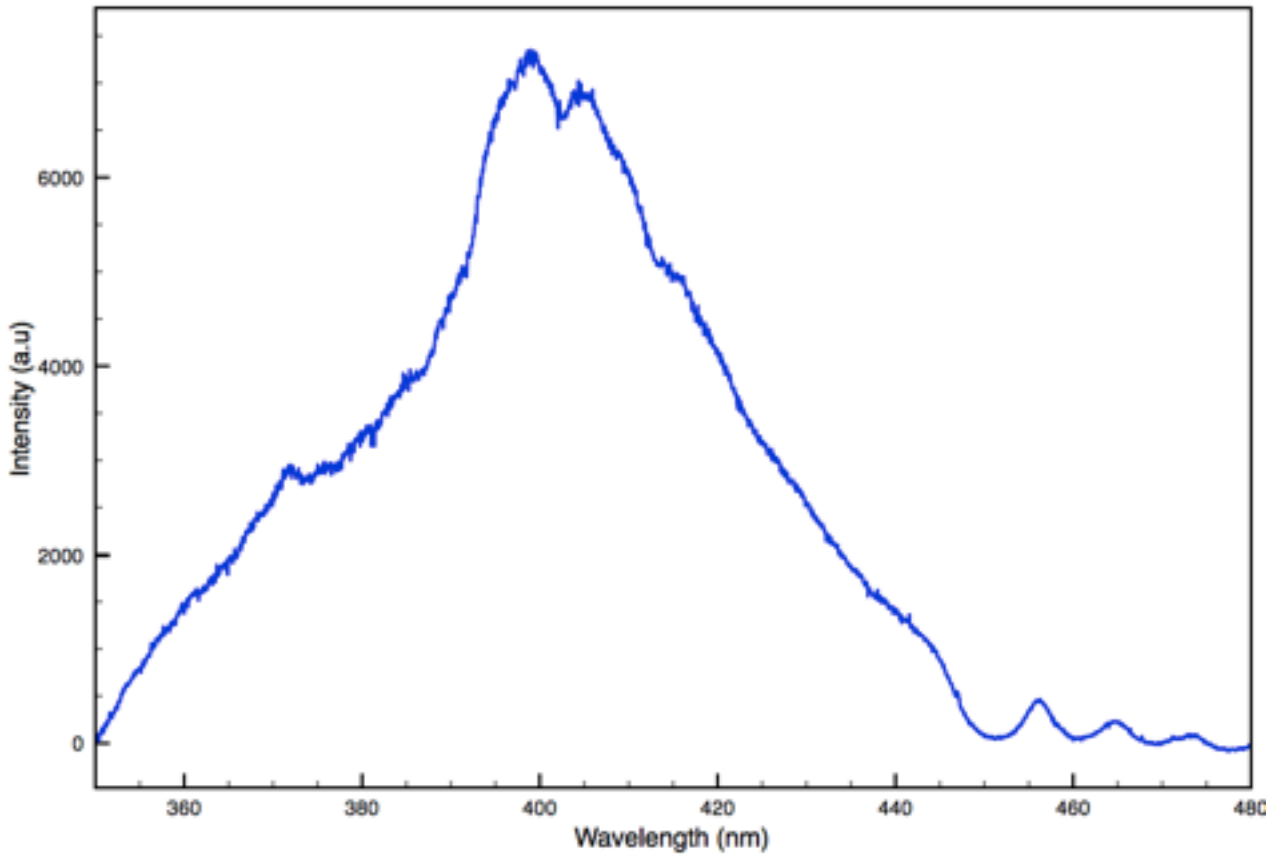

Figure 5.15 *- Room temperature baselined PL spectra for $CuCl_{77}KCl_{23}$ LPE produced sample (10 second acquisition time)*

Informed by the CuCl/KCl phase diagram as well as the XRD data, the optical properties of K_2CuCl_3 or its interaction within the CuCl/K_2CuCl_3 textured samples produced are suspected. Very few spectroscopic studies of these alkali Copper halide crystals have been carried out. Most notably, the K_2CuCl_3 band structure has been determined [10] and the fundamental optical absorption bands were determined. A main absorption peak around 4.5 eV was reported, and a smaller peak at 3.2 eV was also mentioned, but this was ascribed to some decomposition of the K_2CuCl_3 film rather then being an intrinsic property of the crystal itself. This report also confirmed that K_2CuCl_3 is a direct band gap material. However, there was no correlation between reported K_2CuCl_3 luminescence data and the observed broad emission from our LPE grown samples.

In an attempt to clarify the source of some of the peak structures comprising the spectra, peak fitting was undertaken in order to create a simple model to fit the observed spectral acquisitions. Using Gaussian fitting, peak positions were identified at approximately λ ~371 nm, λ ~400 nm, λ ~405 and λ ~413 nm Additionally, the expected Z_3 exciton emission was included at λ 387 nm. Figure 5.16 below shows the fitted spectra with these assumptions - the yellow line is the model generated from the underlying peaks and is a reasonably close approximation to the line shape of the spectra.

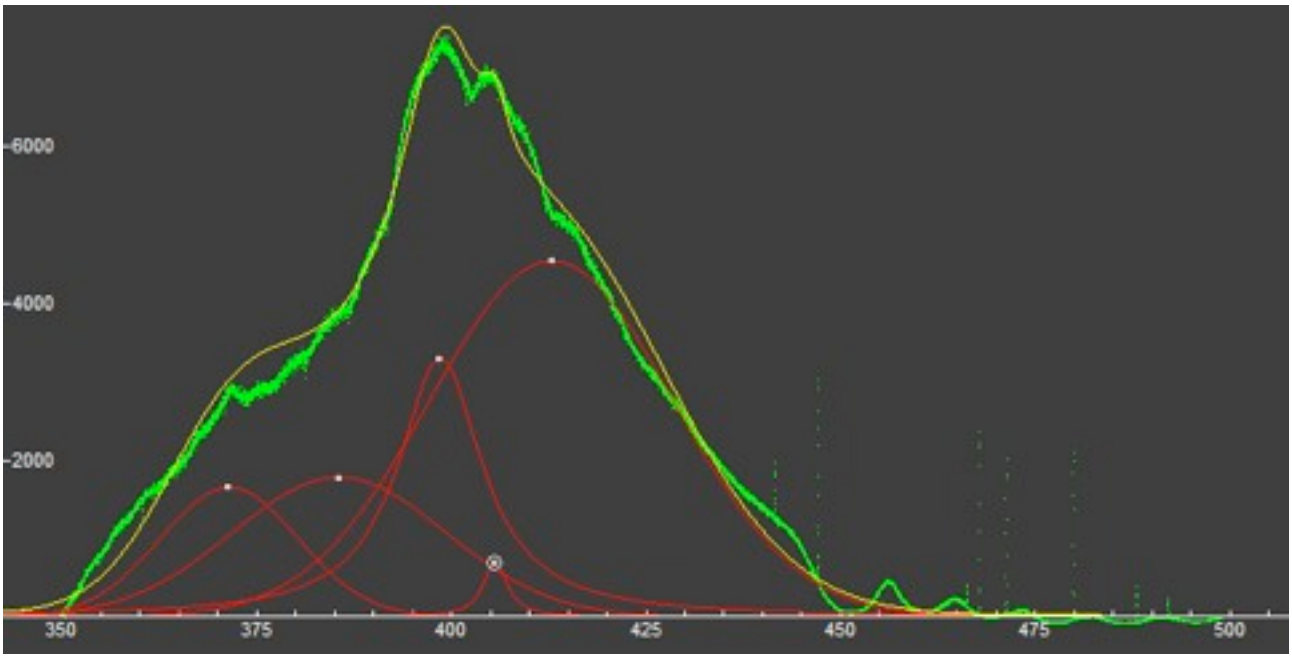

Figure 5.16 *- Peak fitting of candidate peaks for $CuCl_{77}KCl_{23}$ LPE sample at λ ~371 nm, λ ~387 nm, λ ~400 nm, λ ~405 and λ ~413 nm, drawn in red, with the resulting model given by the yellow line. Original PL scan is in green. Peak fitting was performed using the Fityk program [11]*

The assumption of these four spectral peak positions in addition to the Z_3 position proved to be relatively consistent across the PL for the acquired spectral data, and only the fitting parameters for their half-width at half-maximum (HWHM) and intensities need to be adjusted by the fitting program [11]. Complimentary low temperature PL measurements were carried out on the LPE

grown samples, as experimentally detailed previously in chapter 2. Figure 5.17 below shows the acquired temperature dependent PL spectra for a $CuCl_{77}KCl_{23}$ LPE deposited sample.

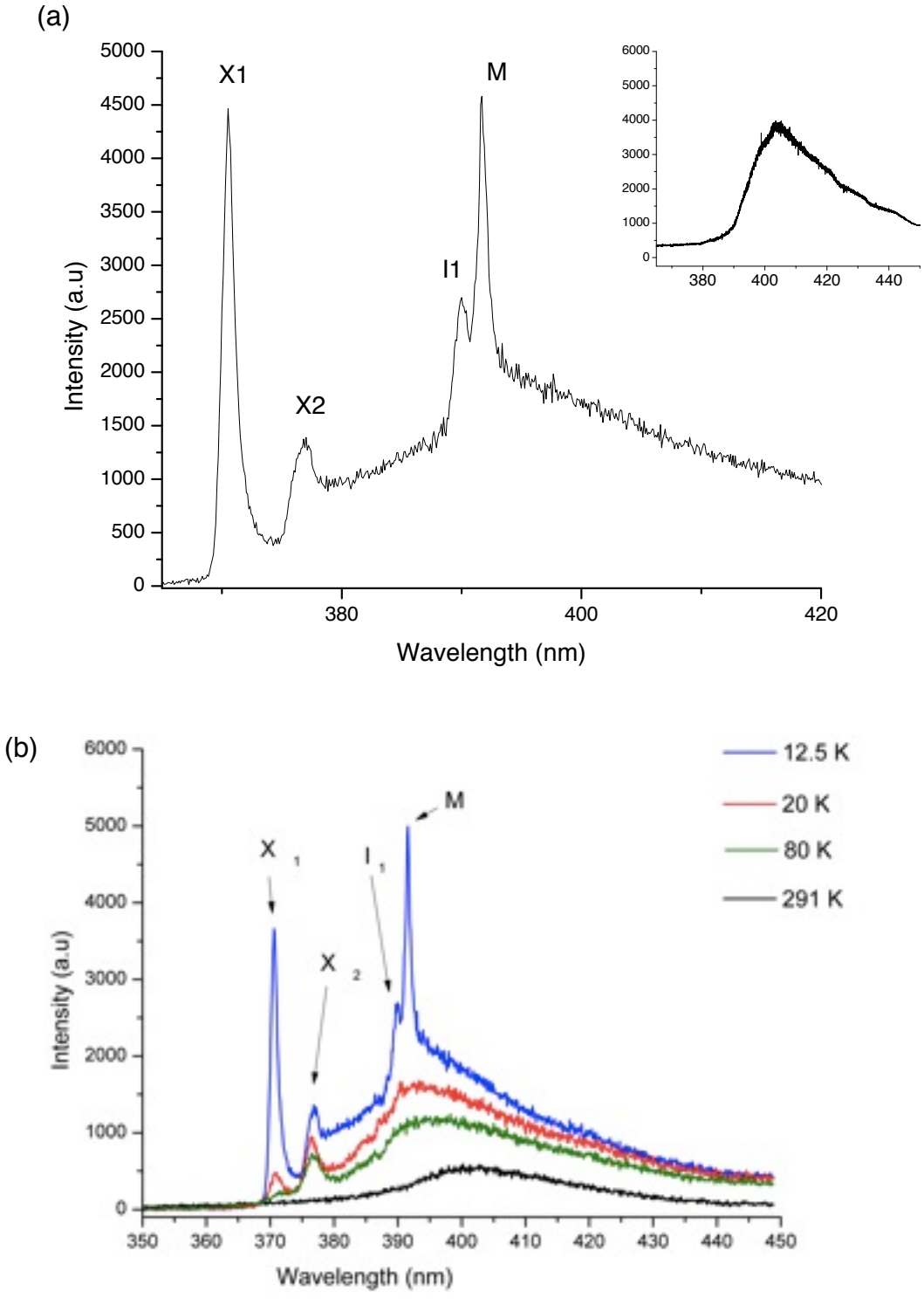

Figure 5.17 *- Low-temperature PL measurement for CuCl-KCl melt produced sample (a) at 12.5 K with expected excitonic features I_1 and M biexciton and (b) formation of peaks as temperature decreases. Inset for (a) shows the room temperature PL data for comparison.*

At 12.5K, the PL measurement of the film reveals four discernible peaks: the M free biexciton at 3.190 eV (~391 nm) as well as the I_1 bound biexciton occurring at 3.18 eV (~389 nm) [12].The newly observed peaks at λ ~370nm and λ ~376nm (labeled X_1 and X_2) are not related to any known CuCl excitonic features, however. Figure 5.17 (b) shows the PL emission at 12.5 K, 50 K and at room temperature, approximately 300 K, which shows the development of the identifiable peaks as the temperature decreases as well as the blue shifting of the broad emission band observed at room temperature. The energies for I_1 and M exciton peaks agree exactly with previously reported emission measurements for CuCl bulk crystal at 8 K [13] and thin films deposited on Al_2O_3 substrates [14].

The peaks X_1 and X_2 are, as mentioned, not directly attributable to any known CuCl excitonic structures, but their development as a function of temperature is potentially informative. Since excitons represent the lowest energy state for electron hole pairs, such states are only usually seen at low temperatures and in sufficiently defect free crystals. Otherwise, local fields can break up the exciton into free carriers [15]. It should be noted also that the ~370 nm peak aligns with a possible peak position within the room temperature PL spectrum for CuCl-KCl produced samples, although there is no similar correlation with the X_2 peak, which remains unattributed to any known CuCl process.

Clearly absent is the free exciton Z_3 peak. Possibly owing to the intermixed nature of the CuCl and K_2CuCl_3 layer, the exciton cannot directly exist, however this is unusual considering the clear existence of the biexcitonic molecule, M, which suggests that free excitons are present in the material in sufficiently large quantities to form the biexciton. It is also possible that the characteristic free exciton Z_3 peak is present, albeit drowned out by the broadening effect seen in the spectra.

One tentative explanation for the anomalous appearance of the X_1 and X_2 peaks is a Stark effect induced blue shifting of the Z series excitons. The textured nature of the samples grown via our LPE process, in which the K_2CuCl_3 compound exists alongside the y-CuCl, could potentially act as a photo-induced electric dipole which in turn could lead to a exctionic blue shift of the $Z_{1,2}$ doublet or, potentially, a splitting of this exciton, as was observed in reflectance studies of CuCl [16]. Irrespective of the underlying mechanism, it is probable that the presence of the K_2CuCl_3 compound plays a critical role in the formation of the X_1 and X_2 peaks. Owing to the mixed crystal that the CuCl and K_2CuCl_3 crystallites form, in addition to the relatively sparse details on the K_2CuCl_3 compound itself, it is difficult to provide a definitive explanation for the origin of these new low temperature peaks.

Regarding the room temperature PL emission for the grown samples, it should be noted that the recorded intensity is, qualitatively, much stronger then previously observed for CuCl thin films. In complimentary work involving another alkali halide, KBr, and CuBr (which is presented in Chapter 7), as well as in work involving co-evaporation of KCl and CuCl [17] and work by Kondo *et al.* [18], similar improvements to the base luminescence of the CuHa material in question were recorded. Two mechanisms for this improvement which may be applicable in the CuCl-KCl based growth are presented. Firstly, the observed luminescence improvement is based on the migration of Cu^+ and K^+ ions within the film, which can be understood by considering the crystal structure of the polycrystalline CuCl as made up of vacancies and interstitials [18, 19]. These crystalline imperfections can act as recombination centers, trapping electrons and holes and reducing the effective carrier concentration for emission processes. The displacement of the Cu+ and K+ ions within the polycrystalline sample, driven by their chemical affinities for negative ions (i.e. the Cl- anion), however, free up additional anions which can close some of the vacancies present, thus boosting the carrier concentration within the sample and the emission intensity. The unique

formation of the samples from the CuCl-KCl melt is also another mechanism - similar to the work reported by Kondo *et al.*, the intermixing of the alkali halide compound with the CuCl could allow for the formation of higher optical quality crystallites within the sample, owing again to the chemical interaction of the KCl and CuCl, and the potential for the formation of CuCl (or K_2CuCl_3) crystallites free of Cu+ and Cl- ion vacancies.

The highly damaged CuCl-based epilayer grown on Si, shown previously in figure 5.12, was also optically characterized using PL. A very weak PL spectrum is obtained (see figure 5.18) when the acquisition time of the spectrometer is adjusted to acquire for 60 seconds. The Z_3 excitonic emission for CuCl can be observed at $\lambda \sim 387$ nm. This would indicate the presence of trace amounts of CuCl on the substrate, which is confirmed via the previous XRD scan (see figure 5.14) and some likely candidate crystals can be observed in the SEM image (figure 5.12(a)). The weakness of the signal relative to the measurements of the sample as shown in figure 5.14 makes comparisons difficult, but the comparatively weak reflections attributed to the K_2CuCl_3 compound in the XRD scan and the lack of any of the assumed peaks (i.e., at λ ~371 nm, λ ~387 nm, λ ~400 nm, λ ~405 and λ ~413 nm) in this PL spectra would indicate that the unexpected PL peaks occurring from the LPE sample are confined to the bulk of the sample

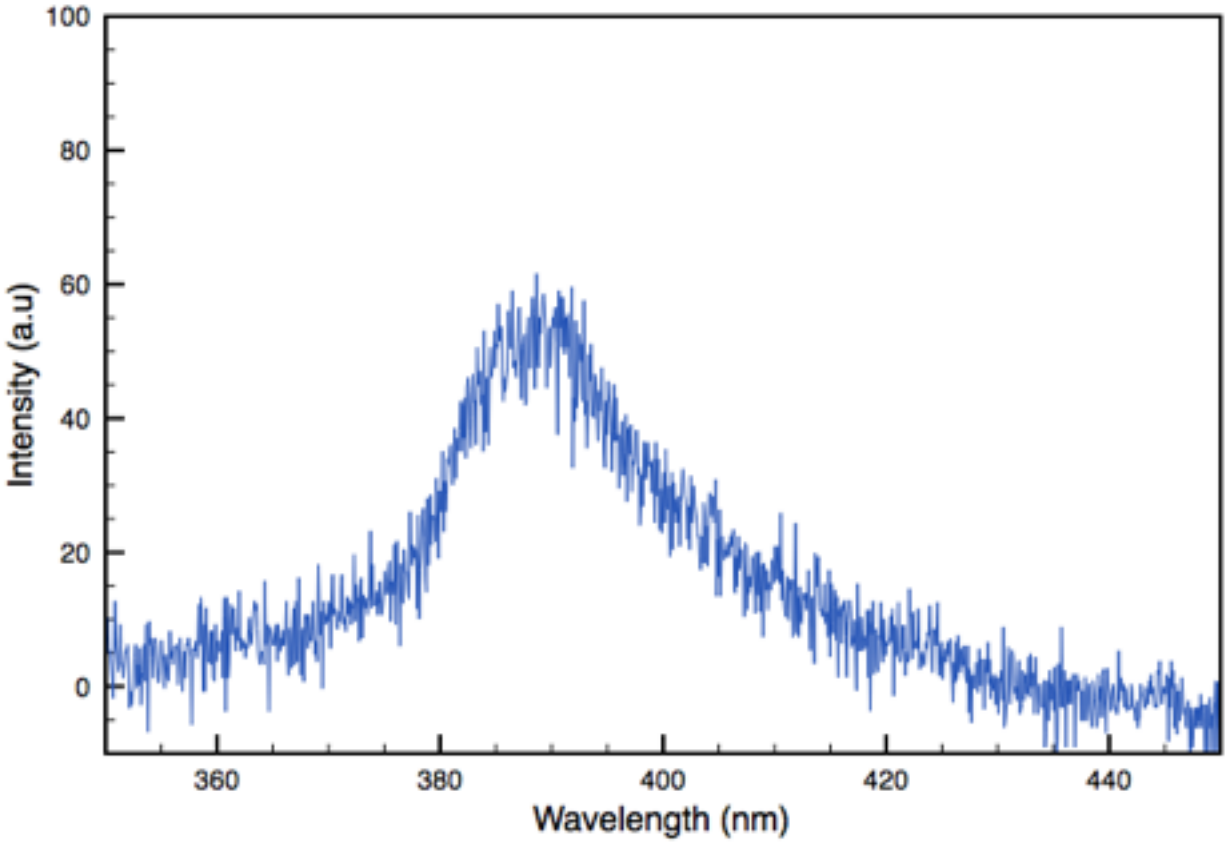

Figure 5.18 *- Room temperature PL measurement (60 second acquisition time) of 300 °C LPE grown CuCl based epilayer, with corresponding SEM image appears in Fig 5.12; residual CuCl crystallites are observed via SEM and a very weak PL signal is generated.*

5.6.1 XEOL Measurements

Using the synchrotron facilities at ANKA and HASYLAB, as detailed in chapter 2, XEOL measurements were carried out on a selection of the LPE grown samples. The images below in figure 5.19 shows the experimental mounting of the sample as well as the observed luminescence under white-beam synchrotron excitation. Images were captured from the CCD camera within the beamline hut. Under synchrotron radiation exposure, it can be seen that the sample displays remarkably bright photoemission. Spectra were acquired using the experimental setup outlined in chapter 2.

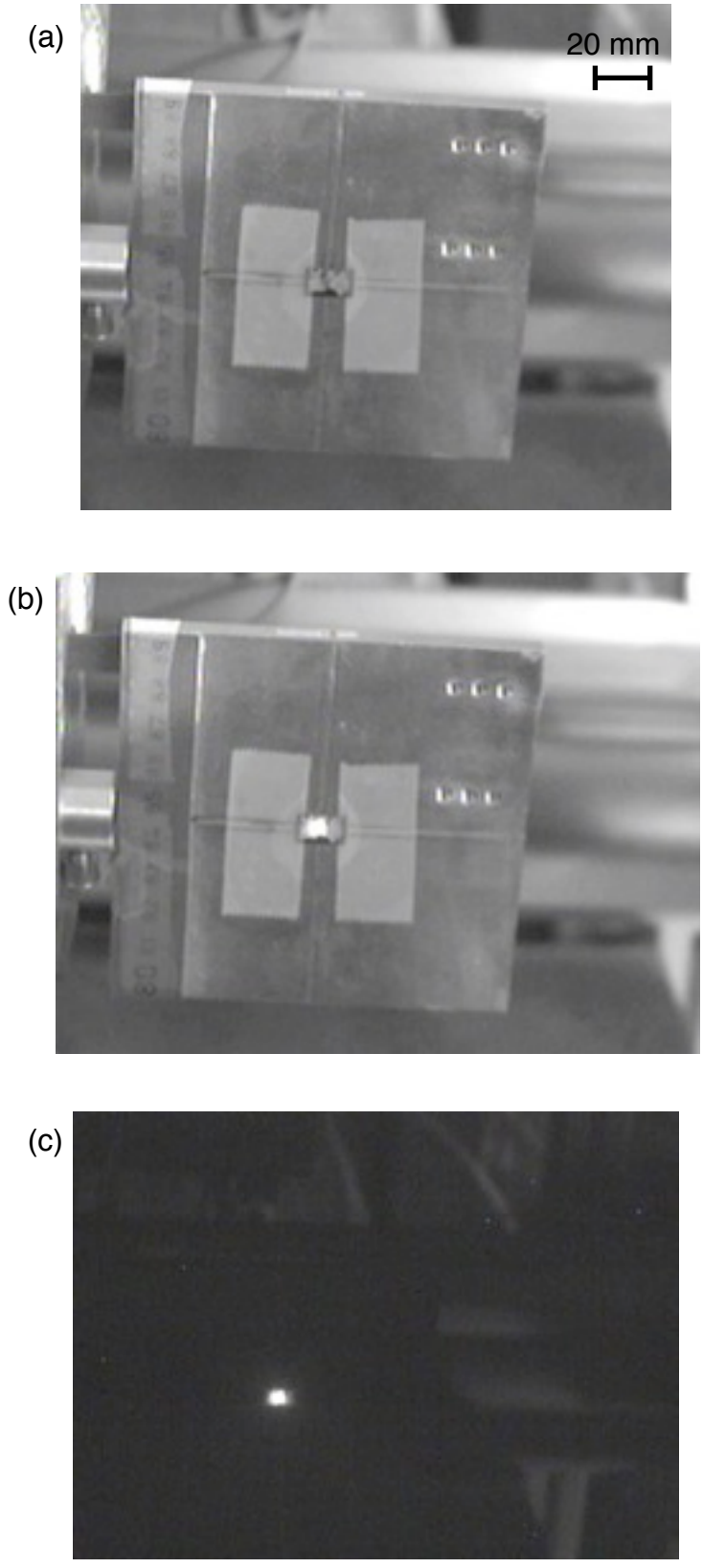

Figure 5.19 *- $CuCl_{77}KCl_{23}$ LPE Sample under XEOL measurement; (a) sample is mounted with scotch tape, (b) beamline shutter is opened, exposing the sample to the synchrotron radiation and (c) same as (b), but with the experiment hut lights turned off.*

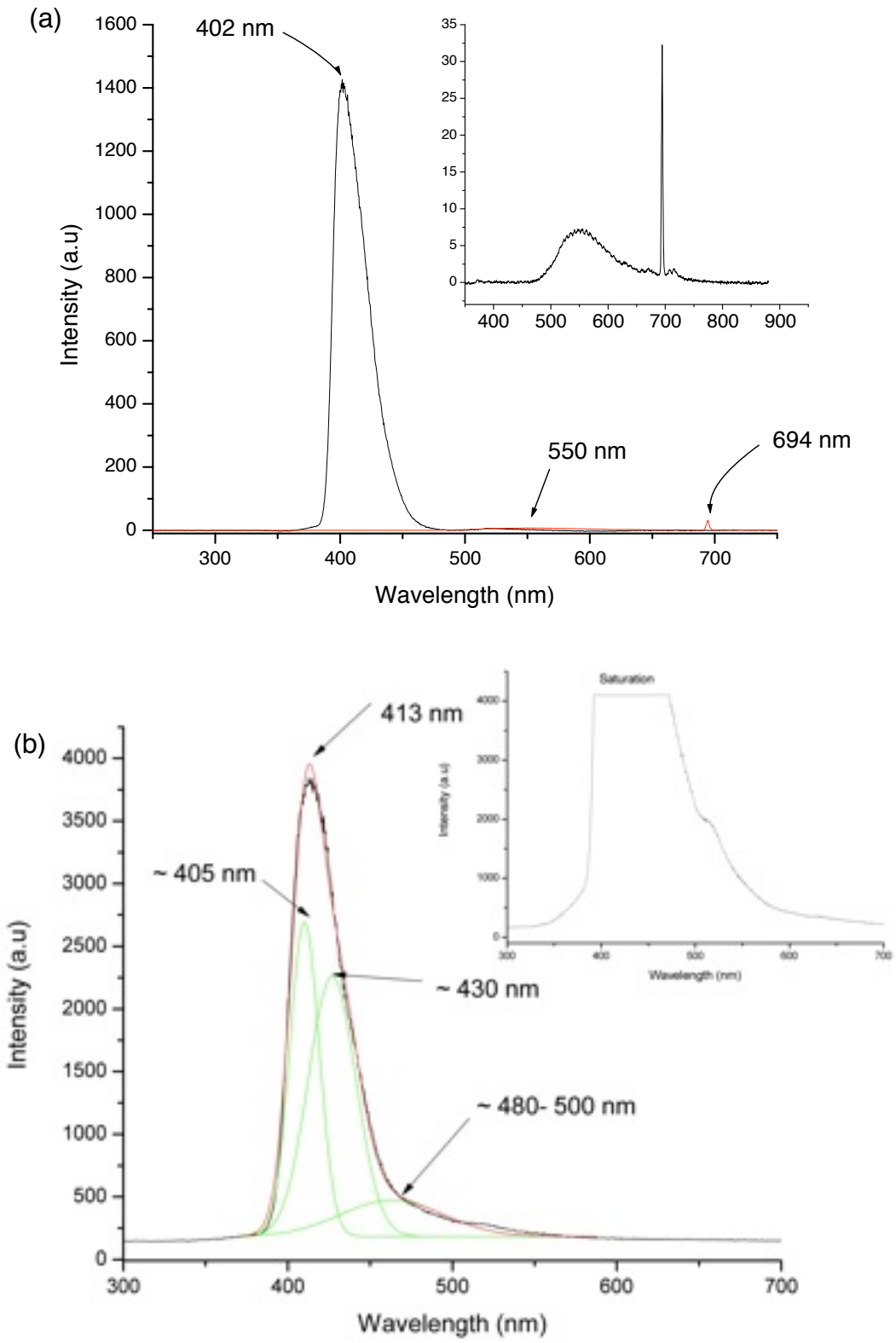

Figure 5.19 *- (a) XEOL spectrum for $CuCl_{77}KCl_{23}$ on Si with overlaid GaN spectrum in red (magnified within the inset), taken with same experimental conditions and on the same scale (acquisition time, 3ms), (b) peak fitting of same spectra (inset showing effect of saturation for acquisition times > 3 ms)*

Figure 5.19 (a) shows a typical XEOL spectra for an LPE produced CuCl/KCl sample, consistently observed across the nominal growth parameter range for different samples. The XEOL spectrum of a nominally undoped single crystal GaN (on Al_2O_3 substrate) is shown on the inset of figure 5.19 (a) for comparison and is equally scaled. The GaN sample was grown via the epitaxial lateral overgrowth (ELO) technique and has a thickness ranging between 5-7μm. Previous PL measurements of the GaN sample show a yellow band emission at λ ~550nm [20]. The well-known Al_2O_3 peak at λ ~694nm is also clearly visible. This spectrum was taken under identical experimental conditions. It can be clearly seen that the luminescence from the LPE grown CuCl/KCl sample film is considerably brighter by ~ 3 orders of magnitude compared to that of the GaN sample. It is also approximately an order of magnitude brighter than previously observed vacuum deposited CuCl samples studied with XEOL.

This luminescence enhancement effect can also be seen clearly in the XEOL spectra in Figure 5.19, where a strong luminescent peak occurs at λ ~413 nm. This peak position aligns closely with the similar proposed peak found in the room temperature PL scans mentioned previously (see figure 5.15). By applying peak fitting to the XEOL spectra, a number of contributing peaks can be observed. In figure 5.19 above, the inset shows the same sample but with an exposure time of 10 ms, which is sufficient to saturate the detecting spectrometer (as shown inset to figure 5.19 (b)). The presence of a shoulder to the right of the main peak can be seen near λ ~ 520 nm, which can clearly be distinguished with a higher acquisition time. However, this leads to a saturation of the detector (as shown in figure 5.19 (b) inset).

There is one notable correlation between the observed XEOL spectra and the room temperature PL measurements and the assumed PL peak positions, which is the

aforementioned ~413 nm peak. In the XEOL spectra, this constitutes the primary, most intense, observed peak. The assumed fitting analysis of the XEOL spectral output, shown in figure 5.19 (b) shows a likely contributing peak to this main ~413 nm emission around the ~405 nm position, which also corresponds to an assumed peak position for the room temperature PL. The absence of the higher energy peak positions and characteristic excitonic features seen in room temperature PL and the addition of lower energy shoulder in the ~ 480 - 500 nm and ~ 520 nm range is difficult to ascribe to any particular process, but was consistently observed on all XEOL examined samples.

5.7 Difficulties with LPE

The interaction of substrates with melts in LPE is not unprecedented - Astles *et al.* [21], discussed the degradation of the substrate from rapid in-diffusion of Ga for $Ga_{1-x}In_xAs$ (x = 0.7–0.9) on (111) InAs substrates, and Ga meltback of GaAs LPE growths is also well known [22]. However, the reaction observed with CuCl and Si is considerably more damaging to the substrate and may essentially preclude the viable epitaxy of CuCl on Si using LPE with melt compositions that would require growth above ~ 250 °C. The wetting of the melt to the substrate is also an issue. Figure 5.20 below shows the result of a growth run where the melt did not sufficiently wet the whole substrate, and when the melt was pushed off, exposed only a partially wetted substrate. The differing ionicities between the extremely ionic CuCl and KCl constituents and the covalent Si substrate, positioned as they are at the extreme ends of the ionicity range, is a likely reason for the non-optimal wetting.

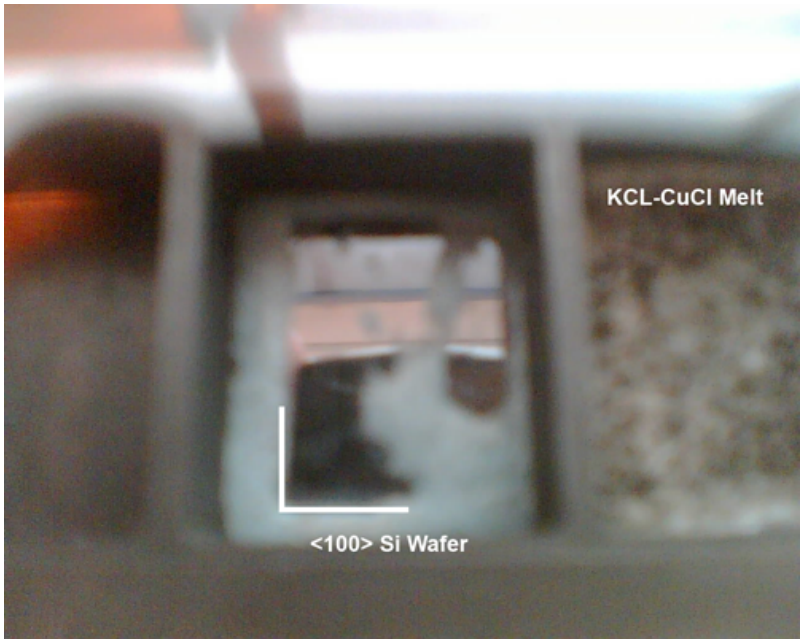

Figure 5.20 *- Image of Si substrate, post growth wipe off, showing the poor coverage of the CuCl-KCl melt as a result of poor wetting.*

Additionally, the phase diagram for the CuCl-KCl system and the requirement for melt composition to precipitate in the CuCl and liquid phase presents some difficulties. Large supersaturation of CuCl leads to spontaneous nucleation within the melt [23]. As mentioned in chapter 4, LPE is a semi-limited growth, where the nucleation is dependent on the arrival of constituent material at the growth interface. Due to the large saturation of CuCl present in the melt, not only does this result in 3-d growth and thus precipitation within the melt, but it would also limit the potential time for the precipitating material to reach the substrate surface before being consumed by adjacent crystal growth within the melt.

In addition, the type of LPE growth used in these experiments, being in the range of 220 - 390 °C is rather low considering the literature on LPE. Within AlGaAs LPE work, it was found that low-temperature growth was difficult to achieve due to poor substrate wetting with the melt, resulting from the presence of an oxide film ‘skin’ on the surface of the melt. The

reactivity of CuCl and its readiness to form oxyhalide compounds is a substantial problem in this regard. During the growths when the melt was observed, it was clear that there was a transparent 'skin' surrounding the melt. At the high temperature phase of the LPE run, there was no readily discernible evidence of the skin. At lower temperatures, closer to the point when the substrate would be exposed to the melt, this 'skin' effect became more noticeable. This may also be a time related issue, since the melt would have been formed for over 4 hours by the time growth would commence. It also may be related to the viscosity of the melt at lower temperatures compared to observations at higher temperature.

Discussions with Dr. Zbigniew Zytkiewicz of the Institute of Physics of the Polish Academy of Sciences, Warsaw, on the problem of substrate wetting lead to experiments using a selection of techniques that could be tried in order to clarify the problem and find an effective solution. These experiments were based on the assumption that an unknown substance was covering the substrate or the presence of a skin covering the surface of the melt - in either case, the effect would be no direct contact of pure CuCl/KCl melt with the Si substrate.

The first assumption is that an unknown film, created in the LPE system, covers the substrate, prevents wetting by the melt (possibly caused by a chemical reaction of species present in gas phase with the substrate) and thus nucleation and growth on the Si surface. A technique used to investigate this assumption is illustrated in Figure 5.21, wherein the sliding boat system has been modified to include a small sharp scratching wire.

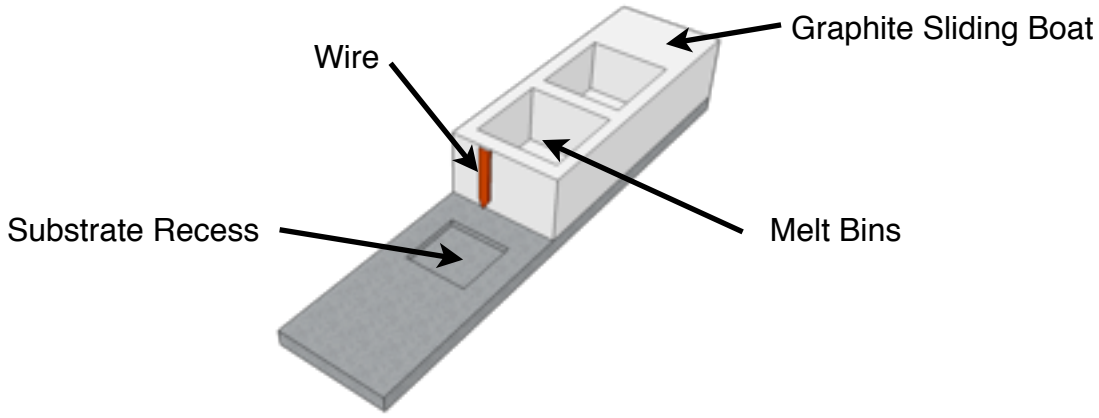

Figure 5.21 *- Experimental setup for LPE graphite boats, using a small abrasive wire, highlighted in red.*

When the slider moves the melt bin into the growth position, the wire will scratch the surface of the substrate just before growth, mechanically removing any film before the melt contacts. It would be hoped that some growth could be observed where the surface was scratched. A similar experiment using the multi bin sliding boat involved using a Ga precursor melt to dissolve the surface prior to the growth melt moving into place was also carried out. In both these cases, however, no improvement to the produced bulk CuCl/KCl films was noted.

Another suggestion would be to apply the mechanical cleaning approach to remove any skin on the melt prior to contacting the substrate, using the piston boat LPE technique. This would address the second assumption outlined above. The melt is squeezed through a small hole by the use of a piston system. This mechanically strips the skin from the melt and ensures that only pure melt contacts the substrate. This technique has been employed for AlGaAs/GaAs systems previously, wherein the Al is known to oxidize and form a skin around the melt surface [24]. Although a full piston system was technically impractical with our LPE setup, the technique was adopted partially in the modified

tipping boat design, illustrated previously in figure 5.22. The narrow channel between the melt bin and the substrate holder was envisioned as a means of providing a mechanical way to try remove any melt skin by restricting the flow through the channel and pulling the skin free prior to rolling onto the substrate.

Use of H_2 flow was also used in order to try minimize the effect of the native SiO2 layer on achieving a good epi-ready surface. The native oxide present on the Si substrate is a concern for wetting of the melt and substrate, and a considerable amount of research has been carried out using H_2 flow in oxide reduction [25, 26]. While the aforementioned etch routine would remove the native oxide, the inevitable desorption of oxygen and water vapor from the tube and graphite coupled with the heating regime used, could lead to further oxidation of the silicon. This further highlights the importance of baking out the graphite components prior to a growth run. The removal of the oxide is believed to occur from the reaction [26]:

$$2SiO_2 \leftrightarrow 2SiO + O_2 \tag{5.6}$$

where the SiO is a volatile by-product, and the H_2 flow acts as a catalyst for the process. By this reaction, H_2 flow has been used for oxide removal providing that the oxide is not more than 4 nm thick. For our LPE growths, the use of H_2 flow was found to be problematic, as the Hydrogen was observed to react with the CuCl melt. Figure 5.22 below shows a recovered graphite boat with CuCl/KCl melt and Si substrate in place.

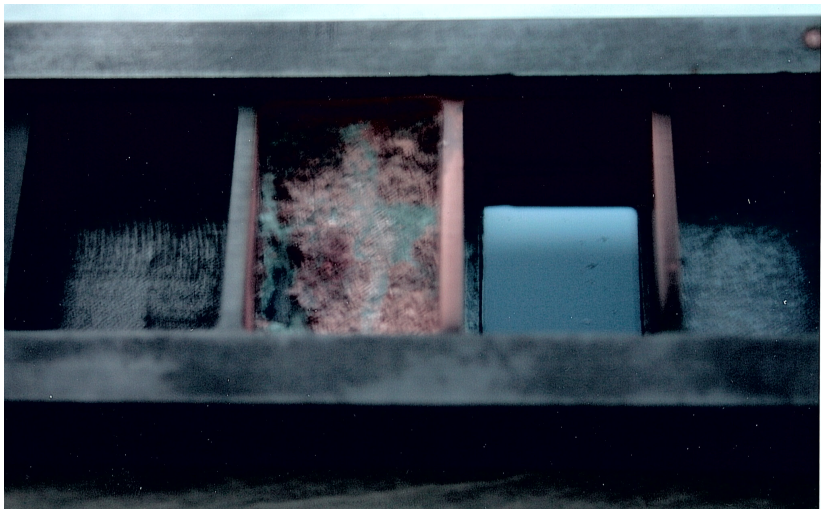

Figure 5.22 *- Decomposition of CuCl/KCl melt from use of H_2 flow during growth.*

There is a clear reaction on the surface of the cooled melt - this reaction was observed during the heating stage of the growth, where it formed and persisted as a thick skin on the surface of the liquid melt. The gas flow downstream results in the deposition of this discoloured material on the graphite melt bin. It is likely this deposition and discolouration are due to a reaction between evaporated CuCl and the H_2 flow. The colour of the residue seems suggestive of Cu, which may indicate that there is a H_2/Cl reaction occurring. Due to the reaction with the melt and the cost involved in utilizing hydrogen flow, the use of H_2 was not pursued in further experiments.

5.7 Conclusions

The fundamental motivation for this research has been the question of whether it is possible to grow γ-CuCl epilayers on lattice matched Si substrates utilizing the LPE technique. In order to avoid the deleterious phase transition, KCl salt is used to depress the liquidus temperature of the melt below the β-CuCl to γ-CuCl phase transition point as well as below the known CuCl/Si reaction point. To date, samples produced display a textured polycrystalline composition, made up of CuCl and K_2CuCl_3, which can be clearly seen from the XRD data acquired for grown samples.

Optical characterization via photoluminescence studies and XEOL measurements reveal dramatic improvements to the luminescence intensity of the samples, likely owing to the presence of KCl and the K_2CuCl_3 compound originating from the LPE growth method. It is speculated that this improvement is owed to the filling of the Cl- anion centers in the CuCl crystal by contributions from the KCl and/or the K_2CuCl_3 present within the deposited material.

The luminescence observed is likely comprised of different emission mechanics compared to nominal CuCl emission. Low temperature PL at 12.5 K reveals the presence of some well known CuCl excitonic features such as M the free biexciton at 3.190 eV (~391 nm) as well as the I_1 bound biexciton occurring at 3.18 eV (~389 nm). New peaks at λ ~370nm and λ ~376nm (designated X_1 and X_2) are not related to any known CuCl excitonic feature, however. It is suggested that these peaks could be due to the interaction of the CuCl and K_2CuCl_3 compounds within the grown layer.

A number of difficulties exist when using LPE for γ-CuCl growth, which make this approach a technically challenging one to implement. Notably, LPE growth at these low temperatures, necessary to avoid the phase change and CuCl/Si reaction, represent an extreme in LPE literature. The extreme degree of CuCl saturation within the KCL/CuCl system required also leads to a

preferential nucleation within the melt itself (i.e., 3-d nucleation) rather then on the substrate. It should be noted that the understanding of the CuHa eutectic systems acquired during this phase of the PhD study would prove fruitful and would inspire the work seen later in this thesis in Chapter 7.

5.8 References

[1] M.J. Rice, S. Straessler and G.A. Toombs, Phys. Rev. Let., Volume 32, 1974, page 596.

[2] D.K. Shuh and R. S. Williams, Phys. Rev. B 44, 5827 (1991)

[3] J. Sasai, K. Tanaka and K. Hirao, Scrpta mater. 44, 1225 (2001)

[4] Milipore Manufacturer website: http://www.millipore.com/catalogue/module/c72876

[5] D.E. Etter & C.J. Wiedeheft, Solar Energy Materials 2, 1980, pages 423-431.

[6] G.Weber, D. Viale. H. Souha, B. Gillot and P. Barret, Solid State Ionics, Volume 32-33, 1989, pages 250-257.

[7] L. O'Reilly, 'Growth and characterisation of wide-bandgap γ-CuCl on near lattice-matched Si', PhD thesis, 2006, Dublin City University.

[8] R.F. Schnabel, M. Grundmann, R. Engelhardt, J. Oertel, A. Krost, D. Bimberg, R. Optiz, M. Schmidbauer and R. Köhler, Journal of Crystal Growth, Volume 156, 1995, pages 337–342.

[9] S. Sakai, R.J. Matyi and H. Shichijo, Journal of Applied Physics, Volume 63, 1988, pages 1075–1079.

[10] K. Edamatsu, M. Ikezawa, H. Tokailin, T. Takahashi, T. Sagawa, Journal of Physical Society Japan, Volume 55, 1986, page 2880.

[11] Fityk curve fitting software homepage: http://fityk.nieto.pl/

[12] M. Certier, C. Wecker, and S. Nikitine, Journal of Physics and Chemistry Solids, Volume 30, 1969, page 2135.

[13] T. Goto, T. Takahashi, M. Ueta, Journal Physics Society Japan,Volume 24, 1968, page 314.

[14] M. Nakayama, H.Ichida, H. Nishimura, Journal of Physics: Condensed Matter, Volume 11, 1999, page 7653.

[15] J. Pankove, 'Optical Processes in Semiconductors', Dover Publications, 2010.

[16] E. Mohler, Physica status solidi (b), Volume 38, 1970, pages 81-94.

[17] F. Lucas, A. Cowley, P. J. McNally, Physica status solidi(c), 2009.

[18] S. Kondo, Y. Hata, T. Saito, Materials Letters, Volume 62, 2008, pages 33-36.

[19] M. Ueta, 'Excitonic Processes in Solids', Wiley, 1986

[20] B. J. Ryan, D. P. Lowney, M. O. Henry, P. J. McNally, E. McGlynn, K. Jacobs, L. Considine, Thin Solid Films, Volume 473, 2005, page 308.

[21] M. G. Astles, O. D. Dosser, A. J. MacLean, P. J. Wright, Journal of Crystal Growth, Volume 54, 1981, pages 485-492.

[22] A. Baldus, A. Bett, U. Blieske, O. V. Sulima, W. Wettling, Journal of Crystal Growth, Volume 146, 1995, pages 299-304

[23] V. Wrick, G. J. Scilla, L. F. Eastman, Electronics Letters, Volume 12, 1976, pages 394-395.

[24] A. W. Nelson, E. A. D. White, Journal of Crystal Growth, Volume 57, 1982, pages 610-612.

[25] Lin Lanying, Fang Zhaoqiang, Zhou Bojun, Zhu Suzhen, Xiang Xianbi, Wu Rangyuan, Journal of Crystal Growth, Volume 56, 1982, pages 533-540.

[26] K. Weber & A. Blakers, Applied Physics Letters, Volume 66, 1995, page 1243.

Chapter 6 - γ-CuBr Thin Films and Electroluminescent Devices

6.1 Introduction

In this chapter we will outline the results of our depositions of CuBr thin films on Si, glass and ITO coated glass substrates for film thicknesses of between 100 and 500 nm. The preparation and fabrication of these thin films will be presented and the structural and optical properties will be discussed. The stability and electrical degradation (as well as degradation in ambient atmosphere, if untreated) of these deposited films will also be reported. The development of a novel hot-electron electroluminescent device based on γ-CuBr will also be detailed.

6.2 Substrate Preparation and Cleaning

As discussed in chapter 3, the vacuum evaporation PVD process was used to deposit γ-CuBr films on Silicon (<100> and <111>) and glass substrates, as well as ITO coated glass for device structures. Substrates were thoroughly degreased and cleaned prior to any deposition using the following process:

1. Si or glass substrates were washed with DI water from a clean bottle, while being held with tweezers.
2. Samples were then subjected to manual cleaning with Decon 90 (Sigma Aldrich) detergent solution using cotton buds, with another stage of DI washing subsequently to clear the Decon.

3. Substrates were then placed into a clean beaker with Decon solution and placed in an ultrasonic bath for 20 minutes.

4. Similar to the setup for the LPE etching routine described in Chapter 5, cleaned PTFE containers were filled with Acetone, DI water and Isopropanol. Substrates were then dipped into the Acetone, rinsed directly with DI water, submerged and stirred in the DI container, rinsed again and finally dipped into Isopropanol and given a final rinse with DI water.

5. For Si substrates, an additional step is required. Removal of the native oxide layer was carried out using a hydrofluoric acid etch (48% ACS reagent grade), diluted 5:1 HF to DI water. Samples were gently stirred in the etch solution for 1 minute before removing. Residual etch solution was washed away by a DI rinse.

6. All substrates were dried using a Nitrogen stream and visually inspected for any blemishes before being readied and loaded into the vacuum evaporator.

Si substrates used for the PVD process were supplied by University Wafer [1] and were single-side polished, p-type boron-doped, with a resistivity in the range of 0 – 20 Ωcm.

6.3 Deposition of γ-CuBr Films

Evaporation of CuBr powder (99.999%, Sigma Aldrich) was carried out in the Edwards Vacuum Coater system described in Chapter 3. The evaporation boat was a Tungsten boat supplied by Testbourne Ltd. [2]

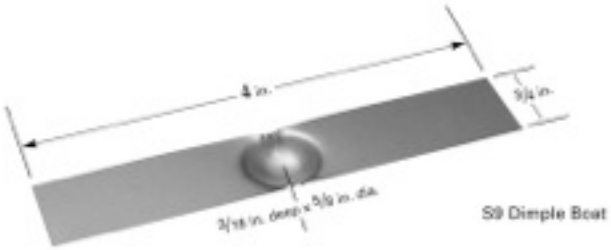

Figure 6.1 *- Tungsten boat used for CuBr evaporation within the Edwards Vacuum Coater system.*

Thin films of γ-CuBr of thickness between 100 - 500 nm were thermally evaporated using the vacuum evaporator system. The distance from the tungsten boat to the substrate was approximately 13 cm. Evaporations were carried out at a base pressure of ~4 $x10^{-6}$ mbar, although pressure would increase to 10^{-5} mbar when evaporation commenced. The rate of evaporation was controlled by adjusting the current, thus the resistive load through the tungsten boat. The deposition rate was maintained between 0.3-0.5 nm/s by calibration and monitoring of the resonant frequency of the crystal within the thickness monitor. It was found that a current flow of between 2 and 2.5 A would give the required deposition rate, however the deposition rate had to be closely monitored throughout the evaporation in order to avoid the current moving beyond this range and adversely affecting the deposition rate. Table 6.1 below summarizes the experimental parameter range used during this study

Tool	Edwards E306 Auto Evaporator
Substrate	Si <111>, Si <100>, Glass, ITO coated Glass
Sample Thickness	100 - 500 nm
Material	Cu(I)Br (Sigma Aldrich, 99.999%)
Evaporation Rate	0.3 - 0.5 nm/s
Chamber Pressure	10^{-6} mbar (base pressure), 10^{-5} mbar (evaporating)

Table 6.1 *- Some experimental parameters for PVD vacuum evaporation of CuBr thin films.*

6.4 Structural Properties of Evaporated γ-CuBr Films

Deposition of CuBr on prepared Si and glass substrates via vacuum evaporation was carried out and the resulting thin films have been examined using XRD, EDX and SIMS. In order to provide a scan representative of as-deposited γ-CuBr and as best practice, samples were prepared on the day of measurement or were stored under vacuum conditions prior to measurement.

From Chapter 4 previously, table 4.2 provides the diffraction data for the principal γ-CuBr reflections observed from the samples, namely the <111>, <220> and <311> peaks. It should be noted that other peaks for CuBr exist, but only these primary three reflections were observed within our XRD measurements. Figure 6.2 shows a typical XRD scan for ~500 nm γ-CuBr on <100> Si deposited via vacuum evaporation. It can be clearly seen that the <111> γ-CuBr peak is the most intense, with the smaller <220> and <311> reflections also present. There is a notable discrepancy from the reported expected intensities for γ-CuBr peaks at <220> and <311> compared to those observed from our XRD scan, which are expected at 60% and 35% relative to the 100% <111> peak. Our as-deposited scan shows the <220> and <311> intensity at ~7% and ~3% of reported values, respectively.

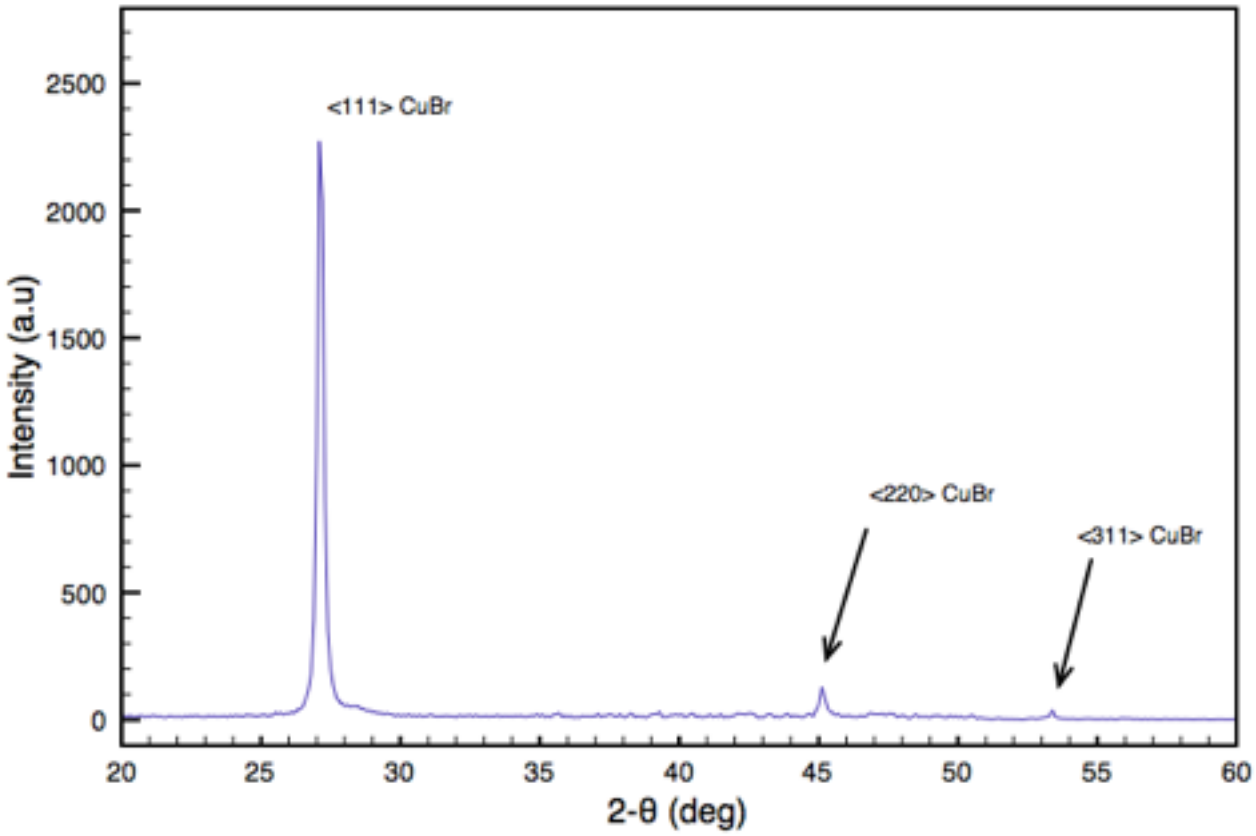

Figure 6.2 *- XRD θ-2θ scan for ~500 nm γ-CuBr on <100> Si.*

It is clear from the XRD information that <111> is the preferred orientation for epitaxial growth of γ-CuBr. One advantage of XRD is the possibility to use this method to estimate the crystallite size of the CuBr on the film from measuring the broadening of the XRD reflection by using the Scherrer formula [3], outlined previously in section 2.4.2.

Using this approach, the crystallite size of γ-CuBr on Si <100> across four as-deposited samples were calculated as ~75.61 nm. Similarly deposited γ-CuBr on glass substrates were examined via XRD and can be seen in figure 6.3.

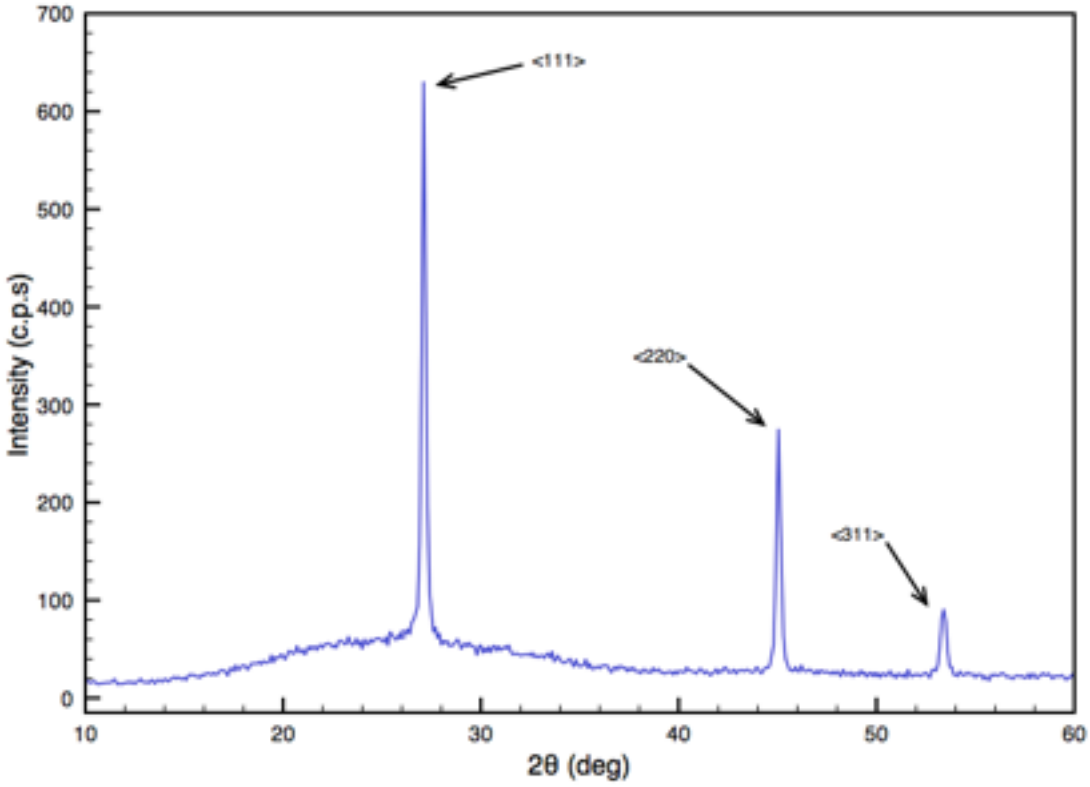

Figure 6.3 *- XRD θ-2θ scan for ~500 nm γ-CuBr on glass substrate.*

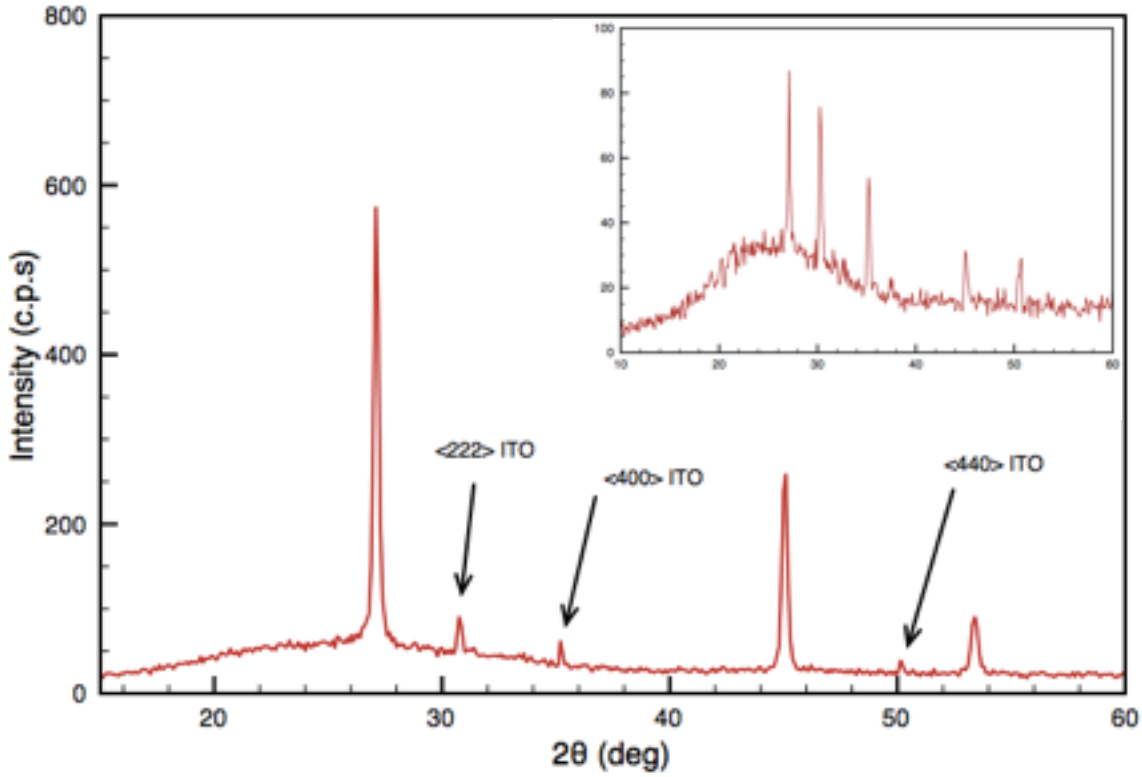

Figure 6.4 *- XRD θ-2θ scan for ~500 nm γ-CuBr on ITO coated glass substrate, inset XRD θ-2θ scan for ~100 nm γ-CuBr on ITO coated glass substrate.*

Figure 6.4 shows a ~500 nm CuBr sample on ITO coated glass substrate, where the <222>, <400> and <440> reflections are apparent. There is little apparent difference, excepting the CuBr reflection intensity) between the ~500 nm sample and a similar ~100 nm sample on ITO, as evidenced by the inset XRD scan in figure 6.4. The crystallite size was also calculated across a range of sample thickness (100 to 500 nm) on Si <100>, glass and ITO coated glass substrates, however there was little variation in grain size within a range of +/- 10 nm across the thicknesses and substrates.

GIXRD was also used to investigate the deposited γ-CuBr thin films. A glancing angle of 4° was used which limits the penetration depth of the x-rays into the CuBr film. Figure 6.5 shows the GIXRD scan of a ~500 nm thick CuBr sample on Si <100> substrate. The surface region penetrated

by the x-rays reveals the film to be comprised of the distinctive <111>, <220> and <311> reflections. Additionally, a small shoulder peak can be observed on the left of the <100> peak on all GIXRD samples. This small peak corresponds with the <100> 25.35° reflection of β-CuBr, and can be understood in terms of the evaporation process. As discussed, the deposition rate is controlled by the thermal load driven by resistive heating of the tungsten boat, controlled by alternating the current source. The resistive heating applied to the boat will fluctuate over the range of 2-2.5 A, which can be sufficient to cause a trace amount of the γ-CuBr to undergo the phase change to the wurtzite structure. This is not unprecedented in thermally evaporated CuBr, as reported by Cardona [4]. Similar studies underway within our lab, involving the sputtering of CuBr, have shown no traces of β-CuBr in their respective XRD θ-2θ scans, likely owing to the thermally stable, well controlled process of sputtering relative to vacuum evaporation.

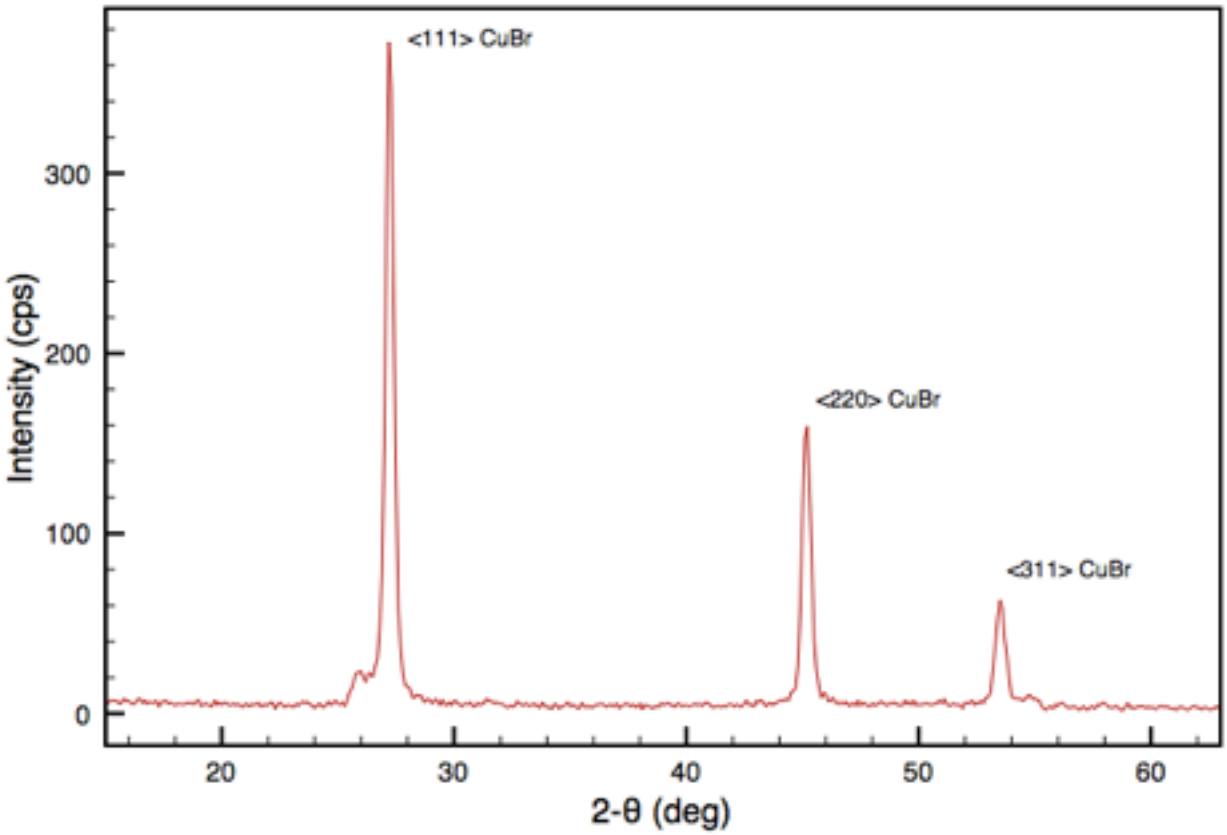

Figure 6.5 *- GIXRD scan at 4 °deg on ~500 nm thick γ-CuBr sample on Si <100> substrate.*

Analysis of the XRD data allows for the calculation of the texture coefficients for the dominant <hkl> peaks observed (i.e., the <111>, <220> and <311> peaks). The texture coefficient for each of these reflections can be calculated thus [5]:

$$TC(hkl) = \frac{I(hkl)}{I_o(hkl)} \left\{ \frac{1}{n} \sum \frac{I(hkl)}{I_o(hkl)} \right\}^{-1} \qquad (6.1)$$

where *TC* is the texture coefficient for the specific <hkl> reflection, $I_o(hkl)$ is the powder diffraction intensities relating to the material, *I(hkl)* is the measured intensity of the specific reflection and *n* is the number of recorded experimentally measured reflections used. From this expression, table 6.2 shows the texture coefficients for evaporated γ-CuBr samples calculated for ~500 nm γ-CuBr thin films deposited on Si, glass and ITO coated glass substrates. The strongest reflection, corresponding to the <111> reflection also has the largest texture coefficient on Si <100>, with a notable decrease for glass and ITO coated glass substrates which align closer with the powder diffraction intensities. The large variation for γ-CuBr on Si is likely owing to the underlying crystalline substrate, compared to the amorphous glass and ITO coated glass substrates.

	Si <100>	Glass	ITO/Glass
<111>	1.32	1.11	1.15
<220>	0.65	0.93	0.87
<311>	0.16	0.67	0.7

Table 6.2 *- Calculated texture coefficients for the primary γ-CuBr reflections on Si, glass and ITO coated glass substrates.*

Complimentary to the XRD, the surface morphology of deposited γ-CuBr films was examined using contact mode AFM. Figure 6.6 depicts the image of the sample surface. From the image, a rough triangular shape of the crystallites can be inferred (illustrated with an aid in Fig. 6.6 (b)). The

threefold symmetry of the CuBr crystals can be seen, which correlates well with the XRD data which shows that the <111> orientation is the preferred growth direction.

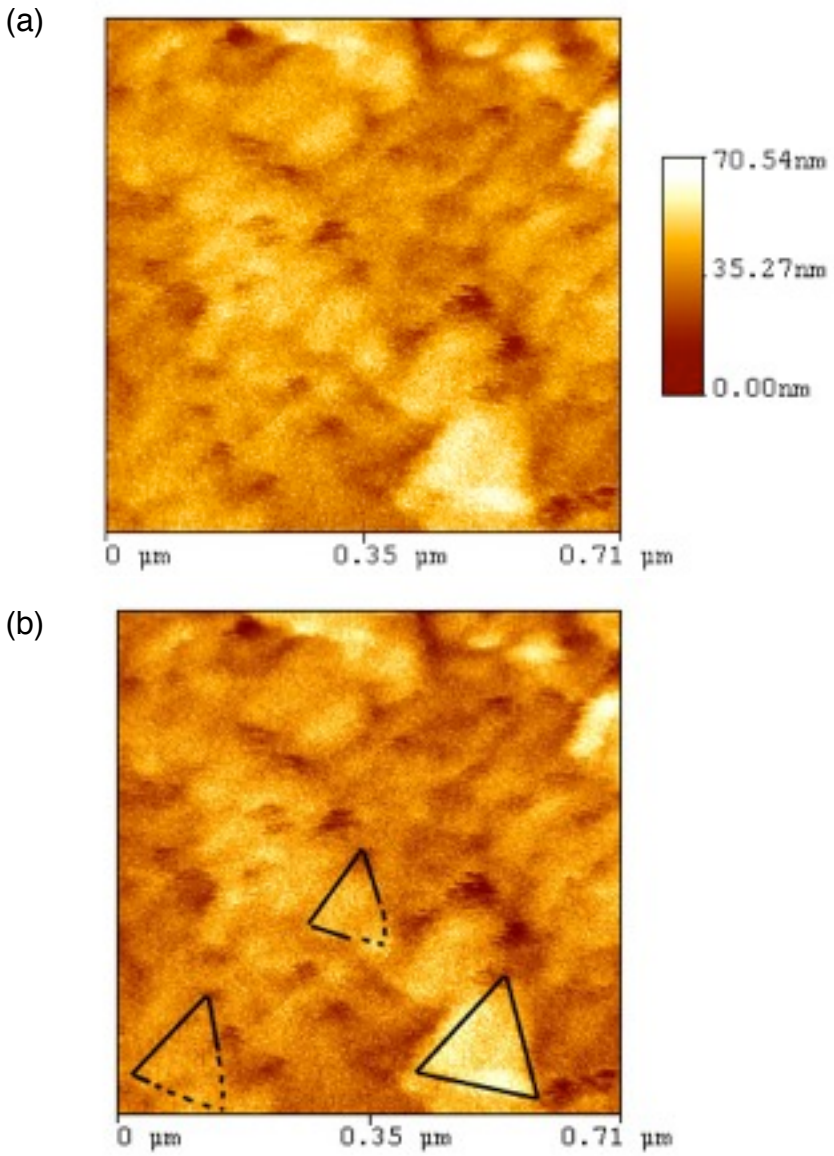

Figure 6.6 *- (a) Contact mode AFM image of as-deposited ~500 nm y-CuBr thin film on Si <100>, (b) image processed to clearly show the threefold symmetry of the CuBr crystallites.*

Surface roughness analysis was carried out for γ-CuBr on Si <100> and Si <111>, glass and ITO coated glass substrates with thicknesses ranging from 100 - 500 nm using the software provided by Pacific Nanotechnology. The root mean square (RMS) and roughness average (RA) were calculated

and averaged over the thicknesses, and are presented in table 6.3. There was no substantial statistical variation in the RMS and RA values across the thickness of the deposited films investigated, nor was there any notable variation on the differing Si orientated substrates. From the table, it can be seen that there is a minor variation depending on the substrate however this difference is negligible across the substrates.

	RMS (nm)	RA (nm)
γ-CuBr/Si <100>	5.71	7.24
γ-CuBr/Si <111>	5.8	7.55
γ-CuBr/Glass	7.12	7.3
γ-CuBr/ITO	8.1	6.41

Table 6.3 *- Root mean square (RMS) and Roughness Average (RA) for γ-CuBr films on various substrates.*

It was generally difficult to produce a SEM image of the surface, owing to charging of the sample surface, however a 'best effort' image of a ~500 nm γ-CuBr sample on Si <100> is presented in figure 6.7 below where some of the crystallite grains can be seen.

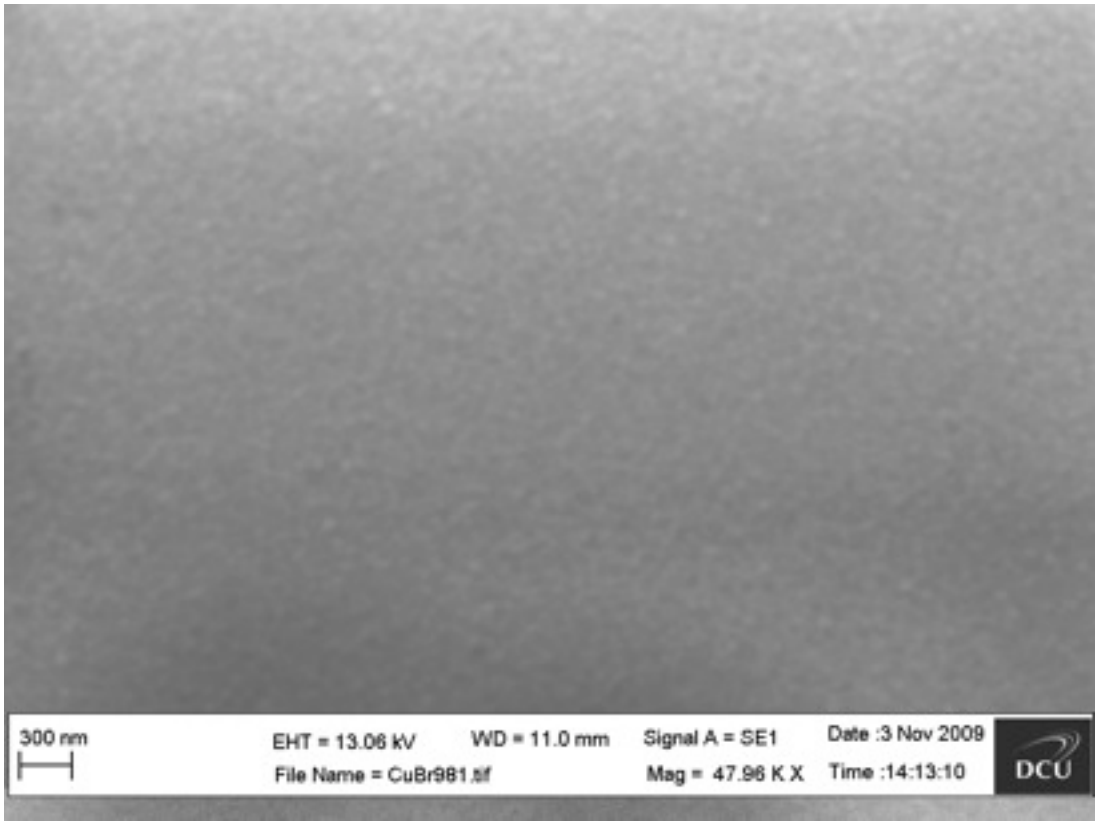

***Figure 6.7** - SEM image of surface of a ~500 nm y-CuBr thin film on Si <100>.*

In addition to topographical and structural characterization of deposited films, elementary analysis was carried out using EDX. Figure 6.8 shows a typical EDX spectrum acquired for an as-deposited ~500 nm γ-CuBr thin film on Si. From the spectra, the presence of both Cu and Br atoms is confirmed with no other elemental peaks present. An elemental assay of the results is presented in table 6.4. While there is an apparent deviation from a 50:50 stoichometry as would be expected for a CuBr film, repeated EDX acquisition on different areas of the sample would often show a Cu deficiency and other areas a Br deficiency. However, the deficiency never exceeded 3% in either situation and can be reasonably attributed to a systemic margin of error in the EDX measurement.

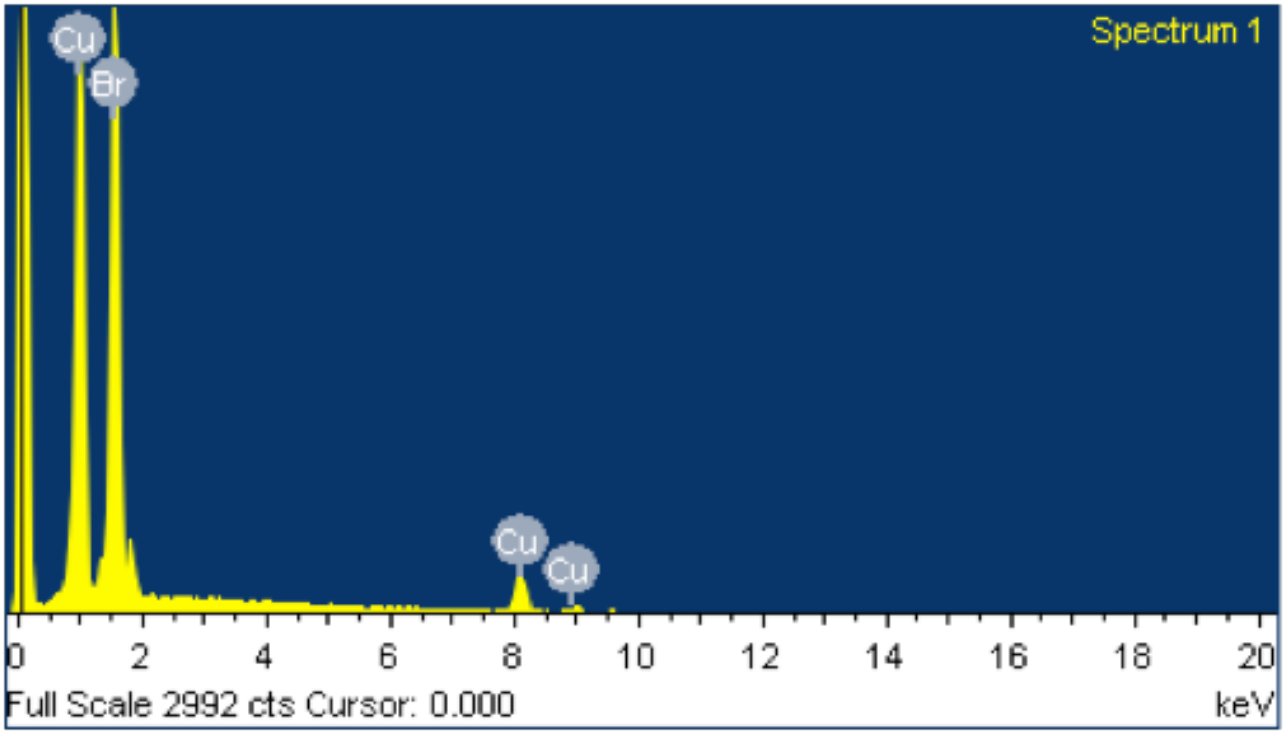

Figure 6.8 *- EDX spectra for as-depoisted ~500 nm γ-CuBr thin film on Si substrate, showing elementary composition of the film.*

Element	Weight (%)	Atomic Presence (%)
Cu	47.23	52.95
Br	52.77	47.05
Totals	100.00	

Table 6.4 *- EDX elemental assay of as deposited film shown in Fig 6.5.*

In addition, low-energy Secondary Ion-mass Spectroscopy (SIMS) was carried out on an as-deposited ~500 nm γ-CuBr film on Si substrate in conjunction with Dr. Richard Morris at Warrick University. In order to investigate the compositional uniformity of our samples, a depth profile measurement was carried out and the resulting profile can be seen in figure 6.9. From this, it can be clearly seen that there is no significant compositional variation throughout the film for the Cu and Br levels for the duration of the scan (to a depth of ~220 nm, determined post measurement via AFM).

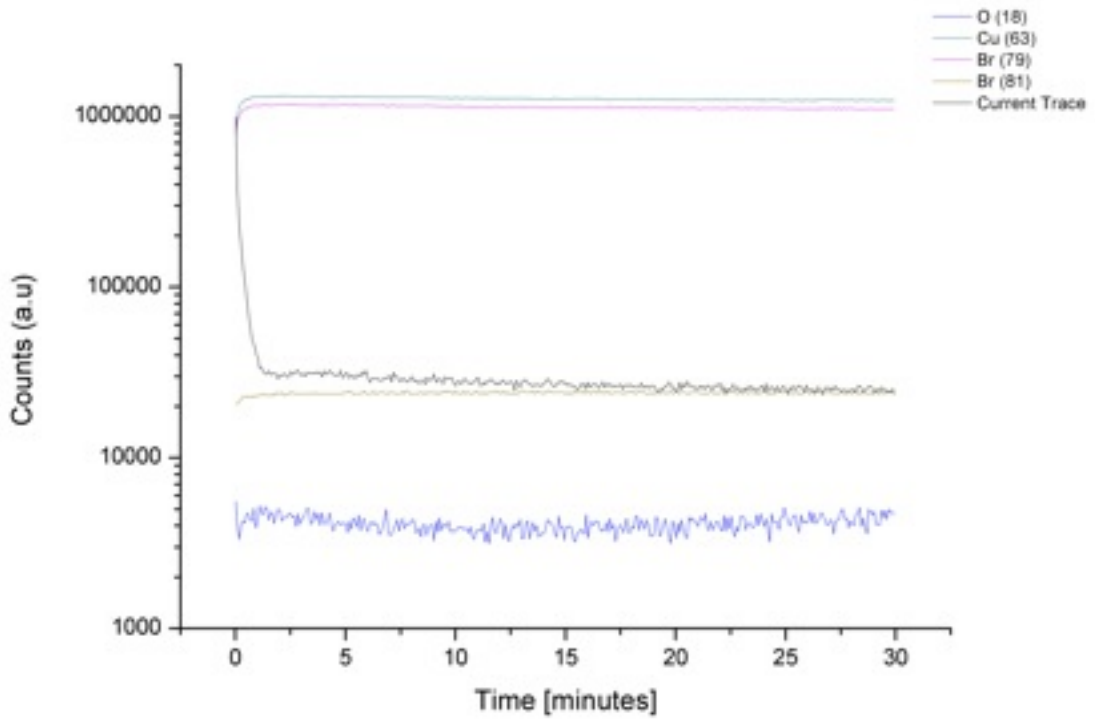

Figure 6.9 *- SIMS depth profile of γ-CuBr thin film.*

6.5 Optical Properties of Evaporated γ-CuBr Films

Deposited films were optically characterized using UV-Vis, PL and XEOL. A characteristic room temperature PL spectrum for a typical as deposited γ-CuBr film, ~500 nm thick, on Si <100> substrate is presented below in figure 6.10.

From the spectra, a strong emission is clearly observed, centered at ~417.1 nm (~2.97 eV), which corresponds with the free exciton emission, Z_f discussed previously in Chapter 4. The deviation from the nominal low temperature value of 418 nm reported for Z_f emission in CuBr [6] can be explained by examining the temperature dependent characteristics of CuBr (presented in section 6.5.1 below).

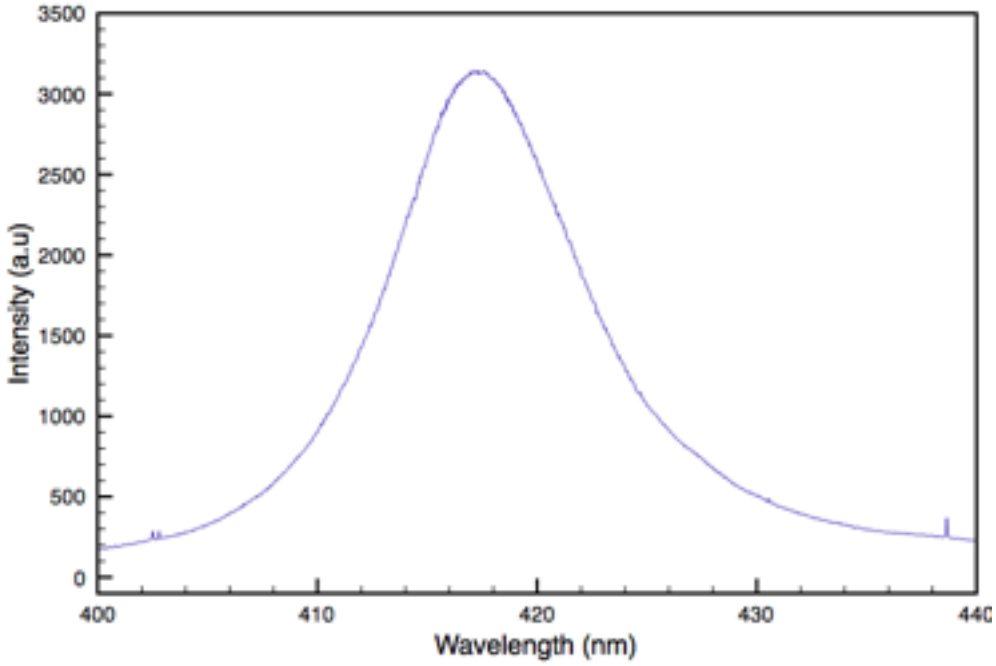

Figure 6.10 *- Room temperature PL spectrum for ~500 nm γ-CuBr on Si substrate, 1 second acquisition.*

The UV-Vis absorption spectrum for a typical 500 nm y-CuBr/Glass sample is shown in figure 6.11 below. The spectrum is notable for the evident contribution of the high and low excitonic bands, the $Z_{1,2}$ and Z_3 excitons, originating from the coupling of the Γ_6 conduction band state to the valence band holes Γ_8 and Γ_7 (as discussed previously in chapter 4). The peak at $\lambda \sim 391$ nm (3.17 eV) corresponds to the Z_3 exciton and the peak at $\lambda \sim 411$ nm (3.01 eV) corresponds to the $Z_{1,2}$ exciton - these values are in good agreement with previously reported values [6, 7].

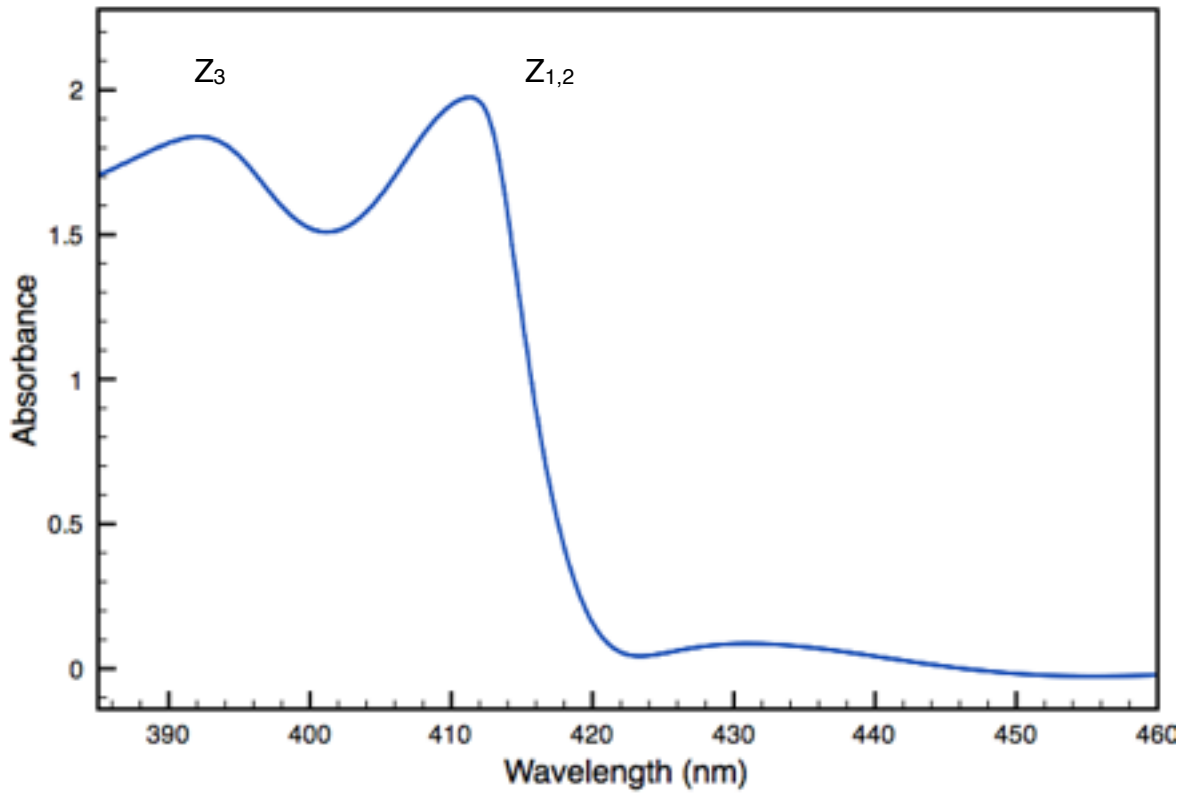

Figure 6.11 *- UV-Vis absorption spectra for typical 500 nm y-CuBr/Glass structure.*

6.5.1 Low-K PL Measurements of γ-CuBr Thin Films

Figure 6.12 below shows the temperature dependent PL measurements for a typical ~500 nm γ-CuBr thin film on Si substrate. Measurements were taken using the low-K setup outlined previously in section 2.2 at Trinity College, Dublin. Two peaks are clearly evident in the spectra as the temperature decreases: Z_f and I_1 corresponding to the free exciton and impurity bound exciton for CuBr, respectively. The inset graph shows the room temperature PL for the same sample.

As previously discussed in Chapter 4, for CuBr crystals, the free-exciton PL is attributed to the lowest energy triplet-exciton state [8]. The bound impurity exciton I_1 is attributed to the Cu^+ ion vacancies in CuBr [7]. In our temperature dependent PL, the peak intensities for the I_1 and Z_f can be seen to change with decreasing temperature with the I_1 peak intensity overtaking the free exciton

peak intensity near 80–100K. At higher temperatures the Z_f peak is dominant, in part due to the large excitonic binding energy for CuBr of 108 meV.

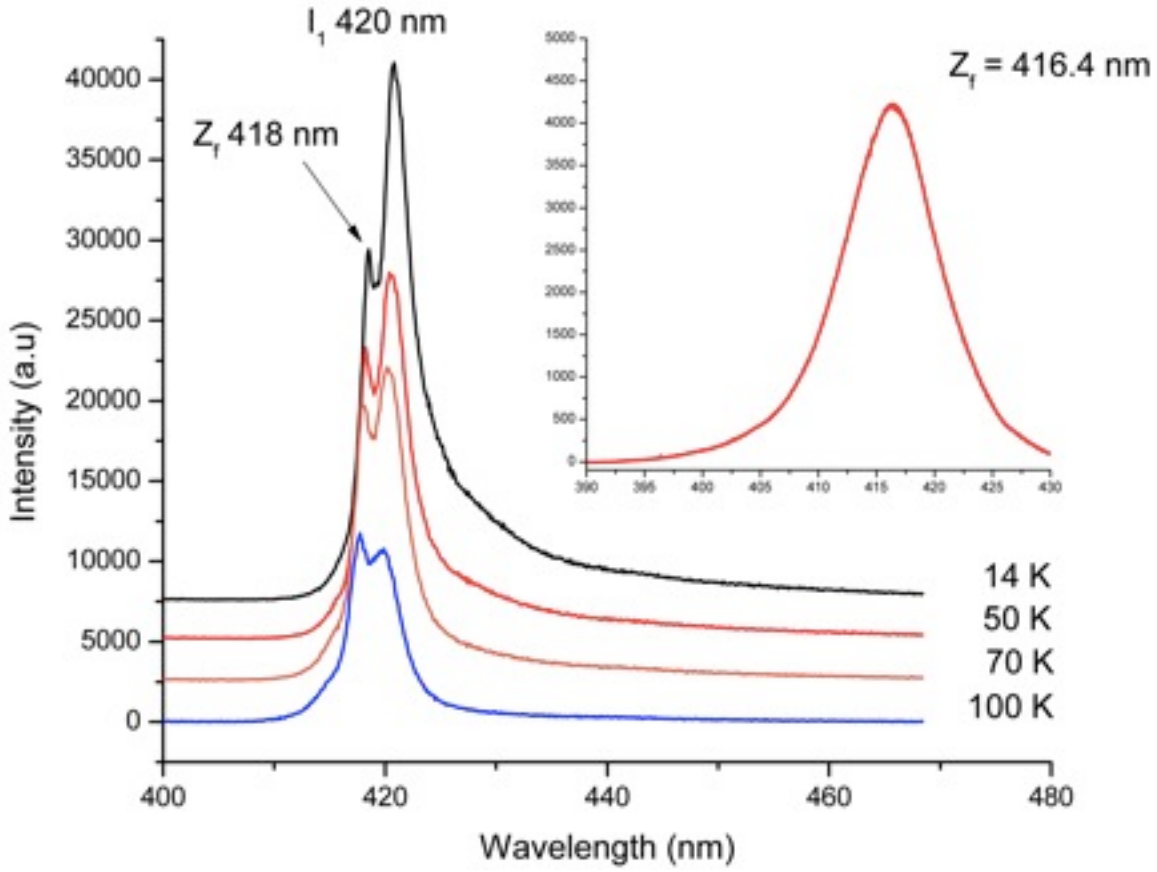

Figure 6.12 *- Temperature dependent PL measurements of γ-CuBr thin film ~500 nm thick, on Si <100> substrate. Inset graph shows RT (~300 K) measurement.*

In our films there was no observation of the wide donor–acceptor pair recombination band that was observed in previously evaporated γ-CuBr/Al_2O_3 films [9], which is attributed to the high quality of our deposited γ-CuBr/Si films.

The dominant Z_f PL peak can be observed in the room temperature spectrum at ~416.4 nm, which is anomalous considering the well-documented Z_f peak at 418 nm (12 K). However, this can be explained in terms of an increase in the band gap energy with the increasing temperature. This phenomenon has been previously accounted for in CuCl and is attributed to electron–phonon

renormalization of the band gap as described by Garro *et al.* and Serrano *et al.* [10, 11]. Garro *et al.* also claim that this explanation should hold for CuBr.

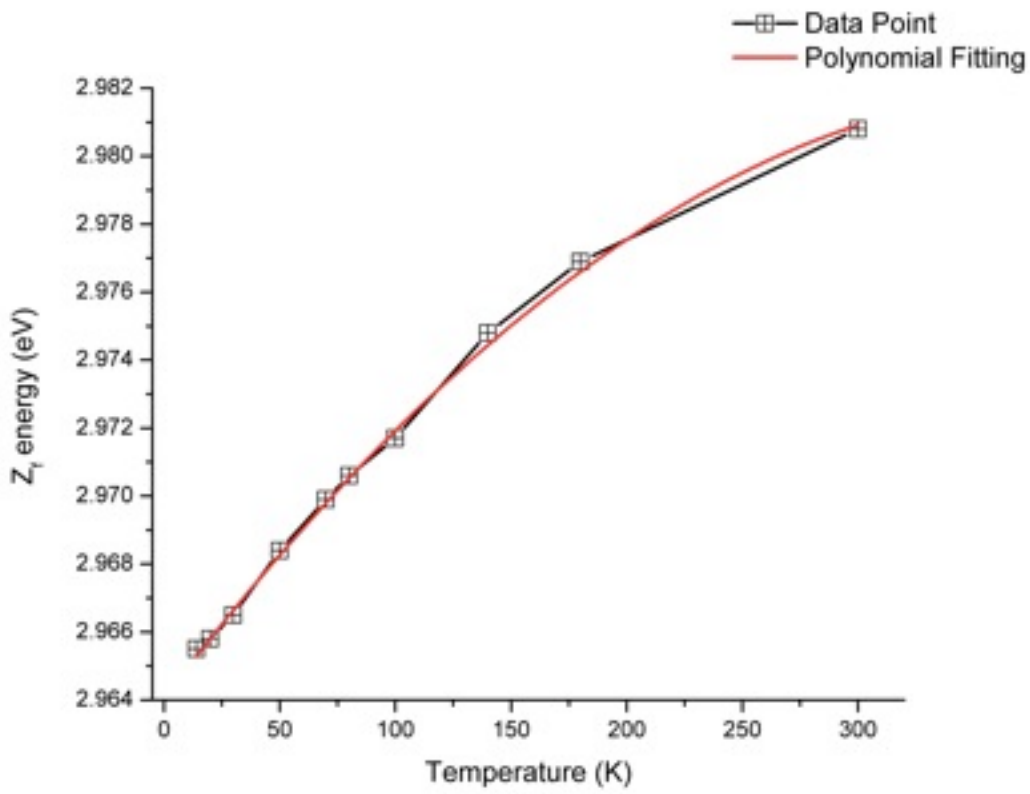

Figure 6.13 -*Variation of free exciton (Z_f) energy for ~500 nm CuBr thin film on Si <100> as a function of temperature.*

Figure 6.13 shows the energy of the Z_f PL peak as a function of temperature. The data clearly shows the increasing energy for the Z_f exciton PL, with a change from a linear slope around the ~80–100 K region. An Arrhenius plot of the natural log of the Z_f PL emission intensity against the inverse temperature is shown in figure 6.14 below. The PL emission intensity can clearly be observed to be relatively independent of temperature variation below ~80 K. Above this temperature (i.e. < 100K), the intensity is observed to decrease dramatically. This is in good agreement with Garro's work and confirms that the band gap temperature dependence shown with CuCl films extends to CuBr as well.

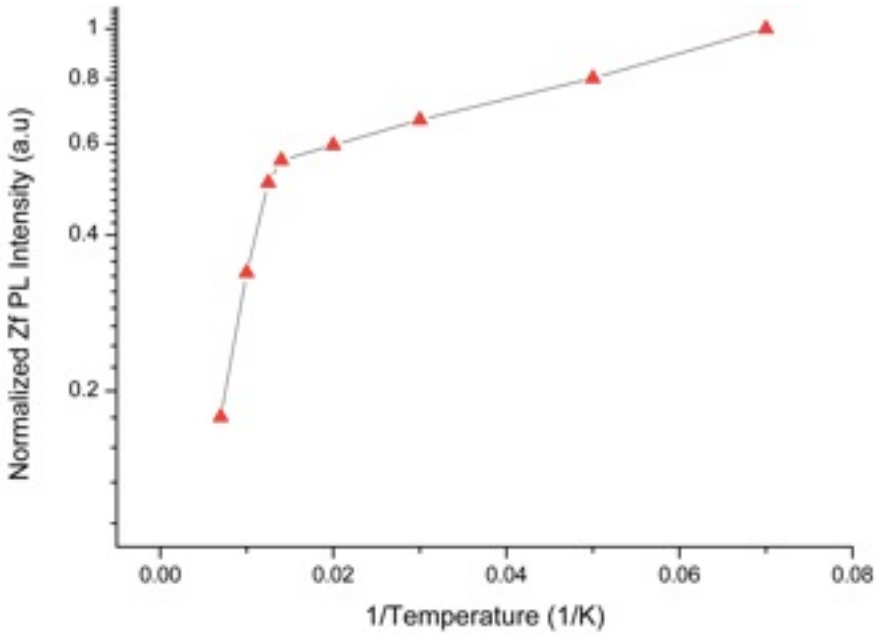

Figure 6.14 *- Arrhenius plot of normalized free exciton intensity (Z_f) vs inverse temperature.*

6.5.2 XEOL of γ-CuBr Thin Films

Using the experimental setup detailed previously (see Chapter 2), XEOL measurements of deposited CuBr thin films on Si substrates were carried out. Figure 6.15 below shows an acquired characteristic spectrum for a ~500 nm thick γ-CuBr deposited film on Si substrate. The characteristic Z_f peak excitonic peak can be clearly seen. The same measurement was taken for ~100 nm and ~300 nm CuBr thin films, however there was no observed deviation in peak position, and apart from a slight broadening of the FWHM (measured as 0.81 nm, 0.109 nm and 0.121 nm for 100, 300 and 500 nm thin films, respectively). This broadening can be attributed to the increased film thickness. Functionally, however, the CuBr thin film samples examined under XEOL were characteristically identical, with a well defined peak at ~416 nm at room temperature.

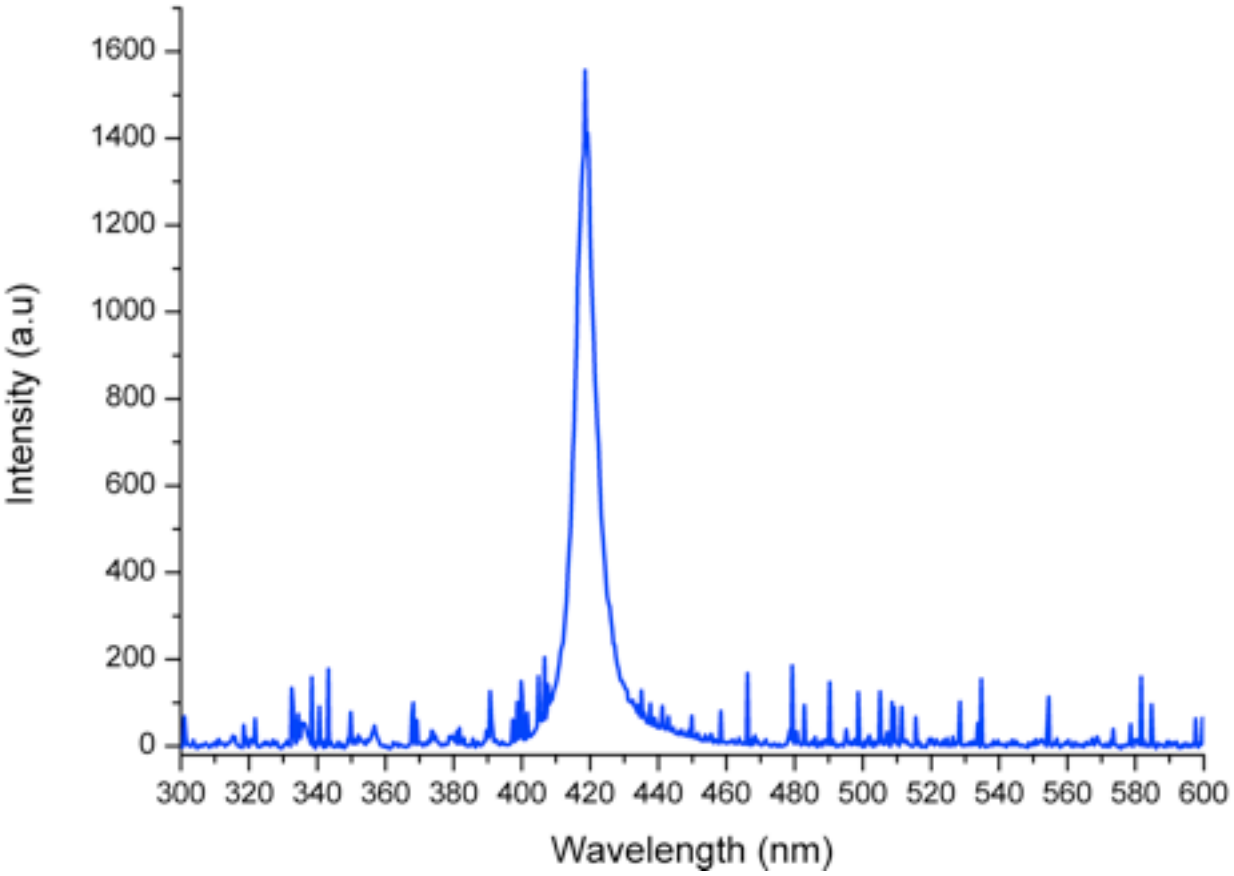

Figure 6.15 *- XEOL spectra for γ-CuBr ~500 nm thin film on Si substrate.*

6.6 Stability of γ-CuBr Thin Films

As mentioned previously, one of the main disadvantages to working with the CuHa material is their sensitivity to ambient atmosphere. The family reactivity for the Halides decreases as function of their position on the periodic table, i.e. Chlorine → Bromine → Iodine and so forth. Previously, it has been observed that vacuum evaporated γ-CuCl samples have a short lifespan when exposed to air - rapid formation of oxyhalide compounds (Cu(OH)Cl) is observed on these films when purposely left in air to degrade [12]. Thus for γ-CuCl samples, the storage of experimental samples in vacuum is standard practice as well as the aforementioned development of capping layers to protect samples for application purposes. The case for CuBr from a stability perspective is much more compelling, however. Vacuum deposited γ-CuBr on Si and glass substrates were experimentally found to have much longer optically active lifespans without the need for

application of a protective, insulating capping layer. In order to investigate the stability of the vacuum deposited γ-CuBr films, a ~500 nm CuBr on glass substrate sample was prepared and exposed to ambient atmosphere for a period of one year. The sample was stored in a dark laboratory desk drawer and was only removed from storage for measurements.

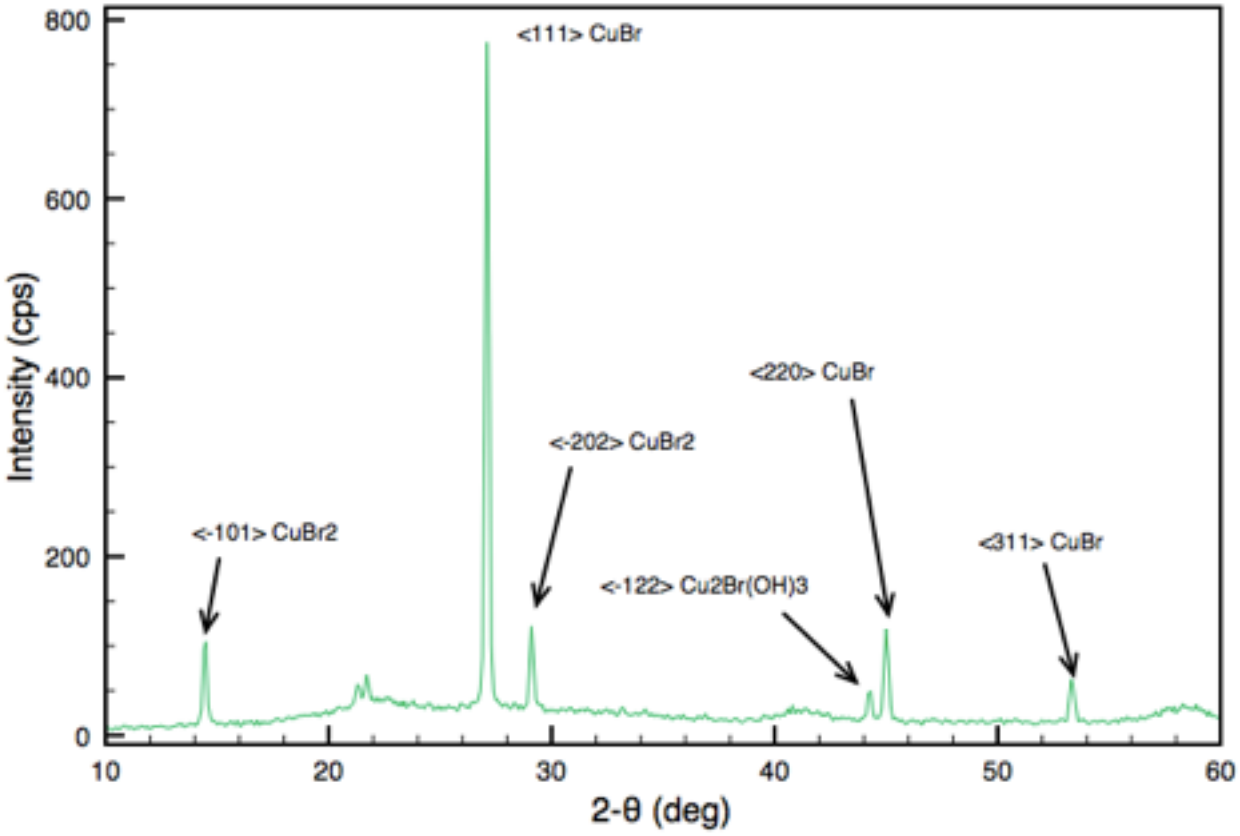

Figure 6.16 *- XRD scan of CuBr film (~500 nm) on glass substrate after exposure to ambient atmosphere for 9 months.*

Figure 6.16 shows the XRD scan for the sample after one year. Remarkably, the characteristic <111>, <220 and <311> γ-CuBr reflections are still present. For previous CuCl samples, significant degradation of the samples would take place after two days of exposure and a complete re-crystallization of the CuCl film would take place within three weeks, as evidenced by XRD [12]. However, for CuBr samples, this was not observed to have occurred. It is clear that the CuBr degradation occurs with the formation of other compounds such as $CuBr_2$ and $Cu_2Br(OH)_3$, which

can be evidenced in the XRD measurement, but the main CuBr reflections are still present. There is a small peak doublet at ~ 21.5° and ~ 21.9°, however this does not correspond to any known or expected CuBr based compound.

The UV-Vis absorbance measurements taken over a year can be seen in figure 6.17 below.

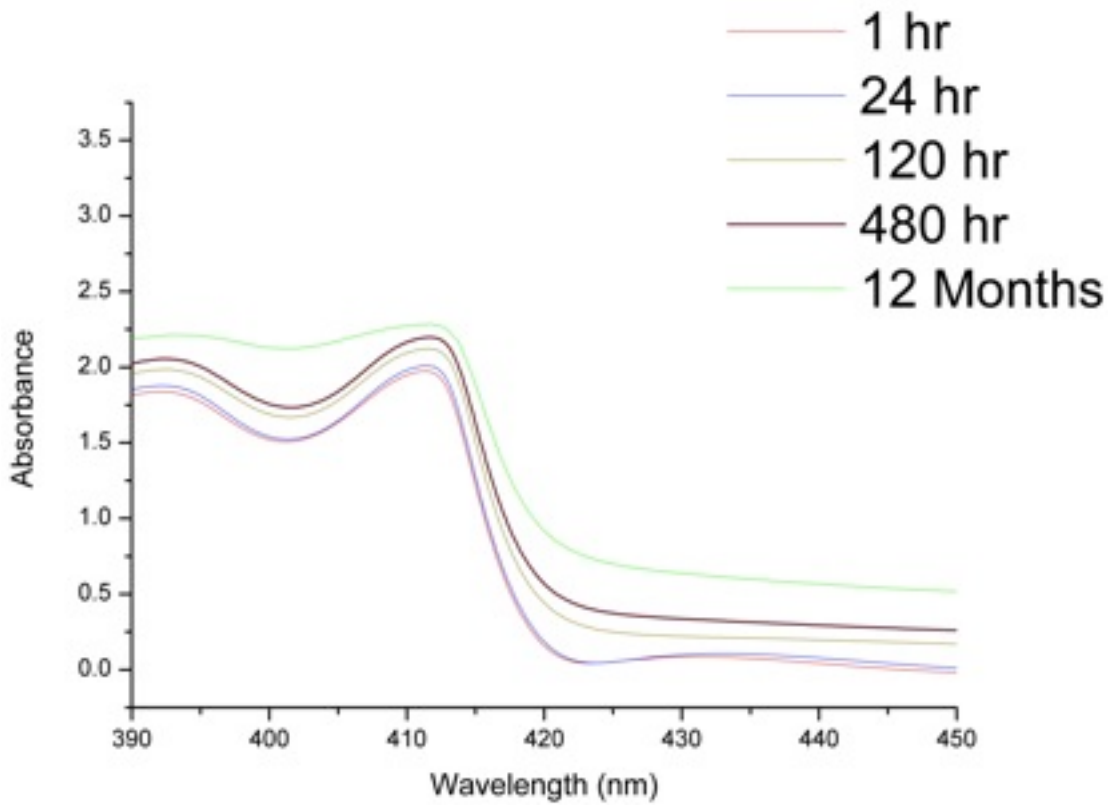

Figure 6.17 *- UV-Vis absorbance measurement for CuBr film over 1 year period.*

It can be seen that even after a year the deposited sample remains optically active, with the excitonic structure seen in CuBr UV-Vis measurements still present, albeit diminished relative to the as-deposited case. This is a considerable improvement relative to CuCl, wherein the optical quality was observed to rapidly degrade within 3 weeks when kept in similar experimental conditions [12].

As the film ages, the as deposited opalescent appearance begins to cloud though is still reasonably transparent. The absorbance is seen to increase over the year long period. There is an initial stable period immediately after deposition, before a gradual trend of increasing absorbance takes effect. This trend can be seen to slow as time progresses - this may be suggestive of a rate limiting reaction occurring.

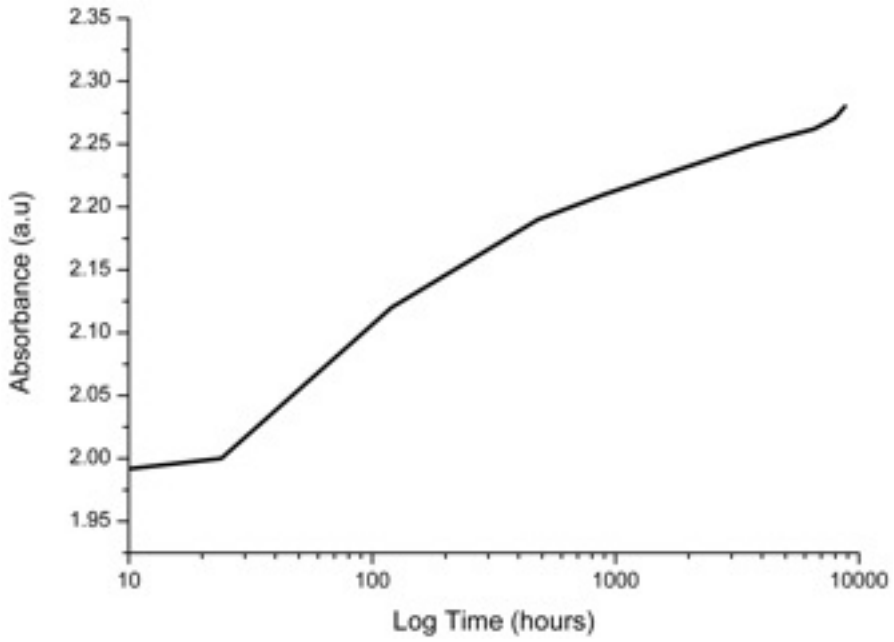

Figure 6.18 *- UV-Vis absorbance as a function of time (expressed logarithmically).*

6.6.1 Electrolytic Decomposition of γ-CuBr Film under AC/DC Applied Voltage

Towards development of a γ-CuBr TFELD, an understanding of the behavior of electrodes deposited on CuBr is necessary. It has previously been shown that CuCl films with Au contacts shows electrolytic decomposition, whereby a polar material (i.e, CuBr) is subjected to a steady state voltage which exceeds its decomposition threshold, which is ~0.7 V for CuBr [13, 14]. The high ion mobility of Cu within CuBr makes the electrochemical decomposition observable at room temperatures. The previous work showed that cathodic decomposition of Cu metal was observed when steady state DC voltages of 5 V were applied to CuCl films with similar Au planar contact

[12]. A similar experimental setup was used to investigate the electrolytic decomposition of CuBr thin films with Au electrodes, and is illustrated below.

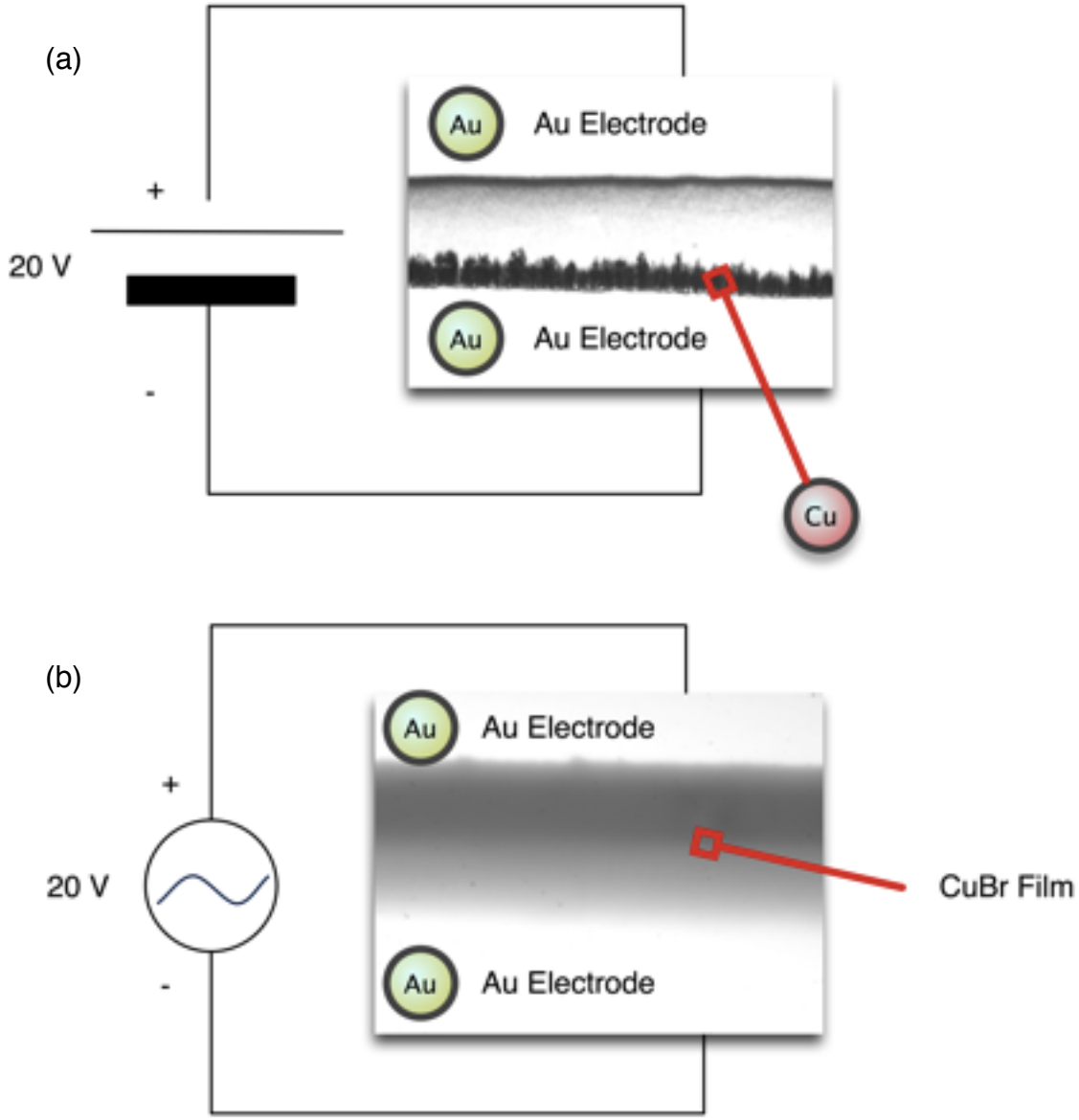

Figure 6.19 *- Setup for investigation of electrolytic decomposition of CuBr, showing (a) Setup using DC bias @ 20 V for 2 hours, (b) setup using AC bias for 2 hours.*

A thin film of ~500nm CuBr is deposited on glass and planar Au contacts are subsequently evaporated into place using a shadow mask technique. The inter electrode spacing was 0.25 mm.

The image of the electrode area seen below in figure 6.20 is a CCD microscope image of the film after being subjected to an AC 20 V peak to peak stimulation for 2 hours under light vacuum (~ 10^{-1} mbar) conditions. As can be seen there is no sign of any dendritic formation, a clear sign of electrolytic decomposition, having taken place.

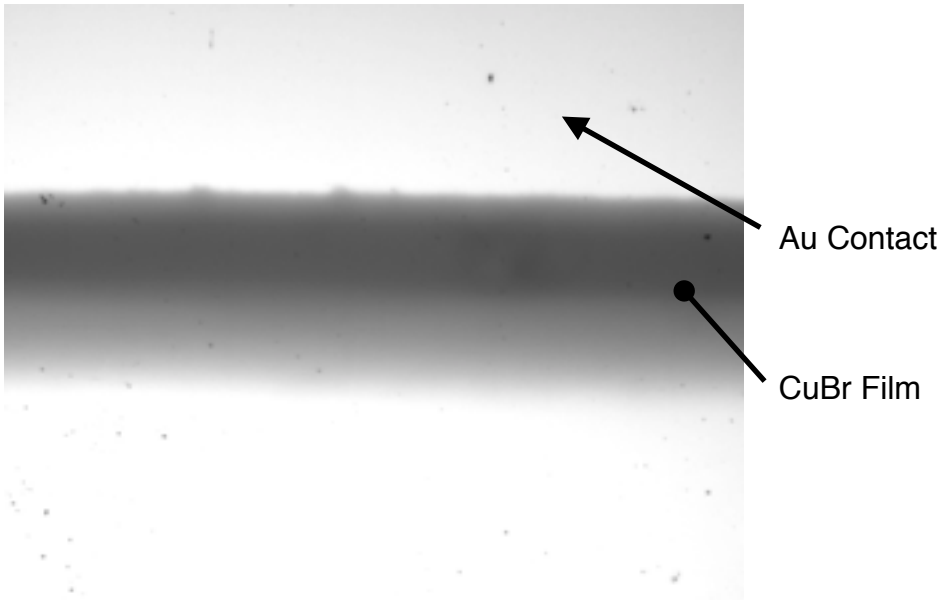

Figure 6.20 *- Optical CCD Image of CuBr film after being subjected to 20 v AC bias for 2 hours.*

The captured images shown in figure 6.21, however, are taken of an identical sample under the same experimental conditions but exposed to a 20 V DC bias. There is a notable formation of dendrites emerging from the cathode into the CuBr region.

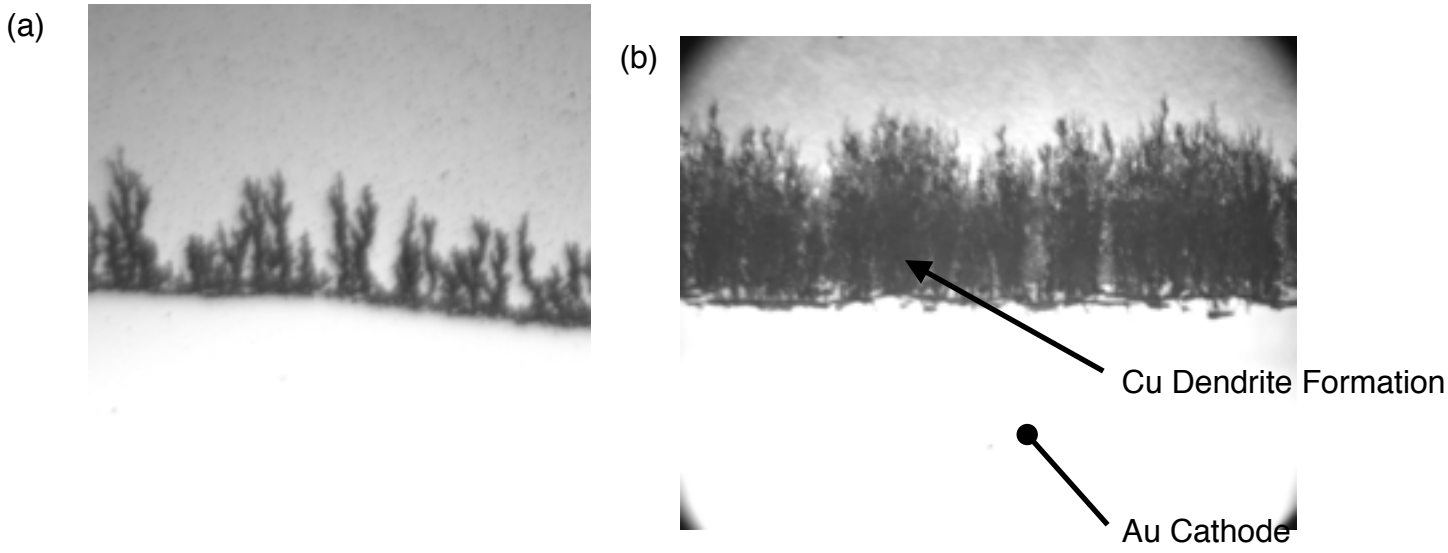

Figure 6.21 *- (a) Dendrite formation due to electrolytic decomposition of CuBr film (1 hour @ 20 V DC) magnified, (b) 2 hour @ 20 V DC.*

From the experiments with the 25 mm inter-electrode distance, a growth rate of approximately 0.7 mm per hour was observed, with a complete bridging of the dendrites to the opposite electrode after approximately ~4 hours. EDX measurements on the generated dendrites were taken which confirm the presence of elemental copper (figure 6.22).

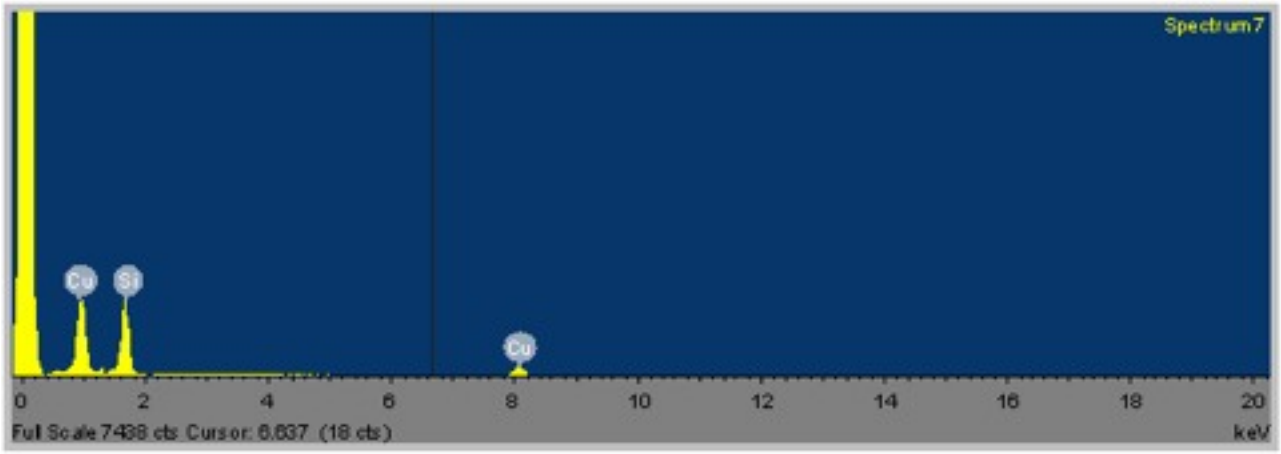

Figure 6.22 *- EDX spectra of the cathodic decomposition showing the presence of elemental Cu.*

Additionally, XRD scans were taken of a CuBr film with Au planar contacts before and after the applied DC voltage experiment, however there was no sign of Cu within these scans. It is possible that the overall concentration of elemental Cu was too low for detection.

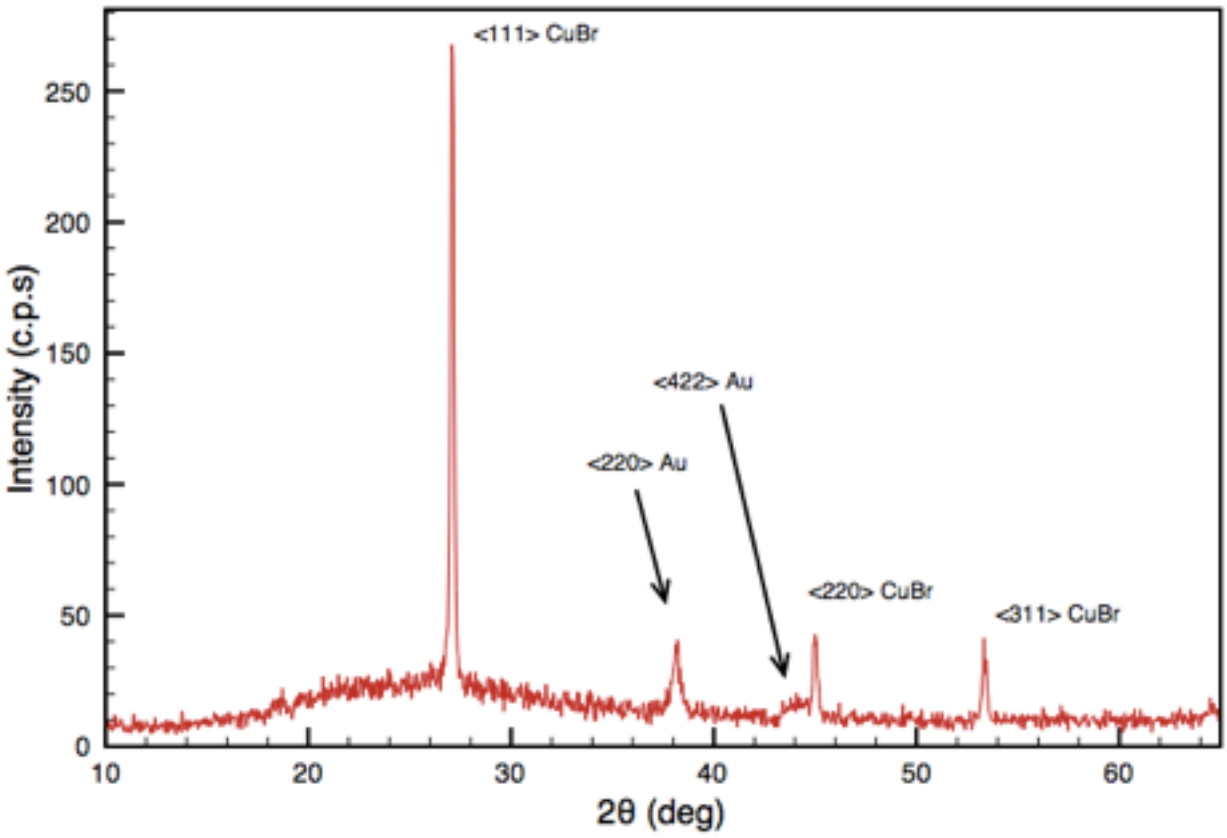

Figure 6.23 *- XRD 2θ scan of ~500 nm CuBr on glass substrate with Au planar contacts, post exposure to 20 V DC bias for 2 hours.*

6.7 Towards a γ-CuBr based EL Device

Using vacuum evaporation to deposit films of γ -CuBr, work has been carried out to develop a prototype TFELD based on the structure in figure 6.24 (a) with a CuBr active layer, based on the principles outlined in chapter 2. ITO coated glass substrates were obtained from Sigma Aldrich (15–25 Ω/sq surface resistivity). The ITO substrates had ~20 nm of SiO_2 deposited prior to the growth of ~100 nm γ-CuBr active layer. The SiO_2 was deposited by the plasma-enhanced chemical vapour deposition (PECVD) technique using hexamethyldisiloxane (HMDSO) and O_2 in a capacitively

coupled reactor connected to a 13.56 MHz RF generator. The SiO_2 thickness was determined via ellipsometry measurements and model fitting on a JA Woollam XLS-100 ellipsometer. Further details on the growth and characterization of the deposited SiO_2 via PECVD have been reported previously [15].

For the prototype devices, it was decided to keep the γ-CuBr layer thin so as to reduce the impact of the thickness on conduction of charge into the active layer. For the circular contacts on the ELD samples, gold wire from Sigma Aldrich (99.999%) was evaporated using a simple shadow mask. The SiO_2 layer also helps in insulating the ITO from any potential short circuit after Au contacts are deposited via pinholes in the CuBr layer. Contacts to the Au and ITO contacts were made using a gallium–indium eutectic melt supplied from Sigma Aldrich (99.99%).

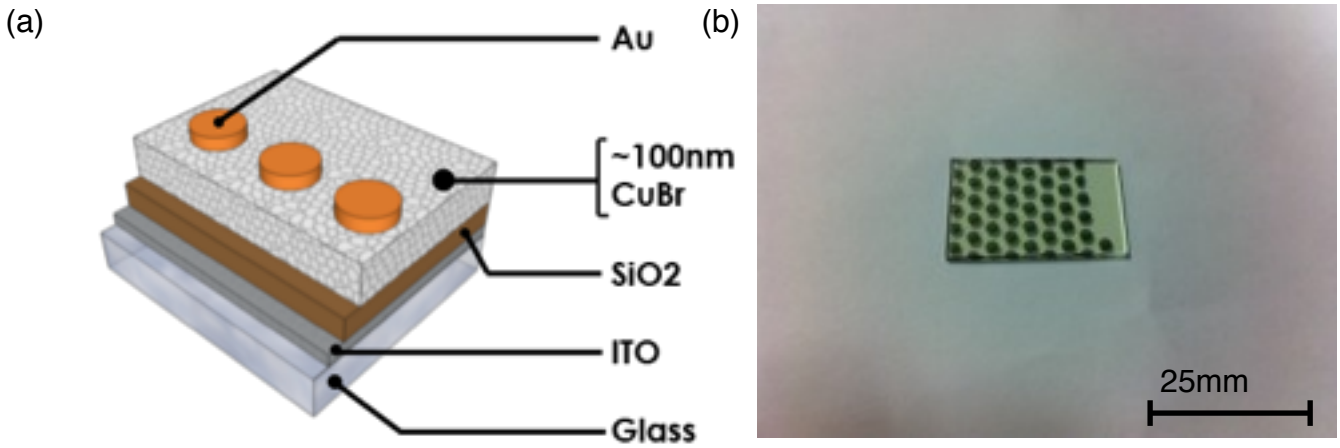

Figure 6.24 *- (a) Illustration detailing layers used in prototype CuBr ELD stack structure, (b) image of fabricated CuBr ELDs.*

For our EL measurements, a variable AC supply generator with an operating frequency of 50 Hz was used. At voltages of ~4–5 V up to ~16–17 V (peak to peak) we could observe blue light emission. The light was generated from around the Au contact periphery. The emission intensity

does tend to dim and flicker but otherwise stays constant for periods up to approximately 10 seconds.

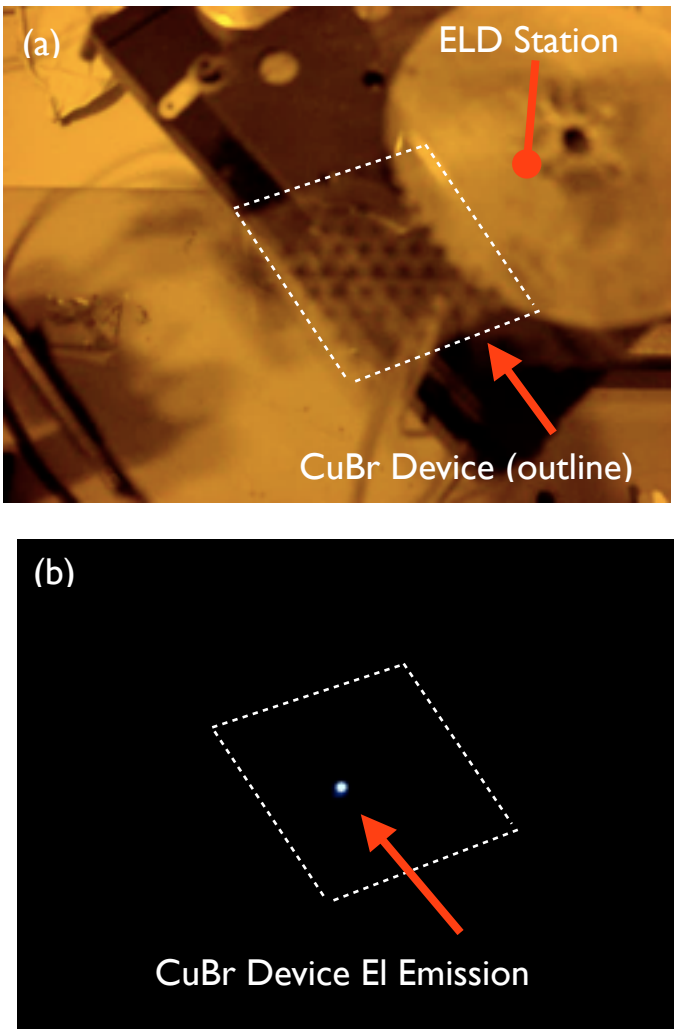

Figure 6.25 *- (a) Image of ELD experiment station with mounted CuBr device, (b) with lights off, image capture of observed EL from the device.*

Figure 6.26 below is a typical EL spectrum acquired for these ELDs. A number of peaks are clearly discernible with the ~418nm potentially attributable to the Z_f free exciton emission energy for CuBr. However, the other visible peaks cannot be attributed to known CuBr emission and owing to the similarity of the peak structure for the ~418 nm emission, it is likely that this emission does not represent the EL emission for CuBr. For a possible explanation of these peaks, we refer to emission studies on copper doped alkali halides and glasses. In these systems, varying emission peaks are

observed at similar energies to our own observations, namely at ~320nm, ~403nm, ~410nm, ~450nm and ~590nm. These emissions are thought to correspond to the 3d10 → 3d94s transitions of the Cu^+ ions and have been previously reported in the literature for luminescence studies of Alkaline Halide materials containing monovalent Cu^+ impurities [16–18].

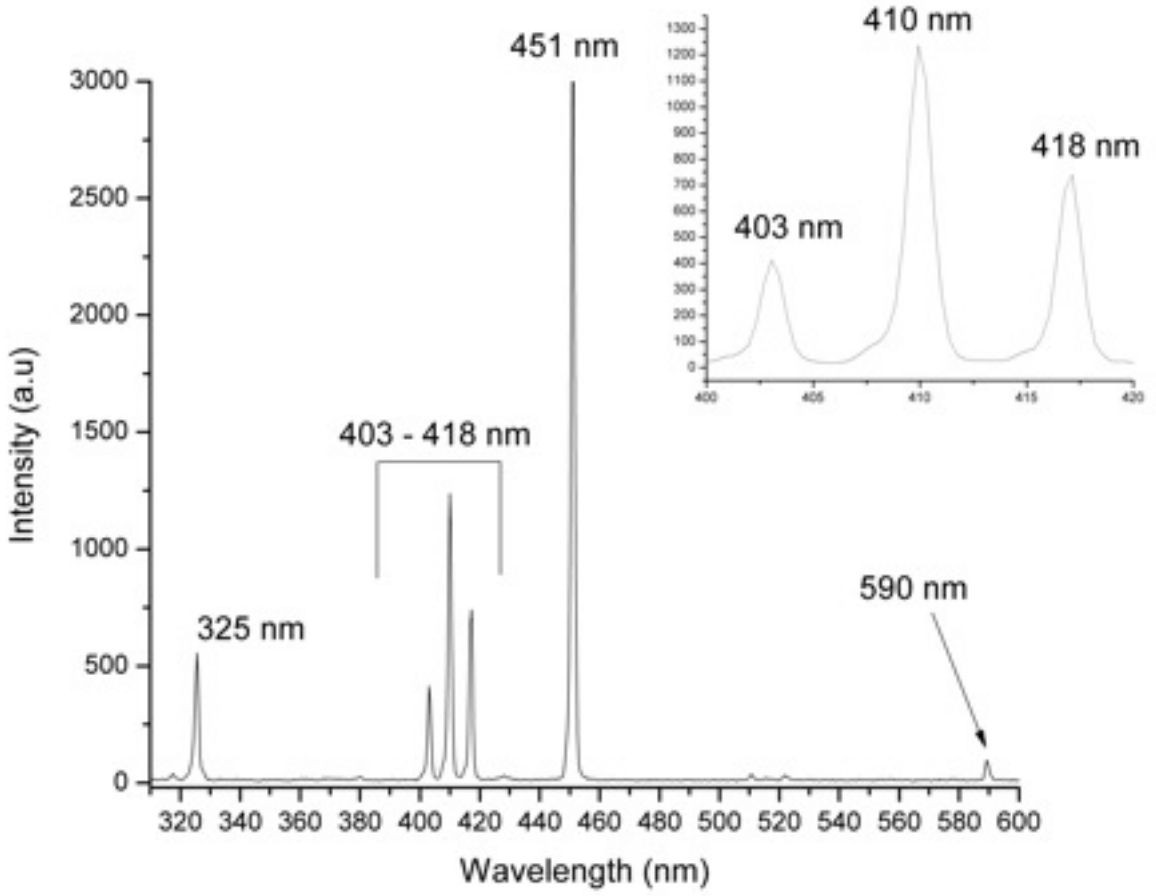

Figure 6.26 *- EL spectrum for ~100 nm γ-CuBr ACTFELD, inset shows magnified 400-420 nm region.*

6.8 Conclusions

Building on the previous chapter and the study of CuCl therein, research was begun into the deposition of CuBr via PVD processes. The driving motivation was to investigate the possibility of utilizing CuBr as the active layer in an ACTFELD structure. Stoichometrically uniform deposition of γ-CuBr films has been carried out using vacuum evaporation onto Silicon, glass and ITO coated glass substrates. Structural characterization involving XRD observed preferential growth along the <111> crystallographic axis, in addition to smaller reflections from the <220> and <311> orientations. Using AFM, the threefold <111> symmetry of vacuum deposited thin films on Si could be seen and a consistent surface roughness was measured across various sample thicknesses and substrates. From the XRD measurements, the texture coefficients were calculated for deposited CuBr on the different substrates, with the highest preferential growth observed on Si <100> substrates with the <111> CuBr reflection.

Optical investigation of the CuBr thin films reveals a characteristic Z_f emission at ~416 nm at room temperature. Low temperature PL down to 12.5 K reveal the Z_f exciton emission and the I_1 impurity bound exciton emission, found at ~ 418 nm (~2.96 eV) and ~ 420nm (2.95 eV) respectively, in good agreement with prior spectroscopic measurements of CuBr at low temperatures. A temperature dependent shift of the Z_f emission was observed from 12.5 K to room temperature. This effect is related to electron-phonon renormalization of the CuBr material as temperature increases.

Additionally, the stability of CuBr films was investigated by exposing a ~500 nm thick sample, deposited on glass, to ambient atmosphere over the period of a year. UV-Vis measurements show an increase in the absorbance of the film and XRD shows the formation of some oxyhalide compounds. Remarkably however, the film was still optically active and the $Z_{1,2}$ and Z_3 excitons can still be clearly seen in the UV-Vis measurements a year after deposition, without the aid of any

preservation techniques (e.g. capping layers) which is a substantial improvement over a similar study using CuCl.

In order to investigate CuBr for potential application as an active layer in an ELD, CuBr films using Au contacts were fabricated and subjected to steady 20 V AC and DC bias over different times. The AC biased films showed no evidence of electrolytic decomposition. Films subjected to DC bias, however, exhibited dendritic growth - clear evidence of cathodic decomposition.

Using the vacuum evaporation PVD technique we have successfully fabricated and tested a ACTFELD using CuBr as an active layer. The characteristic Z_f CuBr excitonic peak as well as possible Cu^+ emissions were observed. It is suggested, based of previous studies involving Alkaline Halide materials containing Cu^+ impurities, that these additional peaks correspond to the 3d10 → 3d94s transitions of the Cu^+ ions.

6.9 References

[1] Silicon Wafer supplier: http://www.universitywafer.com/

[2] Evaporation crucible supplier, Testbourne Ltd: http://www.testbourne.com/instruments/evaporation-sources/w-ta-mo-boat-sources/

[3] H. Borchert, E. V. Schevchenko, A. Robert, Langmuir, Volume 21, 2005, pages 1931-1936.

[4] M. Cardona, Physical Review, Volume 129, 1963, pages 69-78.

[5] S.P. Harimkar, N.B. Dahotre, Journal of Applied Physics, Volume 100, 2006, pages 24901.

[6] T. Goto, T. Takahashi, M. Ueta, Journal of the Physical Society of Japan, Volume 24, 1968, page 314.

[7] M. Ueta, 'Excitonic Processes in Solids', Springer, 1986.

[8] H. Ichida , M Nakayama, H Nishimura, Journal of Luminescence, Volume 87, 2000, page 235.

[9] S. Kondo, K. Mikami, T. Saito, Optical Materials, Volume 30, 2008, page 1473.

[10] N. Garro, A. Cantarero, M. Cardona, Solid State Communications, Volume 98, 1996, pages 27-30.

[11] J. Serrano, Physical Review B, Volume 65, 2002, page 125110.

[12] L. O'Reilly, 'Growth and characterisation of wide-bandgap γ-CuCl on near lattice-matched Si', PhD thesis, 2006, Dublin City University.

[13] M. Bendahan, C. Jacolin, P. Lauque, J –L Seguin, P. Knauth, Journal of Physical Chemistry B, Volume 105, 2001, page 8327.

[14] R. C. Weast, 'Handbook of Chemistry and Physics', CRC Press, 1987.

[15] R. Prasad, S. Daniels, D. Cameron, B. McNamara, E. Tully, R. Kennedy, 2005, Surface & Coatings Technology, Volume 200, 2005, pages 1031-1035.

[16] O. T. Antonyak, V. N. Vishnevskii, N.S. Pidzyrailo, M. V. Tokarivskii, Russian Physics Journal, Volume 17, 1974, pages 1158–1161.

[17] W. Wanmaker, H. Spier, Journal of The Electrochemical Society, Volume 109, 1962.[17] B. Moine, C. Pedrini, Journal de Physique IV France, Volume 1, 1991.

Chapter 7 - CuBr/KBr Microdots

7.1 Introduction

The potential improvement in excitonic PL that can be gained from novel approaches to film preparation involving KBr and existing CuBr deposition techniques is promising. Using a novel approach involving a specifically machined shadow mask, the vacuum deposition of KBr spots onto similarly deposited γ-CuBr epitaxial layer on a Si substrate has been investigated as part of research into potential new growth mechanisms for γ-CuBr, with the aim of emulating the vapor-liquid-solid (VLS) growth mode used for the formation of Si 'whiskers' or nanowires [1]. Conventional thin films of γ-CuBr have been deposited, as detailed in the previous chapter, and post-deposition annealing of the samples in conjunction with a small CuBr flux from a target source leads to the formation of intermixed CuBr/KBr microdots. The fabrication process for producing these microdots is detailed in this chapter and the structural and optical properties are characterized. A potential growth method is proposed based on the well established VLS growth mode.

7.2 General Fabrication

Si substrates are cleaned and prepared as per the process discussed previously in chapter 6. Onto these substrates, thin films of γ-CuBr of thickness of 150, 300 and 600 nm were thermally evaporated using the vacuum evaporator system. Experimental conditions used for deposition were otherwise the same as those used for the thin film work previously (see Chapter 6).

Subsequent to the deposition of the γ-CuBr layer, the evaporator was reopened and a specifically machined shadow mask was placed over the film. These masks were made from stainless steel and using a proprietary laser percussion drilling technique, micron sized holes were drilled in an array like structure. The minimum obtainable hole size was ~3 um in diameter. The machining was carried out by BlueAcre

Technology Ltd [2]. Figure 7.1 shows SEM imagery of one of the shadow masks with ~ 10 um diameter size holes clearly visible.

(a)

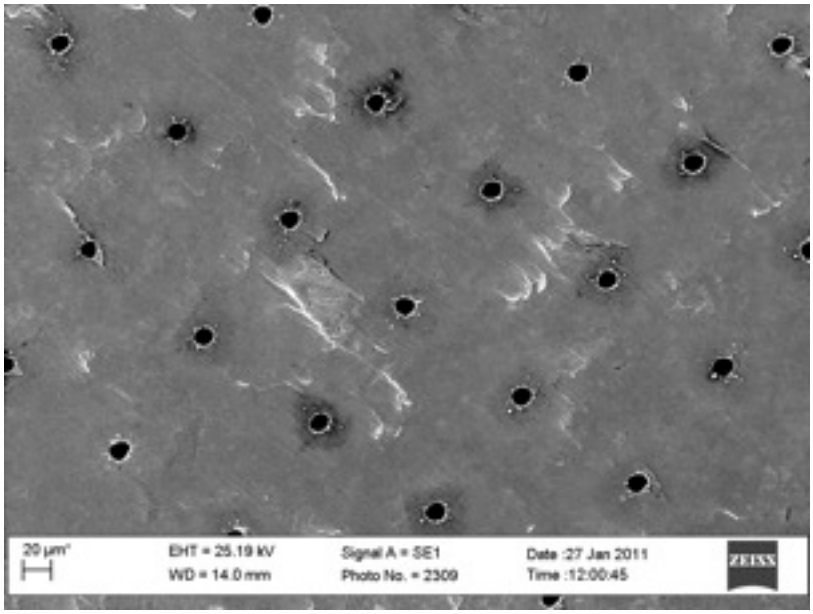

(b)

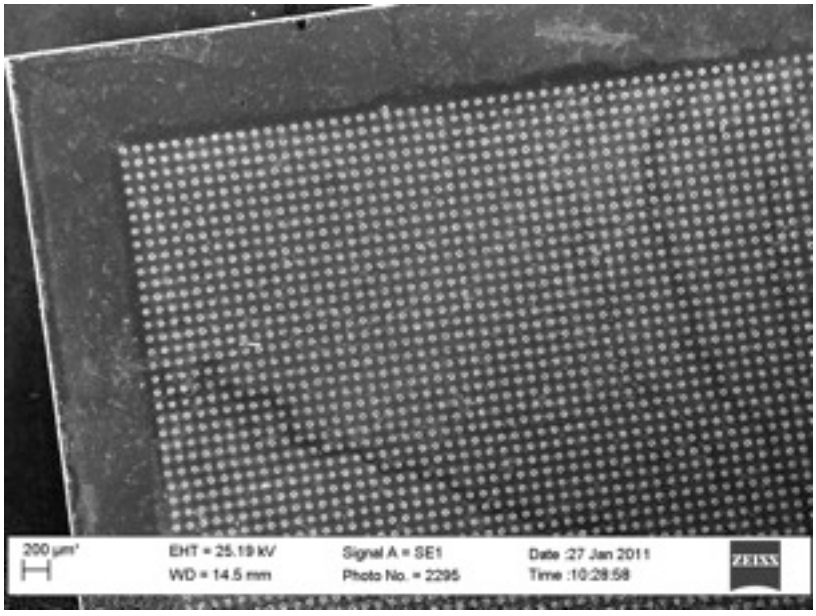

Figure 7.1 *- SEM images of (a) ~ 10 um feature size laser drilled holes on stainless steel foil, (b) wide field view of mask array.*

Following the placement of the mask, a second evaporation was carried out with KBr. Similar to the use of KCl salt previously for LPE growth, the KBr was baked out prior to use for 8 hours. Thickness was not determined using the thickness monitor, and instead the amount of KBr used was

weighed out prior to deposition (for all KBr evaporations, a constant amount, 0.5 g was used). Evaporation proceeded until the contents of the tungsten evaporation boat was empty. Post evaporation measurements using AFM showed that the average height of the KBr spots was approximately 30 nm. Figure 7.2 below procedurally illustrates the fabrication process.

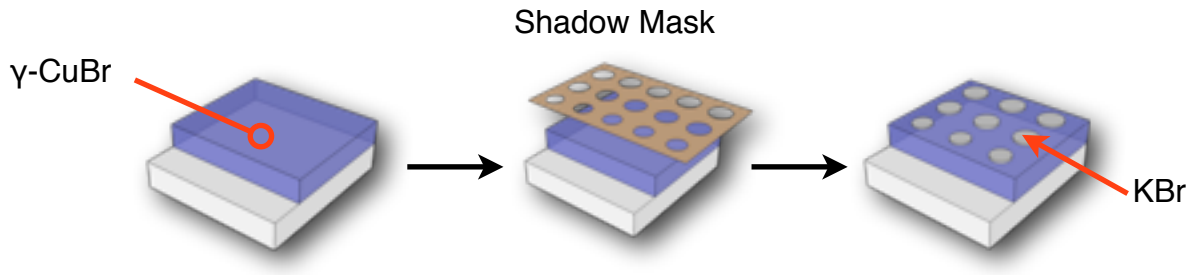

Figure 7.2 *- Stepwise fabrication procedure for deposition of KBr spots onto γ-CuBr/Si substrate using shadow mask.*

SEM images of the deposited KBr spots on the CuBr film can be seen in figure 7.3. The crystalline grains of the deposited KBr are particularly evident.

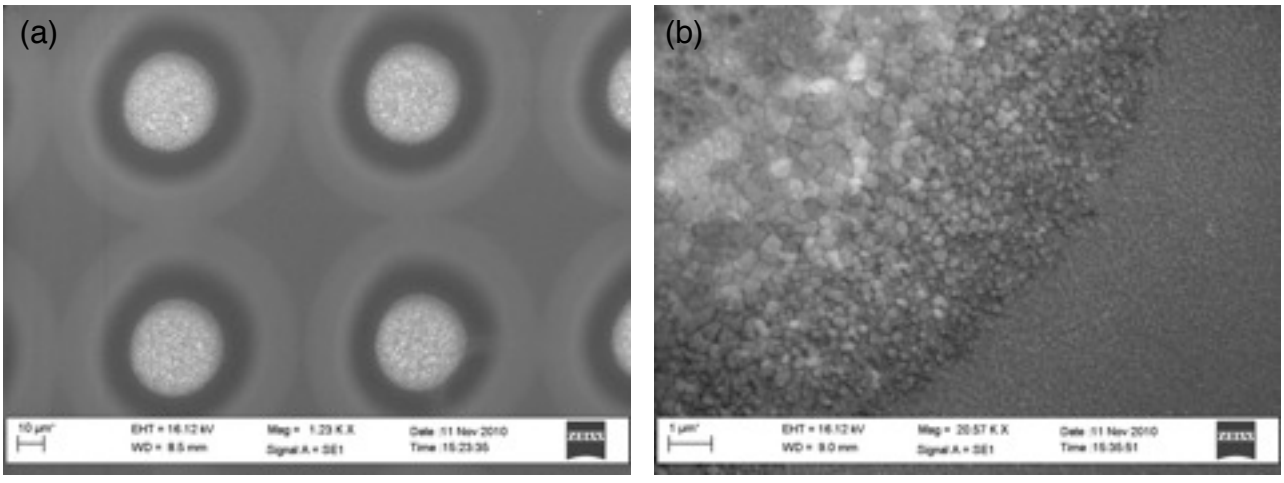

Figure 7.3 *- (a) SEM image of the KBr spot array and (b) magnified region showing detail of the KBr crystallites on top of the underlying γ-CuBr film.*

The notable contrast between the KBr spot region and the underlying CuBr film is a result of sample charging. This charging effect is caused by the buildup of excess electrons on the surface of the sample - with a conductive sample, the majority of the electrons pass into the sample and then out through the ground of the SEM sample holder. Vacuum evaporated γ-CuBr however is a poor conductor for this process, leading to a general difficulty in using SEM to topologically inspect CuBr thin films prepared with this PVD process. The KBr spots are in stark contrast to the underlying CuBr film, however, and can be clearly imaged. The apparent 'aura' around the spot is purely an artifact of the charging discrepancy between the CuBr film underneath and the KBr spot on top (see figure 7.4 below).

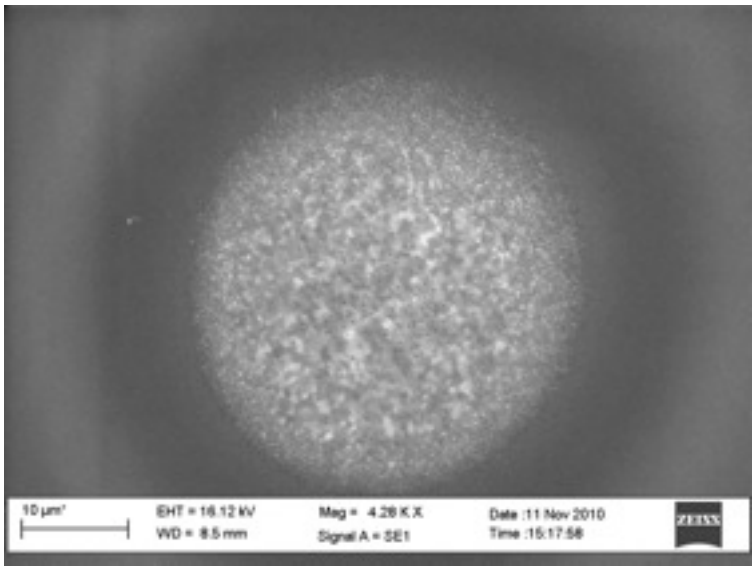

Figure 7.4 *- SEM image of the KBr spot, showing the effect of the electron 'charging' effect on the sample.*

7.2.1 Formation of Intermixed Microdot

Subsequent to the deposition of the KBr using the shadow mask, the sample is then subjected to a thermal anneal at 220° C for 30 minutes. In addition, the sample is situated above a small quartz glass crucible containing γ-CuBr (Sigma Aldrich, 99.999% purity) - this experimental setup can be seen in figure 7.5 below. The setup is within a tube furnace and is carried out under vacuum

conditions (10^{-5} mbar). The CuBr here is intended to act as a flux and is critical to the formation of the microdot (section 7.3 details the growth mechanism behind the formation of the microdots).

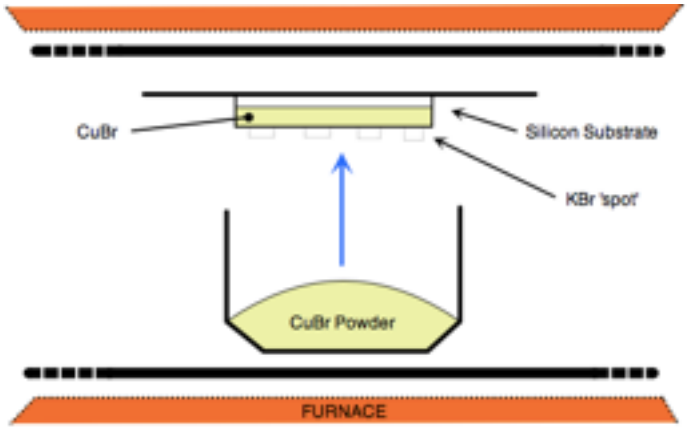

Figure 7.5 *- Experimental setup for the annealing & CuBr flux within a tube furnace.*

Investigation of the samples after this annealing stage shows that the KBr salt has reacted with the underlying CuBr layer and formed a eutectic solution, with the addition of the CuBr flux, which results in the formation of a distinct microdot feature with a clearance of bare Si around the feature after cooling to room temperature. The SEM image in figure 7.6 illustrates one such microdot and figure 7.7 shows an array of microdots.

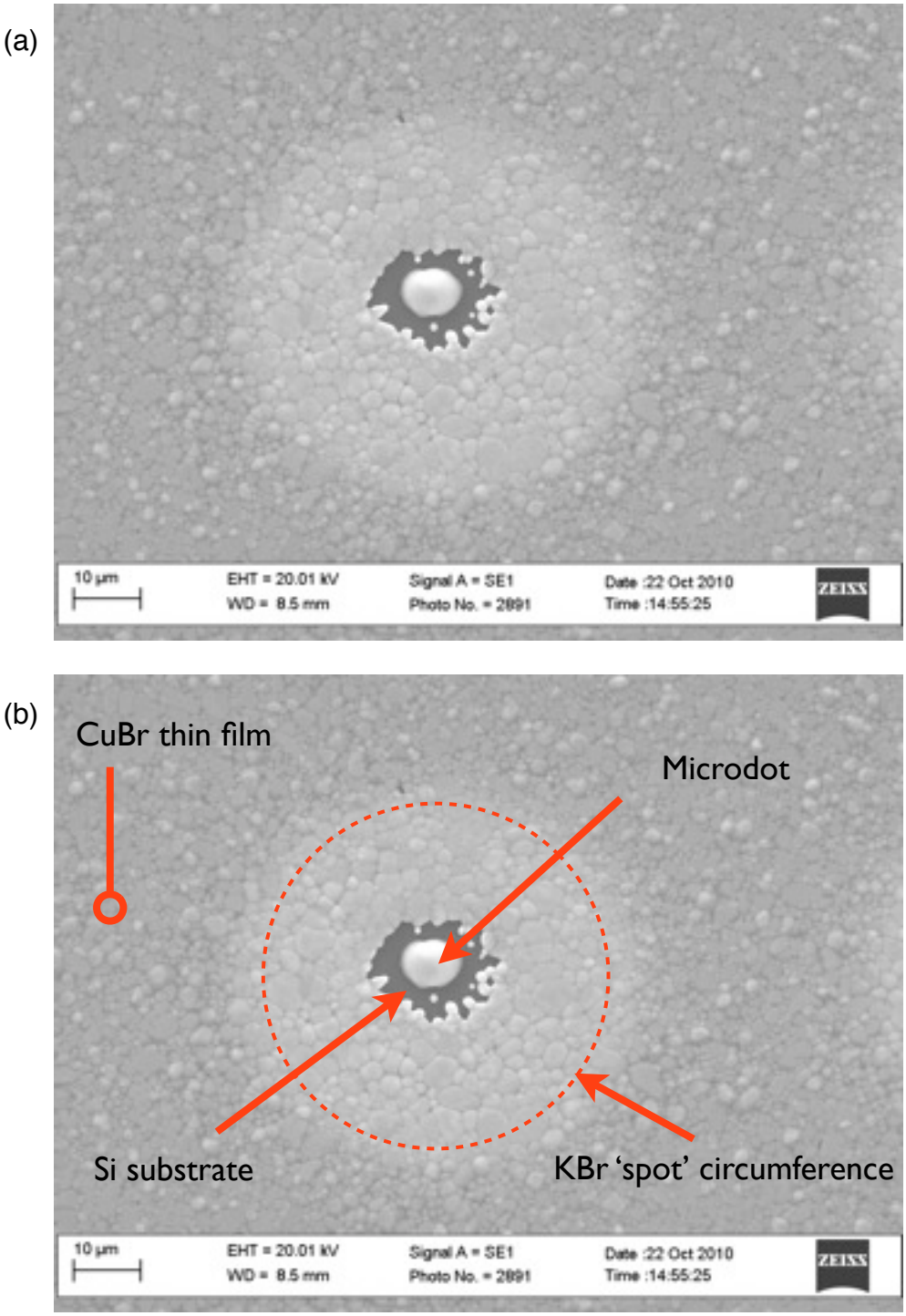

Figure 7.6 *- (a) Microdot feature resulting from eutectic interaction of CuBr layer with the KBr deposited via vacuum evaporation using a shadow mask. Image is of microdot formed on a ~300 nm CuBr under-layer, (b) annotated image.*

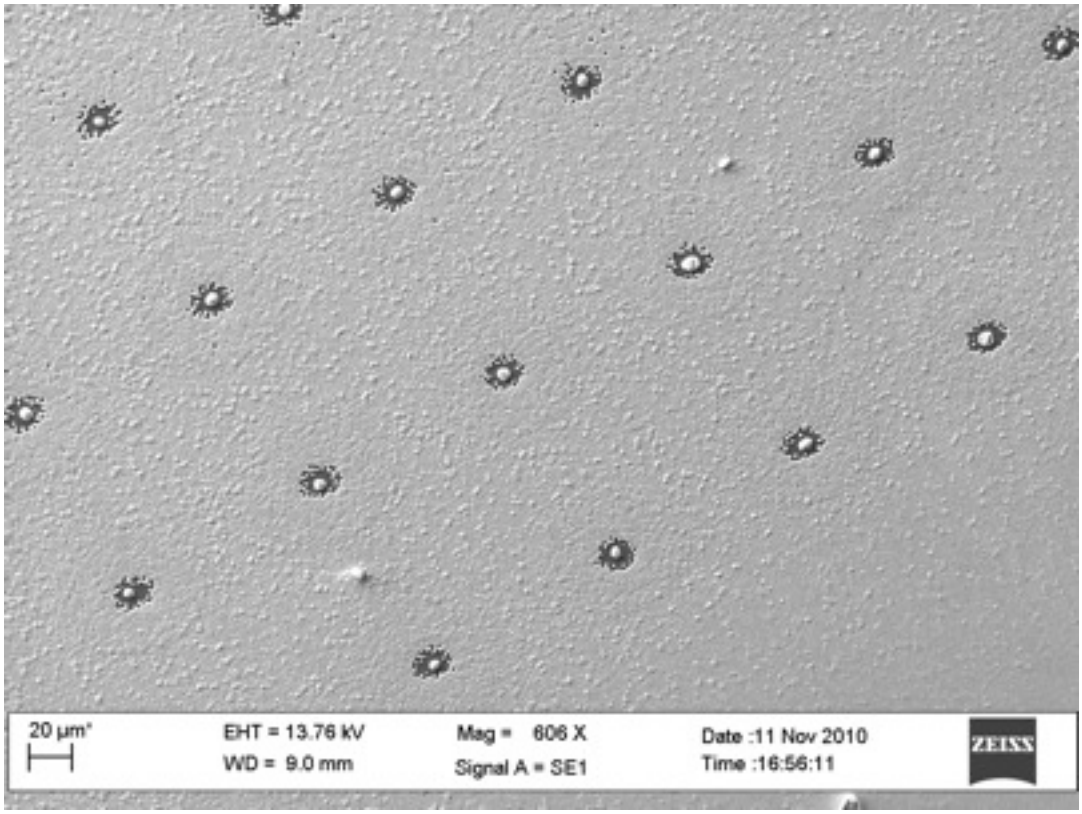

Figure 7.7 *- Array of CuBr/KBr microdots, arising from the shadow masking process. Image is of microdot array formed on a ~300 nm CuBr underlayer.*

7.3 Structural Characterization of CuBr/KBr Microdot Arrays

The resulting microdot array is reasonably well ordered consisting of notable demarcation between the underlying CuBr and the area encompassed by the deposited KBr, followed by a central cavity where the bare Si substrate can be seen. Within this cavity can be found the formed microdot, usually isolated but occasionally in contact with the surrounding film and sometimes accompanied by a number of secondary, smaller microdots. For samples prepared with underlying film thicknesses of ~150 nm and ~300 nm, the central features as shown previously in figure 7.6 were commonly observed. Samples prepared with the thicker ~600 nm CuBr underlayer however usually displayed much smaller clearance regions around the microdot and an increased chance of finding a join between the central dot feature and the surrounding film. In addition, the microdot size was usually much smaller than those observed with the 150 and 300 nm samples. It is likely that this is a

result of the thicker CuBr underlayer reducing the clearance area around the microdot which in turn can also result in linking up of the microdot to the underlayer sidewalls.

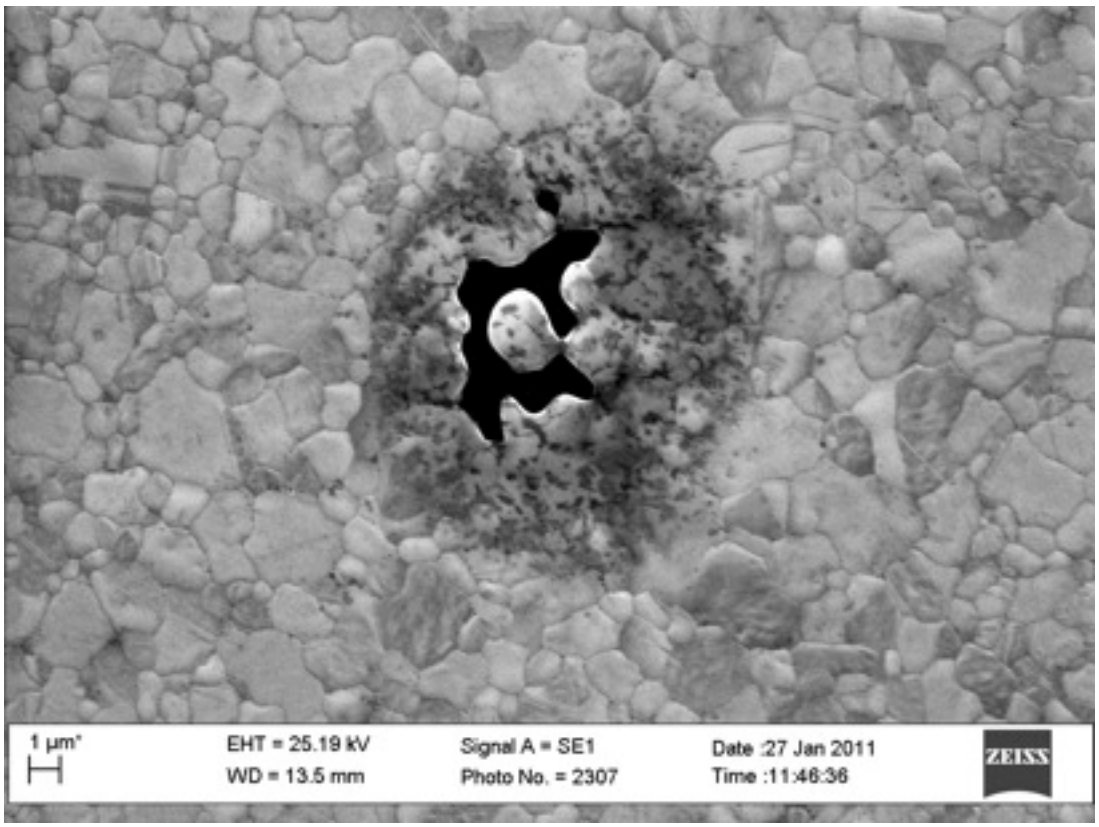

Figure 7.8 *- SEM image of a microdot prepared on a ~600 nm γ-CuBr underlayer. The micodot is approximately ~1.2 µm in size, but is linked to the surrounding thin film.*

Most remarkable about the ~150 nm and ~300 nm samples produced using the aforementioned fabrication method is the height of the microdot with respect to the surrounding γ-CuBr thin film. Figure 7.9 below shows an AFM scan of the microdot region on a ~150 nm thick γ-CuBr sample. From the scan it can be seen that the formation of the microdot has a substantial vertical growth phase. Additional AFM images are presented in Appendix B. A number of different microdot regions were investigated across the sample via AFM in order to ascertain the median height of the grown microdots. For 150 nm and 300 nm thick samples, the height was found to vary substantially from site to site that were inspected. Microdot heights with ranges from ~730 nm to ~3.7 µm were

observed on both samples, however the microdot sizes for the 600 nm sample were found to be less then the film thickness itself, i.e. less then 600 nm and did not exhibit the same vertical growth.

(a)

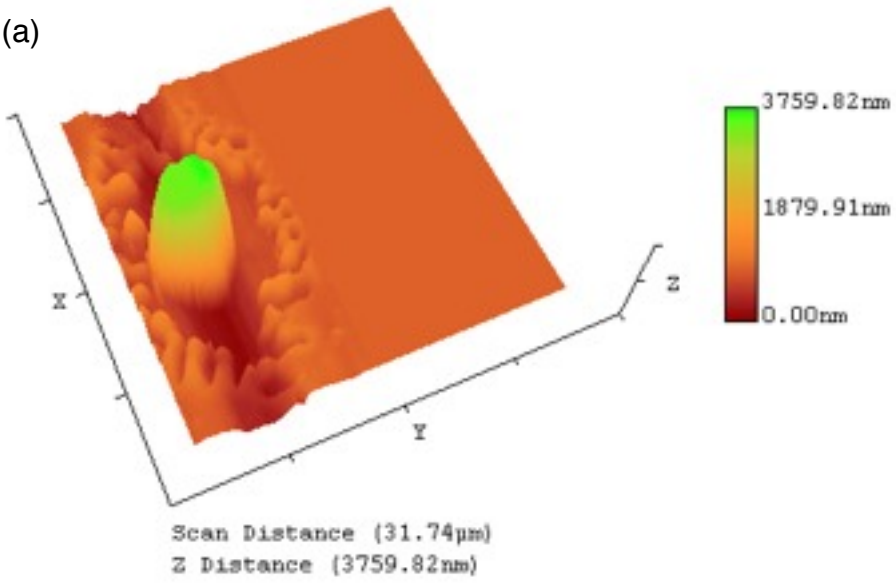

(b)

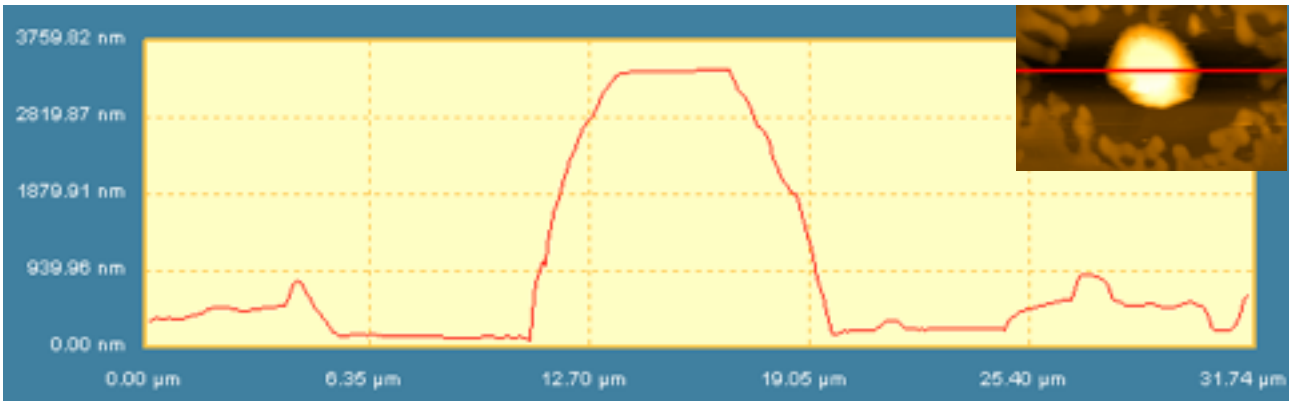

Figure 7.9 *- (a) AFM 3-d image of a microdot region on a ~300 nm sample, (b) annotated side profile of same region showing height variation relative to underlying CuBr film (inset image shows top down view, with red line denoting the profile plane).*

There is a general difficulty in using AFM to gather accurate imagery of the microdot side topology due to the large vertical incline that the cantilever must traverse, however it is clear that substantial vertical growth in excess of the initial CuBr deposition thickness has occurred. Figure 7.10 (a) also

shows a number of smaller microdots that have similar, unexpectedly high growth aspect ratios. A SEM image analogous to the AFM image can be seen below in figure 7.11.

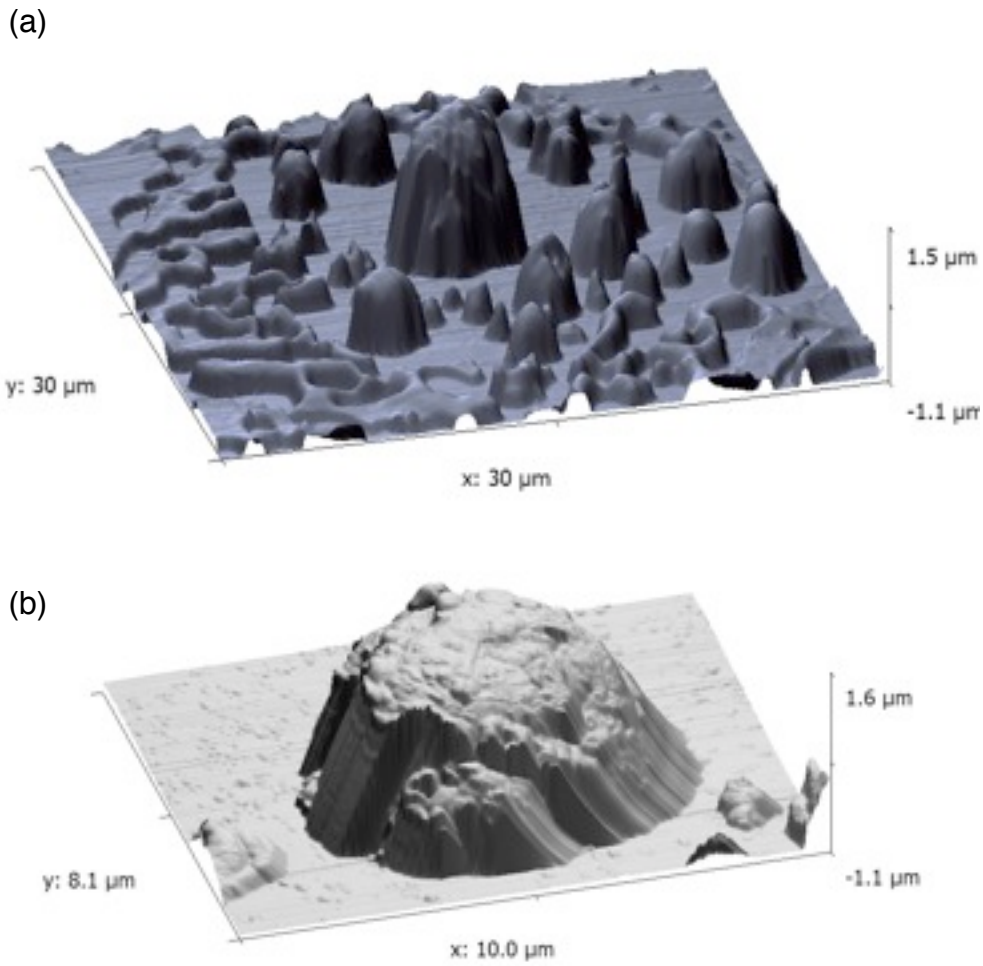

Figure 7.10 *- (a) Annotated AFM scan of a microdot region on a ~150 nm thick sample. Central microdot has a vertical dimension of approximately ~1.5 µm, (b) detailed scan of the microdot.*

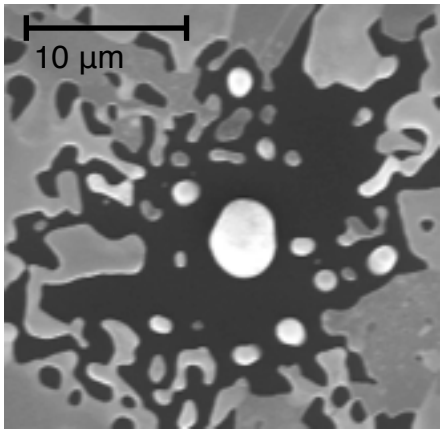

Figure 7.11 *- SEM image of microdot region on ~150 nm thick γ-CuBr sample where the main microdot can be seen in addition to smaller secondary dots.*

7.4 Growth Mechanics

The approach taken in order to form these microdots has been fundamentally driven by the question of whether it is possible to emulate VLS growth with CuHa materials, taking the lessons learned in the earlier work on CuCl LPE and the eutectic reaction of the CuCl and KCl salt used therein. Owing to the stability improvements found in the work on CuBr (relative to the previously used CuCl), it was decided to approach this question using CuBr and the corresponding eutectic forming salt, KBr. The phase diagram for this system is presented in figure 7.12 and shares many similarities with the CuCl/KCl phase diagram detailed previously in chapter 3, notably forming a eutectic solution at temperatures > ~180 °C.

Since the 1960's, the use of a eutectic solution (most notably Au) has been used to grow Si 'whiskers' with substantial diameters [4], and is well understood and iterated upon over the years, with readably achievable nanometre scale sizes for a variety of material systems. In the absence of single crystal CuHa substrates, an approach using CuBr vacuum deposited on Si substrates was devised, leveraging the experiences gained in the earlier CuBr thin film work.

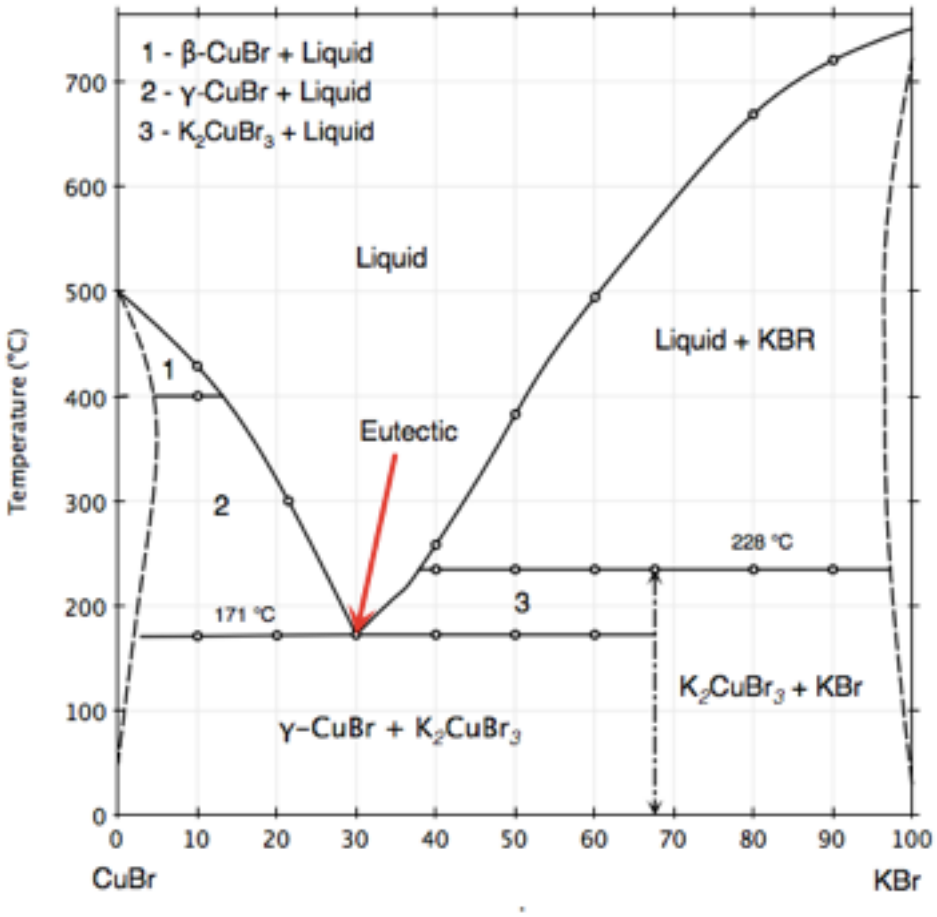

Figure 7.12 *- Phase diagram for the CuBr/KBr system, reproduced from [3].*

7.4.1. Conventional Vapor Liquid Solid Growth

VLS type growth has been studied extensively from the 1960's since the early work of Wagner *et al*. in the growth of Si, micron sized, 'whiskers'. Over the decades since, the dimensions have rapidly shrunk to the nanometre scale and nano-rod type structures can be grown from numerous compounds using the VLS approach [1, 4, 5, 6].

For Si, the VLS process is illustrated in figure 7.13 below. Initially, a thin film of Au is deposited onto a Si surface by a PVD process. This Au deposition is patterned so as to leave distinct Au regions on the surface - the pattern can be applied via various techniques such as lithography. Subsequently, the Si substrate is annealed at temperatures higher then the known Au/Si eutectic point so as to form Au/Si alloy droplets on the surface. The addition of a Si flux, delivered via

chemical or physical vapor deposition, causes the local supersaturation of the Au/Si eutectic droplets. Since Si has a higher melting point (~1414 °C) relative to the eutectic temperature of the droplet (from the Au/Si phase diagram, ~363 °C), the precipitation of the Si atoms out of the supersaturated eutectic droplet is in the solid phase and occurs at the eutectic droplet/Si substrate interface. This in turn forces the droplet upwards, allowing for the vertical growth of the Si whisker. The mechanism for the formation of classical Si 'whiskers' is illustrated in figure 7.13 below.

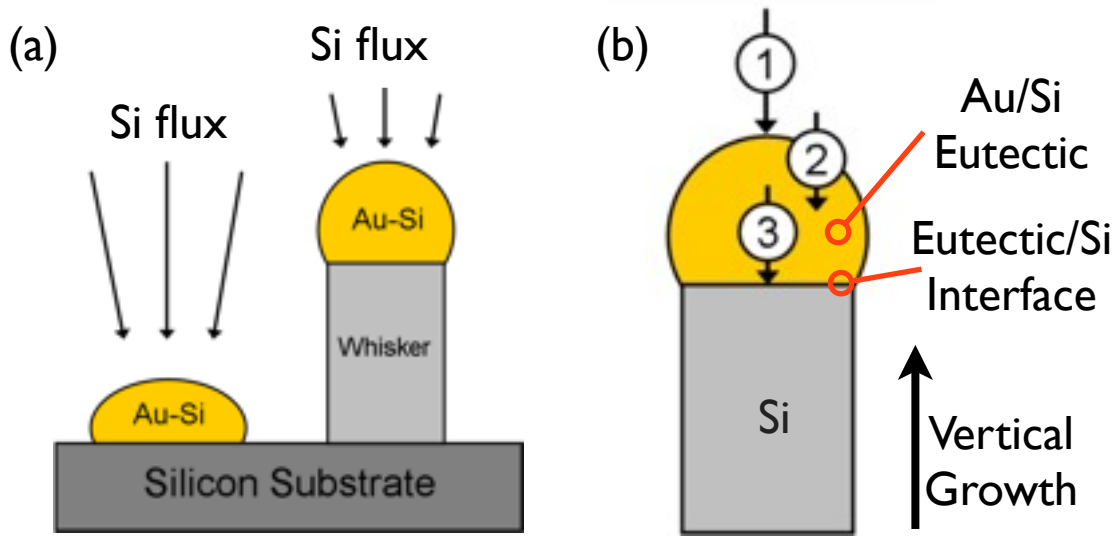

Figure 7.13 *- (a) Illustration of the growth of Si 'whisker' from Si substrate, catalyzed by the use of the Au/Si eutectic droplet, (b) route of absorbed materials through the droplet to the growth interface. Initial flux arrives (1) and is absorbed into the eutectic droplet (2) - finally, the supersaturated droplet precipitates out the Si as a solid at the growth interface (3), giving rise to the vertical growth of the Si whisker.*

7.4.2 VLS growth of CuBr using KBr

Taking inspiration from traditionally applied VLS growth, an approach using the CuBr/KBr eutectic system was envisioned. The fabrication processes was detailed previously in this chapter. The proposed growth mechanism for the microdot features is presented below in figure 7.14. There are a a number of notable features that are empirically observed via SEM and AFM that are unusual

relative to conventional VLS growth, and are likely characteristics of the unique approach taken in using the CuBr thin film as an underlayer in lieu of a single crystal CuBr substrate.

From the SEM and AFM imagery, there is a notable clearance of CuBr material around the microdot feature, exposing the underlying Si substrate. This feature can likely be explained by considering the behaviour of the eutectic droplet as it forms. Once the experimental temperature reaches the eutectic forming range (around 180 °C), the droplet will begin to form at the centre of the KBr spot, cannibalizing the underlying CuBr layer.

As this process begins, a central cavity is formed. This was empirically observed by stopping a growth run after 15 minutes and measuring the surface morphology via AFM and can be seen in figure 7.14 (sample was of a ~300 nm thick CuBr underlayer experiment). This cavity likely contains the central eutectic droplet, which will proceed to sink down into the film, absorbing CuBr into the eutectic droplet. Once this droplet reaches the Si substrate, it will flatten out and absorb surrounding CuBr from the 'sidewall' regions, creating the clearance area around the central droplet feature. At this point, it is proposed that the droplet switches from downwards movement to that of conventional VLS growth. The vertical growth component occurs with the CuBr flux being absorbed into the eutectic droplet feature, creating a supersaturation of CuBr and forcing the precipitation of solid γ-CuBr and K_2CuBr_3. This can be evidenced by examining the CuBr/KBr phase diagram in figure 7.12.

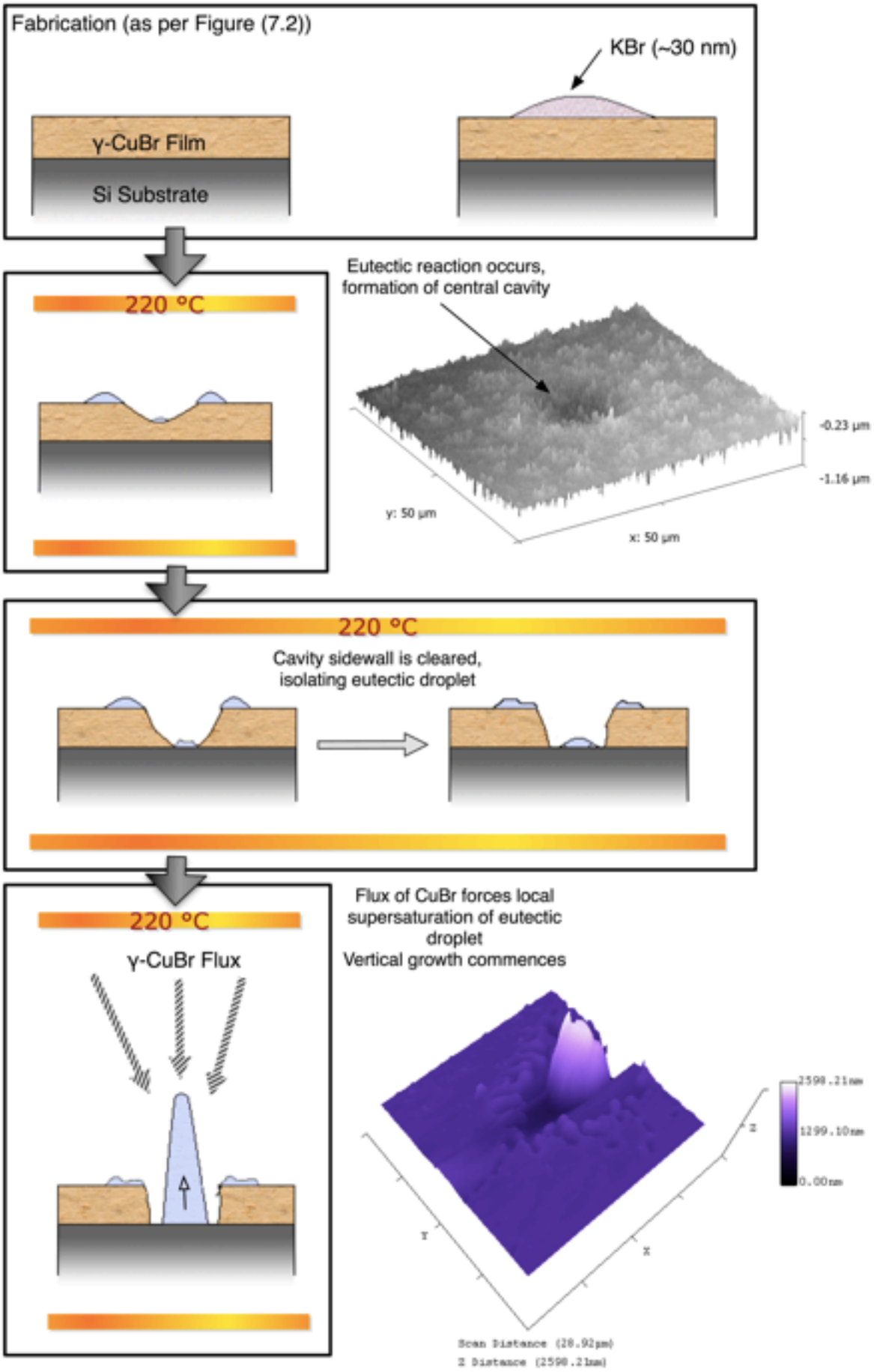

Figure 7.14 *- Proposed growth mechanism for formation of CuBr/KBr microdots.*

Additionally, XRD scans of microdot samples were taken and a typical scan can be seen in figure 7.15 below. From this scan, a number of peaks can be observed, not totally dissimilar to the XRD data taken for the LPE CuCl/KCl samples. The presence of the orthorhombic K_2CuBr_3 compound is clear in addition to residual KBr and the characteristic γ-CuBr <111>, <220> and <311> reflections discussed previously in chapter 6. The XRD data corroborates well with the likely growth mechanism and the information presented in the CuBr/KBr phase diagram.

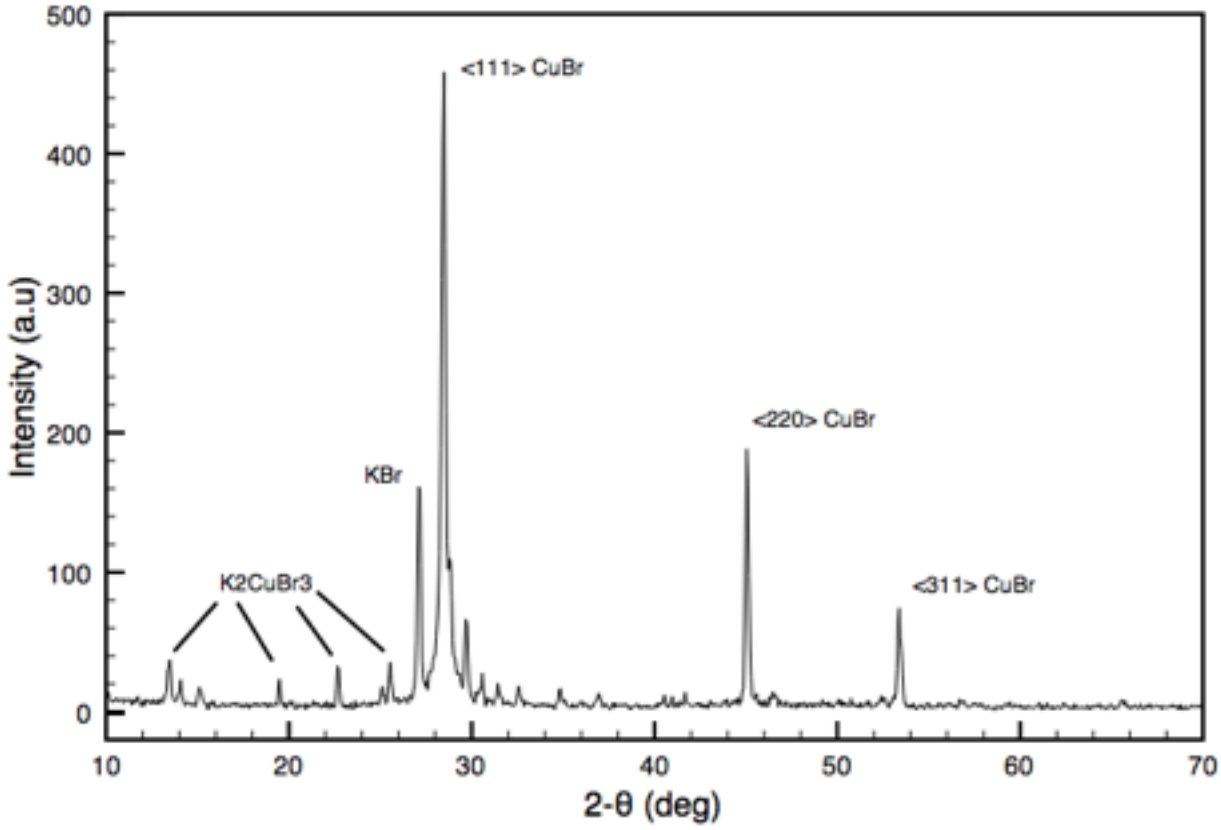

Figure 7.15 *- XRD scan of microdot sample (~300 nm γ-CuBr underlayer) on Si <100> substrate.*

As mentioned, microdot growth with the VLS type vertical component were readily observed for samples prepared using the ~150 nm and ~300 nm thick γ-CuBr under-layer, however this growth aspect was notably absent in the thicker ~600 nm sample. For these samples, the clearance area around the microdot was usually much reduced relative to the ~150 nm and ~300 nm samples, and linkage of the microdot to the sidewalls was commonly observed. It is proposed that the thickness

of the underlying γ-CuBr layer might play a limiting parameter for the formation of distinct microdot features. For the 150 nm and 300 nm samples, when the eutectic droplet is moving down through the film (cannibalizing it into the droplet), it is argued that any capillary force acting on the droplet is small, owing to the relatively thin thickness of the film. For the 600 nm sample however, the droplet has a larger distance to travel before it can reach the Si substrate. During this period, the likelihood of being drawn into a sidewall (leading to the linkages observed for these samples) is greater, which may effect the reduced clearance area around the microdot feature we observe.

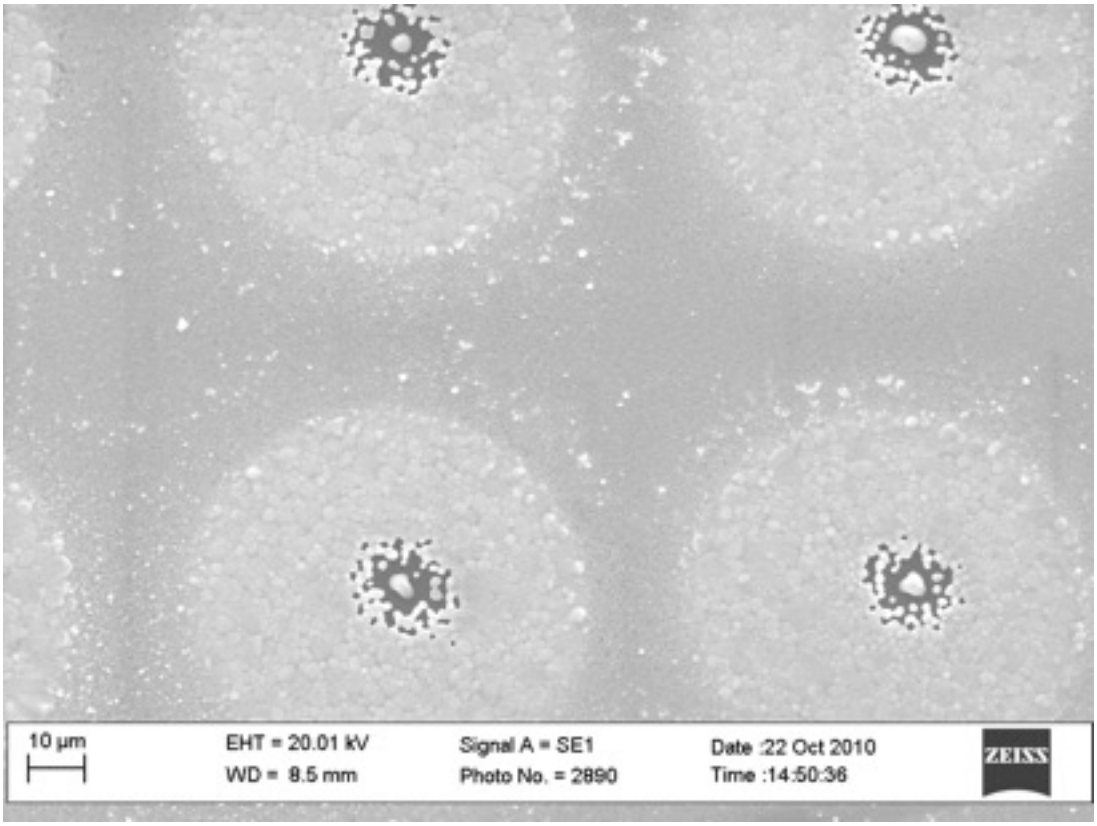

Figure 7.16 *- SEM image of microdot region on ~300 nm thick γ-CuBr underlayer.*

Another notable feature found throughout the series of experiments was the increased grain size of the crystallites within the KBr spot region. The SEM image in figure 7.16 above illustrates this phenomenon. It is observed that the region encompassed by the diameter of the original KBr spot has much larger crystal grain sizes, relative to the underlying γ-CuBr film. It is likely that this 'coarsening' is due to the KBr/CuBr reaction during the annealing stage, with the resulting imaged

grains likely being a intermix of K_2CuBr_3 as well as CuBr. An AFM image taken of a sample that was only annealed for 15 minutes can be seen below (figure 7.17), in which this coarsening phenomena can be partially observed. Clearly, an *in situ* observation would be more fruitful since the sample must be cooled before measurement, however this AFM is informative in that the central cavity can be clearly seen as can some coarsening or grain growth regions within the diameter of the original KBr spot.

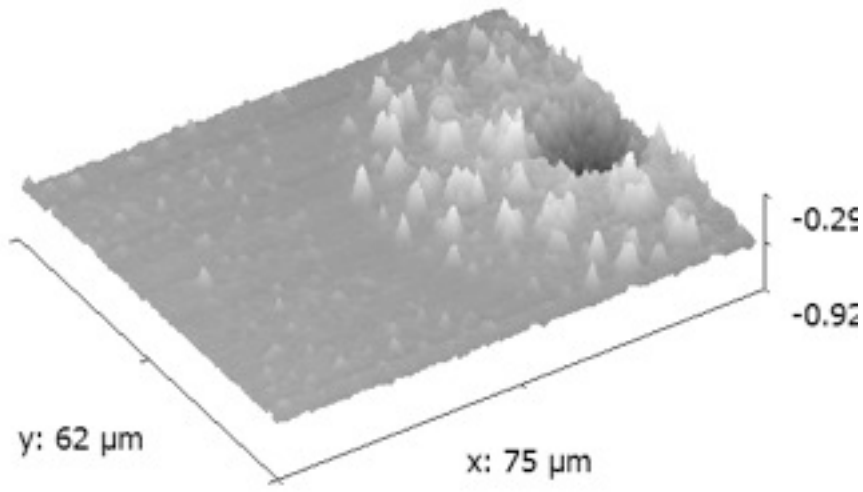

Figure 7.17 *- AFM image of ~ 300 nm sample after 15 minutes - region encompassed by the KBr spot can be seen in addition to the coarsening of the film in this area.*

7.5 Optical Characterization

In order to examine the optical properties of the microdots, conventional single point PL measurements were taken as detailed previously. In addition, the PL intensity could be spatially resolved by raster scan of the sample with the probe laser in order to create a mapping of a particular line. For all microdot samples, PL characterization reveals extremely bright UV-Blue

excitonic emission centered on the Z_f free exciton peak at ~418 nm, far superior to Z_f emission from γ-CuBr films deposited previously. This can be seen in a comparative PL scan below in figure 7.18. The room temperature PL spectrum for a microdot feature on a ~300 γ-CuBr underlayer sample is given as the blue line, acquired for 0.3 ms. A corresponding PL measurement is taken on a vacuum evaporated ~300 nm thick γ-CuBr sample, as detailed in chapter 6. It is clear that there is a substantial improvement in the Z_f emission relative to the nominal PVD γ-CuBr layer.

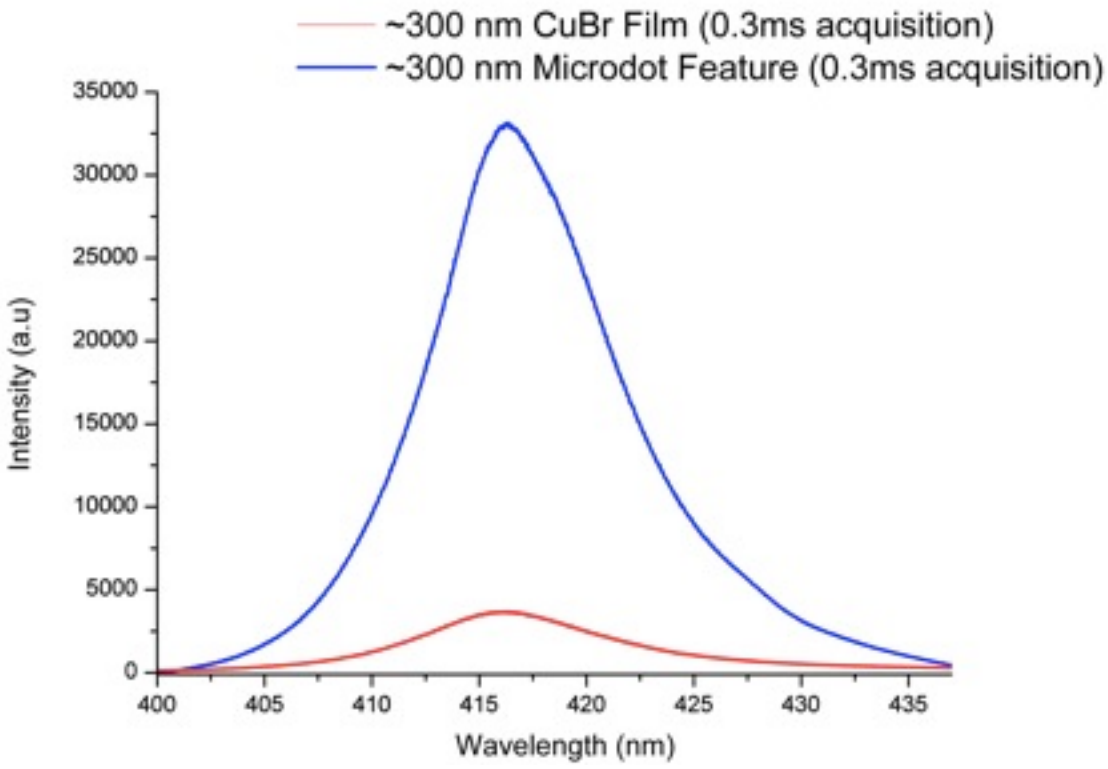

Figure 7.18 *- Comparative room temperature PL measurement corresponding to the free exciton emission intensity for a microdot feature (blue) against a nominal PVD deposited ~300 nm thick γ-CuBr thin film (red).*

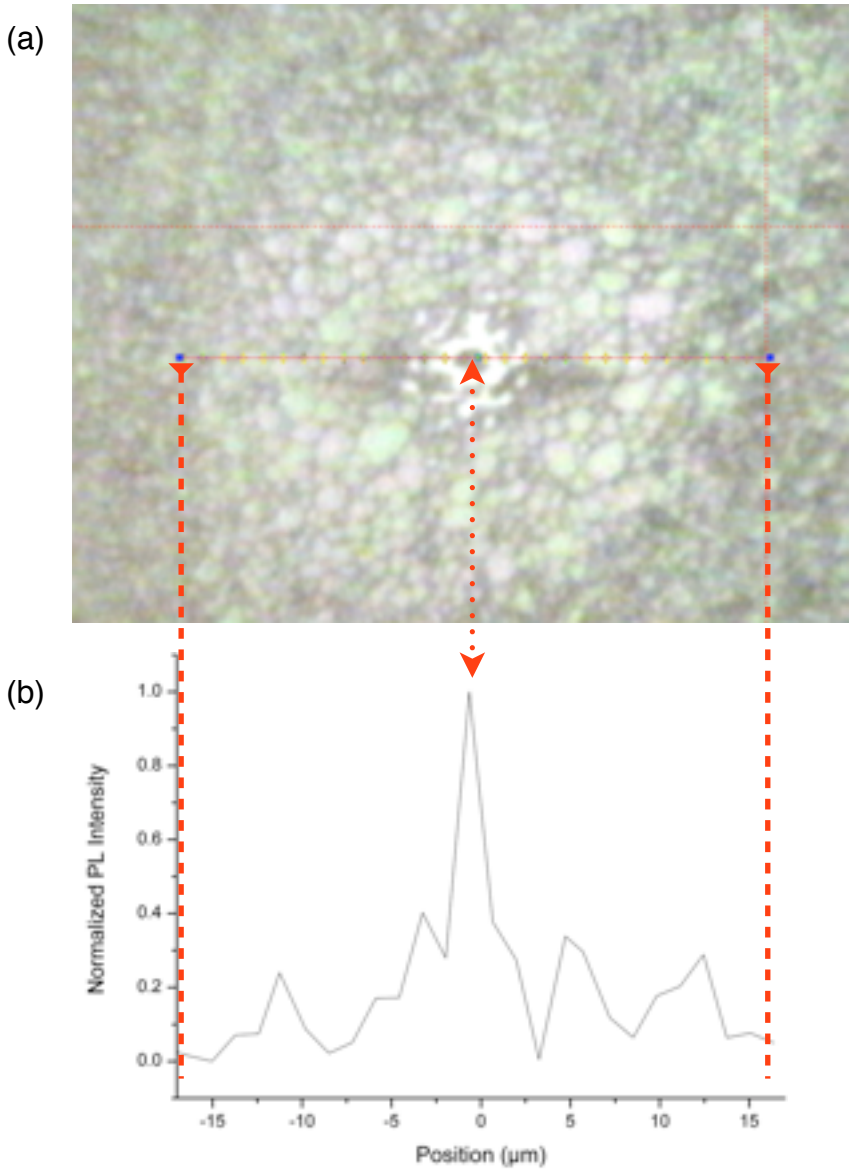

Figure 7.19 *- PL Intensity line scan across microdot feature and surrounding region on ~300 nm thick sample; (a) CCD capture of region, the horizontal red line denotes the line scan, (b) Normalized PL intensity mapped across the spatial positions, with maximum point of intensity corresponding to the microdot feature, 0.3 ms acquisition time.*

The above PL line scan reveals that the point of maximum intensity corresponds with the microdot feature. This characteristic is observed across all measured microdot samples, i.e. the maximum point of intensity corresponds with the microdot feature. Additionally, though not always observed

or easily mapped, there is usually a correlation between the clearance region and a local minima in the line scan, as illustrated in the figure 7.20 below.

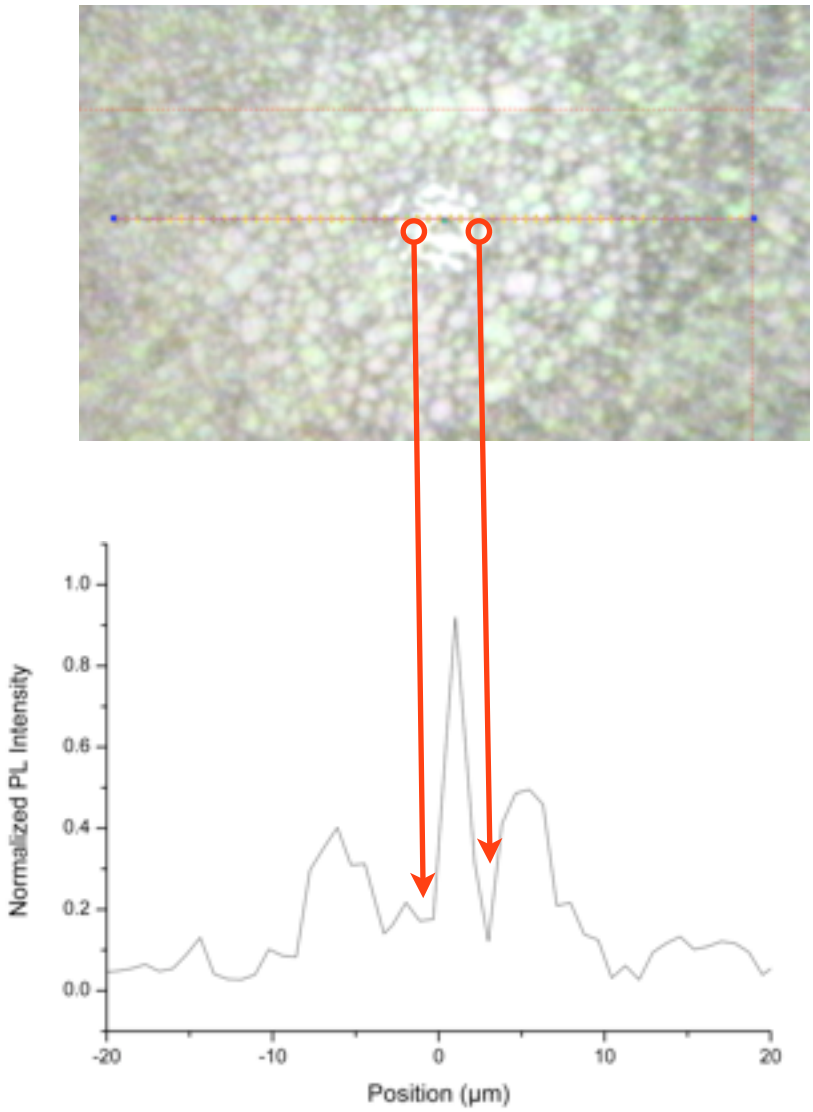

Figure 7.20 *- Normalized PL line scan of microdot region, showing correlation between reduction in luminescence and the bare Si region around the central microdot.*

A low level of luminescence persists at these locations, owing to scattered emission from the laser spot. The mechanism for the observed brilliance of the emission relative to nominal PVD deposited γ-CuBr thin films can likely be attributed to a number of possible explanations. Firstly, as detailed previously, the PL enhancement reported in work involving KHa and CuHa [7] can be extended to include microdot samples. The necessary use of the KBr salt for the formation of the eutectic droplet allows for the inclusion of KBr within the crystal. The additional anions introduced can fill

up the Br^- vacancies present and boost the peak intensity of the CuBr emission. The luminescence enhancement can also be observed in the area surrounding the microdot feature, previously encompassed by the KBr salt. This enhancement is relative to the untreated CuBr film region (though it is likely that some KBr could have migrated to these regions during the annealing stage). The presence of K within the microdot region was confirmed via EDX measurement (figure 7.21 below).

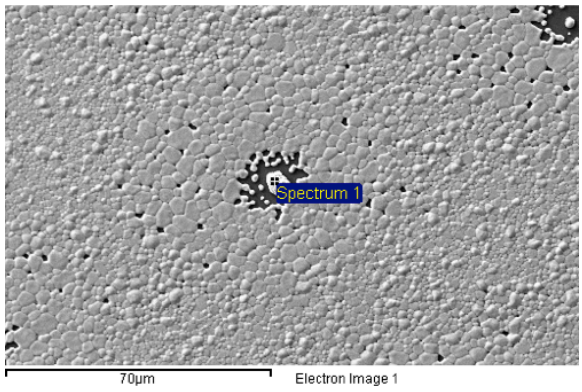

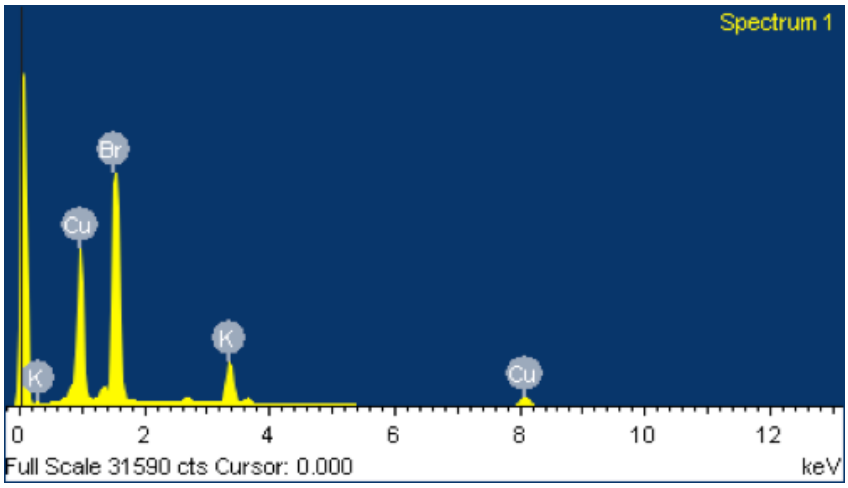

Figure 7.21 *- EDX spectra of central microdot feature.*

Assuming VLS growth, the precipitation of intermixed CuBr and, most likely, K_2CuBr_3, from the eutectic droplet during the VLS growth is also a potential source of the enhancement observed (by

the aforementioned contribution of anions). It is also possible that the microdots have a higher degree of crystallinity relative to their surrounding polycrystalline material, owing to their ordered precipitation from the eutectic droplet.

As has been discussed before, the relatively sparse information available on compounds such as K_2CuCl_3 and K_2CuBr_3 make it difficult to state exactly how they might contribute to the observed luminescence. The observation of the singular Z_f peak, as opposed to the host of contributing peaks observed in the earlier work with LPE samples involving KCl/CuCl melts, would likely suggest that the primary emission mechanism is still driven by the CuBr excitons with a probable enhancement owing to the interaction between the Potassium compounds and the CuBr itself.

7.6 Conclusions

Using a novel approach utilizing shadow masking, the vacuum deposition of KBr spots onto similarly deposited γ-CuBr epitaxial layers on a Si substrate has been carried out. Post-deposition annealing of the samples at 220 °C in conjunction with a small CuBr flux from a target source leads to the formation of specific, repeatable features, most notably large micron scale dots. A considerable vertical growth component of this microdot is observed for thin films with underlying γ-CuBr layers of ~150 nm and ~300 nm thicknesses, with observed heights ranging up to ~ 3.7 μm.

Certain features are commonly observed in the formation of these microdots, including a specific clearance around the microdot exposing the Si substrate and a coarsening of the grains within the region encompassed by the KBr. These features are explained in terms of the eutectic droplet forming and cannibalizing the underlying CuBr film. The coarsening of the remaining grains within the region out to the KBr diameter is likely due to the KBr interaction with the CuBr at the eutectic forming temperature.

The microdot features exhibit strong blue PL room temperature emission centered around the Zf emission at ~ 416 nm. The emission is far more intense then any previously observed CuBr thin film room temperature emission and it is suggested that this enhancement is due to the optically beneficial interaction between the KBr and the CuBr. It is also possible that the enhancement may be due to improved crystallinity of the material owing to the VLS type growth suggested.

It is likely that the observed growth method for the vertical growth is VLS type, which would be the first demonstration of VLS type growth of a CuHa material. It is probable that this method can be applied to the other CuHa materials using a similar experimental approach and could be scalable to a nanometre regime, allowing for potential growth of CuHa nano-wires with further research.

7.6 References

[1] C. Rao, F. Deepak, G. Gundiah, A. Govindaraj, Progress in Solid State Chemistry, Volume 31, 2003, pages 5–147.

[1] BlueAcre Technology Ltd. website: http://www.blueacretechnology.com

[3] R.M. Biefeld, Materials Research Bulletin, Volume 10, 1975, pages 1151-1156,

[4] R. Wagner, W. Ellis, Applied Physics Letters, Volume 4, 1964, page 90.

[5] L.V. Yashina, V.I. Shtanov, Z.G. Yanenko, Journal of Crystal Growth, Volume 252, 2003, pages 68-78.

[6] H. Yumoto, T. Sako, Y. Gotoh, K. Nishiyama, T. Kaneko, Journal of Crystal Growth, Volume 203, 1999, pages 136-140.

[7] S. Kondo, T. Saito, Journal of Luminescence, Volume 130, 2009, page 191-205.

Chapter 8 - Conclusions & Further Research

The objective of this thesis has been to investigate novel means for the deposition and growth of CuHa materials for potential optoelectronic applications. In this chapter, the conclusions of the research in the areas of CuCl LPE, CuBr thin films and the CuBr/KBr intermixed microdots are presented as well as suggested avenues for further research.

8.1 Liquid Phase Epitaxy

Growth of γ-CuCl on Si was one of the primary objectives for the work undertaken during this project, but achieving single crystal γ-CuCl epilayers proved technically challenging. While the case is seemingly strong for the potential of LPE growth of this material, a number of issues plague the CuCl-Si material system that make this difficult to achieve using the LPE setup detailed in this work:

- The CuCl-Si solid state surface reaction, as detailed in chapter 5, results in the formation of a copper silicide layer. This reaction greatly restricts the potential temperature range within which the CuCl/KCl melt can be driven to precipitate out an epilayer and logically constrains the room for LPE experimentation with the CuCl/KCl system to the extreme end of recorded (to the author's knowledge) low temperature LPE.
- The reactivity of CuCl and its readiness to form a visible skin on the surface, which would be an impediment to good wetting of the melt on the substrate.
- The discrepancy in the ionicity of the CuCl/KCl melt and the covalently bonded Si substrate. The differing bonding characteristics between the melt and the substrate make wetting of the melt and the substrate an issue as well as impacting on the potential formation of an epilayer.

- The nature of the CuCl/KCl eutectic system is also an issue. Ideal solvents for LPE should have a high solubility of the solute of a few percent at a workable temperature and have a temperature dependance of the solubility, which allows a precise adjustment of the supersaturation temperature. In the case of the CuCl/KCl eutectic system, solubility control is within a workable margin, however the large saturation of CuCl required to drive the melt into the CuCl and liquid phase (see figure 5.1) makes the melt prone to spontaneous nucleation, i.e. three dimensional growth within the melt rather than on the substrate. Unfortunately, the family of CuHa/AHa eutectic phase diagrams all follow a similar structure throughout their series and it is probable that these systems would manifest the same problem within their respective melts.

While the direct growth of single crystal γ-CuCl on Si has proven difficult, it should be noted that the formation of the intermixed textured polycrystalline CuCl/K_2CuCl_3 material has revealed many novel optical properties, notably the strong, broad room temperature emission under PL investigation and the extremely bright emission observed from samples under XEOL measurement.

This work made use of the horizontal sliding boat system as well as a novel modified tipping adaptation, however there exist a number of alternate LPE boat and system geometries that have been demonstrated and were mentioned in chapter 1. Each of these systems was usually designed so as to overcome a specific melt problem (e.g., the piston system was used in order to assist with melt skin oxide removal) or to further optimize and improve an existing method. The use of a piston type system could alleviate issues with wetting of the melt and substrate, but would require a more complicated experimental setup than the current LPE system can support.

Little is known about the K_2CuCl_3 (and similarly with K_2CuBr_3) compounds outside of their structural properties. Their optical properties with respect to luminescence studies are particularly

lacking, in part due to the difficulty in their production for study. It is noted from their phase diagrams for both the CuCl and CuBr compounds, that there exists a phase within which K_2CuCl_3/ K_2CuBr_3 can be directly precipitated from the melt. While the difficulties for such a growth would most likely align closely with those difficulties found with the growth of CuCl from LPE as discussed, the potential for a better understanding of these compounds would be worthwhile and it may be worth pursuing as future research.

Additionally, the LPE of CuBr has not been investigated previously. It is notable that CuBr and GaAs are near lattice matched (a_{CuBr} = 5.6773, a_{GaAs} = 5.65) and their relative ionicities are also closer (CuBr ionicity is 0.735 relative to GaAs at ~0.31) than the comparative CuCl/KCl and Si materials setup.

8.3 CuBr Thin Films & TFELD

This work provides a benchmark for future work on γ-CuBr thin films by giving an overview of the characteristics of vacuum evaporated γ-CuBr on Si, glass and ITO coated glass substrates. Using this PVD process, the structural and optical characteristics were examined. The γ-CuBr samples exhibited strong room temperature PL emission corresponding to the well known Z_f excitonic emission. Low temperature PL measurements also showed the Z_f exciton and the impurity bound, I_1, exciton. These measurements were in excellent agreement with previously reported spectroscopic studies of CuBr.

Structurally, our CuBr samples manifested a preferential growth along the <111> crystallographic direction on Si, in addition to smaller reflections at <220> and <311>. This confirmed the textured polycrystalline nature of the produced film and was consistent with previous work with γ-CuCl deposition.

Using the vacuum evaporation method, we have fabricated and tested a TFELD using γ-CuBr as an active layer. From this structure, Cu^+ emissions resulting from an applied potential difference (~20 V peak to peak) across the device were observed. It is tempting to assign the free exciton emission to the observed peak at ~418 nm, however the observed spectral peak shape is not characteristic of room temperature EL, where inhomogenously broad features are generally observed.

The general ease of deposition of CuBr via vacuum evaporation opens the possibility of deposition of highly crystalline γ-CuBr films on a number of potential substrates for blue optoelectronic applications. One area for future work with vacuum evaporation of CuBr is the investigation of potential dopants. The future use of a co-evaporation technique could also allow for the doping of these CuBr films, which could pave the way for a p–n type light emitting CuBr device.

8.5 CuBr/KBr Microdots

Further work investigating the intermixed CuBr/KBr microdots is also promising - as mentioned, it may be possible to scale the feature growth down to the nanometre range. One possible approach would be the use of colloidal nano-lithography as a means to create a shadow mask with nanometre sized openings. For example, by depositing colloidal nano-spheres on top of a CuBr underlayer and then evaporating KBr into the gaps between the colloids, nanometre resolution could be reached.

The results shown for the work with the CuBr/KBr interaction and likely VLS growth are quite remarkable considering the relatively un-sophisticated experimental setup used (see figure 7.5). It can be seen that both the CuBr flux and the sample itself are thermally coupled, i.e. it is not possible to alter the temperature for either the flux or the sample independently within this setup. A more

sophisticated setup, whereby the temperature of the two systems are decoupled, would allow for higher CuBr fluxes while still maintaining the eutectic temperature at the sample.

8.4 CuHa Optoelectronics

As reported in chapter 1, the growth of CuHa single crystals via numerous growth methods such as Czochralski, Bridgeman, etc, has been successfully achieved by previous researchers. To date, however, no work has been carried out in investigating the optoelectronic potential for Blue/UV light emission of these single crystals. It is envisioned as a follow on project from this work that a simple Czochralski or Bridgeman system could be designed using some of the available furnaces and utilizing the experiences learned with the LPE construction during the project. Since much of the experimental setup for single crystal growth has been undertaken and reported, it is hoped that this work can be replicated and ingots of CuHa material produced and cleaved for potential device development or as a substrate material. Coupled with recent work [1-3] in this area involving doping studies of polycrystalline, vacuum deposited and sputtered CuHa materials, it is likely that n-type doping using Zn could be incorporated directly into the growth melt. A secondary process using immersion in an Oxygen plasma could result in p-type doping, which could form the basis for a rudimentary p-n type junction.

8.5 References

[1] L. O Reilly, A. Mitra, F. Lucas, G. Natarajan, Journal of Material Science: Materials in Electronics, Volume 20, 2007, pages 76-80.

[2] K.V. Rajani, F. Olabanji Lucas, S. Daniels, D. Danieluk, A.L. Bradley, A. Cowley, M.M. Alam, P.J. McNally, Thin Solid Films, 2011.

[3] D. Danieluk, A. L. Bradley, A. Mitra, L. O'Reilly, F. Lucas, A. Cowley, P. J. McNally, B. Foy, E. McGlynn, Journal Material Science: Materials in Electronics, Volume 5, 2007.

Appendix A - XRD Diffraction Data for CuHa and Related Compounds

K_2CuBr_3

2θ	Intensity	H	K	L
13.487	25	0	2	0
14.205	10	2	0	0
15.211	30	1	2	0
19.537	15	2	2	0
21.394	15	1	3	0
22.783	35	1	1	1
25.208	25	3	2	0
25.652	30	1	2	1
28.587	15	2	2	1
28.967	65	0	3	1
29.258	75	4	1	0
29.828	100	1	3	1
30.591	75	2	4	0
31.555	60	4	2	0
32.729	30	3	2	1
34.925	50	1	4	1
36.071	15	4	1	1
36.884	70	2	5	0
37.917	15	4	2	1
40.991	15	4	3	1
41.745	50	0	0	2
45.765	30	3	5	1
46.713	40	3	6	0
48.376	20	6	0	1
48.874	20	1	7	0

K_2CuCl_3

2θ	Intensity	H	K	L
10.191	1	1	1	0
14.102	297	0	2	0
14.752	524	2	0	0
15.925	421	1	2	0
20.463	95	2	2	0
22.303	104	0	1	1
22.490	17	1	3	0
23.322	82	3	1	0
23.516	176	1	1	1
25.873	103	2	0	1
25.944	95	2	3	0
26.575	393	1	2	1
26.846	271	2	1	1
28.424	24	0	4	0

29.585	528	2	2	1
29.757	178	4	0	0
30.127	176	0	3	1
30.615	186	4	1	0
31.055	999	1	3	1
31.677	45	3	1	1
32.169	303	2	4	0
33.070	632	4	2	0
33.701	20	2	3	1
34.064	212	3	2	1
36.363	83	3	4	0
36.493	187	1	4	1
36.493	187	1	5	0
36.787	52	4	0	1
36.787	52	4	3	0
37.502	16	4	1	1
37.745	116	3	3	1
38.146	13	5	1	0
38.861	208	2	4	1
38.861	208	2	5	0
39.581	155	4	2	1
40.197	22	5	2	0
41.618	2	4	4	0
41.896	27	0	5	1
42.484	143	3	4	1
42.484	143	3	5	0
42.598	181	1	5	1
42.857	81	4	3	1
43.038	432	0	0	2
43.435	64	5	3	0
44.015	79	5	1	1
44.651	2	2	5	1
45.306	4	6	0	0
45.512	21	0	2	2
45.738	39	2	0	2
45.849	33	5	2	1
45.849	33	6	1	0
46.170	35	1	2	2
46.338	19	2	1	2
47.132	2	4	4	1
47.132	2	4	5	0
47.687	110	5	4	0
47.687	110	6	2	0
47.918	175	3	5	1
48.103	98	2	2	2
48.785	162	5	3	1
49.112	20	1	3	2
49.112	20	3	6	0
49.214	26	1	6	1
49.519	15	3	1	2
50.502	43	6	0	1
50.502	43	6	3	0
51.060	110	2	6	1
51.060	110	6	1	1

51.201	61	3	2	2
51.496	14	1	7	0
52.229	9	4	5	1
52.385	11	0	4	2
52.728	9	6	2	1
52.728	9	5	5	0
52.979	11	1	4	2
53.198	42	4	0	2
53.352	50	2	7	0
53.352	50	4	6	0
53.736	47	4	1	2
53.939	40	3	3	2
53.939	40	7	1	0
54.034	19	3	6	1
54.355	6	6	4	0
54.733	87	2	4	2
55.326	199	4	2	2
55.326	199	6	3	1
55.525	116	7	2	0
55.700	24	0	7	1
56.269	107	1	7	1
57.430	111	5	5	1
57.576	86	3	4	2
57.704	24	1	5	2
57.956	93	2	7	1
57.956	93	4	6	1
58.105	79	7	3	0
58.576	32	7	1	1
58.816	21	0	8	0
58.816	21	5	1	2
59.005	12	6	4	1
59.005	12	6	5	0
59.365	58	2	5	2
59.365	58	1	8	0
60.070	8	4	7	0
60.070	8	7	2	1
60.348	11	5	2	2
60.702	70	3	7	1
60.999	13	2	8	0
61.413	1	4	4	2
61.600	5	7	4	0
61.799	11	8	0	0
62.072	46	3	5	2
62.288	27	8	1	0
62.635	31	0	6	2
62.802	41	5	3	2
63.405	56	6	5	1
63.751	35	8	2	0
63.751	35	1	8	1
64.264	3	6	0	2
64.426	10	6	6	0
64.426	10	4	7	1
64.742	4	2	6	2
64.742	4	6	1	2

64.864	7	5	7	0
65.320	5	2	8	1
65.899	30	7	4	1
65.899	30	7	5	0
66.166	74	5	4	2
66.166	74	6	2	2
67.299	20	4	8	0
67.299	20	3	6	2
67.576	16	1	9	0
67.743	11	1	1	3
67.966	3	3	8	1
67.966	3	8	2	1
68.506	13	6	3	2
68.803	5	2	0	3
69.136	13	2	9	0
69.136	13	1	2	3
69.266	19	2	1	3
69.266	19	1	7	2
70.090	36	7	5	1
70.335	24	8	3	1
70.335	24	5	5	2
70.645	23	2	2	3
70.865	34	2	7	2
70.865	34	4	6	2
71.038	41	7	6	0
71.038	41	9	1	0
71.191	23	0	9	1
71.429	68	4	8	1
71.429	68	1	3	3
71.607	36	3	9	0
71.607	36	1	9	1
72.402	1	9	2	0
72.726	12	7	2	2
72.917	8	2	3	3
73.129	19	3	2	3
73.129	19	2	9	1
73.457	8	8	4	1
73.457	8	8	5	0
74.589	12	1	4	3
74.589	12	9	3	0
74.771	10	4	0	3
74.973	27	7	3	2
75.068	28	7	6	1
75.068	28	9	1	1
75.219	17	4	1	3
75.307	16	5	6	2
75.600	23	0	8	2
75.600	23	3	9	1
75.849	24	5	8	1
76.054	16	2	4	3
76.054	16	1	8	2
76.214	8	1	10	0
76.405	7	9	2	1
76.553	13	4	2	3

76.712	8	4	7	2
77.226	2	6	8	0
77.472	15	8	5	1
77.472	15	2	8	2
77.668	23	2	10	0
78.081	6	7	4	2
78.081	6	0	5	3
78.260	8	8	0	2
78.475	10	3	4	3
78.585	14	1	5	3
78.585	14	9	3	1
78.700	11	8	1	2
78.763	11	4	3	3
79.014	10	4	9	1
79.417	4	5	9	0
79.574	8	5	1	3
79.870	6	10	0	0
80.019	15	8	2	2
80.019	15	3	10	0
80.308	8	10	1	0
80.620	2	6	6	2
80.809	8	7	7	1

Appendix B - Additional AFM Images of CuBr/KBr Microdots

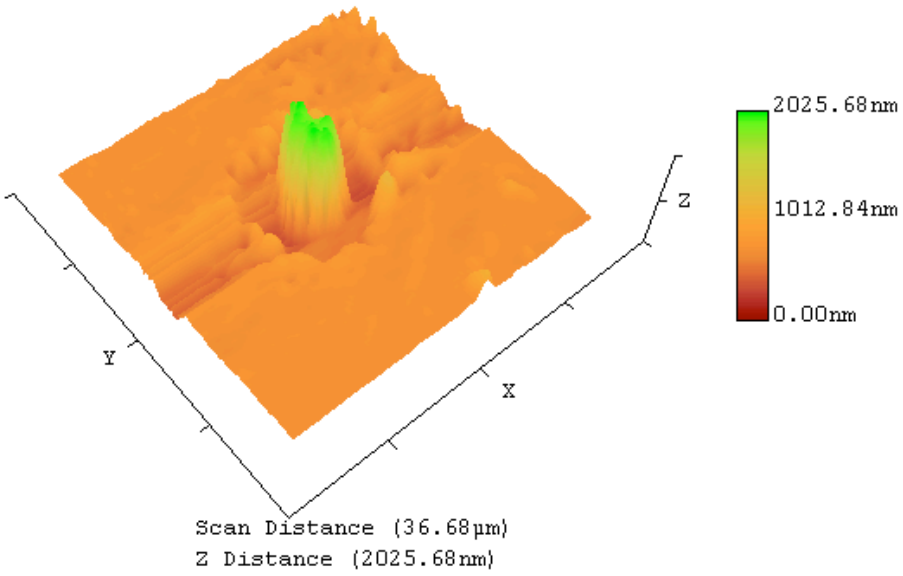

Figure B1 *- Microdot feature on ~150nm γ-CuBr underlayer.*

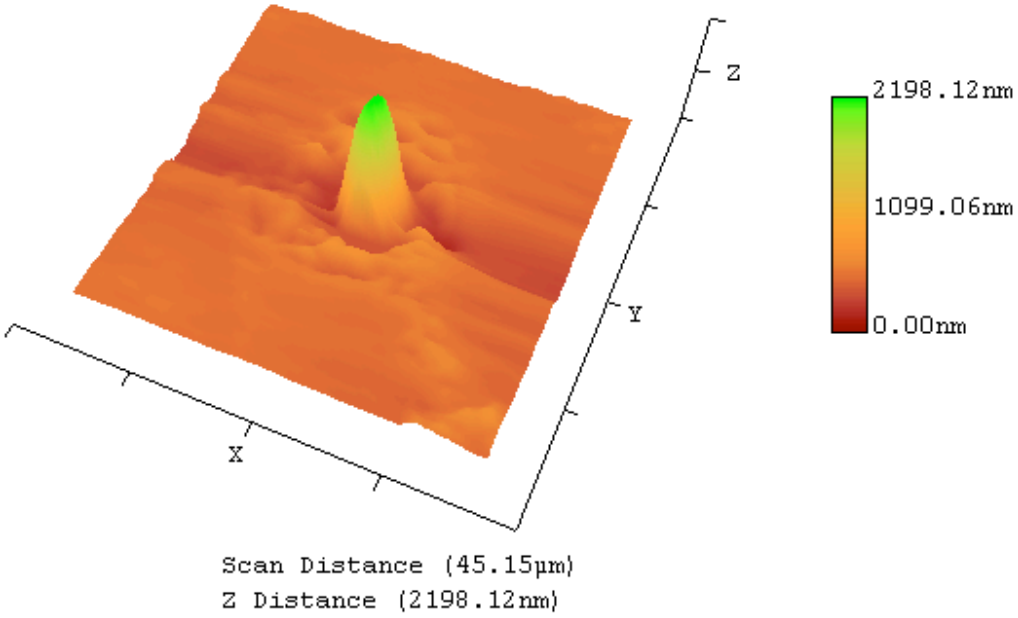

Figure B2 *- Microdot feature on ~300nm γ-CuBr underlayer.*

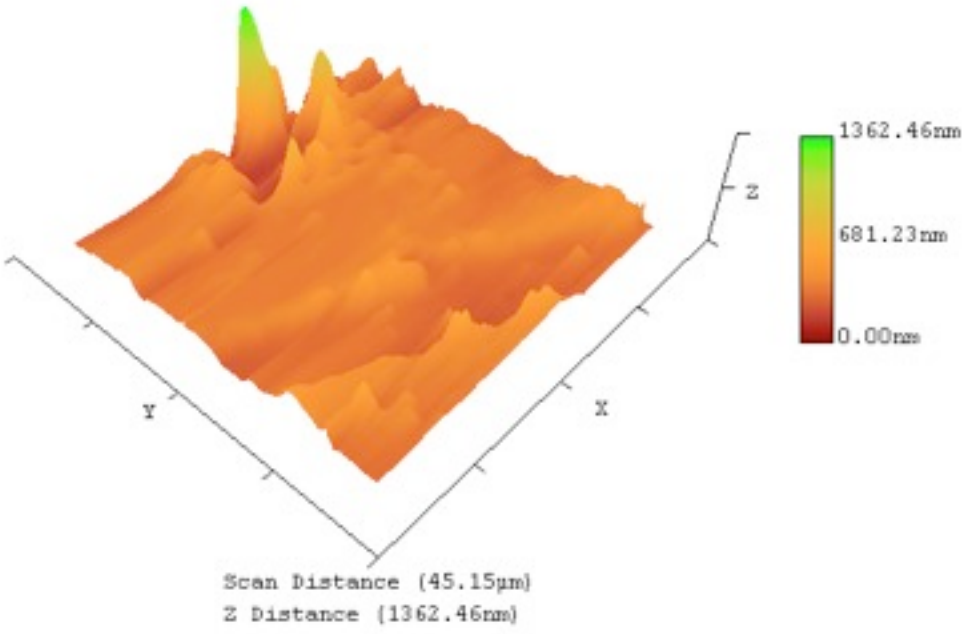

Figure B3 *- Microdot feature on ~150 nm γ-CuBr underlayer. A notable tweezer scratch can be seen running horizontally.*

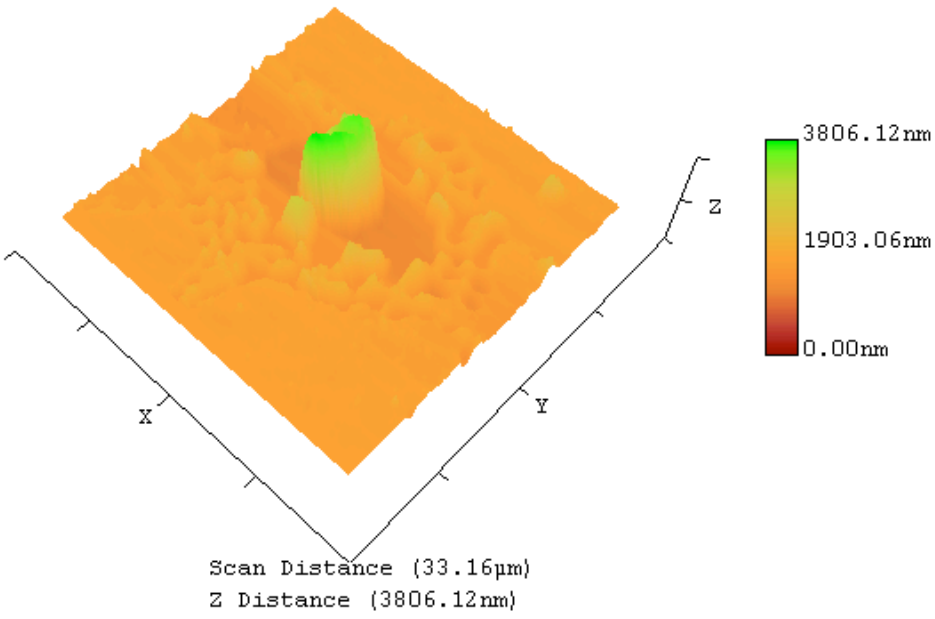

Figure B4 *- Microdot feature on ~150nm γ-CuBr underlayer.*

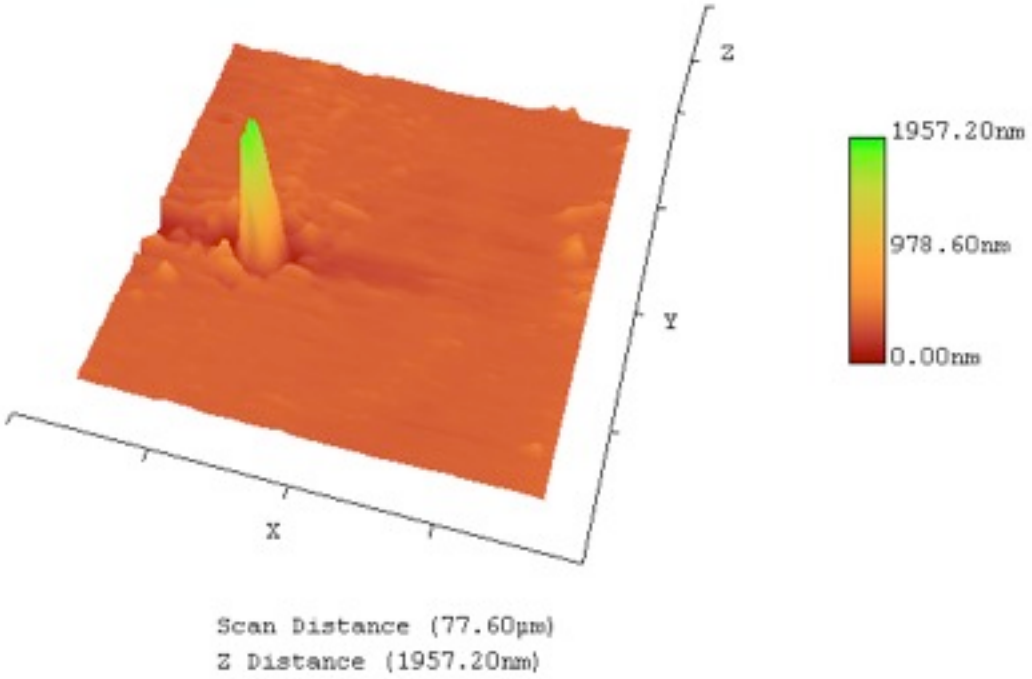

Figure B5 *- Microdot feature on ~300nm γ-CuBr underlayer.*

Appendix C - Publications

Published Papers:

- A. Cowley, F. Lucas, E. Gudimenko, M. Alam, D. Danieluk, A. L. Bradley, P. J. McNally, 'Electroluminescence of γ-CuBr thin films via vacuum evaporation deposition', Journal of Physics D: Applied Physics, Volume 43, 2010.

- A. Cowley, B. Foy, D. Danilieuk, P. J. McNally, 'UV emission on a Si substrate: Optical and structural properties of γ-CuCl on Si grown using liquid phase epitaxy techniques', Physica Status Solidi (a), Volume 206, 2008, page 923.

- F. O. Lucas, A. Cowley, S. Daniels, P. J. Mcnally, 'CuBr blue light emitting electroluminescent thin film devices', Physica Status Solidi (c), 2011.

- K. V. Rajani, F. Lucas, S. Daniels, D. Danieluk, A. L. Bradley, A. Cowley, M. Alam, P. J. McNally, 'Growth of n-type γ-CuCl with improved carrier concentration by pulsed DC sputtering: Structural, electronic and UV emission properties', Thin Solid Films, In Press.

- B. Foy, E. McGlynn, A. Cowley, P. J. McNally, M. O. Henry, 'Spatially Resolved Investigation of the Optical and Structural Properties of CuCl Thin Films on Si', AIP Conference Proceedings, 2009, pages 209-212.

- F. Lucas, A. Cowley, P. J. McNally, 'Structural, optical and electrical properties of Co-evaporated CuCl/KCl films', Physica Status Solidi (c), Volume 6, 2008, page 114.

- D. Danieluk, A. L. Bradley, A. Mitra, L. O'Reilly, F. Lucas, A. Cowley, P. J. McNally, B. Foy, E. McGlynn, 'Optical properties of undoped and oxygen doped CuCl films on silicon substrates', Journal of Materials Science: Materials in Electronics, Volume 5, 2007.

- M. M. Alam, F Olabanji Lucas, A. Cowley, D. Danieluk, A L Bradley, S. Daniels and P. J. McNally, 'Temperature dependent photoluminescence of nanocrystalline γ-CuCl hybrid films', Journal of Luminescence, 2011.

- M. M. Alam, A. Cowley, S. Daniels and P. J. McNally, 'Evaluation of conduction mechanism and electronic parameters for Au/Organic-Inorganic CuCl hybrid film/ITO structures', Semiconductor Science and Technology, 2011.

- M. M. Alam, F. Olabanji Lucas, A. Cowley, K. Crowley, S. Daniels, K.V. Rajani, P. J. McNally; 'Synthesis and Characterization of Copper (I) Chloride (CuCl) Nanocrystals in Conductive Polymer for UV light Emitters', MRS Conference Proceedings, 2010 (Accepted for publication).

<u>Conference Presentations:</u>

- European Materials Research Society Spring Meeting (EMRS), Nice, France, 2011 - Oral presentation entitled 'Enhanced excitonic Photoluminescence from intermixed CuBr/KBr microdots'.

- International Conference on Optical and Optoelectronic Properties of Materials and Application(ICOOPMA), Budapest, Hungary, 2010 - Oral presentation entitled 'CuBr Blue Light Emitting ElectroluminescentThin Film Device'.

- Photonics Ireland, Kinsale, Ireland, 2009 - Poster entitled 'Towards CuBr based light emitting devices: Optical and structural properties of vacuum evaporated γ-CuBr films'.

- International Conference on Optical and Optoelectronic Properties of Materials and Application(ICOOPMA), Edmonton, Canada, 2008 - Oral presentation entitled 'UV emission on a Si substrate: Optical and structural properties of Liquid Phase Epitaxy of γ-CuCl on Si'